LONDON SOUTH BANK UNIVERSITY

Transforming Carbon Quantum Dots Synthesis: Innovative Continuous Hydrothermal Flow Methods for Environmental Advancements and Beyond

by

Kiem Giap Nguyen

ORCID no. 0000-0002-8366-3947

A Thesis submitted in partial fulfilment of the requirements of
London South Bank University for the degree of Doctor of
Philosophy

London, United Kingdom

2023

Acknowledgements

The successful completion of this thesis would not have been possible without the support and guidance of many people. I am deeply grateful to everyone who has helped me along this rewarding PhD journey.

I would like to express my deepest gratitude to my supervisor, Dr Suela Kellici, for her invaluable guidance and support throughout my research project and thesis writing. I consider myself incredibly fortunate to have had the opportunity to work under her supervision. Her immense knowledge and passion for research have been a constant source of inspiration. Thank you for always making time for my questions and discussions. I appreciate the research skills and scientific rigor she has instilled in me through her mentoring. From brainstorming ideas, designing experiments, analysing data to writing papers, her step-by-step guidance has nurtured me into an independent researcher. I could not have successfully completed this project without her patience, encouragement, and unwavering confidence in me. It has been a privilege to work with someone so passionate about research and committed to their students' success. I hope to carry forward her lessons through the rest of my academic and professional career.

I would like to extend my sincere gratitude to my second supervisor, Dr Tariq Sajjad, for his invaluable training and guidance. Dr Sajjad, your extensive expertise in photoluminescence and wide-ranging knowledge of optical characterisation instruments has enriched my research skills tremendously. Thank you for taking the time to comprehensively train me on the working principles and applications of techniques like fluorescence, lifetime measurements, and quantum yield determination.

To all the current and former members of the Nano2D Lab group - my colleagues. I would like to express my heartfelt gratitude to all of you, Dr Ioan Alexandru Baragáu, Dr Zhen Lu, Mr Conor Paul Davids, Dr Uthman Alli, Dr Sunil J. Hettiarachchi, Mr. Heider Salazar, Guru Prasanna and Dr Matthew Billing. I sincerely appreciate the camaraderie we shared - brainstorming ideas, troubleshooting experiments, celebrating successes, and learning from setbacks together. Your diverse talents, perspectives, and kindness enriched my graduate school experience tremendously. I hope I was able to give back a tiny fraction of the encouragement and motivation you selflessly offered me.

To the team of technicians at LSBU, I wish to thank Mr Andrew Ascroft, Mr William Cheung, and Mr Ken Unadkat for generously sharing their time, knowledge, and hands-on skills, which enabled me to progress with the demanding experimental works. I would like to thank the London South Bank University for my PhD scholarship in the School of Engineering.

I would also like to sincerely thank the following collaborators for their invaluable assistance and contributions: Dr. Tobias Heil at the Max Planck Institute of Colloids and Interfaces for acquiring outstanding TEM images, Dr Adela Nicolaev and at National Institute of Materials Physics for XPS characterisation. Dana G. Popescu and Daniel Gherca at National Institute of Materials Physics for XRD-Rietveld refinement. Dr James Bowen at Open University for your help with AFM characterisation. Dr Andrei Sapelkin at Queen's Mary University for Raman measurement. Dr Radga Gromnicova at Open University is thanked for acquisition of TEM images of samples reported in chapter 4. Dr Valadimir Korolkov at Park System for the AFM measurement reported in chapter 7. Dr Laura Elena Abramiuc at National Insitute of Physics for XPS characterisation, results of which are reported in chapter 6. Dr Shaoliang Guan at Harwell-XPS for UPS characterisation, results of which are reported in chapter 5,6 and 7.

Last but foremost, I am eternally grateful to my fantastic wife, who has been my rock through this process. Thank you for always believing in me, even when I doubted myself. Your unwavering confidence in my abilities motivated me daily. Despite my busy PhD schedule, you took care of everything at home with a smile so I could focus on my research. I could not have done this without your love, patience, and understanding. You are my source of strength. To my wonderful mother and loving aunt, thank you both for instilling in me from a young age the value of education and hard work. You taught me perseverance and grit - qualities that guided me through the challenges of PhD research.

I lovingly dedicate this thesis to my mum, wife, and aunt!

Abstract

Carbon quantum dots (CQDs) are an emerging class of nanomaterials exhibiting unique size-dependent optical and electronic properties. Owing to their high photoluminescence, chemical stability, low toxicity, and surface functionalization capabilities, CQDs show tremendous potential for diverse applications in energy harvesting, sensing, optoelectronics, and biomedicine. However, conventional CQD synthesis methods involve toxic organic solvents, high energy consumption, long reaction times, and poor control over particle size distribution and properties. This PhD research focused on the continuous hydrothermal flow synthesis (CHFS) of CQDs from renewable precursors as a rapid, sustainable, and scalable production route. A systematic investigation was undertaken to establish relationships between synthesis conditions (precursor composition, dopant concentrations) and final CQD characteristics. State-of-the-art spectroscopic and microscopic characterisation techniques provided fundamental insights into nucleation, growth mechanisms, and surface chemistry during CQD formation via CHFS. By tuning the CHFS parameters, photoluminescent CQDs with uniform size distribution, tailored surface chemistry, and reproducible optoelectronic properties were synthesised. This thesis demonstrates the first comprehensive study utilising CHFS for controlled and optimized synthesis of CQDs. The fundamental understanding of CQD formation mechanisms and structure-property correlations established here will aid the customised design of CQDs for diverse cutting-edge applications in sensing, catalysis and beyond.

Research Output

List of publish cations

- Nguyen, K.G., Baragau, I.-A., Gromicova, R., Nicolaev, A., Thomson, S.A.J., Rennie, A., Power, N.P., Sajjad, M.T., Kellici, S., 2022. Investigating the effect of N-doping on carbon quantum dots structure, optical properties and metal ion screening. *Sci Rep* 12, 13806. https://doi.org/10.1038/s41598-022-16893-x. (This article is in the top 25% of all research outputs scored by Altimetric)

- Baragau, I.-A., Buckeridge, J., Nguyen, K.G., Heil, T., Sajjad, M.T., Thomson, S.A.J., Rennie, A., Morgan, D.J., Power, N.P., Nicolae, S.A., Titirici, M.-M., Dunn, S., Kellici, S., 2023. Outstanding visible light photocatalysis using nano-TiO_2 hybrids with nitrogen-doped carbon quantum dots and/or reduced graphene oxide. *J. Mater. Chem.* A 11, 9791–9806. https://doi.org/10.1039/D2TA09586F. (Inside cover of the journal and 2023 Journal of Materials Chemistry A Most Popular Articles).

- Iborra-Torres, A., Huš, M., Nguyen, K.G., Vamvakeros, A., Sajjad, M.T., Dunn, S., Mertens, M., Jacques, S., Beale, A.M., Likozar, B., Hyett, G., Kellici, S., Middelkoop, V., 2023.3D printed $SrNbO_2N$ photocatalyst for degradation of organic pollutants in water. *Mater. Adv*. 4, 3461–3472. https://doi.org/10.1039/D2MA01076C. (a part of collection: Popular Advances and Advanced Functional Materials and Manufacturing Process).

Participation in Conferences/Seminars

- Carbon 22 Conference, Imperial College: “Continuous hydrothermal synthesis of biomass derived carbon quantum dots” Oral presentation (2022).
- London Doctoral Academy Postgraduate Research Summer School, London South Bank University: “Continuous hydrothermal synthesis of biomass derived carbon quantum dots” Oral presentation (2022).
- Chemical Science Symposium, Royal Society of Chemistry: “Unique pathways in the “artificial atoms” synthesis”, Oral and Poster presentation (2022).
- London Centre Energy Engineering symposium: “Continuous hydrothermal synthesis of biomass derived carbon quantum dots” – Oral presentation, (2022).
- The 28th IUPAC Symposium on Photochemistry 2022 (Amsterdam, Netherlands) and ACS Spring 2023 (USA), “Transient absorption studies of TiO_2 and TiO_2 with rGO”, Poster presentations in collaboration with Edinburgh Instruments.

Table of Contents

List of Figures

List of Tables

List of Abbreviations

0D - zero-dimensional

1D - one-dimensional

2D - two-dimensional

AFM - atomic force microscopy

at% - atomic percentages

au - absorbance units

a.u. - arbitrary units

BET - Brunauer–Emmett–Teller theory

BPR: back-pressure regulator

CBM - conduction band minimum

CHFS - continuous hydrothermal flow synthesis

CNDs – carbon nano dots

CQDs - carbon quantum dots

CPDs – carbon polymer dots

eV - electron-volt

FTIR - Fourier-transform infrared spectroscopy

HOMO - highest occupied molecular orbital

HRTEM - high-resolution transmission electron microscopy

IFE - Inner Filter Effect

kPa – kilopascal

LUMO - lowest unoccupied molecular orbital

LSBU: London South Bank University

NCQDs - nitrogen-doped carbon quantum dots

N-doped - nitrogen-doped

P25 - Degussa (commercial TiO_2)

PLQY- photoluminescence quantum yield

PL - photoluminescence

ppm - parts per million

ppb - parts per billion

QY - quantum yield

rpm - rotations per minute

UV-Vis - ultraviolet and visible spectrophotometry

XPS - X-ray photoelectron spectroscopy

XRD - X-ray diffraction analysis

λ: wavelength

List of Definitions

- **Band structure** refers to the permitted energy levels electrons can occupy in a material. It consists of the valence band, conduction band, and forbidden band gap between them. Electron transitions from valence to conduction band occur when they gain enough energy to cross the band gap.

- **Band gap** is the minimum energy needed for electrons to jump from the valence to conduction band. Large band gaps require high energy for transitions, making a material an insulator. Band gap is measured in electron-volts (eV).

- **Blueshift** is decreasing emission wavelength with changing excitation.

- **Direct bandgap**: A direct bandgap refers to a semiconductor material in which the minimum of the conduction band and the maximum of the valence band occur at the same value of crystal momentum (k-vector)

- **Electron-volt** is a unit of energy equal to the amount gained by an electron accelerated by 1-volt potential difference.

- **Excitation wavelength** is the wavelength at which a material absorbs photons and reaches an excited state.

- **Emission spectrum** shows the light emitted as excited electrons drop to lower energies.

- **Excitation spectrum** records emission at a fixed wavelength while varying excitation wavelength.

- **Excitation dependent emission** is when emission wavelength shifts based on excitation wavelength.

- **Excitation independent emission** means no shift in emission wavelength with varying excitation.

- **In-direct bandgap:** An indirect bandgap refers to a semiconductor material in which the minimum energy state in the conduction band and the maximum energy state in the valence band occur at different values of crystal momentum (k-vector).

- **Light absorption** is the process where matter absorbs photons and converts their energy.

- **Light emission** involves excited matter releasing photons as electrons relax to lower energy states.

- **Photoluminescence** is light emission triggered by photon absorption at specific energies.

- **Quantum yield** measures emission efficiency as the ratio of emitted to absorbed photons.

- **Wavelength** is the distance between successive light wave peaks, commonly measured in nanometres.

- **Redshift** is increasing emission wavelength with changing excitation.

- **Stoke shift** is the difference between the peak excitation and emission wavelengths in the fluorescence spectrum of a fluorescent material

Chapter 1 : Introduction

1.1 Background and Motivation

The advancement of technology inevitably goes hand-in-hand with the discovery and development of new materials. As emerging technologies require capabilities beyond those of conventional materials, the search for novel materials with enhanced properties becomes imperative. This interplay between materials innovation and technological progress has been demonstrated time and again across history, from the Stone and Bronze Ages to the advent of steel alloys, semiconductors, and nanomaterials. The 2023 Nobel Prize in Chemistry recognised pioneering work on quantum dots, nanocrystals that exhibit unique size-dependent properties.[1] This highlights the enormous potential of ongoing research into quantum dots, especially in the emerging field of carbon quantum dots (CQDs).

CQDs – a new class of carbon-based nanomaterials with tremendous potential to enable solutions for global challenges in fields like energy, environment, and healthcare.[2] carbon quantum dots are also known as graphene quantum dots (GQDs), carbon nanodots (CNDs), and carbon polymer dots (CPDs). Their size (less than 10 nm) and photo-electrochemical properties are akin, yet the difference in the internal structure and chemical surface groups generated their classification.[3] Notably, CQDs not only perform the excellent optical properties as traditional semiconductor quantum dots but also showed advantages in term of non-toxic, environmental, cytotoxicity, and biohazard. In addition, the researchers are attracted by the feature properties of CQDs such as chemical stability, excellent water solubility, photobleaching resistance and ease of surface functionalisation.[4]

CQDs can be synthesised from the abundant, low-cost, renewable precursors such as biomass and biomass waste.[5] The optimised conversion of renewable biomass and waste-related components into useful nanomaterials is one of the biggest challenges for a sustainable world. Although a broad range of raw biomass materials (agriculture product, agricultural residue, municipal solid waste etc) can be used in producing CQDs, generally these synthetic routes are associated with poor control of the CQDs particle size, quality, and homogeneity of the product.[6] Additionally, the production of CQDs via conventional methods involves lengthy reaction times (from few hours up to 48 hours) and high consumption of energy.[7] Therefore, a new approach for the synthesis of CQDs that minimises the process duration and energy consumption along with delivering fine control of the particle size and other properties are needed.

Continuous Hydrothermal Flow Synthesis (CHFS), a bottom-up hydrothermal approach, is emerging as a unique solution to current challenges associated with synthesising high quality carbon quantum dots (CQDs).[8] CHFS offers several key advantages compared to conventional hydrothermal synthesis methods. First, CHFS is primarily water-based, avoiding the use of toxic organic solvents that are common in other methods. This makes CHFS an incredibly green and sustainable process for nanomaterial synthesis.[9] Additionally, the continuous flow nature of CHFS allows for highly controlled mixing and heating conditions, enabling precise tuning of CQD nucleation and growth. CHFS allows tailoring the size, shape, and surface chemistry of CQDs for specific functions. Furthermore, CHFS has been shown to require less energy and shorter reaction times compared to traditional hydrothermal synthesis. Finally, the continuous production enabled by CHFS allows scalable synthesis of high quality, homogeneous CQDs.[10]

This PhD project is to design and synthesise carbon quantum dots (CQDs) with optimised optical and structural properties using a green continuous hydrothermal flow synthesis (CHFS) approach. By gaining fundamental insights into the nucleation and growth mechanisms of CQDs formed through CHFS, the goal is to achieve fine control over the production of uniform CQDs with reproducible properties. Systematic investigation of how factors like dopant concentration, carbon and hetero atom dopant precursors affect CQD formation and final characteristics was carried out. State-of-the-art spectroscopic and microscopic characterisation techniques provide crucial understanding of the relationship between synthesis conditions, particle morphology, crystal structure, and optical/electronic performance. By establishing clear structure-property-processing correlations finely tuneable photoluminescent CQDs were designed via this rapid and environmentally friendly CHFS route for diverse cutting-edge applications in nano-sensing and photocatalyst.

1.2 Research Objectives

The main research objectives are:

- Identify and optimise/develop key CHFS methodologies for CQDs design utilising a selection of targeted biomass precursors and variation of the reaction parameters including the effect of concentration, carbon sources precursors and heteroatom types.
- Evaluate the properties of the synthesised CQDs. The designed materials were extensively studied using state-of-the-art characterisation techniques to understand the key fundamental properties of the synthesised carbon quantum dots including morphology, chemical structure, PL mechanism, nano particles nucleation mechanism. This research accelerates the high-quality materials development by enabling important properties such as uniform particle size, excellent photoluminescence properties and a well-controlled synthetic process.
- Explore innovative approaches of using carbon quantum dots and performance assessment CQDs materials in environmental applications (e.g. photocatalysis, sensing).

1.3 Research Contribution

This research provides insights into the synthesis, properties, and applications of carbon quantum dots (CQDs). A novel, single-step, rapid and green method for synthesizing CQDs via CHFS is presented. The effect of heteroatom (nitrogen) concentration on the morphology, optical properties, and electrical properties of the CQDs was examined providing the optimised synthetic and dopant process via CHFS method. Also, the sensing applications of the CQDs are investigated, elucidating the fluorescence quenching mechanism and demonstrating their usefulness for real-world applications. By studying different carbon sources for CQD synthesis, the effect of the carbon precursor on the properties of the resulting CQDs is uncovered, allowing selection of the ideal carbon source based on the target application. Furthermore, study of using various nitrogen dopant sources provides insight into how the choice of nitrogen precursor impacts nanoparticle formation, optical properties, and morphological distinctions of the synthesised CQDs. This research introduced innovative approaches by using CQDs as an agent to modify the conventional semiconductors, for example TiO_2 resulting in significant enhanced photocatalyst for water treatment application (degradation application).

1.4 Thesis Outline

Chapter 1: Introduction

Chapter 1 introduces the frame of this PhD research project. The background section establishes the scope of the study, reviewing existing challenges and summarizing the current state of knowledge. The research objectives are stated, delineating the specific aims and contributions of the thesis.

Chapter 2: Literature review

This chapter provides comprehensive review of the classification, properties, and applications of carbon quantum dots (CQDs). It thoroughly examines the various methods, techniques and procedures used to synthetically produce CQDs. The chapter explain in detail the different approaches to CQDs synthesis, including top-down methods like laser ablation, electrochemical oxidation, and chemical oxidation, as well as bottom-up methods like microwave-assisted synthesis, and hydrothermal/solvothermal synthesis. Additionally, this chapter provides background information about CHFS processes including the properties of supercritical water, principle of CHFS method, process, and reactor designs.

Chapter 3: Methodologies and characterisations

This chapter details the specific reagents employed in each synthetic approach and outlines the experimental procedures and parameters, for each synthetic rout are presented. It also introduces the fundamental operational principles behind the CHFS process and its application within this project. Furthermore, it provides a thorough presentation of the characterisation techniques used, along with associated parameters for each method.

Chapter 4: Investigation the effect of various carbon precursors on nitrogen carbon quantum dots structure and optical properties.

This chapter reports the results of a study investigating different carbon sources, including chitosan, humic acid, lignin, and citric acid, along with urea as a nitrogen source, to synthesize nitrogen-doped carbon quantum dots (NCQDs). Various characterization techniques were utilised to fully analyse the properties of the resulting NCQDs. The study provides important insights into the effects of the chemical structure of the carbon source precursors on the formation and optical properties of NCQDs. It delivers new insights into the design and tailoring of NCQD properties through careful selection of carbon precursors.

Chapter 5: Synergistic design of nitrogen-doped carbon quantum dots: unravelling the crucial role of nitrogen precursors in tailoring enhanced optical and chemical properties

This chapter presents the findings of a comprehensive study investigating different nitrogen sources for synthesising NCQDs using citric acid as the carbon source. Five nitrogen precursors were used including urea, L-arginine, ß-alanine, ethylenediaminetetraacetic acid di potassium salt dihydrate (EDTA), and trizma base. A range of characterisation techniques including HRTEM, AFM, XPS, Raman, FTIR, PL steady state were employed to fully analyse the synthesised NCQDs to gain insights into how the composition, configuration, and functionality of nitrogen precursors can tailor NCQD properties.

Chapter 6: **Investigating the effect of N-doping on carbon quantum dots structure, optical properties, and metal ion screening.**

This chapter reports the synthesis of NCQDs from glucose and ammonia using CHFS process. Various concentrations of ammonia were used to study the effect of nitrogen doping content on the optical properties of the NCQDs. Characterisation techniques including TEM, XPS, Raman, PL steady state were employed to investigate the origin of optical enhancement. This chapter also explored the application of the as-synthesised NCQDs as a chemical sensor to detect the toxic chromium (VI) ions commonly found in industrial wastewater. The selectivity, sensitivity, and quenching mechanism of the NCQDs were also investigated.

Chapter 7: Synthesis and characterization of N-doped carbon quantum dot-TiO2 nanocomposites for photocatalysis.

This chapter investigates the fabrication of nanocomposites composed of NCQDs and TiO_2. The NCQDs were synthesised via CHFS using citric acid and urea. The as-prepared NCQDs were combined with TiO_2 nanoparticles in situ via CHFS process. The incorporation of NCQDs significantly improves the photocatalytic performance of pristine TiO_2. This study provides important insights into developing high-performance NCQD-based nanocomposites for renewable energy and environmental applications.

Chapter 1: References

1 E. Bub and K. Mill, *The New York times*,2023, https://www.nytimes.com/2023/10/04/science/nobel-prize-chemistry.htmL (Accessed 27 October 2023)

2 L. Cui, X. Ren, M. Sun, H. Liu and L. Xia, *Nanomaterials*, 2021, **11**, 3419.

3 C. Xia, S. Zhu, T. Feng, M. Yang and B. Yang, *Advanced Science*, 2019, **6**, 1901316.

4 K. G. Nguyen, I.-A. Baragau, R. Gromicova, A. Nicolaev, S. A. J. Thomson, A. Rennie, N. P. Power, M. T. Sajjad and S. Kellici, *Sci Rep*, 2022, **12**, 13806.

5 Y. Meng, Y. Zhang, W. Sun, M. Wang, B. He, H. Chen and Q. Tang, *Electrochimica Acta*, 2017, **257**, 259–266.

6 P. G. Luo, S. Sahu, S.-T. Yang, S. K. Sonkar, J. Wang, H. Wang, G. E. LeCroy, L. Cao and Y.-P. Sun, *J. Mater. Chem. B*, 2013, **1**, 2116.

7 Y. Wang, X. Chang, N. Jing and Y. Zhang, *Anal. Methods*, 2018, **10**, 2775–2784.

8 I.-A. Baragau, N. P. Power, D. J. Morgan, T. Heil, R. A. Lobo, C. S. Roberts, M.-M. Titirici, S. Dunn and S. Kellici, *J. Mater. Chem. A*, 2020, **8**, 3270–3279.

9 S. Kellici, J. Acord, K. E. Moore, N. P. Power, V. Middelkoop, D. J. Morgan, T. Heil, P. Coppo, I.-A. Baragau and C. L. Raston, *React. Chem. Eng.*, 2018, **3**, 949–958.

10 I.-A. Baragau, N. P. Power, D. J. Morgan, R. A. Lobo, M.-M. Titirici, V. Middelkoop, A. Diaz and S. Dunn, *ACS Sustainable Chemistry & Engineering*, 2021, **9**, 2559–2569.

Chapter 2 : Literature review

2.1 Introduction

2.1.1 The evolution of carbonaceous nanomaterials

Carbon has been a critical material across the evolution of human civilization. As early as 3750 BCE, ancient Egyptians used natural graphite for primitive writing. By 1500 BCE, early furnace designs in Egypt and Mesopotamia used carbon as a reducing agent for extracting metals from ore.[1] The primary naturally occurring forms of carbon - graphite and diamond - were used in decorative artefacts, tools, and primitive metallurgy. Diamonds found in India were prized as gemstones in jewellery as early as 500 BCE. In the 14th century, carbon black pigment derived from charring organic matter became pivotal for ink used in block printing and woodblock painting, allowing text and images to be mass-produced across Asia. By the 18th century, the production of coke, a purified carbon derived from coal, enabled the smelting of iron on a large scale.[2] This paved the way for the iron and steel industry that underpinned the Industrial Revolution. In the 19th century, coal gas and coal tar became essential industrial feedstocks for synthesizing new organic compounds, dyes, drugs and more - sparking the modern chemical industry. Carbon black reinforcing filler produced from oil and gas combustion became indispensable for reinforcing rubber used in tires, providing enhanced durability. In the late 1800s, carbonized cotton thread was used in early incandescent lightbulbs to provide resistance heating to produce light. This carbon filament technology helped drive the widespread adoption of electric lighting. Around 1900, new synthetic materials derived from coal tar and petroleum, like Bakelite, revolutionized polymers, and plastics.[3]

The journey of carbon nanomaterials began in 1985 with the discovery of buckminsterfullerene, spherical molecules composed of 60 carbon atoms arranged in a geometric cage structure. This novel form of carbon, known as fullerenes, sparked great excitement, and kicked off the nanocarbon research field.[4] In 1991, carbon nanotubes were first observed by electron microscopy. These hollow cylindrical tubes formed from rolled-up graphene sheets exhibited exceptional thermal and electrical conductivity and tremendous mechanical strength. This led to rapid growth in research on synthesizing and utilizing carbon nanotubes over the 1990s.[5] The isolation of single-layer graphene in 2004 by Andre Geim and Konstantin Novoselov marked another major milestone. Graphene demonstrated remarkably high electron mobility, thermal conductivity, specific surface area and optical transparency. This stimulated enormous interest in two-dimensional carbon nanomaterials.[6]

Throughout history, the emergence of new carbon-based materials has consistently unlocked revolutionary technological advancements. Novel carbon-based nanomaterials have been the key enablers spurring new eras of innovation and industry. Recently, Carbon quantum dots (CQDs) have emerged as a promising new class of carbon-based nanomaterials. With sizes below 10 nanometres, carbon quantum dots CQDs not only perform the excellent optical properties as traditional semiconductor quantum dots but also showed advantages in term of non-toxic, environmental, cytotoxicity, and biohazard.[7] These attributes have generated great excitement, establishing CQDs as rising stars in advanced materials research. CQDs show enormous potential for tackling critical global energy, environment, health, and sustainability challenges. Their versatile surface chemistry and small size facilitate their use in diverse technologies like photovoltaics, photocatalysis, energy storage, bioimaging, and sensors.[8] With tailored design, carbon quantum dots could enable breakthroughs in renewable energy conversion and storage, green technology, medical diagnostics and treatment, water purification, and more.

2.1.2 Classification of carbon quantum dots

The first reported synthesis of carbon quantum dots was by Xu et al. in 2004 using a hydrothermal method to produce fluorescent fragments from carbon nanotubes, termed fluorescent single-walled carbon nanotube fragments (FSWCNFs).[9] In 2006, Sun et al. coined the term “carbon quantum dots” (CQDs) to describe fluorescent carbon nanoparticles passivated by polymers.[10] In particular, CQDs are zero-dimensional carbon-based nanomaterial, with small particle size (usually less than 10 nm), fast and easy in surface modification and functionalization. They consist of a sp^2/sp^3 hybridized carbon core along with abundant surface functional groups like carboxyl, hydroxyl, and amine moieties. CQDs are universally accepted to categorised into graphene quantum dots (GQDs), carbon nano-dots (CNDs) and carbonized polymer dots (CPDs) according to their nature, crystalline structure of carbonic core, quantum confinement and carbonisation degree.[11]

Graphene quantum dots (GQDs) are tiny fragments of graphene consisting of the π-conjugated single sheet with chemical groups on the surface or within the interlayer defect, which generate the unique properties for GQDs, such as quantum confinement effect and edge effect. GQDs possess well-defined structure as Nano-sheets of sp^2 carbons, are in the shape of the disc of atom-thick graphene oxide with lateral dimensions normally less than ≈20 nm and height usually less than five layers of graphene sheets (≈2.5 nm). Notably, the quantum confinement of GQDs is not only dependent on the particle size, but it refers to the conjugated π-domains, which are isolated by the defects on the surface graphene. The number of defects on the plane of graphene is increased along with the rising of oxygen element, leading to the more conjugated π-domains as the fluorescent centres.[7]

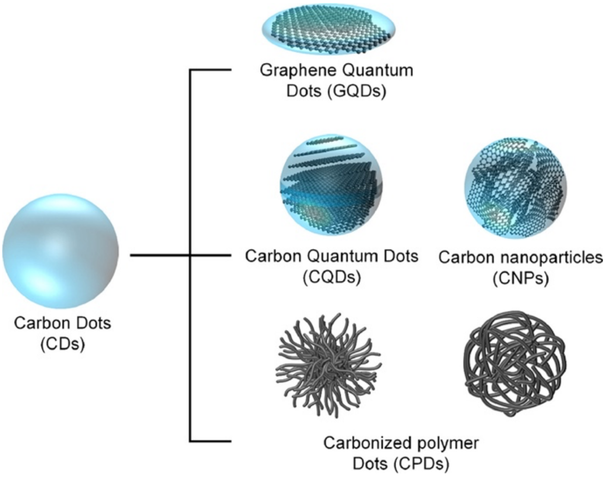

Figure 2.1: Classification of carbon quantum dots: GQD (graphene quantum dot), CND (Carbon Nano Dot), CPDs (Carbon Polymer Dot)[12]

Carbon quantum dots (CNDs) nanoparticles are generally reported in the shape of quasi-spherical or spherical with clearly crystalline structural or high carbonization degree which are mainly composed of sp^3 hybridization, and the particles size normally less than 10 nm. However, a novel form of crystalline quantum dots (CQDs) with a distinctive triangular structure was recently reported by Yuan et al. The triangular geometry displays several advantageous optical and electronic properties compared to spherical CQDs. The sharp tips and edges of the triangular CQDs allow for intensified local electric field effects, enhancing properties like fluorescence. Additionally, the high crystallinity and well-defined faceting of these triangular nanoparticles give rise to exceptional emission characteristics. This successful engineered triangular CQDs opens exciting new possibilities for tailoring CQDs to achieve the desired the nanocrystal shape and high optical performance.[13] In general, CNDs possess chemical groups on the surface which relate to intrinsic photoluminescence state and quantum confinement effect. Besides, the change of CNDs' size plays an important role in regulating the wavelength of photoluminescence.[14]

CPDs have a unique polymer/carbon hybrid structure that distinguishes them from other carbon dots like graphene quantum dots and carbon nanodots. They contain a carbon core surrounded by abundant functional groups and short polymer chains that provide excellent solubility and processability. Unlike graphene quantum dots, CPDs do not exhibit a distinct quantum confinement effect correlated with particle size due to their amorphous carbon or polymer-crosslinked cores. The complex hybrid structure leads to heterogeneous electronic states that depend on the carbonization degree, surface defects, and molecular fluorophores incorporated in the polymer matrix. The photoluminescence mechanism of CPDs mainly relies on the surface state, molecular state, and cross-link enhanced emission (CEE) effect.[15]

2.2 Properties of Carbon Quantum Dots (CQDs)

2.2.1 Solubility of carbon quantum dots (CQDs)

CQDs are widely reported possessing excellent water solubility. Unlike traditional semiconductor quantum dots made from heavy metals, CQDs can readily dissolve and achieve stable dispersion in water without additional modifications. The unique water solubility of CQDs originates from the surface functional groups incorporated into the CQD carbon core during synthesis.[8] Synthetic processes often result in CQDs possessing a variety of oxygen-containing groups like hydroxyl, carboxyl, and epoxy attached to their surfaces.[16] These polar, hydrophilic surface groups can interact favourably with water molecules through hydrogen bonding interactions. The abundant hydrophilic surface groups thus enable CQDs to achieve excellent stability in aqueous media. CQDs' strong water solubility and biocompatibility have enabled a wide range of bio-applications and some of their most promising uses in biomedicine.[7] Their aqueous dispersibility allows CQDs to be directly compatible with biological environments and used for intracellular imaging or drug delivery.[17]

Carbon quantum dots (CQDs) with hydrophobic surfaces have emerged as an area of interest, alongside the more common hydrophilic CQDs. Hydrophobic CQDs can be synthesised directly or by modifying hydrophilic CQDs to make them hydrophobic. Hydrophobicity in CQDs can be achieved by reducing surface hydroxyl groups and adding hydrophobic long chain fragments, either fragmented or unfragmented. The hydrophobicity increases when the CQDs are reacted with higher order alkylamines that have longer carbon chains. CQDs with higher number of carbons are reported to perform an enhanced hydrophobicity.[18] These hydrophobic nanoparticles have promising industrial applications like self-cleaning surfaces, suppressing surface reactions, and improving water resistance.

2.2.2 The stability of carbon quantum dots (CQDs)

- *Thermostability*

Carbon quantum dots (CQDs) exhibit high thermal stability and resistance to degradation at elevated temperatures. Studies using thermogravimetric analysis have demonstrated that CQDs synthesised from various precursors display excellent thermal stability up to temperatures of 300-400°C in air, with gradual mass loss due to the decomposition of surface oxygen functional groups.[19] Nevertheless, the carbon core remains intact and continues to fluoresce under high-temperature conditions, a remarkable property compared to most organic dyes. Studies on the thermal stability of carbon nanotubes (CNTs) with diameters below 10 nm have indicated that factors like heat capacity and degradation temperatures are strongly influenced by the diameter.[20] This suggests that nanoparticle size plays a critical role in governing stability. Smaller particle size CQDs exhibit improved stability due to their higher surface area-to-volume ratio and densely packed surface groups. The relationships could be leveraged to optimize CQDs for technologies requiring extreme temperature durability.[21]

- *Photostability*

Carbon quantum dots (CQDs) have emerged as a new class of fluorescent nanomaterials. Therefore, the photostability of CQDs is a crucial property for the optical applications. Photostability refers to a material's stability when exposed to radiation like ultraviolet (UV), visible, or other light. Conventional fluorescent materials tend to degrade or "photobleached" over time upon light irradiation, decreasing their fluorescence intensity. In contrast, CQDs have been reported to possess an excellent photostability, for example the synthesised CQDs using glucose and glutathione retained 92% of the original fluorescent intensity after 2 hours under a 450W xenon lamp.[22] The excellent photostability is also reported in another study where nitrogen-doped CQDs (NCQDs) were prepared using citric acid and tris (hydroxymethyl) aminomethane (Tris). The NCQDs were exposed to UV irradiation (365 nm, 250 W) from a mercury lamp with a radiant intensity of 20 mW cm^{-2}. Remarkably, even after 360 minutes of exposure, a 96% retention of fluorescence intensity was observed.[23] The NCQDs synthesised from ammonium citrate and urea exhibited exceptional photobleaching resistance, with 96%

of the original intensity remaining even after 180 minutes of exposure to UV lamp irradiation.[24] Crystalline CQDs were synthesised using fennel seeds, and the resulting samples showed no reduction in photoluminescence (PL) intensity even after 4 hours of exposure to a 150 W Xe lamp.[25] Overall, the photostability of CQDs makes them promising candidates for various applications where resistance to photodegradation is essential, such as in bioimaging, sensing, and optoelectronics.

- *Chemical stability*

Chemical stability encompasses the ability of CQDs to maintain their optical, physical, and electronic properties when subjected to different chemical conditions over time. This includes stability in the presence of ions (ion stability), under acidic or alkaline conditions (pH stability), and stability of properties over an extended timeframe (time stability). Assessing chemical stability is crucial for applying CQDs in sensing, imaging, optoelectronics, and other applications where the nanoparticles will encounter a wide variety of chemical environments. Lack of stability would compromise their functioning and reliability in intended operation conditions. In 2019, Baragáu et al. successfully synthesised NCQDs using citric acid and urea. These prepared NCQDs demonstrated stability within a broad pH range of 5 to 12. Furthermore, the photoluminescent intensity remained constant even in the presence of various ions and anions, except for the toxic ion Cr (VI). This observation highlights the selectivity and sensitivity of the synthesised NCQDs towards toxic ions.[26] However, the other CQDs synthesised from glucose and reduced glutathione via hydrothermal batch displayed high sensitivity to pH level. The fluorescence intensity peaked at pH 3 and decreased substantially from pH 3 to 10. Additionally, there was a slight reduction in PL intensity from pH 10 to 13.5.[22] While intrinsic CQD properties contribute to chemical stability, the synthesis method also plays a key role. CQDs produced via hydrothermal, microwave, ultrasonic, and pyrolysis methods can exhibit substantially different ion/pH stability profile.

2.2.3 Optical properties

Carbon quantum dots possess unique and versatile optical properties that have made them one of the most compelling and rapidly advancing fields within carbon nanomaterials research.

- *UV-Vis absorbance*

Carbon quantum dots display strong optical absorption in the UV region spanning into the visible range. The sharp peak below 300 nm corresponds to a π-π* transition of aromatic sp2 carbons (C=C bonds) in the CQD core, indicative of quantum confinement.[27] The 300-400 nm tail is assigned to n-π* transitions of C=O bonds. Absorption above 400 nm originates from surface state transitions involving lone pairs. The n-π* and surface state bands overlap smoothly, enabling tuneable emissions. The low energy peak around 300 nm is due to n-π*, π-π* and interlayer charge transfer transitions. Red-shifted absorption up to the NIR range directly results from the doping of hetero atoms, which injects electrons into π* orbitals, reducing the HOMO-LUMO gap. Oxygen functional groups on the surfaces of CQDs also narrow energy levels, causing red-shifted absorption. Furthermore, molecular orbitals of any surface passivating ligands also contribute to visible absorption. By controlling the surface oxidation, defect density, heteroatom doping, and surface functionalization, the relative intensities of the UV peak and visible shoulder can be tuned to achieve the desired broad absorption across the solar spectrum for photocatalysis and optoelectronic applications.[28]

- *Photoluminescence (PL)*

One of the most striking and fascinating properties of CQDs is their incredibly intense photoluminescence emission with unique photoluminescence properties that can be tailored for diverse optical applications. A signature photoluminescence trait of CQDs is excitation-dependent emission, where the fluorescence peak redshifts to longer wavelengths as the excitation wavelength increases.[29] This is generally explained by the presence of multiple emissive sites or surface defects with varying energy levels on the CDs. However, some synthesised CDs have also demonstrated excitation-independent photoluminescence, producing consistent emission peaks across excitation wavelengths. This is made possible by uniform surface chemistry and internal carbon core structure. Excitation-independent CQDs are promising for biological labelling and optoelectronic applications requiring stable emission.[23,30,31]

CQDs are also reported exhibiting up-conversion fluorescence, an optical phenomenon where the excitation wavelength is longer than the emission wavelength. When excited by near-infrared light, CQDs can exhibit anti-Stokes type up conversion fluorescence in the visible range due to multiphoton absorption and energy transfer mechanisms. Up-conversion fluorescence in CQDs was first observed when visible light emission occurred under 800 nm femtosecond pulsed laser excitation.[32] This enables broader utilisation of CQDs' luminescence across the electromagnetic spectrum.

Furthermore, phosphorescence or long-lasting emission of light after excitation, is an intriguing photophysical property now being explored in CQDs. Achieving phosphorescence in CQDs requires promoting efficient intersystem crossing from singlet to triplet states while also restricting non-radiative relaxation pathways that quench emission.[33] Doping CQDs with heteroatoms like nitrogen also facilitates intersystem crossing, possibly through $n \rightarrow \pi^*$ transitions.[34] However, achieving phosphorescent emission from carbon quantum dots (CQDs) in aqueous solution has proven challenging due to phosphorescence quenching effects caused by water. The presence of dissolved oxygen and solvent-assisted relaxation pathways in water environments tend to suppress CQD phosphorescence.[35]

2.2.4 Photoluminescence mechanism

Through extensive research over many years, the four main photoluminescence mechanisms of carbon quantum dots (CQDs) are categorized into: Carbon core emission, surface state emission, molecular state emission, crosslink enhanced emission.[8,12,34,35,36]

- Carbon core emission

As mentioned earlier, CQDs have sizes smaller than 10 nm, nearing the Bohr exciton radius. Consequently, CQDs are capable of exhibiting the quantum confinement effect. Carbon core nanocrystalline carbon core, producing quantum size effects.[39] The CQDs' PL has been attributed to the radiative recombination of electron-hole pairs confined within the CQDs. Specifically, the size of the CQDs determines their energy bandgap, with smaller CQDs having larger bandgaps. This means the emission wavelength shifts to lower energies (red shifts) as the CQDs size increases, since the bandgap decreases with increasing nanoparticle diameter, as shown in **Figure 2.2**. The reduction in CQD bandgap with increasing particle size resulted in different excitation and emission properties for different sized CQDs.[28] The quantum confined nature of CQDs means their fluorescence can be tuned across the visible spectrum, from blue to red, simply by controlling the graphite like carbon core dimensions during synthesis. This carbon core emission mechanism is also elucidated the optical properties of graphene quantum dots possessing several pristine graphene layers, herein, the desired emission colour can be achieved by tuning the mean and distribution of particle size.

The fluorescence wavelength has been extended into the near infrared via the growth of the carbon core size.[40] Therefore, a narrow distribution of particle size is expected to have high optical performance carbon quantum dots with high emission intensity and PL quantum yield. In addition, the particle size distribution of CQDs has a significant impact on their light absorption characteristics and efficiencies influencing the photocatalyst performance of CQDs.[41]

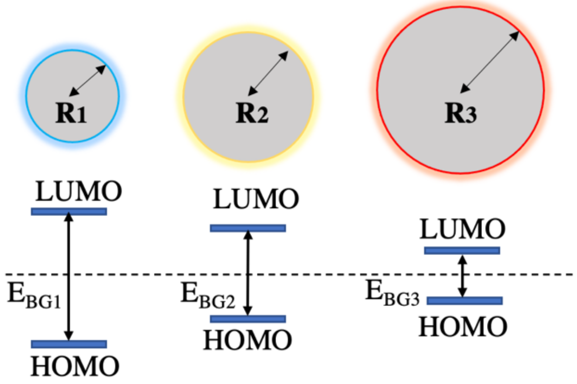

Figure 2.2: The relationship between nanoparticle size and energy bandgap

Having a mix of CQDs with different sizes may theoretically allow harvesting of a wider spectrum of light by leveraging the intrinsic quantum confinement effect in CQDs, larger dots have smaller bandgaps allowing absorption of longer wavelengths into the infrared, while smaller CQDs absorb effectively in the UV and visible region. However, larger CQDs lose the visible light absorption properties that make their quantum-confined counterparts so uniquely suited to photocatalysis.[42] While the photoactive range is broadened, the electron-hole pair generation efficiency at specific useful wavelengths is likely reduced by inclusion of larger particles. Variation of particle size prevents aligning to optimal redox potentials for photocatalysis, likely reducing gains from the broader absorption. Moreover, uniformity of the CQD surface area and interfaces is essential for efficient charge transfer and surface catalytic activity, which is disrupted across variable particles sizes.[43] Therefore, optimised photocatalytic performance of CQDs is attained via controlled CQD syntheses that minimize size variation focused around small <10 nm diameters, rather than any potential advantages from tuning bandgaps by broadening particle size distribution.[44]

- Surface state emission

Surface state emission arises from interactions occurring between surface functional groups attached to the carbon core of CQDs such as C=O, carboxylic acid, and epoxy groups. The degree of surface oxidation and types of functional groups directly influence CQD fluorescence.[45] Reports indicate that the emission with wavelength less than 400 nm stems from the radiative recombination of electron-hole pairs within the carbon core, whereas longer wavelength emission above 400 nm is a consequence of the radiative relaxation from the excited state to the ground state, attributed to the presence of distinct oxygen-containing and hetero atoms (N,S,P,B) - containing groups on the surface of CQDs.[46,47]

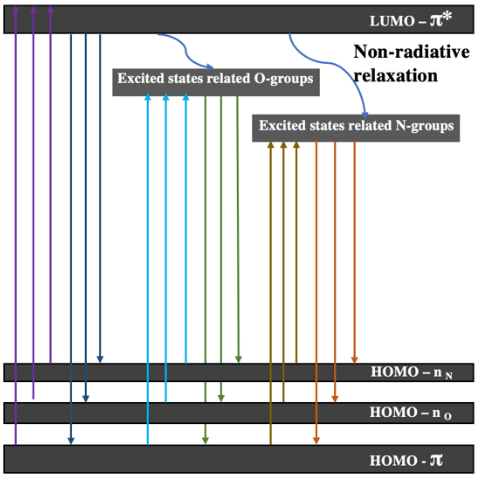

Figure 2.3: Alteration of PL emission of CQDs by introducing oxygen and nitrogen-containing groups

Due to the synthetic process of CQDs extensively involved in the carbonisation process of carbon-containing precursors, thus CQDs are mainly reported to possess a rich of oxygen containing functional groups decorating their surface including epoxide, hydroxyl, carbonyl, and carboxyl.[48] With carbon backbones linked to combinations of epoxide, hydroxyl, carbonyl, and carboxyl, functional groups, intricate and heterogeneous surface defects arise. It is the carbon-oxygen bonds and structures that mediate electronic transitions turning the emissive colours observed in CQDs.[49] In addition, nitrogen is the most commonly reported heteroatom used to enhance the optical properties of NCQDs. Various nitrogen-containing functional groups can be embedded within the carbon core or amorphous shell of NCQDs owing to the comparable electronic configuration and atomic radius between nitrogen and carbon.[50] These groups include amino, amide, pyridinic, pyrrolic, graphitic, nitro, and amidine moieties which greatly impact the luminescence properties of NCQDs arising from surface state transitions. Specifically, these functional groups introduce additional energy states between ground and lower-lying excited states.[51] These novel energy states produce transitions emitting at longer wavelengths when electrons relax from those defect states, as illustrated in **Figure 2.3**. Blue emission arises from n → p* transitions of C=O groups. As surface oxygen content increases, more epoxide/hydroxy groups form below the π* state, creating new energy levels that reduce the n → π* bandgap resulted in the redshift in the PL emission of CQDs.[52] Surface functional groups like C=O and C=N also tune emission by introducing new HOMO energy levels.[53] The primary amine groups located on the edges of CQDs exhibit a higher HOMO energy level compared to hydrogen-terminated edge groups due to the strong orbital interaction between the CQD and the -NH_2 amine groups. Furthermore, by introducing alkylamine groups to CQDs converts the carboxylic acid (-COOH) and epoxy groups on the CQDs' surface into amides (-CONHR) and amines (-CNHR), respectively. The nitrogen-containing groups reduces non-radiative recombination pathways induced by the -COOH and epoxy groups. This switches the CQDs' emission from being dominated by defect states to being dominated by intrinsic state emission.[54] Similarly, reduction processes that convert carbonyls, epoxides and aminos into -OH groups can suppress non-radiative processes. This enhances the integrity of the π-conjugated system in the CQDs' core and reduces defects.[55]

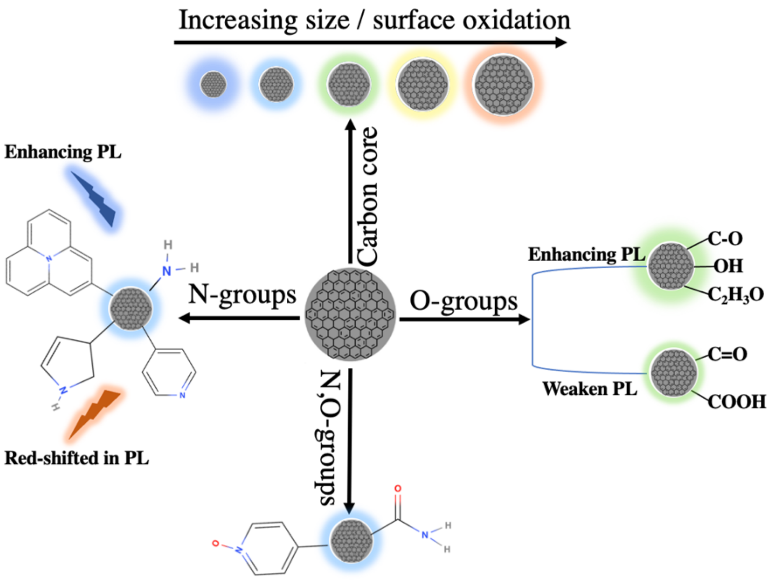

Figure 2.4: The PL emission of carbon quantum dots from the carbon core; and various functional group including oxygen related and nitrogen related groups

The effects of nitrogen and oxygen-containing functional groups on the emission colour of CQDs are summarized in **Figure 2.4** demonstrated how nitrogen and oxygen-related functionalization provides emissive colour tunability. This figure outlines how the different surface functional groups and bonding configurations influence and tune the photoluminescence emission displayed by CQDs. Diverse surface defects derived from amine, amide, pyrrolic, pyridinic, graphitic, and other nitrogen species showed redshifted in the emission colour from blue to yellow. Meanwhile, a range of oxygen functional groups like carbonyl, carboxyl, hydroxyl, and ethers are shown to similarly enable redshift the emissions from violet to red wavelengths.[56]

- Molecular state emission

Molecular state emission originates from specific fluorescent molecular structures present on the carbon quantum dot (CQD) surface that resemble specific organic fluorophores. The use of citric acid as a carbon source and amino acids as nitrogen sources in the synthesis of nitrogen doped CQDs (NCQDs) reveals the presence of these low molecular weight fluorophores.[57] The π-conjugated domains within the carbon core serve as attachment points for residual fluorophores that remain from the synthesis process. These fluorophores located at the periphery of the carbon core constitute the primary photoluminescent state of the synthesised CQDs.[58] The types of fluorophores that form is dependent on the synthetic process used to produce the CQDs. Factors such as temperature, choice of carbon precursor molecules, and dopant sources influence fluorophore formation. For example, synthesis conditions that produce blue-emitting CQDs likely facilitate the generation of non-aromatic fluorophores like aliphatic hydrocarbons and esters. In contrast, the green-emitting CQDs contain fluorophores like ketones, aldehydes and carboxylic acids that come from the partial oxidation of citric acid under different reaction conditions.[59] Further research is still needed to fully confirm the chemical identity and binding modes of proposed fluorophores in CQDs produced from citric acid and other carbon sources. However, the molecular state emission theory provides a rational framework for relating CQDs' structure and excitation independent behaviours.[60]

- Crosslink - enhanced emission

The crosslink-enhanced emission (CEE) effect is an important fluorescence mechanism CQDs and related nanomaterials.[61] CEE arises when crosslinking within the CQD provides a rigid molecular framework that restricts intramolecular vibrations and rotations. These motions can serve as pathways for non-radiative relaxation of excited states, dissipating excitation energy without light emission. By suppressing vibrational and rotational movements, crosslinking reduces non-radiative relaxation rates. This enhances the probability of radiative relaxation, increasing the quantum yield of photoluminescence.[62] Various types of crosslinking interactions can contribute to CEE, including covalent bonding, coupled emissive centres, hydrogen bonding networks, and physical aggregation induced by carbonization. The CEE effect allows tuning of CQD luminescence by controlling the degree of crosslinking during synthesis or via stimuli-induced structural changes.[63]

2.3 Applications of carbon quantum dots (CQDs)

CQDs with the unique optical properties outlined above have been studied and applied extensively in many industries such as chemical sensing, photocatalyst, bio sensing, bio imaging, nanomedicine, photo-catalyst, and electro-catalyst.[64,65]

2.3.1 *Chemical sensing*

With low toxicity, water solubility, high photo-stability, and superior chemical stability, CQDs become novel promising materials for chemical sensing applications.[66] One of the important of utilising CQDs in chemical sensing is the selective detection of heavy metal causing the hazardous effect on the environment and human health, such as Cu^{2+}, Fe^{3+}, Pb^{2+}, Cr (VI) and Ag^{+}.[67,68,69] To enhance the sensitivity of CQD-based fluorescent probes, CQDs are often coated with various polymeric materials, metal-organic frameworks, and silica nanoparticles. Additionally, CQDs have demonstrated their capability in other detection applications, including pH sensing, as well as the detection of anion such as $C_2O_4^{2-}$, PO_4^{3-}, CN^-, F^-, S^{2-}, ClO^- and I^-. The principle behind the CQDs-based sensors and biosensors is the quenching behaviours of CQDs in the presence of toxic ions or anions. The CQDs' quenching mechanisms include the inner filter effect (IFE), dynamic quenching, photo-induced electron fluorescence, static quenching, and fluorescence resonance energy transfer.[70]

- *Inner filter effect*

Inner filter effect (IFE) is an important fluorescence quenching mechanism that can occur in fluorophores like carbon quantum dots. The IFE process involves the presence of an absorbing species (quencher) normally is the toxic ion or anion that has an absorption spectrum overlapping with the excitation and/or emission spectrum of the CQDs.[71] This spectral overlap enables the absorber to act as a 'filter' that intercepts excitation light before it reaches the fluorophore, as well as emitted fluorescent light before it exits the system. Both excitation and emission filtering by the proximal absorber led to decreased intensity of observed fluorescence, effectively quenching it. Many aromatic compounds, nanoparticles, biomolecules can induce IFE quenching in CQDs following predictable Stern-Volmer quantitative relationships. A key distinction of IFE from dynamic quenching is no change in the fluorophore lifetime, only intensity reduction.[72]

- *Static quenching*

Static quenching refers to a fluorescence quenching mechanism that occurs due to the formation of a non-fluorescent ground state complex between the CQDs and a quencher molecule.[73] This binding interaction between CQDs and quencher creates a complex that does not fluoresce upon photoexcitation. The binding can involve electrostatic forces, hydrogen bonding, hydrophobic interactions or other noncovalent associations that bring the two molecules together in the ground state prior to excitation. The grounds state complex formation causes detectable changes in the absorption spectra of the CQDs and reduces fluorescence intensity through non-radiative decay pathways. Since static quenching relies on complex formation, it exhibits dependence on temperature, with increased temperatures able to destabilise the ground state complexes and decrease quenching. Importantly, static quenching does not affect the fluorescence lifetime of the CQDs.[74]

- *Dynamic quenching*

Dynamic quenching refers to a collisional mechanism of fluorescence quenching that requires molecular contact between the CQDs and quencher when the CQDs is in the excited state. Upon diffusional encounters and collisions between the two molecules, the excited state fluorophore returns to the ground state without emission of a photon. Instead, the energy is dissipated non-radiatively by mechanisms energy transfer, charge transfer, or electron exchange with the quencher molecule.[75] Because molecular collisions are essential, dynamic quenching exhibits dependence on temperature and viscosity - higher temperatures increase diffusion and collisions, enhancing the quenching effect. Importantly, fluorescence lifetimes of the fluorophore decrease due to the additional non-radiative relaxation pathway. In contrast to static quenching and IFE, no changes occur in the absorption spectra or ground state properties.[76] Overall, dynamic quenching is identified by its collisional nature, measurable impact on excited state lifetimes, and minimal effects on ground state absorption properties.

- *Photoinduced electron transfer (PET)*

Photoinduced electron transfer (PET) quenching is a process that occurs when there is electron transfer between the CQDs and the quencher upon photoexcitation.[77] The CQDs act as an electron donor, while the quencher acts as an electron acceptor, resulting in the formation of a cation radical from the CDs and an anion radical from the quencher. In this process, a complex is generated between the electron donor CQDs and acceptor quencher that can return to the ground state via a nonradiative pathway without emission of a photon.[78] PET comprises oxidative and reductive mechanisms. In reductive PET, the CQDs act as an electron acceptor, taking an electron from the donor quencher. Oxidative PET is the reverse, with CQDs donating an electron to the quencher. The driving force for oxidative and reductive electron transfers depends on the energy gap between HOMO/LUMO levels. For reductive PET, it is the gap between the quencher's LUMO and the CQDs' HOMO. While for oxidative PET, it is the LUMO gap between the CQDs and the quencher. Indicators of PET mechanisms include decreased CQDs fluorescence lifetimes and appropriate HOMO-LUMO gaps that permit electron transfer between the CQDs and quencher.[79]

- *Förster resonance energy transfer (FRET)*

Förster resonance energy transfer (FRET) is a mechanism of fluorescence quenching that relies on non-radiative energy transfer between an excited donor fluorophore and a proximal acceptor molecule. FRET occurs when the emission spectrum of CQDs and the absorption spectrum of the quencher are overlapped.[80] This resonance condition enables the energy from the CQDs' excited state to be transferred to the acceptor via dipolar interactions. The donor CQDs is quenched due to this non-radiative energy transfer pathway, while the acceptor fluorescence gets sensitized. The rate of energy transfer is strongly dependent on the distance between the donor-acceptor pairs, with typical distances of 1-10 nm for efficient FRET. Closer proximity and greater spectral overlap improve the FRET efficiency.[81] The distance dependence makes FRET a useful technique to measure molecular distances and detect interactions at the nanometre scale. In addition, the PL lifetime of CQDs is reduced due to the additional nonradiative relaxation pathway provided by energy transfer to the quencher In the FRET quenching process.[82]

2.3.2 Photocatalytic

Photocatalysts are semiconductors that accelerate photoreactions by absorbing light and generating excited electron-hole pairs. Conventional photocatalysts absorb UV and visible light, producing charge carriers that drive surface redox reactions for applications like water splitting and pollutant degradation. Key goals in engineering photocatalysts are expanding light absorption into the visible spectrum, promoting charge separation, and providing high surface area for more reactive sites.[83] Carbon quantum dots possess several advantageous properties that make them a promising photocatalyst material. CQDs have a tuneable bandgap structure based on quantum confinement effects, allowing their light absorption and redox potentials to be optimised by controlling the dot size and surface chemistry. CQDs exhibit strong light absorption across UV and visible wavelengths, enabling utilisation of the full solar spectrum. As mentioned, CQDs demonstrate excellent resistance to photobleaching and photodegradation over prolonged irradiation. With the outstanding optical properties, CQDs are ideal candidates as photosensitisers in photocatalytic systems, especially when they are used to combine with traditional semiconductor metal oxides for nanocomposite synthetic. Furthermore, CQDs are low toxicity compared to semiconductor nanoparticles, improving their viability for large-scale water treatment and environmental remediation applications. Together, these attributes make CQDs an ideal candidate as a sustainable and efficient photocatalyst for renewable energy, green chemistry, and environmental technologies**.**

- *CQDs act as photosensitisers*

Photosensitisers are materials that can absorb light and transfer the excited energy to other molecules nearby resulting in catalysis of reactions. CQDs have recently emerged as a promising new class of photosensitizer due to their strong absorption across UV and visible wavelengths and ability to demonstrate an up-conversion effect.[84] Therefore, CQDs can be integrated into the lattice of UV-limited semiconductor photocatalysts like TiO_2 to act as photosensitisers and extend light harvesting into the visible and near-infrared spectral range. Studies have demonstrated CQDs-semiconductor nanocomposites such as CQDs/TiO_2 can achieve significantly faster degradation of organic pollutants under visible light compared to TiO_2 alone. This is due to CQDs absorbing visible photons and transferring the excited electrons to TiO_2, hindering recombination of the photogenerated charge carriers.[85] Additional recent reports have validated the effective CQDs in enhancing the visible light absorption of other CQD-semiconductor photocatalysts including CQDs/$Bi_4Ti_3O_{12}$, CQDs/$BiVO_4$, and CQDs/BiOBr.[86] In conclusion, the sensitization effect of CQDs shifts the photocatalytic activity of the semiconductors from UV light into the visible range, allowing them to harness more of the solar spectrum.

- *CQDs enhance surface area of the photocatalyst*

Surface area plays a critical role in determining the performance and efficiency of photocatalytic systems. As heterogeneous catalysts, photocatalytic reactions occur on the surface of semiconductor particles where reactants can adsorb and interact with photogenerated charge carriers. A higher surface area provides more active sites for these surface reactions to take place and allows for greater adsorption of reactants like pollutant molecules.[87] The nanocomposites of conventional photocatalysts and CQDs exhibit significantly enhanced surface area compared to the standalone photocatalysts, attributed to nanosized effects, and increased interfacial contact in the hybrid system. This is because the photocatalytic reactions occur at two active sites - both at the interface between the semiconductor and CQDs, as well as directly on the surface of the CQDs attached to the interface. The nanoscale size and dispersity of CQDs enables more interfacial contact with the semiconductor particles, providing more reactive sites for the photocatalytic reactions to take place. Ultimately, the high surface area and dual reactivity of the CQD-semiconductor interface and the CQD surface itself allow CQDs to improve the overall photocatalytic efficiency.[88] For example, doping $Bi_2O_2CO_3$ with carbon quantum dots (CQDs) in a nanocomposite structure increased the surface area and pore volume by up to 50% compared to pure $Bi_2O_2CO_3$, as the CQDs modified the morphology of the photocatalyst.[89] Beyond simply increasing surface area, CQDs provide abundant oxygen-containing functional groups like hydroxyls and carboxyls on their surface that can serve as active sites for surface redox reactions and generate long-lived holes to drive photocatalytic processes at the CQD-semiconductor interface.[90]

- *CQDs improve electron-hole recombination process*

When a photocatalyst absorbs light, excited electron-hole pairs are generated to drive redox reactions. Longer-lived charges lead to more electrons and holes reaching reactive sites for photocatalytic reactions instead of recombining. However, the photogenerated charges can also recombine and dissipate the absorbed energy as heat, rather than migrate to reactive surface sites. Suppressing recombination by improving charge separation is critical to maximise efficiency of the photocatalyst.[91] Optimizing photocatalyst design to control the recombination rate and improve charge transfer underlies developing high-efficiency photon energy conversion systems. CQDs have been shown to help suppress recombination when coupled with photocatalysts in nanocomposite structures. The unique electronic structure of CQDs with tuneable bandgaps allows them to readily accept or donate electrons and holes, forming heterojunctions that spatial separate charges.[92] Two common heterojunction types formed CQDs and semiconductor photocatalysts are type-II and Z-scheme. In a type-II heterojunction, the staggered energy bands promote spatial charge separation as electrons migrate downhill to the semiconductor with the lower conduction band edge, while holes migrate in the opposite direction. In the Z-scheme heterojunction, electrons follow a Z-shaped path and accumulate in the higher energy conduction band of one semiconductor while holes accumulate in the lower energy valence band of the other. This maintains stronger reduction and oxidation power since the electrons and holes are concentrated in different components. The Z-scheme construct provides effective charge separation without sacrificing redox potential. Furthermore, the highly dispersed CQDs introduce interfacial defects and trap states that can localize electrons or holes, preventing recombination. A nanocomposite of P25 titanium dioxide and nitrogen-doped carbon quantum dots, synthesised via hydrothermal method from citric acid and urea, exhibited a 13-fold improvement in photocatalytic performance compared to pure P25. This significant enhancement can be attributed to synergistic effects of the Z-scheme band alignment, the biphasic P25 heterojunction, extended visible light absorption from N-doping, and prolonged electron-hole separation lifetimes in the optimized nanocomposite structure.[94]

In conclusion, carbon quantum dots (CQDs) have shown immense potential for enhancing photocatalyst performance across a wide range of applications from water splitting to pollutant degradation. Due to characteristics like low cost and green synthesis, CQD-semiconductor photocatalyst composites have been widely applied in fields such as: degradation of organic pollutants,[95] production of hydrogen fuel,[96] reducing heavy metals in wastewater,[97] conversion of CO_2 into organic compounds,[98] and disinfection of bacteria and fungi.[99] With continuing advances in tailoring the size, composition, and interface properties of CQDs, they are poised to play a key role in developing the next generation of high-efficiency photocatalytic systems for renewable energy production, water purification, and environmental remediation powered sustainably by solar light.

2.3.3 Electronic devices

Recently, nanocomposites of carbon quantum dots (CQDs) have emerged as promising materials for supercapacitors. For example, a CQD/RuO_2 nanocomposite exhibited an excellent specific capacitance of 460 F/g at an extremely high current density of 50 A/g. Moreover, the CQD/RuO_2 nanocomposite displayed outstanding cycling stability over 5000 cycles at 5 A/g, with 96.9% capacity retention. The enhanced performance is attributed to the small CQD particles improving RuO_2 dispersion and the composite's networked structure increasing charge transfer rates during charging/discharging.[100] CQDs are also attractive for light-emitting device applications due to their stable, environmentally friendly, and low-cost light emission.

Incorporating the CQDs into a polymethyl methacrylate polymer matrix provided mechanical support while dispersing the CQDs to achieve bright solid-state luminescence. Furthermore, the current density-dependent emission of CQDs enables multi-colour LEDs by tuning electrode thickness and electron transport layers. The versatile photoluminescence and facile processing of CQDs make them promise for integration into next-generation LED technologies.[101]

2.3.4 Bio-imaging

The most significant advantage of CQDs is their non-toxic and environmentally friendly nature. These outstanding properties make CQDs a very promising replacement for semiconductor quantum dots in visualising biological systems through in vitro and in vivo imaging.[102] However, the surface passivating agents on the CQDs can contribute to cytotoxicity. Fortunately, surface passivation with agents such as PPEI-EI, PEG, PEI, BPEI (branched poly-(ethylenimine)), and PAA (poly acrylic acid) produces CQDs with low cytotoxicity even at high concentrations, enabling safe utilization for biomedical imaging. For example, PEGylated CQDs demonstrated negligible toxic effects in vivo for up to 28 days during toxicity assessments.[103] The biocompatibility, combined with the optical properties, makes CQDs an ideal alternative to conventional quantum dots for a range of bioimaging applications where non-toxicity is critical.

2.4 Synthesis of carbon quantum dots (CQDs)

There are various approaches to the fabrication of CQDs from different precursors, but generally, these methods can be divided into two major groups of methods relied on each reaction mechanisms: top-down and bottom-up approaches.[104] The principal reaction mechanisms of the top-down methods are assigned to the oxidation process (cutting or etching) or mechanical shearing. The top-down processes refer to converting large sp_2 carbon domains into smaller particles size. Although the top-down methods are simple, but not easy to operate and time-consuming. Besides, the precursors are used in the top-down process which limited due to the requirement of a large area of sp_2 carbon domains. Whereas the bottom-up approaches refer to the formation of sp_2 carbon domains from organic molecules through intermolecular coupling and carbonisation process leading to a controllable size and morphology of the nanomaterials. Bottom-up methods consist of pyrolytic process, microwave-assisted method, and hydrothermal treatment.[11, 27]

2.4.1 Top-down method

- *Laser ablation*

The synthesis of CQDs using laser ablation begins with the preparation of the carbon source material, typically graphite powder or carbon nanotubes, which is ground into a fine powder and pressed into a pellet using a hydraulic press. This pellet is then immersed in a liquid dispersion medium such as water, acetone, or ethanol. The synthetic procedure of CQDs using laser ablation is displayed in **Figure 2.5**.

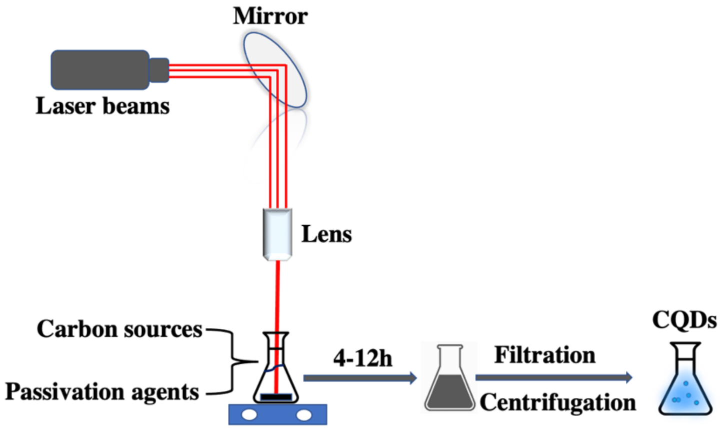

Figure 2.5: The procedure of CQDs synthetic using laser ablation method

A high-energy pulsed laser beam from a is focused directly onto the surface of the carbon pellet. The intense laser irradiation ablates the carbon material, breaking carbon-carbon bonds and creating a plasma plume containing carbon vapor and nanoclusters. This plasma plume gets quenched rapidly in the liquid medium, leading to nucleation and growth of CQDs. The produced CQDs in the liquid dispersion are separated by high-speed centrifugation to remove larger particles. Further purification steps like dialysis, chromatography or extraction are used to isolate CQDs of the desired size range and remove molecular impurities. In a study by Hu et al., CQDs were synthesised using a laser ablation method with graphite powder as the carbon source. The graphite powder was dispersed in three different solvents - diamine hydrate, diethanolamine, and poly (ethylene glycol) (PEG200N) - to form the liquid dispersion medium. The graphite dispersions were then irradiated by a pulsed Nd:YAG laser with a wavelength of 1,064 nm and a power density of 6.0 x 106 W/cm^2.[105] Another example of using laser ablation for preparation CQDs, Gonçalves et al., reported the utilise of direct laser ablation of carbon targets immersed in deionised water to synthesise CQDs, and the prepared carbon particles were not fluorescent. After refluxing in nitric acid for 12h and passivating the surface by using organic species such as PEG 200, and thiomalic acid. Finally, the obtained CQDs emitted light brown fluorescent.[106] The main benefits of laser ablation are the simple, fast, one-step synthesis and the ability to produce highly pure CQDs. However, drawbacks include low yield, broad CQD size distributions, reproducibility issues, requirement for costly laser equipment, and lack of scalability for mass production.

- *Electrochemical carbonisation*

The electrochemical setup for CQD synthesis consists of a two or three electrode system with graphite rods or plates serving as the anode and cathode submerged in an electrolyte solution such as NaOH, AgCl, or alkaline alcohol. An appropriate potential difference in the range of 2-5 volts is applied between the two electrodes to initiate the electrolysis process. At positive potentials, the graphite anode material begins oxidizing and the layers start exfoliating into the surrounding electrolyte in the form of carbon clusters. As the applied voltage is continually increased, further oxidative cleavage of the anode graphite occurs, releasing more carbonaceous fragments into solution. Prolonged electrolysis leads to the generation of a large number of quantum sized carbon dots dispersed in the electrolyte. The CQD dispersed solution is then centrifuged at high speeds to separate the synthesised CQDs from the parent graphite particles and other insoluble components. Further purification can be performed using dialysis or column chromatography to isolate pure CQDs.[107]

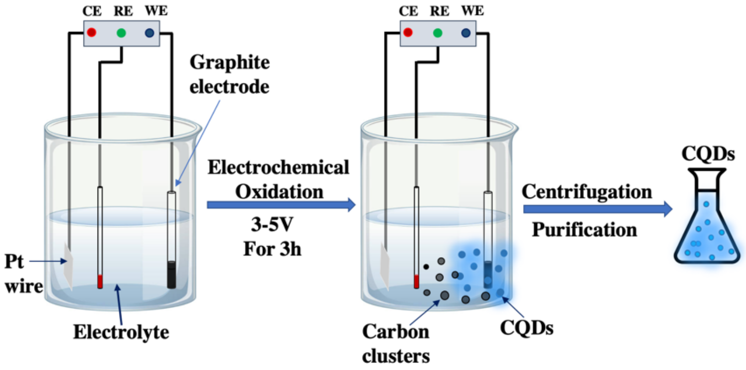

Figure 2.6: The procedure of CQDs synthetic process via electrochemical approach, where CE is counter electrode, RE is reference electrode; and WE is working electrode

The CQDs synthetic procedure using electrochemical method is summarised as shown in **Figure 2.6**. Key parameters like electrode material, electrolyte pH, and oxidation voltage can be tuned to control the carbonization process. Borna et al., reported to successful synthesise CQDs via electrochemical methods. In this process, two graphite electrodes of pencil core with a diameter of 0.5 cm were used for the electrochemical preparation of CQDs. A solution of 0.1 M Ethanol/NaOH was used as electrolyte. The length of each electrode was 5 cm, which was placed 1 cm of each in the electrolyte solution for electrochemical reaction. A 100-mA current was applied to the electrodes using a DC source. Over time, the colour of the solution changed from colourless to light yellow and then to very pale red. The solution was collected after 3h, then placed in an ultrasonic water bath for 30 min and then filtered through 0.22 µm filter paper. The obtained results demonstrated that the synthesised CQDs possess particles size within the range of 1–10 nm, and the CQDs solutions exhibited good fluorescence behaviours.[108]

Advantages of electrochemical CQD synthesis include the simple, fast, low-cost method which is easily scalable and tuneable by varying voltage, electrodes, and electrolyte. However, limitations exist like broader CQD size distributions, more defects, need for functionalization and rigorous purification.

2.4.2 Bottom-up approach

- *Microwave assisted method*

The microwave assisted preparation of CQDs can use a wide range of organic precursor rich in carbon such as citric acid, glucose, or ascorbic acid.[109] The precursor is dissolved in a solvent like water, ethanol, or ethylene glycol. The precursor solution is then irradiated with microwave energy, typically at power levels from 300-900 Watts for duration ranging from 5-60 minutes. The microwave irradiation leads to rapid and homogeneous heating of the precursor solution, which drives dehydration and carbonization reactions resulting in the formation of CQDs dispersed in the solvent. After microwave treatment, the reaction is cooled down to room temperature. The CQDs are then separated from the solution using high speed centrifugation. Further purification is carried out using dialysis or chromatography techniques to remove any unreacted reagents. By tuning parameters such as microwave power, irradiation time and precursor concentration, the yield, and characteristics of the synthesised CQDs can be controlled.[110] In summary, the synthetic process of CQDs using microwave-assisted approach is illustrated in **Figure 2.7**. Guan et al. reported a microwave-assisted method to synthesize fluorescent CQDs using folic acid as the source of carbon and nitrogen. In this process, 15 mg of folic acid was dissolved in 3 mL of diethylene glycol, and then the mixture was heated for 40 seconds using a 750 W microwave oven. Subsequently, the obtained red-brown solution was subjected to dialysis against pure water for three days. The obtained CQDs had an average size of 4.51 nm and showed a high quantum yield of 18.9%.[111]

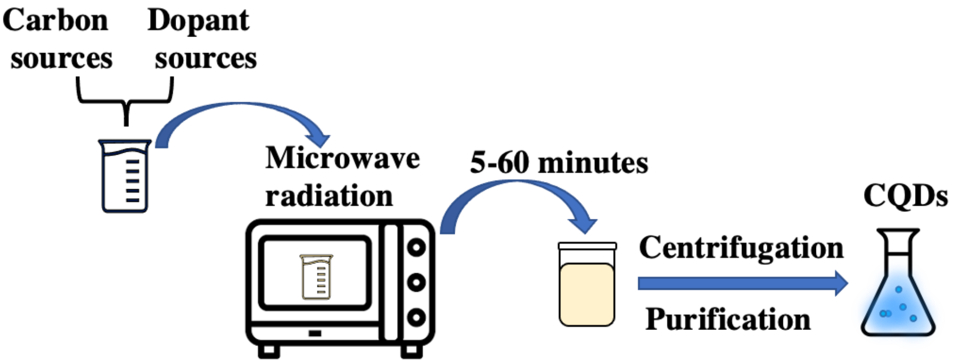

Figure 2.7: The CQDs synthetic process via microwave assisted approach

In addition, Wang and co-workers reported a simple one-step microwave-assisted method to fabricate water-soluble CQDs. Briefly, a mixture containing 2 mL of 70% phytic acid, 1 mL of ethylenediamine, and 25 mL of deionized water was prepared. The mixture was then heated for 8 minutes in a 700 W microwave oven. Subsequently, CQDs were obtained after purifying the crude product. These CQDs possessed phosphorus groups, which were covalently bonded to the aromatic structure of the prepared C-dots. The quantum yield of the prepared phosphorus-containing C-dots was around 21.65%.[112] The key advantages of CQDs produced through microwave synthesis are the ability to rapidly prepare them in minutes, simple single-step preparation and, low cost of the microwave setup. However, there are some disadvantages associated with the CQDs generated through microwave-assisted approach. The defects induced in CQDs due to rapid carbonization may degrade their optical performance. Microwave reactions is poor control resulted in a broader size distribution of CQDs.

- *Batch hydrothermal synthesis*

Hydrothermal carbonisation is an environmentally friendly, non-toxic, and low-cost approach to prepare fluorescent carbon dots.[16] As shown in **Figure 2.8**, a typical hydrothermal process, the reaction precursors are prepared by using small organic molecules or polymers dissolving in water or organic solvent, then the mixture was transferred to a Teflon-lined stainless-steel autoclave, the precursors reacted together at relatively high temperature to fabricate carbon seeding cores and then grow into CQDs with a particle size of less than 10 nm.[113] After hydrothermal treatment, the autoclave is cooled, the CQD solution is collected and centrifuged at high speeds to isolate the CQDs from larger particles. The CQD supernatant then undergoes further dialysis or column chromatography purification to remove unreacted precursors.[114]

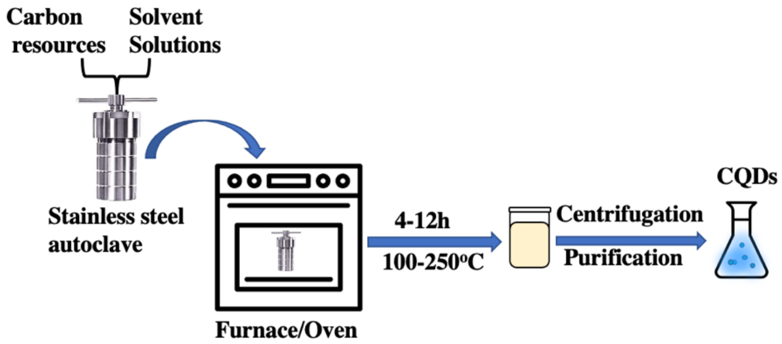

Figure 2.8: The procedure of hydrothermal CQDs synthetic process

For example, Wu and co-workers reported a hydrothermal using microcrystalline cellulose as the precursor for CQDs preparation. In the procedure, microcrystalline cellulose was dispersed in ethylenediamine solution taken in a polyphenol-lined stainless-steel autoclave. The sealed autoclave was subjected to hydrothermal treatment at 240^0C for 12 hours and allowed to cool down. The obtained solutions were centrifuged at 10,000 rpm for 10 minutes and the supernatants containing CQDs were filtered through 0.22 µm membranes. Finally, dialysis was performed on the filtered solutions using a 1,000 Da molecular weight cut-off for about 72 hours to purify the CQDs.[115] Another study demonstrated the hydrothermal synthesis of fluorescent CQDs using orange juice as the precursor. The CQDs were prepared by subjecting orange juice to relatively mild hydrothermal treatment at 120^0C for 150 minutes in a Teflon-lined autoclave. The low temperature hydrothermal processing facilitated decomposition and carbonization of the organic compounds present in orange juice, leading to formation of fluorescent CQDs dispersed in the solution. Characterization revealed that the synthesised CQDs had a small average size of 1.5 to 4.5 nm and exhibited a good quantum yield of 26%.[116]

The hydrothermal approach for producing CQDs is more environmentally friendly and scalable due to its ability to utilise various precursors as carbon sources. However, some limitations exist with the hydrothermal approach. The method requires a long reaction time to facilitate the hydrothermal carbonisation process. Additionally, post-synthesis, complex multi-step procedures are needed to purify the CQDs from by-products and unreacted reagents. Therefore, optimising parameters of the hydrothermal process, such as precursor type, temperature, pressure, and reaction time, are needed for further research.

2.5 Carbon quantum dots doping and CQDs-nanocomposites

In recent times, there has been increasing research focused on using doping methods involving elements such as nitrogen, phosphorus, and sulphur to enhance the photoluminescence properties of fluorescent CQDs. Nitrogen doping has emerged as the most promising approach for improving the optical characteristics of CQDs. The incorporation of nitrogen atoms into the carbon structure is believed to be the primary reason for the enhanced photoluminescence emission from NCQDs. This enhancement stems from nitrogen atoms inducing beneficial changes in the electron density distribution and bandgap structure of CQDs, resulting in improved surface passivation and new emissive trap states.[118] However, the exact mechanisms behind these modulations in CQD properties due to nitrogen doping are still not fully understood, with effects like bandgap tuning, molecular state generation, and altered surface chemistry being proposed. While clearly beneficial, challenges remain in controlling the nitrogen content and bonding configurations in CQDs to achieve specific optical outcomes. Most current strategies rely on nitrogen-rich precursors or post-synthesis treatment with nitrogen sources, but tuning nitrogen levels during direct CQD synthesis remains difficult. Additionally, the impact of nitrogen doping on properties like electronic structure, electron transfer, and exciton dynamics requires further study. Optimizing the intersection between nitrogen doping and factors like CQD size, shape and surface chemistry also needs to be addressed for customised CQD development.[119,120] Other reported co-doping combinations include P-N doped CQDs and S-N doped CQDs exhibiting excellent fluorescent stability, water solubility and low toxicity.[112] Overall, these studies highlight the tremendous potential of both single and co-doping approaches for modulating the optical, electronic, and physical characteristics of CQDs in a targeted manner.

Recently, the fabrication of novel nano-hybrids of CQDs and inorganic nanoparticles (zinc oxide, iron oxide, and titanium dioxide) has gained attention. The metal oxide not only provides the mechanical properties of the oxide cores but also introduces new properties like magnetism, which expands the potential applications for CQDs such as magneto-optical bio-labelling or photocatalysis.[121] Luo et al. reported the use of chitosan derived NCDs to fabricate the nanocomposite TiO_2-NCDs. This study demonstrated NCDs improved the photochemical activity of TiO_2-NCQDs which can be contributed to the synergistic effect of NCDs.[122] Another example, TiO_2/CQD nanocomposites can be synthesised via a hydrothermal method using vitamin C as the carbon source under hydrothermal conditions (200°C for 2h). The prepared nanocomposite has been applied as a photocatalyst for hydrogen generation via water splitting.

Compared to bare TiO_2 nanoparticles, the TiO_2/CQD nanocomposites exhibited a 9.7 times higher H_2 production rate. This excellent photocatalytic performance is attributed to the electron transfer ability and up conversion properties of the CQDs.[123]

2.6 Continuous hydrothermal flow synthesis

2.6.1 A rapid and environmentally friendly method for CQDs synthesising

Continuous hydrothermal flow synthesis (CHFS) utilises unique properties of supercritical water to promote rapid nucleation of nanoparticles. The avoidance of hazardous organic solvents makes it a green synthetic approach.[124] In a typical CHFS process that is primarily water-based, an engineered mixer (as a reactor) is used with the feed flows being superheated water and carbon sources. The critical temperature and pressure of water are 647 K (374°C) and 22.1 MPa (3200 psi or 218 atm), respectively. On reaching these critical values, the properties of water begin to change radically, making it a useful medium for conducting rapid chemical reactions. After mixing, a high temperature typically in the range of 200-400°C is reached, and the residence time is generally around a few seconds to minutes for nanoparticles like CQDs to form.[125] A facile single-step, green approach to synthesize graphene quantum dots (GQDs) using CHFS was reported by Kellici et al. Graphite oxide (GO), synthesised via a modified Hummers method, and calix [4] arene tetra phosphonic acid were used as precursors for CQD fabrication in an alkaline medium. The obtained graphene quantum dots showed PLQY up to 4.5% after surface functionalisation, with excitation-independent emission peaked at 510 nm.[126] Recently, Baragau et al. reported a rapid green route to synthesize NCQDs using CHFS. Citric acid and ammonia were used as carbon and nitrogen sources, respectively. The synthesised NCQDs exhibited an average particle size of 3.3 - 4.0 nm, with a high quantum yield of 14.9 ± 0.24%.[68] More recently, CHFS was reported as a rapid, efficient, and environmentally friendly approach for synthesising CQDs using biomass precursors like glucose. The synthesised CQDs possess excellent water-solubility with an average size of just 2.3 ± 0.5 nm. Notably, the glucose derived CQDs showed excellent sensitivity and selectivity in detecting toxic chromium (VI) ions. Life cycle assessments confirmed the use of CHFS in glucose-CQD synthesis is far more efficient and sustainable than conventional batch hydrothermal methods.[127] Another examples, CHFS was employed to synthesize sulphur-doped CQDs (S-CQDs) from glucose and p-sulfonic acid calix [4] arene. The S-CQDs showed excellent colloidal stability in brine solutions and low retention on sand, along with impressive

17% enhanced oil recovery at very low 0.01 wt.% concentrations. The small mean particle size of 1.7 nm enables the S-CQDs to recover trapped oil from tight reservoirs through log-jamming. Additionally, they can alter wettability of carbonate rocks toward water wet. The S-CQDs also exhibit advantageous photoluminescence, pH stability from 3-11, and excitation-independent emission. This study demonstrated that CHFS is a rapid, environmentally friendly method capable of incorporating various dopant types into CQDs during their synthesis.[128]

The CHFS technique offers several benefits for rapid, single-step CQD fabrication in a flow reactor, enabling large-scale production. The continuous operation with supercritical water allows synthesis of CQDs in seconds or minutes while avoiding lengthy multi-step batch methods. CHFS provides tunability of CQDs properties like size, surface chemistry and photoluminescence by adjusting parameters like temperature, pressure, and residence time. The approach is considered environmentally friendly owing to the use of water instead of toxic solvents. However, CQDs aggregation is a risk due to rapid mixing and interaction. Clogging of the flow reactors can occur if precipitates form. Overall, while CHFS enables scalable rapid synthesis, it requires an optimal process to improve control over CQD fabrication.[129]

2.6.2 *Supercritical water properties*

Supercritical water possesses a unique combination of physical and chemical properties that can be tuned by manipulating temperature and pressure. As show in Figure, when water approaches and passes its critical point of 647K (374°C) and 218 atm (22.1 MPa), the density of water drops precipitously to 0.326 g/cm^3. This represents a nearly 70% reduction in density compared to liquid water. As the temperature increases further beyond the critical point, the density continues decreasing, at typical supercritical water oxidation conditions, the density is only 0.1 g/cm^3. The substantial decrease in density has major implications for solubility, mass transfer, and other physicochemical properties in supercritical water.[130]

The sc-water have the viscosity of 0.298×10^{-2} pa·s which is around an order of magnitude lower than liquid water under ambient conditions. This exceptionally low viscosity, approaching that of air, qualifies supercritical water as a highly fluid substance. As temperature increases, the viscosity declines further, enabling the density of supercritical water to decrease. The reduced viscosity coupled with lower density facilitates rapid diffusion of solute molecules dissolved in the supercritical water. The gas-like fluid dynamics allow supercritical water to act as an ideal medium for fast mass transfer between reactants.[131] In addition, the dielectric constant of sc-water is heavily dependent on temperature and density due to its relation to hydrogen bonding.[132] The ambient conditions water possesses high dielectric constant of 78.46 is attributable to extensive hydrogen bonding networks. However, increasing temperature serves to lower the dielectric constant as hydrogen bonds break down, while increasing pressure counters this effect to some extent by raising density. But the influence of temperature is more pronounced. At 300°C and a density of 0.75 g/cm^3, the dielectric constant of sc-water drops to 21. Further lowering the density to 0.30 g/cm^3 at 500°C further reduces the dielectric constant to just 4.1. The dielectric dramatic decrease at higher temperatures and lower densities is driven by the loss of hydrogen bonding.[133] As water transitions to the supercritical state at higher temperatures and lower densities, these intermolecular hydrogen bonds are disrupted.[134] At a density of 0.1 g/cm3 and temperature of 412°C, only 10-14% of the maximum possible hydrogen bonds remain intact. But at the higher density of 0.5 g/cm3 and slightly lower temperature of 356°C, 30-45% of the hydrogen bonds are still present.[135] The combination of high diffusivity and solvent power provides favourable conditions for rapid mixing, mass transfer, and reactions. Also, at the supercritical point, the water diffusion coefficient is dramatic increased in the water diffusion coefficient by over 10 times when density drops from 1 g/cm^3 to 0.1 g/cm^3.[136] The drastic reduction in intermolecular forces allows water molecules to move freely and rapidly like a gas, rather than being constrained by neighbours as in normal liquids. Therefore, sc-water enables to exhibit gas-like diffusivities while still acting as a solvent and reaction medium.[137]

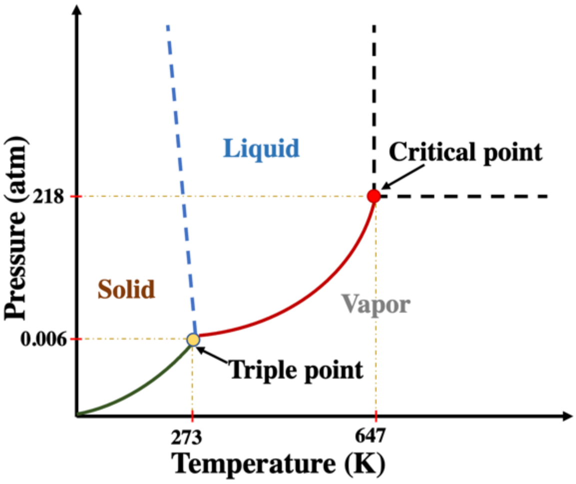

Figure 2.9: The phase diagram of water

The solubility properties of water are inverted when going from ambient to supercritical conditions. Under normal conditions, water readily dissolves most inorganic compounds, while being a poor solvent for organic substances and gases. However, supercritical water exhibits the opposite behaviours. Inorganic salts and minerals become almost insoluble in the supercritical region, whereas solubility of organics and gases increases markedly. This is attributable to the decreased polarity and hydrogen bonding of supercritical water compared to the liquid state.[138] The unusual solubility enables supercritical water to act as a versatile reaction medium. Organic reactants can be dissolved while inorganic products remain insoluble and precipitate out. The ability to solubilize ordinarily immiscible organics and gases also opens novel synthesis pathways. Therefore, the inverted solubility provides unique advantages that make supercritical water a highly useful medium for nanoparticle nucleation processes.[139]

2.6.3 *Nucleation and growth of nanoparticle during CHFS process*

The ability to precisely control the size and distribution of nanoparticles is critical for most synthetic process. CHFS is enabled to provide precise control over nanoparticle nucleation and growth by exploiting the unique properties of sc-water.[140] The density, dielectric constant, viscosity, and solubility of water start to rapidly decrease under the supercrical conditions. The precursors instantly become supersaturated as the surrounding water is no longer able to solvate the dissolved ions. Therefore, the main mechanism for fabrication of nanoparticles in the CHFS process is maximisation of supersaturation, resulting in the rate of nucleation is increased.[125] Supersaturation is the ratio of the concentration of a species in solution to the saturation concentration, thus the lower the saturation concentration, the higher the supersaturation.[141] The dramatic change in conditions for dissolved precursors from ambient to supercritical condition leading to the burst nucleation event within milliseconds, which can be attributed to the LaMer model.[142]

The LaMer mechanism delineates nanoparticle nucleation and growth into three distinct stages. First, the concentration of free monomers in solution increases rapidly (Stage I). When a critical supersaturation threshold is exceeded, the monomers undergo an extremely fast "burst" of nucleation, instantly bringing the monomer concentration back down (Stage II). LaMer described this nucleation rate as "effectively infinite" since the burst occurs quickly. In the Stage III, nanoparticles can continue to grow through different pathway. Nanoparticle growth may proceed via monomer addition, where precursor units from the supersaturated solution deposit onto the existing nuclei. However, Ostwald ripening can also occur, where small, energetically unfavourable nuclei dissolve and re-deposits onto more extensive, more stable, and larger nuclei. Nanoparticle coalescence can also take place if particles collide and fuse.[143]

The insights into the nucleation mechanism during continuous hydrothermal flow synthesis (CHFS) enable tuning of both nanoparticle size and size distribution.

In contrast to conventional hydrothermal synthesis, CHFS offers superior control over nanoparticle nucleation and growth kinetics. Batch hydrothermal methods involve slow heating of the precursor solution, taking hours to reach temperature. This causes the precursor concentration to stay above the critical nucleation threshold for prolonged times. As a result, uncontrolled nucleation occurs continuously alongside growth throughout the reaction, yielding broad particle size distributions. CHFS overcomes this by using ultrafast heating and mixing to induce a short burst of nucleation within milliseconds.[144] A narrow nanoparticle size distribution can be achieved through the highly rapid generation of precursor to swiftly surpass the critical nucleation threshold leading to the nucleation efficiently occur once. This burst of nucleation quickly relieves supersaturation and brings the precursor concentration back below the critical point, prohibiting further nucleation events.[145] Since nucleation occurs in a short spike, the resultant nuclei have minimal size discrepancies, limiting Ostwald ripening. The similarly sized nuclei grow predominately through diffusion, preserving the tight size distribution. The precise size can be controlled by varying the reaction time and adding controlled amounts of precursor while staying below the nucleation concentration. Moreover, nanoparticle growth can be restricted to the initial nucleus size by immediately stopping the reaction after the nucleation spike, either by entirely consuming the limited precursor, rapidly quenching, or removing the driving force for growth-like temperature.[146]

In conclusion, the nucleation mechanism in CHFS arises from the rapid burst nucleation induced by instantaneously supersaturating precursors. The ultrafast mixing and heating in CHFS generate a short spike in nucleation that produces uniform nuclei and temporally separates the nucleation and growth stages. This unprecedented control over the nucleation event enables precise tuning of the final nanoparticle size and distribution, which is not achievable through traditional hydrothermal methods.

2.6.4 *CHFS process and reactor designs*

Since its initial development, the CHFS process and reactor have undergone ongoing optimization to achieve the highest possible efficiency, allowing for scalability and the establishment of a sustainable method for synthesizing carbon-based nanomaterials.

- *The development of continuous hydrothermal process*

The earliest developments in continuous hydrothermal nanoparticle synthesis emerged independently in the U.S. and Japan through two different approaches. Pacific Northwest Laboratories in the U.S pioneered the simplest process design as show in **Figure 2.10**. This simplest process involved pumping a stream of dissolved precursors through a heated furnace under pressure controlling by a back-pressure regulator BPR valve.[147] The product then was cooled down using a water cooler. The gas and liquid products were separated using a column separator.

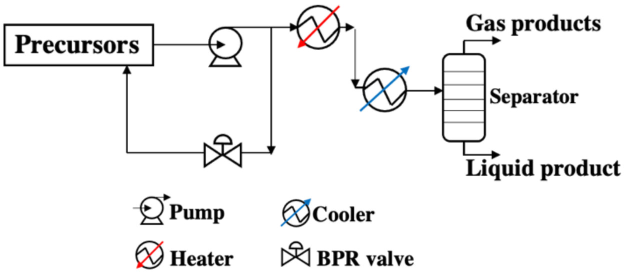

Figure 2.10: Continuous hydrothermal process designed by Pacific Northwest Laboratories

While this simplistic approach has been implemented in some microfluidic reactors and can synthesise a variety of materials, it does not implement the advanced engineering required to precisely control nanoparticle nucleation and growth kinetics.[148] In this simple pumped heating design, new nuclei form continuously as fresh precursor passes through the heated zone, similar to traditional batch hydrothermal reactions. However, the limited residence times make it difficult to achieve size focusing, resulting in broad particle size distributions. Furthermore, growth of existing nuclei is unavoidable, leading to poorly controlled particle sizes. Essentially, this design fails to temporally separate the nucleation and growth stages leading to the lack of engineered nucleation-growth separation inhibits precise control over particle sizes and distributions.

Another continuous hydrothermal process was developed by Adschiri research group, Japan in the early 1992, as shown in **Figure 2.11**. The Adschiri's approach based on the continuous mixing of two separate streams - one containing supercritical water (400^{0}C) and the other containing ambient temperature dissolved precursors.[149] The original process design utilized two high-performance liquid chromatography (HPLC) pumps to deliver the precursor solution and pump the water stream through an inline heater. Initially, this heater consisted of simple coiled tubes in a furnace. However, it was later modified into a custom electrical heater to rapidly heat the water to supercritical conditions before mixing it with the room-temperature precursor stream. The pressure was maintained at 35MPa throughout the entire process using a BPR.[150]

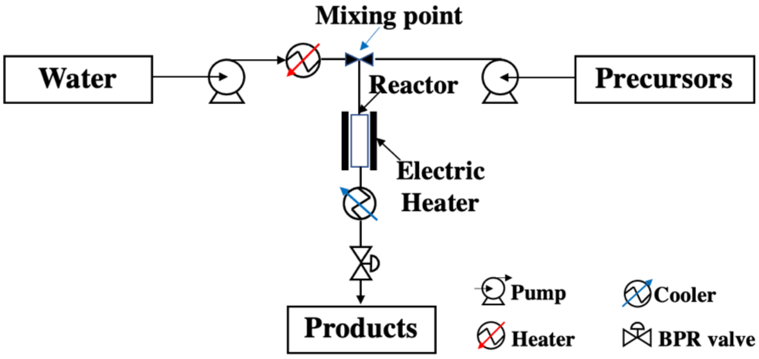

Figure 2.11: CHFS process designed by Adschiri group, Japan

The work by Adschiri et al. laid the groundwork for utilising supercritical water in continuous hydrothermal synthesis. This approach using supercritical water flow is now widely adopted and known as continuous hydrothermal flow synthesis. Modern variations have built on the original two-pump design, implementing three- and four-pump systems to allow greater flexibility and control over precipitation by isolating incompatible precursors.[151,152]

- *The reactor designs*

The mixer design in continuous hydrothermal reactors plays a crucial role in controlling nanoparticle nucleation and growth by governing the mixing dynamics between the sc-water and ambient precursor streams. The aim is to achieve rapid and complete mixing without unwanted preheating or clogging issues.[153] Since the establishment of the first CHFS reactors, there have been ongoing developments in mixing point design utilising different configurations to achieve optimal mixing, as shown in **Figure 2.12**. The T-piece mixer is one of the most basic mixers utilised in continuous hydrothermal reactors, consisting simply of a T-shaped conjunction point where the precursor and water streams converge, as shown in **Figure 2.12.a**.[149] While the simple T-mixer design provides some advantages like inexpensive fabrication from standard fittings, straightforward assembly, and flexible operation across various flow regimes, it has several notable disadvantages for controlling nanoparticle formation. Also, T-mixers suffer from incomplete, asymmetric mixing between the streams resulting in non-uniform mixing with some portions well mixed while others remain unmixed.[153] In the CHFS using T-mixer, the broad distribution of residence times for fluid elements also makes tight control over nucleation conditions difficult. Additionally, the simplicity of the T-mixer lends itself to potential issues like precursor stream preheating or unwanted premature reactions.[154]

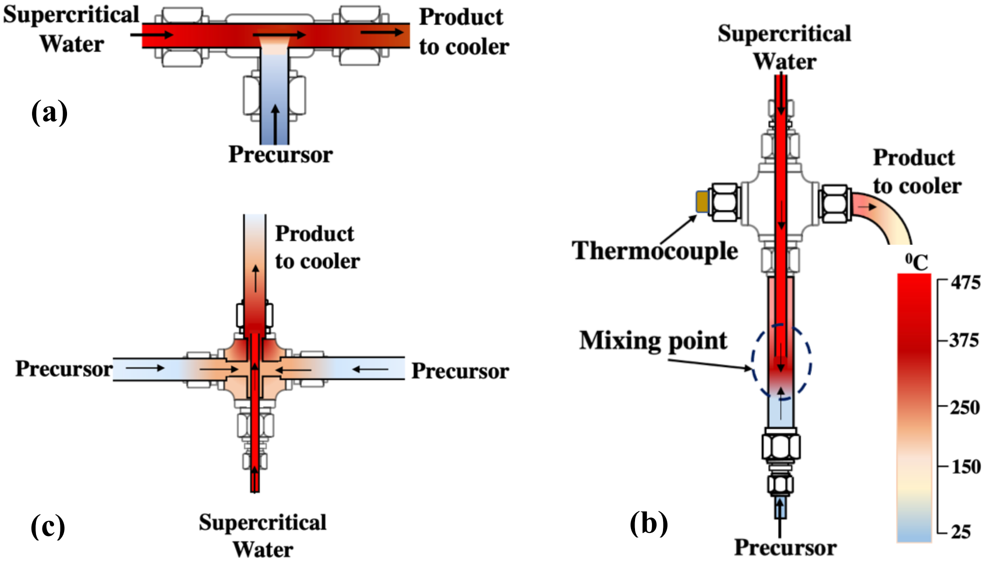

Figure 2.12: The reactor designs: (a) T-piece mixer, (b) counter flow mixer, (c) confined jet mixer

In 2004, Lester and colleagues developed a novel counter-current mixer configuration in order to improve the contacting of the precursor and supercritical water streams. In this vertical mixer, the water enters from the top through an inner tube while the precursor enters from the bottom up through the outer chamber. The two streams meet and mix at the bottom opening of the inner tube, with the mixed stream exiting upwards, as shown in **Figure 2.12.b**.[155] This configuration takes advantage of the density difference between the hot water and cooler precursor to promote mixing. Counter-current design overcomes limitations of T-mixers like incomplete mixing and precursor preheating by superior mixing dynamics. However, with precisely balanced flow rates of the incoming streams, the supercritical water jet showed limited penetration into the precursor stream after initially converging. Also, imbalanced flow ratios led to large fluctuations in temperature sc-water into the precursor stream.[156] Therefore, it is important to optimise the flowrate and the concentration of precursors in the CHFS process using counter-current mixer.

Recently, researchers at UCL developed coaxial or confined jet mixers, as shown in **Figure 2.12.c**. The distinguishing feature of a confined jet mixer is the use of a coaxial nozzle to focus the sc-water stream into a narrow, high-velocity jet.[157] This jet ejects into a chamber containing the precursor streams, causing the jet to penetrate the precursor streams. The confined space forces intense mixing between the streams to occur within milliseconds. The mixing dynamics can be optimised for heat transfer and mass mixing between the streams by tuning factors like nozzle diameter, chamber dimensions, and back pressure.[158] However, the intense mixing can lead to precipitate accumulation and clogging issues. The more complex nozzle and chamber geometries also increase fabrication demands compared to other mixers.[159] Further optimization of confined jet mixer geometries is needed to enhance capabilities for industrial scale nanomaterial production.

2.7 Conclusion

Carbon quantum dots have emerged as a promising and novel class of carbon-based nanomaterials. First discovered in 2004, research related to CQDs has seen rapid development and explosive growth in the last decade. A major advantage of CQDs is that they can be synthesised from various economical and abundant carbon sources via simple synthetic routes like microwave, hydrothermal treatment, and electrochemical synthesis. This allows for scalable and low-cost production, making CQDs suitable for a wide range of applications. Additionally, CQDs possess appealing properties like high photostability, low toxicity, and excellent biocompatibility. With their unique photoluminescence, CQDs have promising applications in optoelectronics, bioimaging, biosensing, and photocatalysis. However, there remain challenges regarding precise control over CQD properties during synthesis. Factors like precursor choice, synthetic method, temperature, reaction time all impact the size, shape, and surface chemistry of CQDs. More research is needed to better understand CQDs nucleation and growth mechanisms and achieve fine-tuned synthesis with high quality CQDs production. Furthermore, surface passivation and doping provide routes to tailor CQD properties, but better control over dopant levels and configurations is also required. Future CQD research should focus on addressing these synthetic challenges to allow rational design and precision engineering of CQDs for target applications. There is also a need for standardised characterization techniques and protocols for CQDs to facilitate data comparison between studies. Overall, CQDs represent an emerging functional nanomaterial with tremendous potential in diverse fields. While synthetic control remains a key challenge, the future is promising for CQD research. Advances in understanding CQD nucleation, growth, and surface chemistry will enable rational design of CQDs with controlled structures and properties. This will open doors for innovating novel applications and technologies based on these low-cost, sustainable carbon nanomaterials. The next decade of research promises to be even more exciting as CQDs transition from lab-based studies toward real-world implementation.

Chapter 2: References

1 M. Sibilia, C. Stani, L. Gigli, S. Pollastri, A. Migliori, F. D'Amico, C. Schmid, S. Licen, M. Crosera, G. Adami, P. Barbieri, J. R. Plaisier, G. Aquilanti, L. Vaccari, S. Buson and F. Gonzato, *Sci Rep*, 2021, **11**, 7231.

2 T. Gupta, *Carbon*, Springer International Publishing, Cham, 2018, pp. 47–70.

3 G. Collin, *Industrial Carbon and Graphite Materials, Volume I*, eds. H. Jäger and W. Frohs, Wiley, 1st edn., 2021, pp. 33–43.

4 J. R. Heath and R. F. Curl, *Nature*, 2016, **533**, 470–470.

5 M. Kokarneswaran, P. Selvaraj, T. Ashokan, S. Perumal, P. Sellappan, K. D. Murugan, S. Ramalingam, N. Mohan and V. Chandrasekaran, *Sci Rep*, 2020, **10**, 19786.

6 K. S. Novoselov, A. K. Geim, S. V. Morozov, D. Jiang, Y. Zhang, S. V. Dubonos, I. V. Grigorieva and A. A. Firsov, *Science*, 2004, **306**, 666–669.

7 J. Liu, R. Li and B. Yang, *ACS Cent. Sci.*, 2020, **6**, 2179–2195.

8 Y. Wang and A. Hu, *J. Mater. Chem. C*, 2014, **2**, 6921.

9 X. Xu, R. Ray, Y. Gu, H. J. Ploehn, L. Gearheart, K. Raker and W. A. Scrivens, *J. Am.Chem. Soc.*, 2004, **126**, 12736–12737.

10 Y.-P. Sun, B. Zhou, Y. Lin, W. Wang, K. A. S. Fernando, P. Pathak, M. J. Meziani, B. A. Harruff, X. Wang, H. Wang, P. G. Luo, H. Yang, M. E. Kose, B. Chen, L. M. Veca and S.-Y. Xie, *J. Am. Chem. Soc.*, 2006, **128**, 7756–7757.

11 L. Cui, X. Ren, M. Sun, H. Liu and L. Xia, *Nanomaterials*, 2021, **11**, 3419.

12 B. D. Mansuriya and Z. Altintas, *Nanomaterials*, 2021, **11**, 2525.

13 F. Yuan, T. Yuan, L. Sui, Z. Wang, Z. Xi, Y. Li, X. Li, L. Fan, Z. Tan, A. Chen, M. Jin and S. Yang, *Nat Commun*, 2018, **9**, 2249.

14 C. Xia, S. Zhu, T. Feng, M. Yang and B. Yang, *Advanced Science*, 2019, **6**, 1901316.

15 J. H. Liu, D. Y. Li, J. H. He, D. Yuan, R. S. Li, S. J. Zhen, Y. F. Li and C. Z. Huang, *ACS Appl. Mater. Interfaces*, 2020, **12**, 4815–4820.

16 X. Wang, Y. Feng, P. Dong and J. Huang, *Front. Chem.*, 2019, **7**, 671.

17 M. J. Meziani, X. Dong, L. Zhu, L. P. Jones, G. E. LeCroy, F. Yang, S. Wang, P. Wang, Y. Zhao, L. Yang, R. A. Tripp and Y.-P. Sun, *ACS Appl. Mater. Interfaces*, 2016, **8**, 10761–10766.

18 P. Zhao and L. Zhu, *Chem. Commun.*, 2018, **54**, 5401–5406.

19 Z. Qiu, L. Li, Q. Zhu, R. Guo, Y. Yao, C. Wu, S. Li and P. Li, *j nanosci nanotechnol*, 2021, **21**, 5312–5318.

20 Z. Luo, A. Oki, L. Carson, L. Adams, G. Neelgund, N. Soboyejo, G. Regisford, M. Stewart, K. Hibbert, G. Beharie, C. Kelly-Brown and P. Traisawatwong, *Chemical Physics Letters*, 2011, **513**, 88–93.

21 V. Rimal and P. K. Srivastava, *IOP Conf. Ser.: Mater. Sci. Eng.*, 2022, **1219**, 012018.

22 C. Wang, Z. Xu, H. Cheng, H. Lin, M. G. Humphrey and C. Zhang, *Carbon*, 2015, **82**, 87–95.

23 Y. Liu, L. Zhou, Y. Li, R. Deng and H. Zhang, *Nanoscale*, 2017, **9**, 491–496.

24 W. U. Khan, D. Wang and Y. Wang, *Inorg. Chem.*, 2018, **57**, 15229–15239.

25 A. Dager, T. Uchida, T. Maekawa and M. Tachibana, *Sci Rep*, 2019, **9**, 14004.

26 I.-A. Baragau, N. P. Power, D. J. Morgan, T. Heil, R. A. Lobo, C. S. Roberts, M.-M. Titirici, S. Dunn and S. Kellici, *J. Mater. Chem. A*, 2020, **8**, 3270–3279.

27 N. A. S. Omar, Y. W. Fen, R. Irmawati, H. S. Hashim, N. S. M. Ramdzan and N. I. M. Fauzi, *Nanomaterials*, 2022, **12**, 2365.

28 K. J. Mintz, Y. Zhou and R. M. Leblanc, *Nanoscale*, 2019, **11**, 4634–4652.

29 G. E. LeCroy, F. Messina, A. Sciortino, C. E. Bunker, P. Wang, K. A. S. Fernando and Y.-P. Sun, *J. Phys. Chem. C*, 2017, **121**, 28180–28186.

30 H. Liu, X. Zhao, F. Wang, Y. Wang, L. Guo, J. Mei, C. Tian, X. Yang and D. Zhao, *Nanoscale Res Lett*, 2017, **12**, 399.

31 X. Li, S. Zhang, S. A. Kulinich, Y. Liu and H. Zeng, *Sci Rep*, 2014, **4**, 4976.

32 X. Wen, P. Yu, Y.-R. Toh, X. Ma and J. Tang, *Chem. Commun.*, 2014, **50**, 4703–4706.

33 L. Cao, X. Wang, M. J. Meziani, F. Lu, H. Wang, P. G. Luo, Y. Lin, B. A. Harruff, L. M. Veca, D. Murray, S.-Y. Xie and Y.-P. Sun, *J. Am. Chem. Soc.*, 2007, **129**, 11318–11319.

34 K. Jiang, Y. Wang, X. Gao, C. Cai and H. Lin, *Angewandte Chemie*, 2018, **130**, 6324–6328.

35 S. Mukherjee and P. Thilagar, *Chem. Commun.*, 2015, **51**, 10988–11003.

36 K. Suzuki, K. Yamato, R. Sekiya and T. Haino, *Photochem Photobiol Sci*, 2017, **16**, 623–626.

37 H. Yi, J. Liu, J. Yao, R. Wang, W. Shi and C. Lu, *Molecules*, 2022, **27**, 6517.

38 B. Wang and S. Lu, *Matter*, 2022, **5**, 110–149.

39 A. Bhattacharya, S. Chatterjee, R. Prajapati and T. K. Mukherjee, *Phys. Chem. Chem. Phys.*, 2015, **17**, 12833–12840.

40 S. Zhu, Y. Song, J. Wang, H. Wan, Y. Zhang, Y. Ning and B. Yang, *Nano Today*, 2017, **13**, 10–14.

41 K. Hola, A. B. Bourlinos, O. Kozak, K. Berka, K. M. Siskova, M. Havrdova, J. Tucek, K. Safarova, M. Otyepka, E. P. Giannelis and R. Zboril, *Carbon*, 2014, **70**, 279–286.

42 D. Bera, L. Qian, T.-K. Tseng and P. H. Holloway, *Materials*, 2010, **3**, 2260–2345.

43 Y. Zhou, E. M. Zahran, B. A. Quiroga, J. Perez, K. J. Mintz, Z. Peng, P. Y. Liyanage, R. R. Pandey, C. C. Chusuei and R. M. Leblanc, *Applied Catalysis B: Environmental*, 2019, **248**, 157–166.

44 S. Gengan, H. C. Ananda Murthy, M. Sillanpää and T. Nhat, *Results in Chemistry*, 2022, **4**, 100674.

45 N. Dhenadhayalan, K.-C. Lin, R. Suresh and P. Ramamurthy, *J. Phys. Chem. C*, 2016, **120**, 1252–1261.

46 M. Azami, J. Wei, M. Valizadehderakhshan, A. Jayapalan, O. O. Ayodele and K. Nowlin, *J. Phys. Chem. C*, 2023, **127**, 7360–7370.

47 R. Umami, F. A. Permatasari, C. D. D. Sundari, F. Muttaqien and F. Iskandar, *J. Phys.: Conf. Ser.*, 2022, **2243**, 012043.

48 C. Xia, S. Zhu, T. Feng, M. Yang and B. Yang, *Advanced Science*, 2019, **6**, 1901316.

49 B. Wang and S. Lu, *Matter*, 2022, **5**, 110–149.

50 A. Sciortino, E. Marino, B. V. Dam, P. Schall, M. Cannas and F. Messina, *J. Phys. Chem. Lett.*, 2016, **7**, 3419–3423.

51 L. Li and T. Dong, *J. Mater. Chem. C*, 2018, **6**, 7944–7970.

52 S. Hu, A. Trinchi, P. Atkin and I. Cole, *Angew. Chem. Int. Ed.*, 2015, **54**, 2970–2974.

53 Y. Zhang, R. Yuan, M. He, G. Hu, J. Jiang, T. Xu, L. Zhou, W. Chen, W. Xiang and X. Liang, *Nanoscale*, 2017, **9**, 17849–17858.

54 S. H. Jin, D. H. Kim, G. H. Jun, S. H. Hong and S. Jeon, *ACS Nano*, 2013, **7**, 1239–1245.

55 Z. Qian, J. Ma, X. Shan, L. Shao, J. Zhou, J. Chen and H. Feng, *RSC Adv.*, 2013, **3**, 14571.

56 H. Ding, X.-H. Li, X.-B. Chen, J.-S. Wei, X.-B. Li and H.-M. Xiong, *Journal of Applied Physics*, 2020, **127**, 231101.

57 J. Schneider, C. J. Reckmeier, Y. Xiong, M. Von Seckendorff, A. S. Susha, P. Kasák and A. L. Rogach, *J. Phys. Chem. C*, 2017, **121**, 2014–2022.

58 Y. Xiong, J. Schneider, E. V. Ushakova and A. L. Rogach, *Nano Today*, 2018, **23**, 124–139.

59 W. Kasprzyk, T. Świergosz, S. Bednarz, K. Walas, N. V. Bashmakova and D. Bogdał, *Nanoscale*, 2018, **10**, 13889–13894.

60 W. Kasprzyk, T. Świergosz, P. P. Romańczyk, J. Feldmann and J. K. Stolarczyk, *Nanoscale*, 2022, **14**, 14368–14384.

61 S. Zhu, Y. Song, X. Zhao, J. Shao, J. Zhang and B. Yang, *Nano Res.*, 2015, **8**, 355–381.

62 X. Liu, H.-B. Li, L. Shi, X. Meng, Y. Wang, X. Chen, H. Xu, W. Zhang, X. Fang and T. Ding, *J. Mater. Chem. C*, 2017, **5**, 10302–10312.

63 S. Zhu, L. Wang, N. Zhou, X. Zhao, Y. Song, S. Maharjan, J. Zhang, L. Lu, H. Wang and B. Yang, *Chem. Commun.*, 2014, **50**, 13845–13848.

64 J. Xu, C. Wang, H. Li and W. Zhao, *RSC Adv.*, 2020, **10**, 2536–2544.

65 M. S. Ali, N. Bhunia, M. S. Ali, S. Karmakar, P. Mukherjee and D. Chattopadhyay, *Chemical Physics Letters*, 2023, **825**, 140574.

66 M. Li, T. Chen, J. J. Gooding and J. Liu, *ACS Sens.*, 2019, **4**, 1732–1748.

67 V. Vinod Kumar, T. Raman and S. P. Anthony, *New J. Chem.*, 2017, **41**, 15157–15164.

68 I.-A. Baragau, N. P. Power, D. J. Morgan, T. Heil, R. A. Lobo, C. S. Roberts, M.-M. Titirici, S. Dunn and S. Kellici, *J. Mater. Chem. A*, 2020, **8**, 3270–3279.

69 X. Gao, Y. Lu, R. Zhang, S. He, J. Ju, M. Liu, L. Li and W. Chen, *J. Mater. Chem. C*, 2015, **3**, 2302–2309.

70 M. J. Molaei, *Anal. Methods*, 2020, **12**, 1266–1287.

71 S. Tang, X. You, Q. Fang, X. Li, G. Li, J. Chen and W. Chen, *Sensors*, 2019, **19**, 228.

72 J. Tang, Y. Zhang, Y. Liu, D. Liu, H. Qin and N. Lian, *RSC Adv.*, 2019, **9**, 38174–38182.

73 A. S. Tanwar, R. Parui, R. Garai, M. A. Chanu and P. K. Iyer, *ACS Meas. Sci. Au*, 2022, **2**, 23–30.

74 F. Noun, E. A. Jury and R. Naccache, *Sensors*, 2021, **21**, 1391.

75 Y. Yang, T. Zou, Z. Wang, X. Xing, S. Peng, R. Zhao, X. Zhang and Y. Wang, *Nanomaterials*, 2019, **9**, 738.

76 J. Wei, Y. Yuan, H. Li, D. Hao, C. Sun, G. Zheng and R. Wang, *New J. Chem.*, 2018, **42**, 18787–18793.

77 A. Santoro, G. Bella, A. M. Cancelliere, S. Serroni, G. Lazzaro and S. Campagna, *Molecules*, 2022, **27**, 2713.

78 D. Aigner, S. A. Freunberger, M. Wilkening, R. Saf, S. M. Borisov and I. Klimant, *Anal. Chem.*, 2014, **86**, 9293–9300.

79 H. Niu, J. Liu, H. M. O'Connor, T. Gunnlaugsson, T. D. James and H. Zhang, *Chem. Soc. Rev.*, 2023, **52**, 2322–2357.

80 Y. Chen, P. Shang, Y. Dong and Y. Chi, *Sensors and Actuators B: Chemical*, 2017, **242**, 1210–1215.

81 Z. Liang, M. Kang, G. F. Payne, X. Wang and R. Sun, *ACS Appl. Mater. Interfaces*, 2016, **8**, 17478–17488.

82 C. Yang, W. Deng, H. Liu, S. Ge and M. Yan, *Sensors and Actuators B: Chemical*, 2015, **216**, 286–292.

83 C. Xu, P. Ravi Anusuyadevi, C. Aymonier, R. Luque and S. Marre, *Chem. Soc. Rev.*, 2019, **48**, 3868–3902.

84 G. A. M. Hutton, B. Reuillard, B. C. M. Martindale, C. A. Caputo, C. W. J. Lockwood, J. N. Butt and E. Reisner, *J. Am. Chem. Soc.*, 2016, **138**, 16722–16730.

85 K. Wang, L. Liang, Y. Zheng, H. Li, X. Niu, D. Zhang and H. Fan, *New J. Chem.*, 2021, **45**, 16168–16178.

86 X. Zhao, H. Yang, Z. Cui, X. Wang and Z. Yi, *Micromachines*, 2019, **10**, 66.

87 F. Amano, K. Nogami, M. Tanaka and B. Ohtani, *Langmuir*, 2010, **26**, 7174–7180.

88 Z. Xu, Z. Chen, T. Ji, D. Jv and P. Guan, *Materials Letters*, 2022, **309**, 131273.

89 J. Ding, Z. Zhang, C. Meng, G. Zhao, Y. Liu and Y. Lu, *Catalysis Today*, 2020, **347**, 10–17.

90 S. Hu, W. Zhang, Q. Chang, J. Yang and K. Lin, *Carbon*, 2016, **103**, 391–393.

91 A. M., B. K. John, A. R. Chacko, C. Mohan and B. Mathew, *ChemPhysChem*, 2022, **23**, e202100873.

92 X. Chen, X. Zhang, X. Xiao, Z. Wang and J. Zhao, *Angew Chem Int Ed*, 2023, **62**, e202216010.

93 X. He, T. Kai and P. Ding, *Environ Chem Lett*, 2021, **19**, 4563–4601.

94 N. Xu, H. Huang, H. Ouyang and H. Wang, *Sci Rep*, 2019, **9**, 9971.

95 L.-Y. Zhang, Y.-L. Han, J.-J. Yang, S.-L. Deng and B.-Y. Wang, *Applied Surface Science*, 2021, **546**, 149089.

96 H. Hou, X. Zeng and X. Zhang, *Angew Chem Int Ed*, 2020, **59**, 17356–17376.

97 J. Liu, Z. Zhang, Z. Dong, X. Zhu, D. Gao, Z. Cheng, X. Cao, Y. Wang and Y. Liu, *J Radioanal Nucl Chem*, 2022, **331**, 2093–2104.

98 M. Li, M. Wang, L. Zhu, Y. Li, Z. Yan, Z. Shen and X. Cao, *Applied Catalysis B: Environmental*, 2018, **231**, 269–276.

99 J. Ma, C. Liu and K. Yan, *Chemical Engineering Journal*, 2022, **429**, 132170.

100 Y. Wei, H. Liu, Y. Jin, K. Cai, H. Li, Y. Liu, Z. Kang and Q. Zhang, *New J. Chem.*, 2013, **37**, 886.

101 P. He, Y. Shi, T. Meng, T. Yuan, Y. Li, X. Li, Y. Zhang, L. Fan and S. Yang, *Nanoscale*, 2020, **12**, 4826–4832.

102 P. G. Luo, S. Sahu, S.-T. Yang, S. K. Sonkar, J. Wang, H. Wang, G. E. LeCroy, L. Cao and Y.-P. Sun, *J. Mater. Chem. B*, 2013, **1**, 2116.

103 Y. Dong, R. Wang, G. Li, C. Chen, Y. Chi and G. Chen, *Anal. Chem.*, 2012, **84**, 6220–6224.

104 Y. Meng, Y. Zhang, W. Sun, M. Wang, B. He, H. Chen and Q. Tang, *Electrochimica Acta*, 2017, **257**, 259–266.

105 S.-L. Hu, K.-Y. Niu, J. Sun, J. Yang, N.-Q. Zhao and X.-W. Du, *J. Mater. Chem.*, 2009, **19**, 484–488.

106 H. Gonçalves and J. C. G. Esteves Da Silva, *J Fluoresc*, 2010, **20**, 1023–1028.

107 M. Xu, W. Zhang, Z. Yang, F. Yu, Y. Ma, N. Hu, D. He, Q. Liang, Y. Su and Y. Zhang, *Nanoscale*, 2015, **7**, 10527–10534.

108 S. Borna, R. E. Sabzi and S. Pirsa, *J Mater Sci: Mater Electron*, 2021, **32**, 10866–10879.

109 B. Thangaraj, P. R. Solomon, S. Chuangchote, N. Wongyao and W. Surareungchai, *ChemBioEng Reviews*, 2021, **8**, 265–301.

110 B. Al Farsi, R. G. S. Sofin, H. Al Shidhani, E.-S. I. El-Shafey, A. S. Al-Hosni, F. Al Marzouqi, A. Issac, A. Al Nabhani and O. K. Abou-Zied, *Journal of Luminescence*, 2022, **252**, 119326.

111 M. Xue, W. Guan, W. Gu, C. Guo, S. Su, P. Xu and L. Ye, *IJN*, 2014, 5071.

112 W. Wang, Y. Li, L. Cheng, Z. Cao and W. Liu, *J. Mater. Chem. B*, 2014, **2**, 46–48.

113 L. Cui, X. Ren, M. Sun, H. Liu and L. Xia, *Nanomaterials*, 2021, **11**, 3419.

114 Y. Wang, X. Chang, N. Jing and Y. Zhang, *Anal. Methods*, 2018, **10**, 2775–2784.

115 P. Wu, W. Li, Q. Wu, Y. Liu and S. Liu, *RSC Adv.*, 2017, **7**, 44144–44153.

116 S. Sahu, B. Behera, T. K. Maiti and S. Mohapatra, *Chemical Communications*, 2012, **48**, 8835–8837.

117 T. Atabaev, *Nanomaterials*, 2018, **8**, 342.

118 S. D. Dsouza, M. Buerkle, P. Brunet, C. Maddi, D. B. Padmanaban, A. Morelli, A. F. Payam, P. Maguire, D. Mariotti and V. Svrcek, *Carbon*, 2021, **183**, 1–11.

119 B. Vercelli, R. Donnini, F. Ghezzi, A. Sansonetti, U. Giovanella and B. La Ferla, *Electrochimica Acta*, 2021, **387**, 138557.

120 F. Li, C. Liu, J. Yang, Z. Wang, W. Liu and F. Tian, *RSC Adv.*, 2014, **4**, 3201–3205.

121 R. Alexpandi, C. V. V. M. Gopi, R. Durgadevi, H.-J. Kim, S. K. Pandian and A. V. Ravi, *Sci Rep*, 2020, **10**, 12883.

122 H. Luo, S. Dimitrov, M. Daboczi, J.-S. Kim, Q. Guo, Y. Fang, M.-A. Stoeckel, P. Samorì, O. Fenwick, A. B. Jorge Sobrido, X. Wang and M.-M. Titirici, *ACS Appl. Nano Mater.*, 2020, **3**, 3371–3381.

123 J. Wang, M. Gao and G. W. Ho, *J. Mater. Chem. A*, 2014, **2**, 5703.

124 R. S. Oakes, A. A. Clifford and C. M. Rayner, *J. Chem. Soc., Perkin Trans. 1*, 2001, 917–941.

125 J. A. Darr, J. Zhang, N. M. Makwana and X. Weng, *Chem. Rev.*, 2017, **117**, 11125–11238.

126 S. Kellici, J. Acord, K. E. Moore, N. P. Power, V. Middelkoop, D. J. Morgan, T. Heil, P. Coppo, I.-A. Baragau and C. L. Raston, *React. Chem. Eng.*, 2018, **3**, 949–958.

127 I. A. Baragau, N. P. Power, D. J. Morgan, R. A. Lobo, C. S. Roberts, M. M. Titirici, V. Middelkoop, A. Diaz, S. Dunn and S. Kellici, *ACS Sustainable Chemistry and Engineering*, 2021, **9**, 2559–2569.

128 I.-A. Baragau, Z. Lu, N. P. Power, D. J. Morgan, J. Bowen, P. Diaz and S. Kellici, *Chemical Engineering Journal*, 2021, **405**, 126631.

129 K. G. Nguyen, I.-A. Baragau, R. Gromicova, A. Nicolaev, S. A. J. Thomson, A. Rennie, N. P. Power, M. T. Sajjad and S. Kellici, *Sci Rep*, 2022, **12**, 13806.

130 H. Zheng, T. Yu, C. Qu, W. Li and Y. Wang, *IOP Conf. Ser.: Earth Environ. Sci.*, 2020, **555**, 012036.

131 X. Y. Liu, M. G. He and Y. Zhang, *The Journal of Supercritical Fluids*, 2012, **63**, 150–154.

132 N. Yoshida, M. Matsugami, Y. Harano, K. Nishikawa and F. Hirata, *J*, 2021, **4**, 698–726.

133 S. Deguchi and K. Tsujii, *Soft Matter*, 2007, **3**, 797.

134 M. M. Hoffmann and M. S. Conradi, *J. Am. Chem. Soc.*, 1997, **119**, 3811–3817.

135 T. I. Mizan, P. E. Savage and R. M. Ziff, *J. Phys. Chem.*, 1996, **100**, 403–408.

136 W. J. Lamb, G. A. Hoffman and J. Jonas, *The Journal of Chemical Physics*, 1981, **74**, 6875–6880.

137 S. Kraft and F. Vogel, *Ind. Eng. Chem. Res.*, 2017, **56**, 4847–4855.

138 P. Schienbein and D. Marx, *Phys. Chem. Chem. Phys.*, 2020, **22**, 10462–10479.

139 H. Weingärtner and E. U. Franck, *Angew Chem Int Ed*, 2005, **44**, 2672–2692.

140 C. Campalani and D. Rigo, *Next Sustainability*, 2023, 100001.

141 B. L. Cushing, V. L. Kolesnichenko and C. J. O'Connor, *Chem. Rev.*, 2004, **104**, 3893–3946.

142 V. K. LaMer and R. H. Dinegar, *J. Am. Chem. Soc.*, 1950, **72**, 4847–4854.

143 P. W. Dunne, A. S. Munn, C. L. Starkey, T. A. Huddle and E. H. Lester, *Phil. Trans. R. Soc. A.*, 2015, **373**, 20150015.

144 H. Hayashi and Y. Hakuta, *Materials*, 2010, **3**, 3794–3817.

145 C. de Mello Donegá, P. Liljeroth and D. Vanmaekelbergh, *Small*, 2005, **1**, 1152–1162.

146 S. G. Kwon and T. Hyeon, *Small*, 2011, **7**, 2685–2702.

147 D. W. Matson, J. C. Linehan and R. M. Bean, *Materials Letters*, 1992, **14**, 222–226.

148 D. W. Matson, J. C. Linehan, J. G. Darab and M. F. Buehler, *Energy Fuels*, 1994, **8**, 10–18.

149 T. Adschiri, K. Kanazawa and K. Arai, *Journal of the American Ceramic Society*, 1992, **75**, 1019–1022.

150 A. A. Chaudhry, S. Haque, S. Kellici, P. Boldrin, I. Rehman, F. A. Khalid and J. A. Darr, *Chem. Commun.*, 2006, 2286.

151 T. Adschirib, Y. Hakuta, K. Kanamura and K. Arai, *High Pressure Research*, 2001, **20**, 373–384.

152 Y. Hakuta, T. Adschiri, T. Suzuki, T. Chida, K. Seino and K. Arai, *Journal of the American Ceramic Society*, 2005, **81**, 2461–2464.

153 E. Lester, P. J. Blood, J. P. Denyer, B. J. Azzopardi, J. Li and M. Poliakoff, *Materials Research Innovations*, 2010, **14**, 19–26.

154 S. Toyama, H. Hayashi, M. Takesue, M. Watanabe and R. L. Smith, *The Journal of Supercritical Fluids*, 2016, **107**, 1–8.

155 P. J. Blood, J. P. Denyer, B. J. Azzopardi, M. Poliakoff and E. Lester, *Chemical Engineering Science*, 2004, **59**, 2853–2861.

156 C. J. Tighe, R. I. Gruar, C. Y. Ma, T. Mahmud, X. Z. Wang and J. A. Darr, *The Journal of Supercritical Fluids*, 2012, **62**, 165–172.

157 C. Y. Ma, X. Z. Wang, C. J. Tighe and J. A. Darr, *IFAC Proceedings Volumes*, 2012, **45**, 874–879.

158 R. I. Gruar, C. J. Tighe and J. A. Darr, *Ind. Eng. Chem. Res.*, 2013, **52**, 5270–5281.

159 D. Saha, E. D. Bøjesen, K. M. Ø. Jensen, A.-C. Dippel and B. B. Iversen, *J. Phys. Chem. C*, 2015, **119**, 13357–13362.

Chapter 3 : Methodologies and Characterizations

This chapter provides an overview of the CHFS method utilized in this project. It provides details of synthetic process, including reaction parameters like temperature, flow rate, and pressure. The chemical precursors used for synthesising the NCQDs and NCQDs-TiO2 nanocomposites are also given. Additionally, this chapter outlines the characterization techniques and experimental setups used. This chapter aims to establish context and enable reproducibility of the nanomaterial fabrication and characterization processes central to this work.

3.1 Continuous hydrothermal flow synthesis: The process and reactor design.

The continuous hydrothermal flow synthesis (CHFS) system utilised in this project is illustrated in **Figure 3.1**. The CHFS process employs three pumps with a counter-current reactor design to enable precise control over reaction conditions and continuous production of nanomaterials. The deionised water was heated using an electric heater and pressure of this system was regulated using a Swagelok back pressure regulator (BRP). The production stream then was cooled using a water cooler.

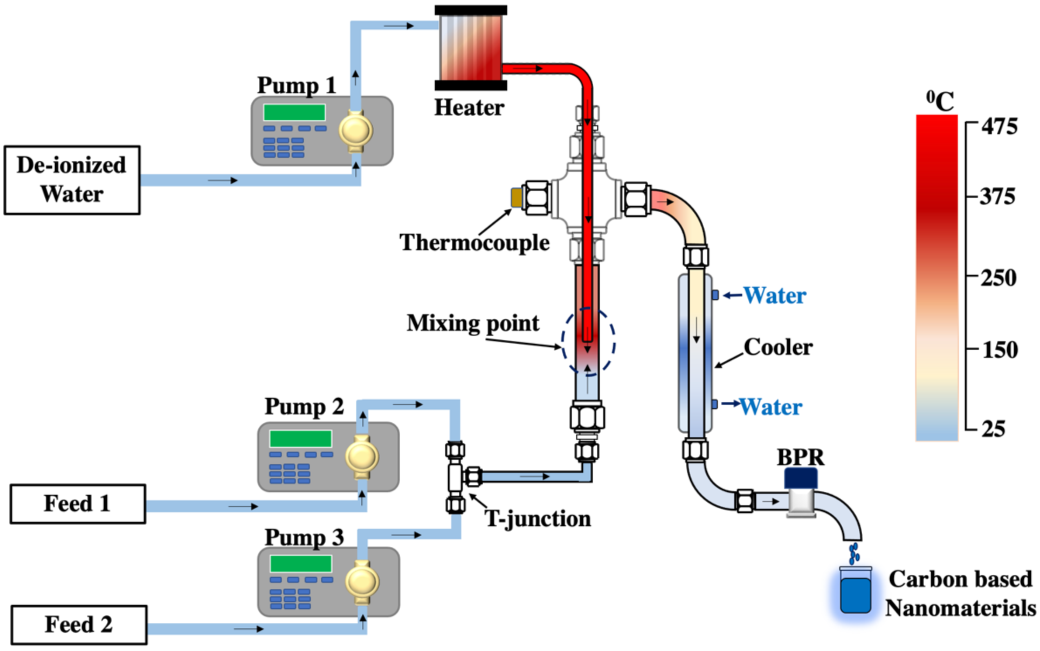

Figure 3.1: The CHFS process diagram used in this research

The continuous hydrothermal flow synthesis (CHFS) reactor was custom-built in house at London South Bank University, allowing for tight control over the reaction parameters during nanomaterial fabrication. The system consists primarily of 1/8” Swagelok 316 stainless steel tubing and fittings, with 1/4” sizes used for the counter-current reactor and cooler. Three high-pressure Gilson HPLC pumps deliver the reactants. Pump 1 is a Gilson 307 HPLC pump with a 25 mL pump head provides supercritical water that has been preheated to 450 °C under pressure of 3600 psi using an electric heater. Pump 2- Gilson 305 HPLC pump with a 10 mL pump head supplies the primary precursor solution (Feed 1), while Pump 3- Gilson 307 HPLC pump with a 10 mL pump head delivers additional reagents like dopants (Feed 2). Feeds 1 and 2 mix at room temperature via a T-junction before injection into the counter-current reactor, where they rapidly react with the supercritical water. This promotes rapid nucleation under continuous flow conditions. The product stream is then cooled using a water cooler. The temperature is monitored in real-time throughout using a thermocouple and PicoLog 6 software for precise process control.

3.2 Synthetic methodologies

In general, the synthesis of NCQDs using the CHFS method in this project follows a consistent procedure. The CHFS process setup as illustrated in **Figure 3.1**, remains unchanged. The first pump was dedicated to denoised water, the second pump was used for carbon sources and the third pump was employed for nitrogen sources. The product after CHFS was filtered using a 0.2 µm alumina membrane. Subsequently, the solutions were continuously dialysed using a range of membranes in a tangential filtration unit to achieve the desired size of NCQDs nanoparticles.

3.2.1 Synthesising NCQDs from different carbon sources and urea

This section provides the detailed synthetic procedure for the manufacture of NCQDs, the result of which are discussed in Chapter 4.

- *Materials*

Lignosulfonic acid sodium salt - $C_{20}H_{26}O_{10}S_2.2Na$ (average Mw ~52,000, average Mn ~7,000), humic acid sodium salt - $C_9H_8Na_2O_4$ (technical grade), chitosan low molecule weight - $C_{56}H_{103}N_9O_{39}$ (technical grade), and citric acid - $C_6H_8O_7$ (99.5%) were purchased from Sigma-Aldrich (U.K). Urea - CH_4N_2O (99%) was purchased from Fisher Chemical (U.K). These were used as received without further modification. In addition, the deionized water (15 MΩ) from the ELGA Purelab system was used for all the experiments.

- Synthesis of nitrogen doped carbon quantum dots

In this study, urea (1.0 M) was used as nitrogen dopant sources, and a series of carbon precursors (lignosofonic acid sodium salt, chitosan, humic acid and citric acid) solution with concentration of 70 mg/mL were utilised as carbon resources for synthesis of NCQDs. Three pumps were used in the continuous hydrothermal flow synthesis (CHFS) process. Pump 1 (P1) delivered deionized water, while Pump 2 (P2) and Pump 3 (P3) delivered the carbon and nitrogen precursors, respectively. A back pressure regulator maintained the system pressure at 24.8 MPa. The deionized water flowed through a 450°C heater to reach a supercritical state. The carbon and nitrogen precursors were mixed at room temperature via a T junction. The nitrogen-doped carbon quantum dots (NCQDs) were synthesised in a counter-current flow reactor where the supercritical water flowed against the mixture of carbon and nitrogen. The flow rates of 20 mL/min, 10 mL/min, and 10 mL/min for P1, P2, and P3, respectively, controlled the 1.6 s reaction time. The NCQDs solution were collected and cleaned with a molecular weight cut-off membrane of 30 kD, and denoted as NCQDs-Lignin, NCQDs-Chitosan, NCQDs-Humic and NCQDs-Citric.

3.2.2 Synthesising NCQDs using citric acid and different nitrogen sources

This section provides the detailed synthetic procedure for the NCQDs, results of which are discussed in Chapter 5.

- *Materials*

Citric acid - $C_6H_8O_7$ (99.5%) and urea - CH_4N_2O (99%) were purchased from Fisher Chemical (U.K). Ethylenediaminetetraacetic acid dipotassium salt dihydrate, EDTA - $C_{10}H_{16}N_2O_8$ (99%), ß-alanine - $C_6H_{14}N_4O_2$ (99%), L-arginine - $C_3H_7NO_2$ (99%) and trizma base - $C_4H_{11}NO_3$ (99%) were purchased from Sigma-Aldrich (U.K.). These were used as received without further modification. In addition, the deionized water (15 MΩ) from the ELGA Purelab system was used for all the experiments.

- *Synthetic procedures*

In this study, citric acid with a concentration of 70.0 mg/mL was used as carbon source, and a series of nitrogen precursors including urea (CH_4N_2O), EDTA ($C_{10}H_{16}N_2O_8$), L-alanine

($C_3H_7NO_2$), ß-arginine ($C_6H_{14}N_4O_2$) and trizma base ($C_4H_{11}NO_3$), all with the same molarity of 1.0 M were utilised as nitrogen dopants for synthesis of NCQDs. The CHFS process involves three pumps: the first pump (P1) delivers the deionised water, while the second (P2) and third pumps (P3) were used for carbon and nitrogen resources, respectively. Additionally, a back pressure regulator was employed to maintain the system pressure at 24.8 MPa throughout the synthetic process. The deionized water was pumped through a heater set at 450°C to reach a supercritical state, while the carbon and nitrogen resources were mixed via a T- junction at room temperature. The NCQDs were synthesised in a counter-current flow reactor where the supercritical water flows against the mixture of carbon and nitrogen precursors. The reaction time (1.6 s) was controlled by the flowrate of the three pumps, P1: 20 mL/min, P2: 10 mL/min and P3: 10 mL/min used for P1, P2 and P3, respectively. The samples were collected and cleaned with a molecule weight cut-off membrane of 30 kDa, and denoted as NCQDs-Urea, NCQDs-Alanine, NCQDs-Arginine, NCQDs-EDTA, and NCQDs-Trizma.

3.2.3 Synthesis of NCQDs from glucose and ammonia: Application in Chromium (VI) ion-sensing

This section provides ta detailed description of the synthetic procedure and performance testing for Cr (VI) for sensing experiments using the NCQDs, the result of which discussed in Chapter 6.

- Chemicals

Glucose-$C_6H_{12}O_6$ (99%) and ammonium hydroxide solution - NH_4OH (32%) were purchased from Fisher Scientific (UK) and were used as received. Deionized water (15 MΩ) from the ELGA Purelab system was used for dilution preparation of the solutions. Glucose with concentration of 70.0 mg/mL was used as carbon sources and ammonia solutions with varied concentrations (0.25 M, 0.5 M, 0. 75 M, 1.0 M, 2.5 M, 5.0 M, 7.5 M, and 10.0 M) was used as nitrogen sources.

- *Synthetic Procedures*

The CHFS process shown in **Figure 3.1** was employed to synthesize NCQDs from glucose (70.0 mg/mL) and ammonia. In this synthetic process, the first pump delivered the denoised water (with the flow rate 20.0 mL/min) and supercritical water is achieved at 450 °C and 3600 psi. The glucose solution (the carbon source) was injected to the system via the second pump with the flowrate of (5.0 mL/min), and the last pump was used to supply the nitrogen source which is ammonia at a flow rate of 5.0 mL/min. The concentration of ammonia varied from 0.25 M to 10.0 M to investigate the effect of dopant concentration in the synthesised NCQDs. The obtained solutions from the CHFS reaction mixtures were filtered using a 0.2 μm alumina membrane followed by the solutions dialyzing the solution using a 30 kDa membrane in a tangential filtration unit.

3.2.4 Synthesising NCQDs-TiO_2 and TiO_2 nanocomposites: Application in photocatalysis

This section provides the detailed synthetic procedures for the NCQDs-TiO_2 and TiO_2 nanocomposites, and photocatalytic experiments for these materials, the results of which are discussed in Chapter 7.

- *Chemicals*

Titanium (IV) bis (ammonium lactato) dihydroxide - $C_6H_{22}N_2O_8Ti$ (50 wt% in water), and potassium hydroxide - KOH (99%) were purchased from Sigma, (U.K). The NCQDs which were synthesised in-situ at LSBU using citric acid - $C_6H_8O_7$ (70mg/mL) and urea - CH_4N_2O (1.0 M). Titanium (IV) bis (ammonium lactato) dihydroxide (50 wt% in water) was diluted into the as-synthesised NCQDs (4.7 mg/mL) solution to achieve a 0.2 M solution.

- *Synthetic procedure*

The continuous hydrothermal flow synthesis **Figure 3.1** was employed to fabricate nanocomposites. In these experiments, the first pump delivered supercritical deionised water (450^0C, 3600 psi) with a flow rate of (20 mL/min), the second pump delivered the mixture of titanium bis dihydroxide (0.2M) and NCQDs, and the third pump delivered KOH (1.0M) solution. The second and third pump were operated with a flow rate of 10 mL/min. The produced aqueous slurries were collected and sent through centrifugation. The wet solids products were freeze-dried, and the dried powder samples were denoted as TiO_2 and NCQDs-TiO_2.

3.3 Characterization techniques

3.3.2 Morphology characterisations

A range of characterisations were employed to investigate the morphology and structure of the synthesised NCQDs and nanocomposites, including HRTEM, AFM.

High-Resolution Transmission Electron Microscopy (HRTEM): The synthesised NCQDs solution (1.0 mL) were diluted in isopropanol (9.0 mL) and applied onto a carbon holey mesh grid (Agar) and allowed to air dry. The samples were then imaged using JEM 2100 (Jeol, Japan) at an acceleration voltage of 200 kV and at a range of magnifications between 15K and 500K. (This set up was used to characterise the samples, result of which are reported in Chapter 6. This HRTEM measurement were done by Dr Radga Gromnicova at Open University, United Kingdom).

High resolution transmission electron microscopy (HRTEM) was carried out by using double-corrected JEOL ARM200F, the prepared NCQDs solution (1.0 mL) were diluted in ethanol (9.0 mL) and deposited onto holey carbon coated Cu-grid (400 µm) and allowed to dry at room condition. The HRTEM were collected using acceleration voltage of 60 kV and 200 kV and the image analysis was conducted using ImageJ software. (This equipment was used to characterize the samples reported in Chapter 4, 5 and 7. HRTEM measurements were done by Dr. Tobias Heil at the Max Planck Institute of Colloids and Interfaces, Germany).

Atomic force microscopy (AFM) was performed in tapping mode using an Asylum Research MFP-3D, operating in tapping mode, using Nano-sensors PPP-NCL probes. The samples for AFM measurements were prepared by depositing the NCQDs solutions onto mica substrates and dried at ambient condition. AFM images processing included plane correction and scar removal using the built-in functions of the software. (This AFM was used to characterize the NCQDs sample reported in Chapter 4 and 5. The AFM measurements and analysis were done by Dr James Bowen at Open University, United Kingdom).

3.3.3 Chemical characterisations

The chemical properties and composition of the synthesised nano-carbon quantum dots (NCQDs) and nanocomposites were characterized and investigated through several analytical techniques, including Fourier-transform infrared spectroscopy (FTIR), Raman spectroscopy, and X-ray photoelectron spectroscopy (XPS), and X-ray powder diffraction (XRD).

The FTIR analysis provided information on the various functional groups present on the surface of the NCQDs and nanocomposites. FTIR spectra of the synthesised materials was recorded using an IR Affinity-1S Fourier transform infrared spectrophotometer instrument (Shimadzu IRAffinity-1S). The samples for FTIR measurement were prepared using the freeze dried

NCQDs and nanocomposites samples, measurements taken between 500-4000 cm^{-1} using external beam, and the number of scans is 100 with resolution of 8. (The measurements were conducted at London South Bank University, United Kingdom).

Raman spectroscopy similarly elucidated the chemical bonding composition, providing complementary vibrational signatures of functional groups within the NCQD and nanocomposite structures. Raman spectra of the prepared NCQDs and nanocomposites were measured with a Horiba LabRAM HR Evolution spectrometer with radiation at 633 nm. The samples for Raman measurements were prepared by depositing the synthesised NCQDs solutions onto SERS-silver, measurements were conducted in the range of 800-2000 cm^{-1}, with the 50% of laser power (This set up was used characterise the samples results of which are reported in Chapter 4, 5 and 7, these Raman measurements were done by Dr Alexandru Baragau National Institute of Materials Physics, Romania). Whereas the Raman spectra of the as synthesised of NCQDs reported in Chapter 6 were collected by using Renishaw in Via confocal Raman microscope using a 442 nm laser with the same set up parameter as mentioned above (Dr Andrei Sapelkin at Queen's Mary University, United Kingdom supported the Raman measurements).

XPS surface analysis quantified the elemental composition and chemical states of elements within the NCQD and nanocomposite materials. The X-ray photoelectron spectroscopy (XPS) analysis of the sample was conducted using a monochromatized Al Kα X-ray source (1486.7 eV), with the photoelectrons recorded by a hemispherical (180 mm radius) electron energy analyzer with a reference intensity of over 50.000 counts per seconds (cps) and maximum spectral resolution of 0.7 eV. The X-ray source operated at 300 W (15 kV × 20 mA), with a spot size of 0.7 mm. Partial charge compensation was reached by using a flood gun operating at 1.52 A filament current, 2.73 V charge balance, and 1.02 V filament bias. The base pressure during the measurements was around 10^{-8} Pa. This set-up was used to analyse NCQDs samples as reported in Chapter 4. Whereas, for samples results of which are reported in chapter 5,6 and 7, the X-ray photoelectron spectroscopy (XPS) analysis has been performed in an AXIS Ultra DLD (Kratos Surface Analysis) setup using Mg Kα (1253.6 eV) radiation produced by a non-monochromatized X-ray source at operating power of 144 W (12 kV × 12 mA). The samples for XPS measurement were prepared by depositing the NCQDs solutions on silver substrate, then the deposited NCQDs/silver substrate was placed in a vacuum oven (80°C) for 60 minutes. (These XPS measurements were conducted by Dr Adela Nicolaev and Dr Laura Elena Abramiuc at National Institute of Materials Physics, Romania).

X-ray diffraction measurements were conducted using an Anton Paar XRDynamic 500 powder diffractometers equipped with a CuKα1 (1.5406 Å) Primux 300. The Le Bail Refinement was performed using the FullProf software. The samples for XRD measurements were prepared using the original synthesised TiO_2 nanocomposites; and the XRD measurements were performed using a fixed tube X-ray (Cu Kα, current 50 mA and voltage 40kV), measurements are conducted between 5-90^o 2θ with step size of 0.02^o and 301s per step. (This XRD was used to characterise the synthesised TiO_2-nanocomposite samples reported in Chapter 7. The XRD measurements and analysis were done by Dana G. Popescu and Daniel Gherca at National Institute of Materials Physics, Romania).

3.3.4 Optical properties characterisation

The optical an electronic property of the synthesised NCQDs and nanocomposites were extensively studied through an array of spectroscopic and photometric techniques, including ultraviolet-visible spectroscopy (UV-Vis), photoluminescence lifetime measurements (PL lifetime) and photoluminescence quantum yield measurements, and ultraviolet photoemission spectroscopy (UPS).

Ultraviolet-visible spectroscopy was utilized to indicate the electronic transitions and optical bandgap arising in the synthesised NCQDs and nanocomposites. The UV-Vis absorbance spectra were recorded using an UV–Vis spectrophotometer Shimadzu UV-1800, measurements taken in the range of 200 to 800 nm, and a 10 mm quartz cuvette was used to contain diluted NCQDs/nanocomposites solutions. The samples for UV-Vis measurement were prepared by diluting 1.0 mL of NCQDs/10.0 mg of nanocomposite powder into 50.0 mL de-ionized water. (These UV-Vis measurements were conducted at LSBU, United Kingdom).

Photoluminescence (PL) spectroscopy: The steady-state fluorescence spectra of all the samples were measured with Shimadzu RF-6000 fluorophotometer. The emission spectra were recoded using the excitation wavelength from 300 nm to 500 nm with step size of 20 nm. In preparation for conducting photoluminescence characterisation of the synthesised NCQDs, the original as-synthesised solutions of NCQDs were diluted using deionized water to achieve optimized optical density solutions of 0.1 OD (optical density units) for the photoluminescence analysis. (These measurements were done at LSBU, United Kingdom).

Edinburgh Instrument, FLS1000 Photoluminescence spectrometer was used to measure the PL lifetime and the PLQY of the samples. The lifetime was measured using a 375 nm pulsed LED, and the data was fitted with 3-exponentials after deconvolution with instrument response function. The absolute quantum yield (QY^{abs}) of the samples were investigated by using integrating sphere accessory with a standard method. Then, the true fluorescence quantum yield (QY^{true}) is calculated by using the equation (1) where: a is the fraction of the re-absorbed area.

$$QY^{true} = \frac{QY^{abs}}{1-a+a.\frac{QY^{abs}}{100}} \qquad \text{(eq.1)}$$

Both PL lifetime and PLQY measurement used 0.1 OD NCQDs solutions as the sample. (These measurements were conducted at LSBU, United Kingdom).

Ultraviolet photoemission spectroscopy (UPS) measurements were performed using He I (21.2 eV) radiation source fitted in a Thermo NEXSA with a bias of -9 V. (These measurements were done by Dr Shaoliang Guan at Hardwell-XPS, United Kingdom).

3.4 Application

3.4.1 Study on the pH stability of NCQDs study

Solutions with pH values ranging from 1 to 13 were prepared by using various concentrations of HCl (1.0 M) and NaOH (1.0 M) solution. The pH of the solutions was measured using a pH meter. A dilute NCQDs aqueous solution (optical density, OD = 0.1) in deionised water was prepared. Subsequently, 100 µL of the diluted NCQDs solution was added to 3000 µL of the prepared solution with different pH levels. The fluorescence spectra of these solutions were recorded using a Shimadzu RF-6000 Spectro fluorophotometer.

3.4.2 Chromium (VI) ion-sensing experiment

The detection of Cr (VI) ion experiment was conducted with various metal ions (as reported above), each prepared with a concentration of 50 ppm. In a typical experiment, 100 µL, NCQDs (0.1 OD) was added to the 3.0 mL aqueous metal ion solution. The fluorescence spectrum of the prepared mixture solutions was recorded. In addition, the fluorescence lifetime was investigated to achieve a deeper understanding of the quenching mechanism using Edinburgh Photonics Instrument FLS1000. The sensitivity of the NCQDs fluorescent sensor for Cr (VI) was investigated further to evaluate their limits of detection (LOD) and limits of quantification (LOQ). In this experiment, Cr (VI) ion solutions with various concentrations of 300 ppm, 200 ppm, 100 ppm, 50 ppm, 30 ppm, 10 ppm, 5 ppm, 2 ppm, 1 ppm and 0.5 ppm were prepared. Then, 100 µL NCQDs were added to 3.0 mL of the prepared Cr (VI) ion solutions. The fluorescence spectra were recorded to estimate the LOD and LOQ by using Stem-Volmer graphs, LOD = $3\sigma/K_{sv}$, LOQ = $10\sigma/K_{sv}$, where K_{sv} is the slope of the graphs, and σ is the error of the intercept.

3.4.3 Photocatalysis experiments

The photocatalytic activities of the titania nanocomposites (TiO_2 and NCQDs-TiO_2) were evaluated by studying the photodegradation of methylene blue (MB) in water. Firstly, 10.0 mg of the nanocomposite was dispersed in 50.0 mL of methylene blue solution with concentration C_o = 15 ppm by using a magnetic stirrer. Then, the mixture was constantly stirred (500 rpm) and irradiated using a solar simulator (LSH7320-Newport). The light spectrum of the solar simulator is illustrated in Figure 3.2 below.

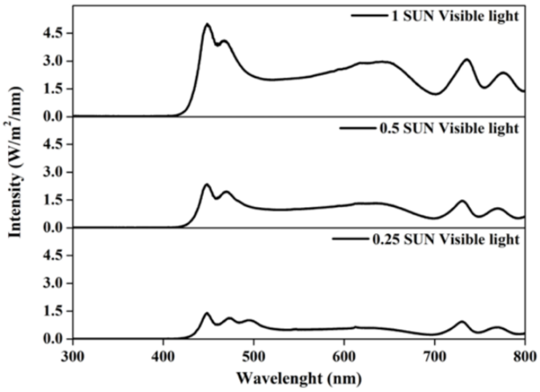

Figure 3.2: The solar spectrum of the LSH7320-Newport

The degradation of the MB dye was evaluated by using a UV-Vis absorbance spectrophotometer. The absorbance at the λ_{max} = 664 nm was recorded after every 15 minutes to compute the concentration of the MB dye remaining in the solution during the photodecomposition using a calibration equation representing the relationship of absorbance intensity and MB concentration. The distance from specimen and solar light was kept constant at 27 cm. The photocatalytic activity of the nanocomposites was examined in two different light intensity 1 sun (100 mW/cm^2) and 0.5 sun (50 mW.cm^2).

3.5 Conclusions

This PhD research project focused on engineering and developing new continuous hydrothermal flow synthesis (CHFS) methods for synthesising of carbon quantum dots and its nanocomposites. These novel CHFS processes utilize water-soluble precursors or stable dispersions of nanomaterials in water. The continuous flow reactors enable rapid reactions under hydrothermal conditions. Compared to conventional batch hydrothermal techniques, the CHFS methods offer superior performance in terms of faster reaction times, more environmentally friendly synthesis, real-time control over process parameters and product quality, and lower costs.

The developed CHFS processes have strong potential to be scaled up for industrial-level production. The as-synthesised nanomaterials and nanocomposites were successfully integrated into platforms for ion sensing, and photocatalytic degradation of organic water pollutants under solar irradiation.

The continuous flow reactors allow for independent control of temperature, pressure, and residence times during hydrothermal synthesis. This level of control enables tuneable, optimized production of nanomaterials. Furthermore, the CHFS process intensifies heat and mass transfer, which accelerates nanoparticle nucleation and growth kinetics compared to batch methods. The projects demonstrated that CHFS is a versatile and efficient approach for rapidly synthesising tailored nanomaterials for environmental application and beyond.

Chapter 4 : Investigating the effect of various carbon precursors on nitrogen doped carbon quantum dots structure and optical properties

4.1 Introduction

Considerable research efforts have focused on developing and optimizing methods to synthesize CQDs with precise control over crucial properties such as particle size, surface chemistry, and photoluminescence emission. However, developing sustainable, inexpensive, and scalable synthesis methods for CQDs remains a key challenge.[1] Sustainable sources of carbon are becoming increasingly important for economical and eco-friendly synthesis of CQDs. Various carbon sources, from small organic molecules to polymers and biomass, have been utilized to achieve CQDs with high quantum yields and desired functionalities via different methodologies.[2] Recently, there has been growing interest in utilising renewable and sustainable high molecular weight precursors as carbon sources for CQD synthesis.[3] Citric acid is the most common carbon source for synthesising CQDs due to its abundant availability, low cost, renewable derivation from plants, high carbon content from its central backbone and carboxyl groups, and versatility for use in different synthesis methods and surface functionalisations.[4] Biopolymers like chitosan as well as biomaterials like humic acid and lignin have shown promise as CQD precursors. Lignin is an abundant natural polymer found in plant cell walls that is underutilized as a sustainable precursor for activated carbons. Extracting value from lignin waste streams from pulping and biorefineries could provide environmental and economic benefits.[5] Chitosan is a natural polysaccharide derived from chitin that possesses unique properties for biomedical and environmental applications. Converting chitosan into CQDs expands its potential uses.[6] Humic acid is an abundant natural organic substance found in soils, peat, brown coals, and natural waters. It possesses carboxylic, phenolic, and other oxygen-rich functional groups that are useful precursors for synthesizing carbon-based nanomaterials.[7] These high molecular weight precursors from natural resources allow sustainable, low-cost, and scalable CQD production. They provide abundant surface functional groups for facile surface passivation and doping. However, challenges remain in controlling the CQD size distribution and preventing aggregation when using these polymeric and heterogeneous precursors.[8]

Continuous hydrothermal flow synthesis (CHFS) has emerged as a promising approach that offers precise control over reaction parameters, including temperature, pressure, and residence time.[9] Additionally, CHFS enables continuous production without batch-to-batch variability. This allows tight control over nanoparticle size, morphology, and properties. CHFS provides rapid heating and quenching cycles to promote carbonization and activation reactions from lignin precursors in a controlled manner.[10] The high heat and pressure of supercritical water breaks down lignin's structure so it can repolymerize into novel carbon materials. This method may allow better control and tuning of lignin-derived carbons compared to conventional techniques resulting in high frequency uniform CQDs nanoparticle size. Unlike the conventional carbonisation techniques like pyrolysis tend to destroy its desired structure, CHFS utilizes super-critical water to carbonize carbon sources that better preserve its ring-like arrangement.[11] In CHFS systems, the hydrolysis and polycondensation of reactive groups under super-critical water temperatures promote self-assembly of carbon core networks.[12]

This study will provide new insights into CQD formation mechanisms by tracking how the structure and composition of the four precursors including lignosulfonic acid sodium salt, chitosan, humic acid sodium salt and citric acid impact the optical, physical, chemical, and morphological properties of CQDs produced under the same continuous hydrothermal carbonization conditions. Lignin's complex aromatic structure is expected to decompose into N-doped CQDs with a high density of surface defects and oxygen functionalities. Humic acid's diverse functionality generates heterogeneous NCQDs with oxygen-rich surfaces. Varying their relative composition can also modulate N-doping levels and surface chemistry. Elucidating these fundamental structure-property relationships is critical to establish guidelines for selecting optimal carbon precursors and tuning reaction pathways. This will expand the library of available renewable feedstocks for scalable NCQDS production. The results will also facilitate material design and process optimization to customize NCQDS size, composition, surface chemistry and fluorescence for targeted applications. Overall, this work will provide key insights into sustainable, controllable synthesis of NCQDs with enhanced performance.

In summary, there is a need to develop inexpensive, green carbon sources and understand CQD formation mechanisms to enable scalable, tailored synthesis. This report will elucidate the effects of lignin, chitosan, humic acid, and chitosan structure on continuous hydrothermal production of NCQDs. It will enhance fundamental knowledge regarding renewable precursor selection, interaction pathways and structure-property relationships. This will guide optimal biomass-derived NCQDS synthesis and customization for advanced applications in biomedicine, energy, and electronics.

4.2 Results and discussion

The NCQDs were synthesised using a variation of carbon containing precursors including Lignosulfonic acid sodium salt - $C_{20}H_{26}O_{10}S_2.2Na$ (average Mw ~52,000, average Mn ~7,000), humic acid sodium salt - $C_9H_8Na_2O_4$, chitosan low molecule weight - $C_{56}H_{103}N_9O_{39}$, and citric acid - $C_6H_8O_7$. Urea - CH_4N_2O was used as nitrogen dopant agent. The synthesised NCQDs are denoted as NCQDs-Lignin, NCQDs-Chitosan, NCQDs-Humic and NCQDs-Citric.

4.2.1 The morphology and chemical properties of NCQDs

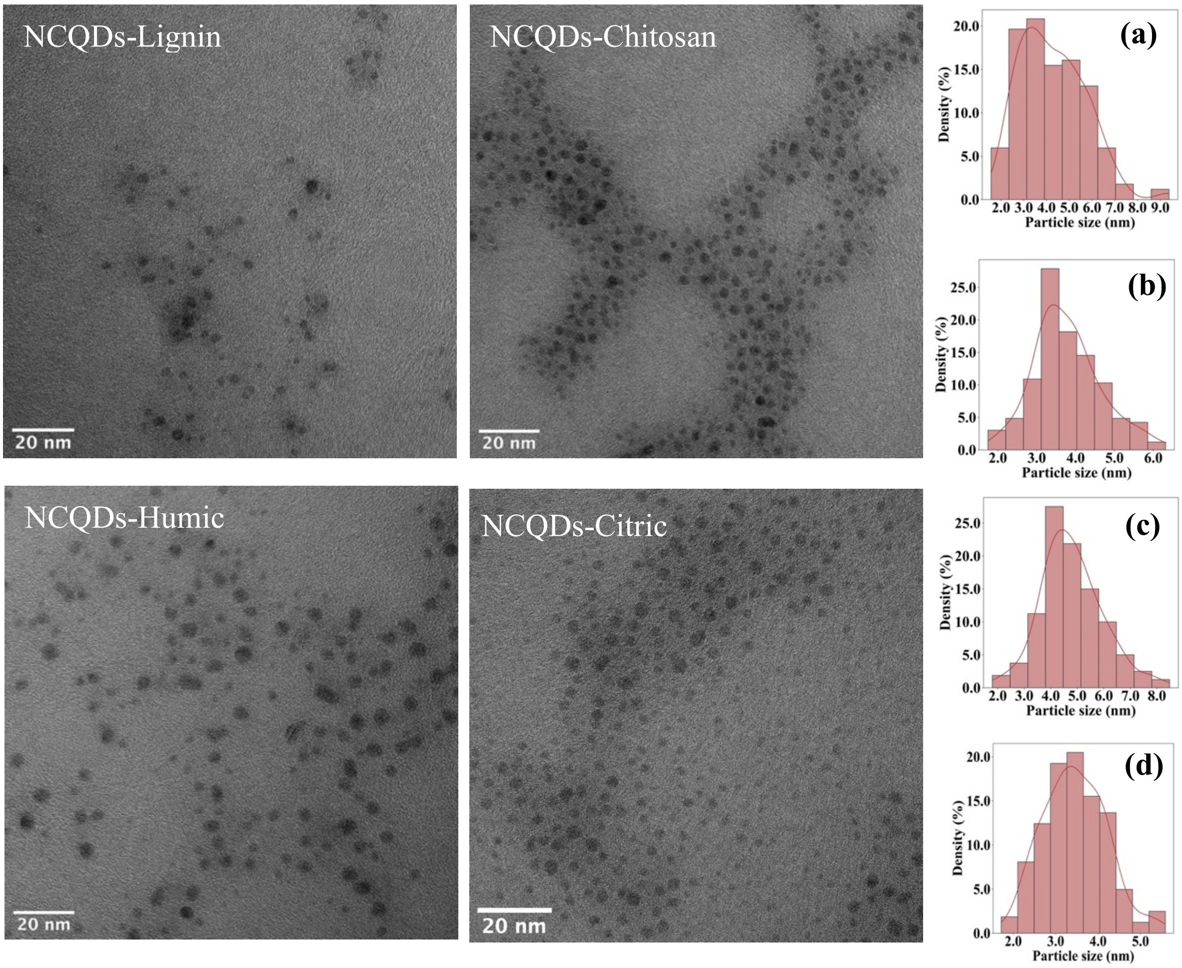

Figure 4.1: HR-TEM images and particles size distribution histogram of the synthesised: (a) NCQDs-Lignin, (b) NCQDs-Chitosan, (c) NCQDs-Humic and (d) NCQDs-Citric. The HRTEM analysis illustrated the effect of precursor on the variation of particle size distribution observed in the synthesised NCQDs

The high-resolution TEM (HR-TEM) analysis provided critical insights into the morphology and graphitic carbon core structure of the synthesised nitrogen-doped carbon quantum dots (NCQDs). The images shown in **Figure 4.1** provide a detailed look at the spherical morphology and nanometre scale size of the synthesised NCQDs. Within each sample, the NCQD particles appear highly uniform in shape and dimensions. However, particle size analysis reveals clear variations in the mean NCQD diameter depending on the carbon source used during synthesis, as summarized in **Table 4.1**. The NCQDs produced using citric acid possessed the smallest average particle size at 3.5 nm. In contrast, humic acid had the largest nanoparticles with an average size of 4.8 nm.

Table 4.1: The mean particles size and height of the synthesised NCQDs

Sample	**Mean Particle size (nm)**	**Mean height (nm)**
NCQDs-Lignin	4.3 ± 1.4	4.3 ± 0.2
NCQDs-Chitosan	3.8 ± 0.9	2.3 ± 0.2
NCQDs-Humic	4.8 ± 1.2	2.4 ± 0.3
NCQDs-Citric	3.5 ± 0.8	1.4 ± 0.2

Furthermore, the NCQDs derived from lignin and humic acid showed a broad particle size distribution spanning from 1.0-8.0 nm. On the other hand, citric acid and chitosan produced NCQDs with a narrower size range, where the largest particles measured about 6.0 nm. The observed differences in NCQD particle size can be attributed to the molecular weight and structure of the precursors. Citric acid and chitosan have relatively low molecular weights compared to the more considerable humic acid and lignin biomolecules. Smaller precursor molecules can form finer nanoparticles during the carbonization process. In addition, citric acid has a simple, symmetric structure, while chitosan also displays a high degree of uniformity. In contrast, the complex, irregular structure of lignin and humic acid stems from their biological origin. The structural complexity and variability of these precursors appear to have produced more disordered nanoparticles with a broader size distribution.

Meanwhile, **Figure 4.2** provides an intriguing look at the atomic lattice of the NCQDs providing the information about the lattice spacing, and crystal planes is exceptionally clear. For the NCQDs-Citric acid sample, the tight 0.21-0.22 nm spacing matches the expected 0.21 nm for the (100) crystal plane of graphite-like carbon.[12,13] This suggests the NCQDs-Citric acid maintained the highly ordered lattice structure of graphite. In contrast, the NCQDs synthesised with lignin, chitosan and humic acid showed lattice spacings of 0.31 nm, consistent with the (002) plane of more disordered graphene-like carbon.[14] Additionally, the multiple lattice spacings visible in each NCQD indicate a polycrystalline structure. This likely stems from defects and distortions introduced by the complex biomass-derived precursors. Notably, chitosan-derived NCQDs exhibited both the 0.31nm graphene-like spacing and a 0.28 nm spacing matching the (1120) lattice plane of graphene.[15]

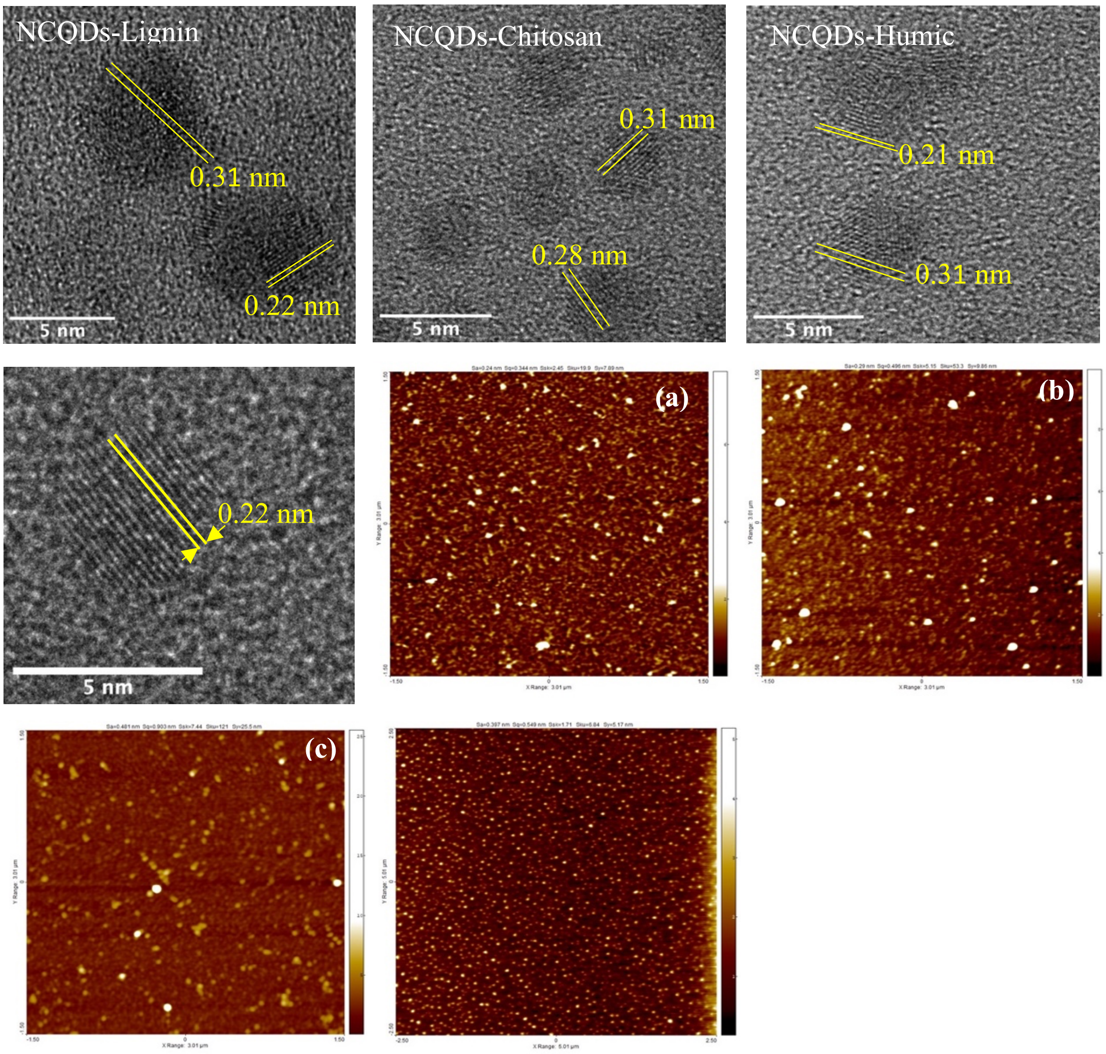

Figure 4.2: The lattice spacing and AFM images of the synthesised NCQDs; (a) NCQDs-Lignin, (b) NCQDs-Chitosan, (c) NCQDs-Humic and (d) NCQDs-Citric

To gain deeper insight into the 3D shape and structure of the as-synthesised NCQDs, Atomic force microscopy (AFM) was utilized to characterize the 3-dimensional morphology and height distribution of the synthesised NCQDs, as shown in **Figure 4.2(a-d)**. The results revealed that the NCQD heights ranged from 1.4 nm to 4.3 nm depending on the precursor material (Table 1). NCQDs produced from citric acid possessed the smallest height of 1.4 nm. In comparison, the use of lignin as a precursor fabricated larger NCQDs with heights up to 4.3 nm. The AFM image analysis corroborated the HRTEM results, with both techniques indicating that complex, high molecular weight carbon precursors tend to produce larger nitrogen-doped carbon quantum dots (NCQDs) nanoparticles.

In order to investigate the effect of different precursors on the formation of chemical bonding of the as-synthesised NCQDs, Fourier transform infrared (FTIR) spectroscopy was utilized to characterize the functional groups present in the synthesised nitrogen-doped carbon quantum dots (NCQDs), as depicted in **Figure 4.2**. All NCQD samples exhibited a broad band from 3250-3500 cm^{-1}, corresponding to O-H stretching vibrations arising from carboxylic acids and alcohols as well as N-H stretches from amines and protonated amines.[12,16] This band was most prominent in the NCQDs derived from chitosan and citric acid precursors. In contrast, the NCQDs produced from lignin and humic acid displayed weaker absorbance above 3250 cm^{-1} along with an increased intensity peak around 3000 cm^{-1} attributed to C-H stretching of alkyl groups.[17] The presence of these nitrogen and oxygen-containing functional groups confirms successful N-doping of the carbon quantum dots. The FTIR results demonstrate that the different molecular precursors impart variation in the surface chemistry of the synthesised NCQDs, as evidenced by the relative intensities of O-H/N-H and C-H absorbance band. Additionally, a peak at 1600 cm^{-1} was observed in the FTIR spectra of the synthesised NCQDs, corresponding to the stretching vibration of C=C double bonds.[18] The fingerprint region showed a peak at 1450 cm^{-1} arising from C-N single bond stretches, confirming the incorporation of nitrogen-containing groups on the NCQD surfaces.

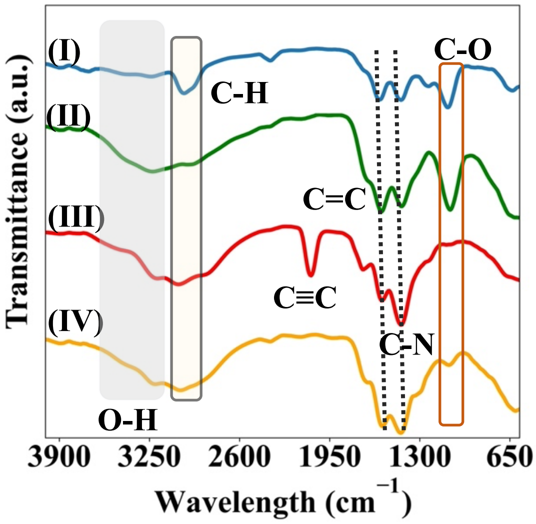

Figure 4.3: Fourier transform infrared spectra of the synthesised NCQDs of: (I) NCQDs-Lignin, (II) NCQDs-Chitosan, (III) NCQDs-Humic, (IV) NCQDs-Citric

A distinguishing peak at 1100 cm^{-1} associated with C-O bond stretches was clearly observed for NCQDs produced from lignin and chitosan precursors.[19] In contrast, this C-O stretch peak was minimal to non-existent in the NCQDs derived from humic acid and citric acid. The presence and intensity variations for the C-O vibrations suggest differing oxygen contents among the NCQDs depending on the carbon precursors. Interestingly, a peak at 2080 cm^{-1}, attributable to C≡C triple bonds, was uniquely observed in the FTIR spectrum of the synthesised NCQDs-Humic, and this distinction peak can be related to the hydrothermal degradation of humic substances could potentially produce unsaturated carbon bonds.[20]

Analysis of the Raman spectra **(Figure 4.4)** provided additional insights into the carbon core structure of the synthesised NCQDs. All samples displayed the expected D and G bands that stem from the graphitic carbon framework. The G band at approximately 1580 cm^{-1} corresponds to the E_{2g} vibrational mode of sp^2 hybridized carbon, confirming the presence of graphitic domains within the NCQDs. Meanwhile, the D band at 1350 cm^{-1} is associated with structural defects and discontinuities in the carbon lattice.[21] Significantly, the NCQDs produced from citric acid and urea exhibited lower I_D/I_G band intensity ratios **(Figure 4.4)** compared to the other samples. This implies the NCQDs-Citric possessed a higher quality graphitic carbon core with less defects. In contrast, NCQDs synthesised using high molecular weight precursors like lignin and humic acid exhibited greater D band intensity relative to the G band. The heightened D band suggests more numerous defects are present in the NCQD carbon core formed from these biomass-derived sources.[22] The increased defects could impact the optical properties of lignin and humic acid-based NCQDs which is described as following.

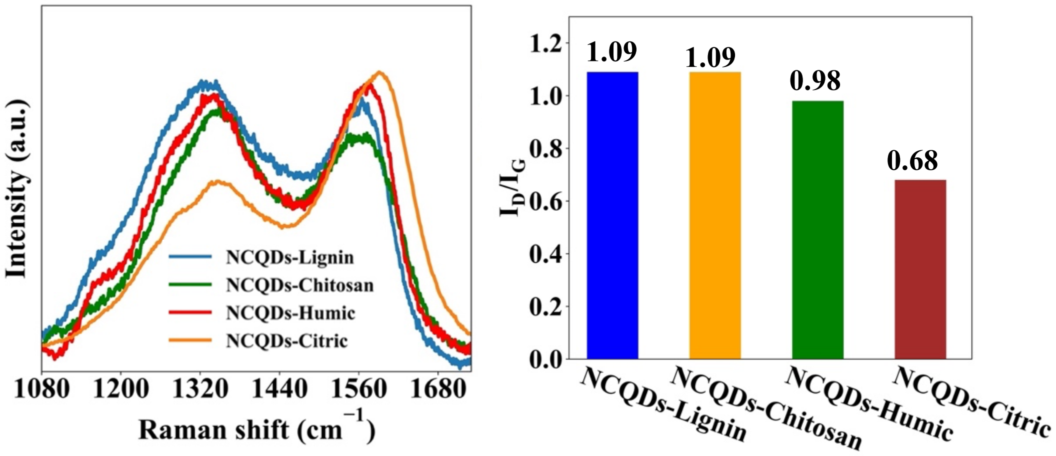

Figure 4.4: The ratio of I_D/I_G presenting for the synthesised NCQDs. The synthesised NCQDs-Citric possess low I_D/I_G indicated the high-quality graphitic carbon core

X-ray photoelectron spectroscopy (XPS) analysis was performed to determine the chemical composition of the synthesised NCQDs. The core level spectra were deconvoluted using Voigt functions, incorporating Lorentzian and Gaussian line widths along with distinct inelastic backgrounds for each component. The minimum number of fitting components was used to optimise the spectral fits. The survey scan XPS spectra revealed three typical peaks, attributed to C1s at 285 eV, O1s at 531 eV, and N1s at 399 eV, providing a fingerprint of the NCQD composition.[23] Analysis of the relative elemental composition, tabulated in **Table 4.2**, showed significantly higher N content above 10% for NCQDs synthesised with citric acid and chitosan precursors.

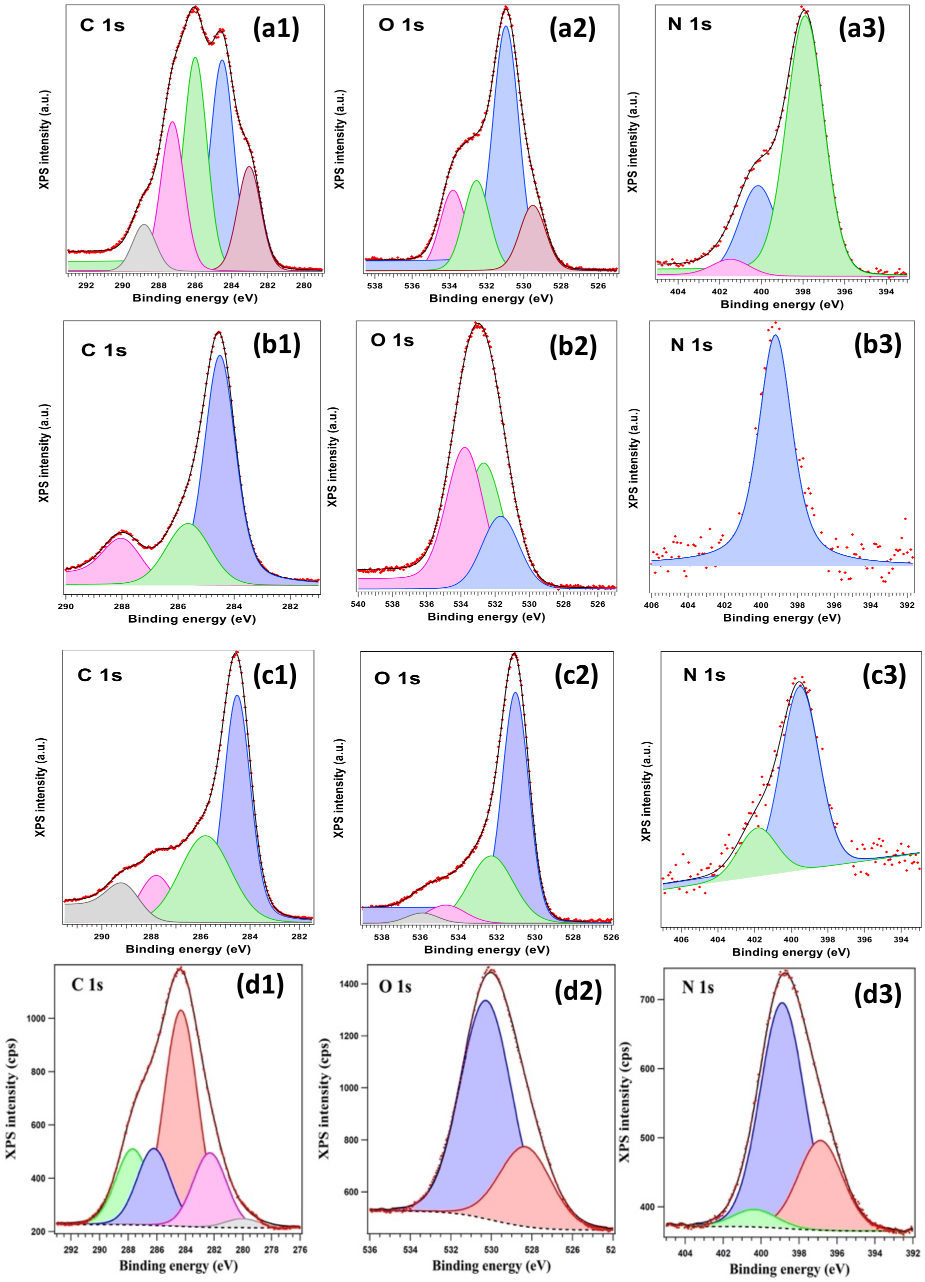

Figure 4.5: The XPS spectra of the synthesised NCQDs: (a1-a3) NCQDs-Chitosan, (b1-b3) NCQDs-Lignin, (c1-c3) NCQDs-Humic and (d1-d3) NCQDs- Citric

In contrast, NCQDs derived from humic acid and lignin displayed poorer nitrogen incorporation~2%, indicative of weaker interaction between these precursors and the N dopant sources during synthesis. In addition to low N content, the NCQDs-Humic and NCQDs-Lignin possessed higher O levels, pointing to an abundance of oxygen-rich surface defects. High resolution N1s spectra (**Figure 4.5**) provided further insights into the nitrogen bonding environments.

Table 4.2: The main elements and the atomic composition for the synthesised NCQDs

Sample	C (%)	O (%)	N (%)	C/N	C/O
NCQDs-Humic	75.65	22.28	2.07	36.54	3.40
NCQDs-Lignin	70.1	27.75	2.15	32.60	2.52
NCQDs-Chitosan	68.76	20.76	10.48	6.56	3.31
NCQDs-Citric	68.96	19.43	11.6	5.94	3.55

The NCQDs-Chitosan exhibited three N_{1s} components at 399.5, 400.2, and 401.5 eV, assigned to pyridinic, pyrrolic, and graphitic N configurations.[24] However, pyrrolic N was absent in the NCQDs-Humic and NCQDs-Lignin samples. The weak fluorescence exhibited by these NCQDs correlates with the limited pyrrolic nitrogen content, which otherwise enhances photoluminescence through excited state proton transfer and surface passivation.[25] In contrast, NCQDs-Citric contained pyrrolic N (398.8 eV), along with pyridinic (396.8 eV) and protonated pyridinic N (400.4 eV), the configuration of nitrogen observed in the as-synthesised NCQDs are depicted in **Figure 4.6**. These results revealed the use of different carbon sources influence in the formation of different nitrogen doped which directly impact the optical properties of the synthesised NCQDs. The incorporation of pyridinic, pyrrolic, protonated pyridinic, and graphitic nitrogen within the sp^2 lattice of CQDs imparts distinct and complementary effects to enhance their overall photoluminescent and optical properties.[26] Pyridinic nitrogen forms localized defects that introduce intermediate bandgap states, enabling lower energy photon emission to tune the fluorescence colour. Meanwhile, its lone electron pair promotes n-type doping to improve charge transfer and electrical conductivity.[27] Additionally, protonated pyridinic nitrogen facilitates proton transfer to further boost quantum yields while also providing positive charges to assist in surface functionalization with brighter emissive chromophores. Graphitic nitrogen directly substitutes carbon sites in the conjugated lattice, leading to bandgap reduction that allows visible light absorption and emission.[28]

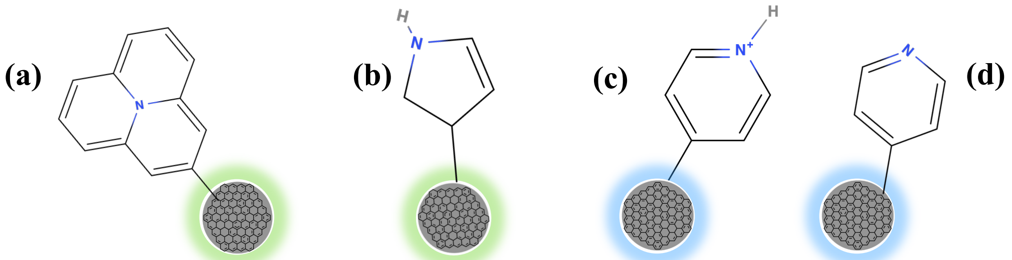

Figure 4.6: The dopant configurations of nitrogen observed in the synthesised NCQDs: (a) graphitic nitrogen, (b) pyrrolic, (c) protonated pyridinic and (d) pyridinic-N

4.2.2 The optical properties of NCQDs

Analysis of UV-Vis absorption spectra provided insights into the impact of different carbon precursors on the optical properties of the synthesised NCQDs. The absorbance was measured in a 10 mm quartz cuvette using deionized water as a reference, with the spectra for each NCQD sample shown in **Figure 4.7**. The NCQDs derived from lignin and humic acid displayed similar broad, featureless absorption bands extending from the UV into the visible region. This reveals their heterogeneous structure and complex optoelectronic transitions. A very broad hump centred around 285 nm likely stems from n-π* transitions of C=O bonds in the disordered NCQD carbon core.[29] In contrast, the NCQDs-Citric exhibited a distinct sharp peak at 330 nm along with an absorption at 270 nm. The 330 nm absorbance band can be assigned to n-π* transitions of nitrogen or oxygen-containing surface groups.[18]

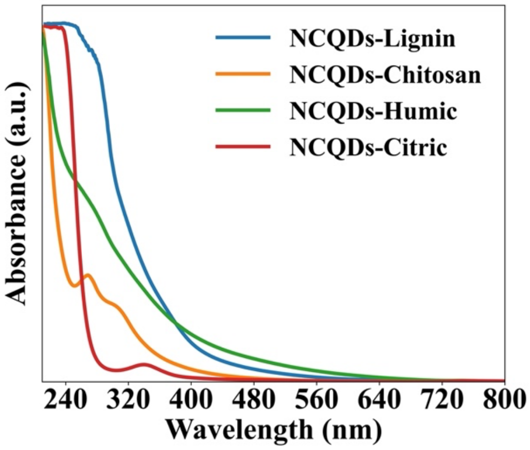

Figure 4.7: The UV-Vis spectra of the synthesised NCQDs, the NCQDs-Lignin and Humic showed a broader range of UV-Vis light absorbance as the result of bigger particle size

Meanwhile, the 270 nm shoulder corresponds to π-π* transitions of sp2 hybridized carbon. Unlike the other samples, chitosan synthesised NCQDs showed a broad asymmetric absorption profile spanning 270-300 nm. This wide hump arises from π-π* transitions of aromatic C=C bonds, implying formation of π-conjugated systems within the chitosan NCQD carbon core.[30]

To achieve a deeper understanding about the optical properties of the synthesised NCQDs, the fluorescence emission properties of the synthesised NCQDs were investigated by exciting diluted NCQD solutions (0.1 OD) at wavelengths ranging from 280-520 nm in 20 nm increments, as shown in **Figure 4.8**. Intriguingly, the NCQD samples displayed both excitation-independent and dependent fluorescence behaviours. The NCQDs-Citric (**Figure 4.8d)** exhibited a rare excitation-independent emission properties, with the peak position fixed at 440 nm across all excitation wavelengths. However, the highest photoluminescence intensity occurred at 340 nm excitation, diminishing significantly above 360 nm. In contrast, the NCQDs-Lignin (**Figure 4.8a)**, chitosan (**Figure 4.8b)** and NCQDs-Humic **(Figure 4.8c)** showed excitation-dependent emission. For NCQDs-Lignin, excitation from 280-400 nm resulted in increasing intensity at 510 nm emission, while longer wavelength excitation above 400 nm caused a red-shift and much weaker emission. Similarly, NCQDs-Chitosan displayed maximum 450 nm emission under 360 nm excitation, while NCQDs-Humic reached to maximum emission at 550 nm under 460 nm excitation.

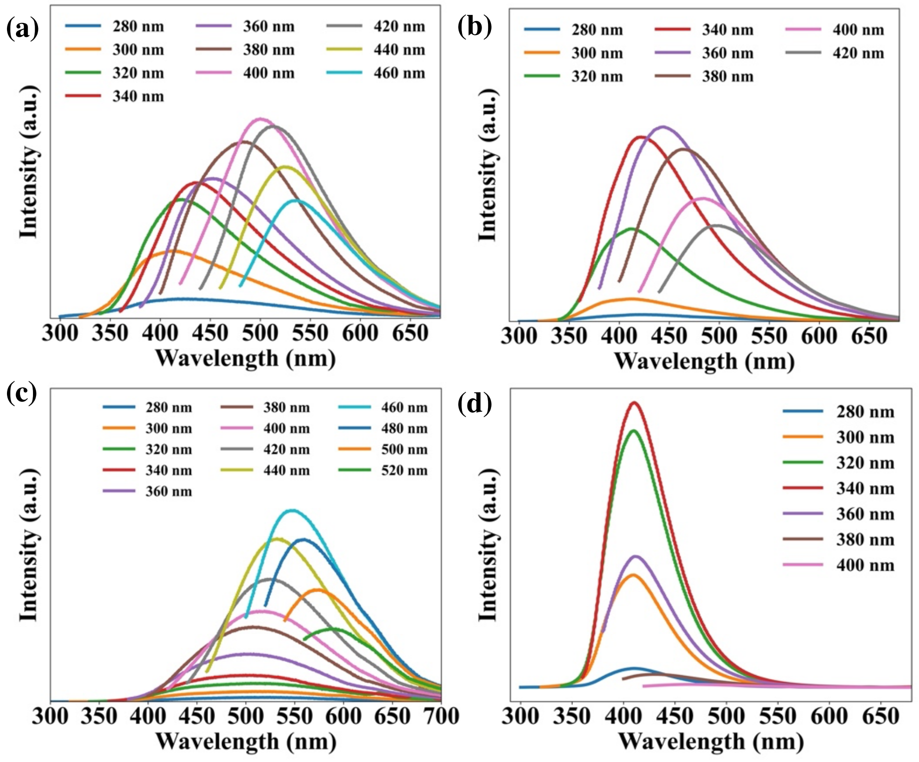

Figure 4.8: The PL spectra of excitation dependent: (a)NCQDs-Lignin, (b) NCQDs-Chitosan, (c) NCQDs-Humic acid, and (d) NCQDs-Citric showing excitation independent

To further probe the impact of different carbon precursors, the photoluminescence quantum yields (PLQY) and fluorescence lifetimes of the synthesised NCQDs were measured.

Fluorescence lifetime data was fitted using multiple exponentials, as highlighted in **Table 4.3**, the PLQY results reveal a significant effect of the carbon sources on emission capabilities. The NCQDs-Citric achieved a high 14% PLQY, representing notable improvement over previous NCQD samples.

Table 4.3: the PL quantum yield and lifetime of the synthesised NCQDs with the computed radiative and non-radiative rates

Sample	**PLQY (%)**	**Average lifetime (ns)**	**Radiative k_r (s^{-1})**	**Non-radiative k_{nr} (s^{-1})**
NCQDs-Lignin	0.52 ± 0.05	5.5 ± 0.6	$9.5x10^5$	$1.8\ x10^8$
NCQDs-Chitosan	3.69 ± 0.4	5.6 ± 0.8	$7.6\ x10^6$	$1.7\ x10^8$
NCQDs-Humic	0.67 ± 0.07	5.9 ± 1.0	$6.6\ x10^6$	$1.7\ x10^7$
NCQDs-Citric	14.0 ± 1.4	7.0 ± 0.7	$1.5x10^7$	$1.1x10^7$

In contrast, chitosan, lignin, and humic acid NCQDs showed far lower quantum yields of 4%, <1%, and <1% respectively. However, all the as-synthesised NCQDs exhibited reasonable fluorescence lifetimes. Analysis of the radiative and non-radiative rates indicates the biomass derived NCQDs have elevated non-radiative rates. This arises from carbon core defects acting as non-emissive recombination centres, as observed in Raman spectroscopy.

4.2.3 The energy band structure

To further investigate the effect of varying the use of carbon precursors on the properties of the synthesised NCQDs, Ultraviolet photoelectron spectroscopy (UPS), a highly valuable technique, is used to examine the electronic structure of the prepared NCQDs. The UPS spectra of the synthesised NCQDs are illustrated in **Figure 4.9**. One critical parameter that can be extracted is the work function (Φ). The work function of the synthesised NCQDs is computed using the following equation 1:

$$\Phi = h\nu - Ek \text{ (Eq.1)}$$

Where: Φ is the work function, h is Planck's constant, ν is the photon frequency, and Ek is the kinetic energy of the emitted photoelectrons.[31] UPS data analysis revealed the largest work function of 5.81 eV for NCQDs-Lignin. NCQDs-Humic and Chitosan showed slightly lower work functions of 5.75 eV. In contrast, citric acid NCQDs exhibited the smallest work function of just 4.94 eV. The trend of higher work functions for biomass-based NCQDs aligns with their larger average particle size compared to NCQDs-Citric. Complementary Tauc plot bandgap measurements displayed an opposite trend.[32] The synthesised NCQDs-Lignin and Humic possess bandgaps of 3.6 and 3.7 eV respectively, NCQDs-Chitosan showed a wider 4.6 eV bandgap, and NCQDs-Citric displayed the largest bandgap of 4.94 eV.

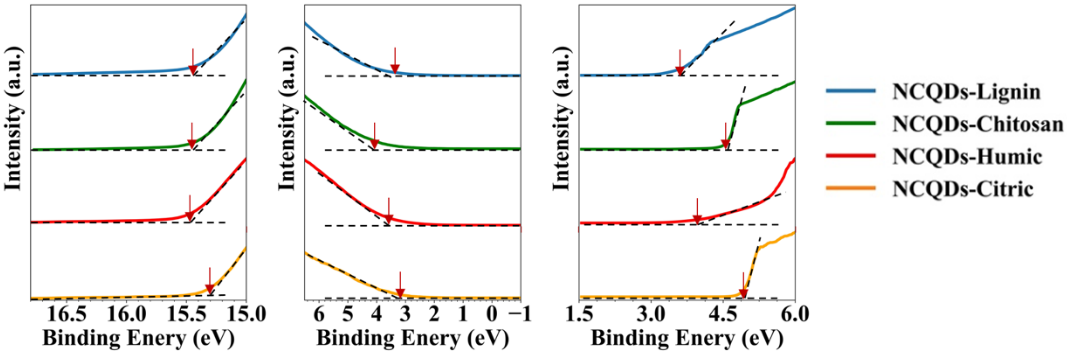

Figure 4.9: the UPS spectra and Tauc plots of the synthesised NCQDs: (a) for determination of the work function, (b) valence band maximum and (c) determination of direct bandgap using Tauc plot.

The smaller bandgaps of NCQDs-Lignin and NCQDs-Humic can be attributed to their larger average particle sizes. The combined data from UPS and bandgap measurements provides a comprehensive picture of the synthesised NCQDs, revealing the effect of different carbon sources in tuning the energy band structures, as shown in **Figure 4.10**.

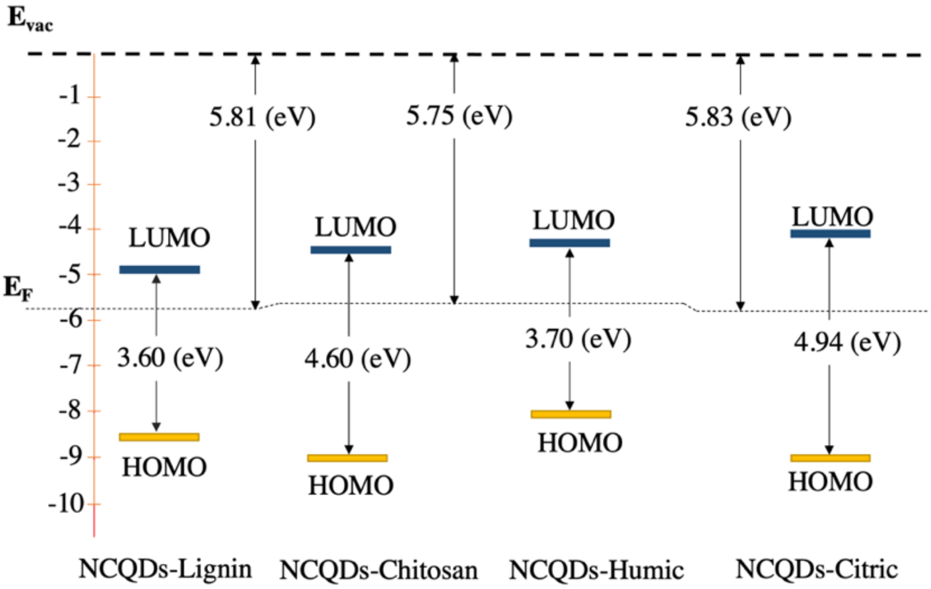

Figure 4.10: The energy band structure of the synthesised NCQDs. The NCQDs-Lignin and Humic acid possess narrower energy bandgap as the average particle sizes are bigger

4.2.4 PL states of the synthesised nitrogen doped carbon quantum dots (NCQDs)

The photoluminescence (PL) mechanism strongly depends on the synthetic conditions and source materials.[2] Elucidating these relationships provides insights into tailoring NCQD optoelectronic properties for different applications. In this work synthesizing NCQDs from various carbon-containing precursors, citric acid stands out in yielding NCQDs with superior optical features like excitation-independent emission and higher quantum yields compared to NCQDs derived from chitosan, lignin, and humic acid. This points to fundamental differences in the PL mechanism based on the carbon source. For the NCQDs synthesised in this work from high molecular weight precursors like chitosan lignin and humic acid, the excitation-dependent behaviour and lower quantum yields indicate carbon core state emission from quantum confined conjugated π-domains.[33] The amorphous carbon core creates quantum-confined states that dominate light emission. The effects are analogous to the synthesised NCQDs-Lignin, Humic, and Chitosan where bigger sizes redshift the emission.[34] Surface defects likely allow nonradiative relaxation pathways, reducing quantum yields.[35]

In contrast, citric acid-derived NCQDs exhibit excitation-independent PL and a comparable quantum yield (~14%), contributed to the molecular state emission from distinct fluorophores.[36] It has been proposed in literature that the prepared NCQDs-Citric consists of fluorophores like derivatives of citrazinic acid under hydrothermal synthesis conditions through cyclization and condensation pathways.[37] Citrazinic acid displays a strong blue fluorescence which is excitation independent with the maximum excitation wavelength at λ_{ex}= 340 nm, and the maximum emission wavelength at λ_{em}= 440 nm. The UV-Vis spectra of citrazinic acid show a typical around 330 nm.[38] The absorption and photoluminescent patterns of citrazinic is similar with the observation of the synthesised NCQDs-Citric confirming the presence of the fluorophore like citrazinic acid in the structure of NCQDs-Citric. While molecular state emission is present dominant in the citric acid derived NCQDs, the carbonized core likely still influences optical properties. During membrane filtration of the NCQDs, we observed fluorescent solid emission in both the permeate and retentate, indicating the removal of some fluorophores not incorporated into the NCQD nanoparticles. This suggests the synthesised NCQDs-Citric have a structure comprised of a sp_2-sp_3 carbon core with attached fluorophores like citrazinic acid derivatives on the surface and edges. In contrast, the prepared NCQDs from lignin salt, humic acid salt and chitosan lack measurable fluorescence in the permeate after filtration, consistent with an absence of molecular fluorophores. We propose that these precursors' complex, heterogeneous structures disfavour the formation of specific emissive fluorophores. Instead, polymerisation and carbonisation reactions dominate under continuous hydrothermal flow synthesis conditions.

However, with the best of our knowledge, up to now, the basic properties of citrazinic acid derivatives in aqueous environments are still not well understood. Previous studies found that citrazinic acid itself is not a source of stable fluorescence in water, with an 80% decrease in photoluminescence observed after just seven days.[37] In contrast, we observed no change in photoluminescence over the same time for our NCQDs-Citric. This suggests the sp_2- and sp_3-hybridized carbon core may act as an anchor to stabilize fluorescent structures like citrazinic acid over time. Report also indicate that the formation of this species is also dependent on the reaction conditions, for example temperature.[39] The relationship between fluorescent molecules generation and the evolving carbon nanoparticle matrix during synthesis needs further investigations. Optimizing the incorporation of molecular fluorophores versus carbonised domains lays the foundation for producing the next generation of NCQDs with controlled optical properties for diverse emitter applications.

4.3 Conclusion

This work demonstrates a green, rapid, and sustainable continuous hydrothermal approach for synthesizing NCQDs from various biomass-derived precursors. The successful synthesis of NCQDs from various carbon precursors like chitosan, lignin, humic acid, and citric acid using the tuneable, rapid, single step continuous hydrothermal flow synthesis (CHFS) process demonstrates the capability of this method to produce CQDs from a wide range of carbon-containing precursors. High-resolution transmission electron microscopy (HRTEM) analysis revealed the effect of the precursor structure on the size of the fabricated NCQD nanoparticles, with more complex precursors tending to yield larger CQDs. Comparing the distinct optical properties of the as-synthesised NCQDs provides valuable insights into their complex photoluminescence mechanisms and the role of molecular fluorophores. Citric acid stands out in yielding NCQDs with excitation-independent emission, higher quantum yields, and optical signatures potentially matching models like citrazinic acid, pointing to molecular state emission. In contrast, NCQDs derived from the polymeric precursors exhibit excitation-dependent, red-shifted, lower efficiency emission consistent with carbon core-confined states. These results highlight that the carbon source strongly influences the balance of molecular versus carbonized emitting states in NCQDs produced under similar flow synthesis conditions.

The complex, heterogeneous polymeric precursors favours carbonization and lack specific reactive sites to from distinct fluorophores. The optical properties of the NCQDs, including their fluorescence, depend on the particle size as well as the configuration of nitrogen dopants. The weak fluorescence exhibited by these NCQDs correlates with their limited pyrrolic nitrogen content. Furthermore, the electronic structure of the NCQDs, as discussed, agrees with the other characterisation results and the principles of quantum confinement effects. Overall, this work demonstrates the power of continuous hydrothermal flow reactors to sustainably generate NCQDs from waste biomass streams with tailored properties based on the precursor chemistry. It provides molecular-level insights into the interplay between carbon sources and unique NCQD photoluminescence mechanisms.

Chapter 4: References

1 A. S. Rasal, S. Yadav, A. Yadav, A. A. Kashale, S. T. Manjunatha, A. Altaee and J.-Y. Chang, *ACS Appl. Nano Mater.*, 2021, **4**, 6515–6541.

2 Y. Wu, C. Li, H. C. Van Der Mei, H. J. Busscher and Y. Ren, *Antibiotics*, 2021, **10**, 623.

3 S. Jing, Y. Zhao, R.-C. Sun, L. Zhong and X. Peng, *ACS Sustainable Chem. Eng.*, 2019, **7**, 7833–7843.

4 R. Pramudita, Marpongahtun, S. Gea, A. Daulay, M. Harahap, Y. Z. Tan, R. Goei and A. I. Y. Tok, *Case Studies in Chemical and Environmental Engineering*, 2022, **6**, 100277.

5 J. Zhuang, S. Ren, B. Zhu, C. Han, Y. Li, X. Zhang, H. Gao, M. Fan and Q. Tian, *Chemical Engineering Journal*, 2022, **446**, 136873.

6 Ł. Janus, M. Piątkowski, J. Radwan-Pragłowska, D. Bogdał and D. Matysek, *Nanomaterials*, 2019, **9**, 274.

7 Y. Dong, L. Wan, J. Cai, Q. Fang, Y. Chi and G. Chen, *Sci Rep*, 2015, **5**, 10037.

8 A. Pundi and C.-J. Chang, *Polymers*, 2022, **14**, 2153.

9 I.-A. Baragau, N. P. Power, D. J. Morgan, T. Heil, R. A. Lobo, C. S. Roberts, M.-M. Titirici, S. Dunn and S. Kellici, *J. Mater. Chem. A*, 2020, **8**, 3270–3279.

10 S. Kellici, J. Acord, K. E. Moore, N. P. Power, V. Middelkoop, D. J. Morgan, T. Heil, P. Coppo, I.-A. Baragau and C. L. Raston, *React. Chem. Eng.*, 2018, **3**, 949–958.

11 K. G. Nguyen, I.-A. Baragau, R. Gromicova, A. Nicolaev, S. A. J. Thomson, A. Rennie, N. P. Power, M. T. Sajjad and S. Kellici, *Sci Rep*, 2022, **12**, 13806.

12 I.-A. Baragau, N. P. Power, D. J. Morgan, R. A. Lobo, M.-M. Titirici, V. Middelkoop, A. Diaz and S. Dunn, *ACS Sustainable Chemistry & Engineering*, 2021, **9**, 2559–2569.

13 S. D. Dsouza, M. Buerkle, P. Brunet, C. Maddi, D. B. Padmanaban, A. Morelli, A. F. Payam, P. Maguire, D. Mariotti and V. Svrcek, *Carbon*, 2021, **183**, 1–11.

14 H. Dong, M. Li, Y. Jin, Y. Wu, C. Huang and J. Yang, *Front. Energy Res.*, 2020, **8**, 148.

15 S. Dorontić, S. Jovanović and A. Bonasera, *Materials*, 2021, **14**, 6153.

16 F. Lu, S. Yang, Y. Song, C. Zhai, Q. Wang, G. Ding and Z. Kang, *Mater. Res. Express*, 2019, **6**, 065030.

17 V. Singh, S. Kashyap, U. Yadav, A. Srivastava, A. V. Singh, R. K. Singh, S. K. Singh and P. S. Saxena, *Toxicol. Res.*, 2019, **8**, 395–406.

18 Y. Wang, Y. Liu, J. Zhou, J. Yue, M. Xu, B. An, C. Ma, W. Li and S. Liu, *RSC Adv.*, 2021, **11**, 29178–29185.

19 Y.-J. Tong, L.-D. Yu, Y. Huang, Y. Li, N. Li, Q. Fu, Y.-X. Ye, F. Zhu, J. Pawliszyn, J. Xu and G. Ouyang, *iScience*, 2022, **25**, 104421.

20 L. D. Movsisyan, M. D. Peeks, G. M. Greetham, M. Towrie, A. L. Thompson, A. W. Parker and H. L. Anderson, *J. Am. Chem. Soc.*, 2014, **136**, 17996–18008.

21 E. Dervishi, Z. Ji, H. Htoon, M. Sykora and S. K. Doorn, *Nanoscale*, 2019, **11**, 16571–16581.

22 A. Kolanowska, G. Dzido, M. Krzywiecki, M. M. Tomczyk, D. Łukowiec, S. Ruczka and S. Boncel, *ACS Omega*, 2022, **7**, 41165–41176.

23 Q. Zhang, S. Xie, Y. Yang, Y. Wu, X. Wang, J. Wu, L. Zhang, J. Chen and Y. Wang, *Journal of Analytical Methods in Chemistry*, 2018, **2018**, 1–9.

24 K. Holá, M. Sudolská, S. Kalytchuk, D. Nachtigallová, A. L. Rogach, M. Otyepka and R. Zbořil, *ACS Nano*, 2017, **11**, 12402–12410.

25 F. A. Permatasari, R. Umami, C. D. D. Sundari, T. R. Mayangsari, A. L. Ivansyah, F. Muttaqien, T. Ogi and F. Iskandar, *Nano Res.*, 2023, **16**, 6001–6009.

26 M. Sudolská and M. Otyepka, *Applied Materials Today*, 2017, **7**, 190–200.

27 L. Sun, Y. Luo, M. Li, G. Hu, Y. Xu, T. Tang, J. Wen, X. Li and L. Wang, *Journal of Colloid and Interface Science*, 2017, **508**, 154–158.

28 T. Pillar-Little and D. Y. Kim, *RSC Adv.*, 2017, **7**, 48263–48267.
29 J. Song, L. Zhao, Y. Wang, Y. Xue, Y. Deng, X. Zhao and Q. Li, *Nanomaterials*, 2018, **8**, 1043.
30 M. R. Hasan, N. Saha, T. Quaid and M. T. Reza, *Energies*, 2021, **14**, 986.
31 A. Kahn, *Mater. Horiz.*, 2016, **3**, 7–10.
32 P. Makuła, M. Pacia and W. Macyk, *J. Phys. Chem. Lett.*, 2018, **9**, 6814–6817.
33 Q. Zhang, R. Wang, B. Feng, X. Zhong and K. Ostrikov, *Nat Commun*, 2021, **12**, 6856.
34 S. Gavalas and A. Kelarakis, *Nanomaterials*, 2021, **11**, 2089.
35 R. Jiang, H. Wu, D. Manzani, W. Zhang and C. Liu, *Applied Surface Science*, 2023, **622**, 156931.
36 W. Kasprzyk, T. Świergosz, P. P. Romańczyk, J. Feldmann and J. K. Stolarczyk, *Nanoscale*, 2022, **14**, 14368–14384.
37 X. Yao, Y. Wang, F. Li, J. J. Dalluge, G. Orr, R. Hernandez, Q. Cui and C. L. Haynes, *Nanoscale*, 2022, **14**, 9516–9525.
38 S. Mura, L. Stagi, L. Malfatti, C. M. Carbonaro, R. Ludmerczki and P. Innocenzi, *J. Phys. Chem. A*, 2020, **124**, 197–203.
39 F. Mocci, C. Olla, A. Cappai, R. Corpino, P. C. Ricci, D. Chiriu, M. Salis and C. M. Carbonaro, *Materials*, 2021, **14**, 770.

Chapter 5 : Synergistic Design of Nitrogen-Doped Carbon Quantum Dots: Unravelling the Crucial Role of Nitrogen Precursors in Tailoring Enhanced Optical and Chemical Properties

5.1 Introduction

Carbon quantum dots (CQDs) have emerged as a promising class of nanomaterials with applications in optoelectronics, biomedicine, and sensing. Their unique optical, electronic, and chemical properties, such as high photoluminescence, low toxicity, and easy functionalization, make them attractive for various purposes.[1] The synthesis of CQDs can be achieved by a variety of methods, with continuous hydrothermal flow synthesis method (CHFS) gaining prominence due to its simplicity, scalability, low cost, and the ability to produce high-quality CQDs.[2,3,4] In CHFS, the reaction mixture is continuously pumped through an engineered reactor at a constant flow rate, providing a highly controlled and homogeneous reaction environment. CHFS offers several advantages over the traditional hydrothermal synthesis, including improved control over the reaction parameters, shorter reaction times, tunability, higher yields and enhanced optical properties.[5, 6]

Despite their potential, the low photoluminescence quantum yield (QY) of carbon quantum dots, remains a challenge that limits their practical applications. To improve their optical properties, nitrogen doping of CQDs has been shown to enhance their QY and modify their bandgap.[7] However, there are still challenges in controlling the size and nitrogen doping level of the CQDs, which can affect their properties and performance. Additionally, the exact mechanisms behind the formation of nitrogen doped CQDs are still not fully understood, which hinders the optimization of synthesis conditions.[8] The choice of nitrogen precursor can significantly impact the properties of nitrogen doped carbon quantum dots (NCQDs) including topology, optical and electrical structure properties.[9] Therefore, there is a need for further research to investigate the effect of different types of nitrogen dopants and synthesis methods on the properties and performance of NCQDs.

In this study, we aim to investigate the impact of different nitrogen dopant precursors in the continuous hydrothermal flow synthesis of nitrogen doped CQDs. By comparing the properties and performances of the resulting NCQDs, we seek to gain insights into the effect of different nitrogen dopant precursors on the quality and characteristics of the NCQDs. The nitrogen precursors utilised were urea, ß-alanine, L-arginine, and ethylenediaminetetraacetic acid dipotassium salt dihydrate (EDTA), and trizma base. Urea, a common nitrogen precursor, is a cost-effective and readily available source of nitrogen,[10] while ß-alanine and L-arginine are inexpensive amino acids and expected to introduce beneficial nitrogen functionalities for doping CQDs. The amino groups act as reactive sites for controlled nucleation and growth of dots. Additionally, the carboxylic acid and guanidine side chains enable surface passivation for enhanced hydrophilicity, colloidal stability, and photoluminescence. The biocompatibility of ß-alanine and L-arginine also imparts low cytotoxicity for the synthesised NCQDs.[11,12] Ethylenediaminetetraacetic acid dipotassium salt dihydrate (EDTA), as a chelating agent, has the potential to form stable complexes with nitrogen doped CQDs.[11] Whereas, the combination of hydroxyl/amine reactivity, excellent solubility, and ability to dope and passivate makes trizma base as an excellent nitrogen precursor for engineering high quality fluorescent NCQDs.[14]

Through this study, we explored how different nitrogen sources influence the formation and nucleation of nitrogen-doped carbon quantum dots (NCQDs) during continuous CHFS process. By shedding light on the early-stage processes of NCQDs formation, we enhanced our understanding of nitrogen-doped CQDs synthesis, which is crucial for optimising their properties for various applications. Moreover, to complement our experimental findings, we employed state-of-the-art modelling techniques to study their structural, electronic, and optical characteristics. The combination of experimental data and advanced modelling allows for a comprehensive investigation into the formation, growth, and properties of NCQDs, contributing to the advancement of this versatile class of nanomaterials.

5.2 Results and discussion

In this study, citric acid - $C_6H_8O_7$ was used as the carbon resources to synthesise NCQDs. A series of nitrogen containing precursors were utilised as dopants, including urea - CH_4N_2O, ethylenediaminetetraacetic acid dipotassium salt dihydrate, EDTA - $C_{10}H_{16}N_2O_8$, ß-alanine - $C_6H_{14}N_4O_2$, L-arginine - $C_3H_7NO_2$ and trizma base - $C_4H_{11}NO_3$. The as-synthesised NCQDs are denoted as NCQDs-Urea, NCQDs-Alanine, NCQDs-Arginine, NCQDs-EDTA and NCQDs-Trizma. The characterisation results of the produced NCQDs are presented in the following sections.

5.2.1 The morphology and chemical properties of NCQDs

High-resolution TEM (HR-TEM) and atomic force microscopy (AFM) imaging revealed distinct differences in the size and distribution of the synthesised NCQDs depending on the nitrogen source employed.

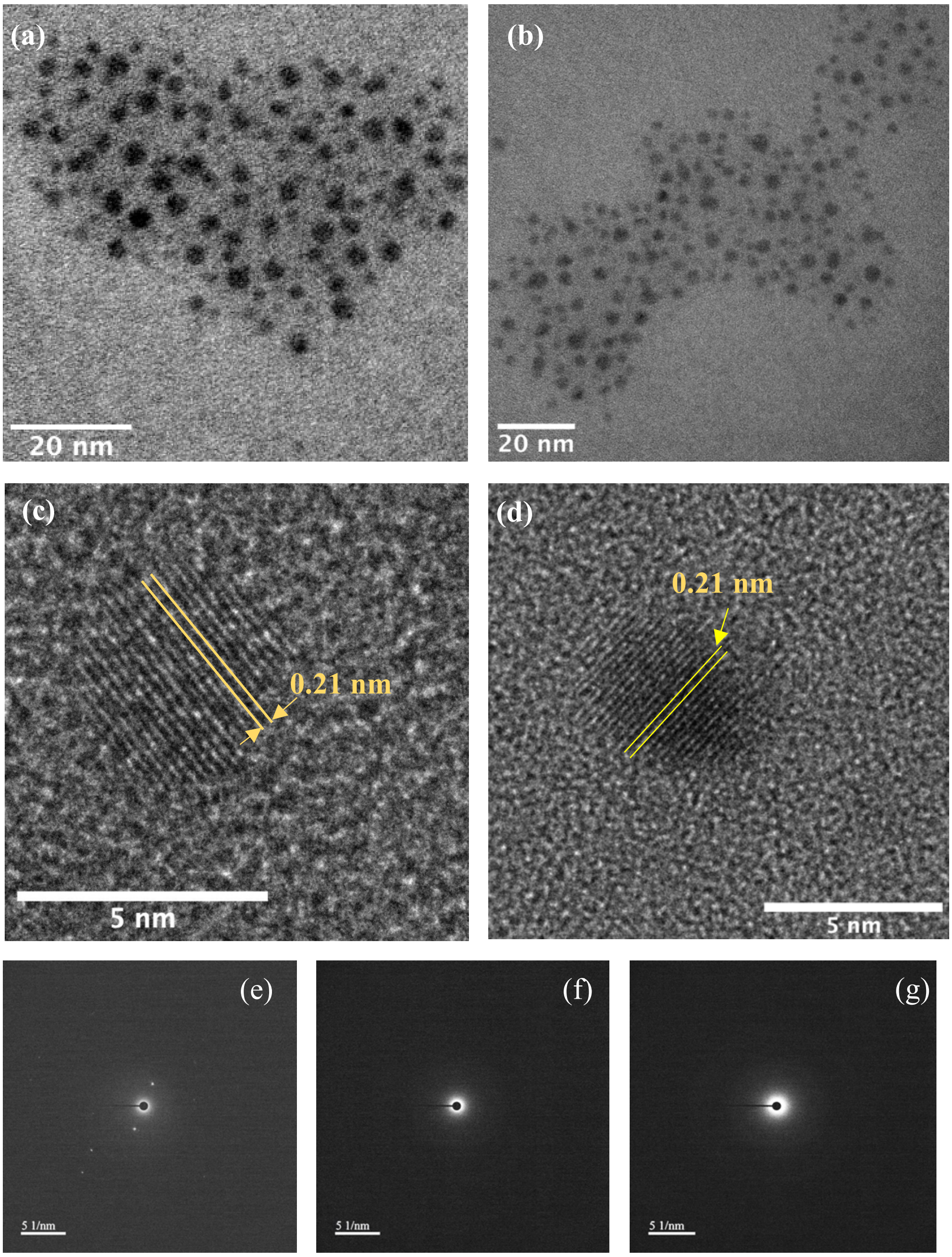

Figure 5.1: HRTEM images of NCQDs-Urea and trizma at different magnifications: (a) NCQDs-Trizma-, (b) NCQDs-Urea, (c) graphitic core lattices of NCQDs-Urea with d-spacing of 0.21 ± 0.01 nm, and (d) lattice d-spacing of NCQDs-Trizma, SAED patterns of : (e) NCQDs-Alanine, (g) NCQDs-Arginine, and (f) NCQDs-EDTA

HR-TEM images in **Figure 5.1** illustrate the round shape and uniformity of NCQDs-Urea and NCQDs-Trizma samples. Importantly, **Figure 5.1 (c&d)** demonstrates the crystalline nature of NCQDs (observed for samples synthesised with urea and trizma), displaying a lattice spacing of ~0.21 ± 0.01 nm that corresponds to the graphitic core.[3] This finding aligns with our previous reports, further confirming the effectiveness and reliability of the CHFS method for NCQDs synthesis.[5] Conversely, NCQDs prepared with alanine, arginine and EDTA as dopants revealed amorphous SAED patterns, indicating their unstructured morphology Figure 5.1 (e-g). Complementary insight into the morphology, topography and particle size analysis was provided by AFM images **(Figure 5.2)**.

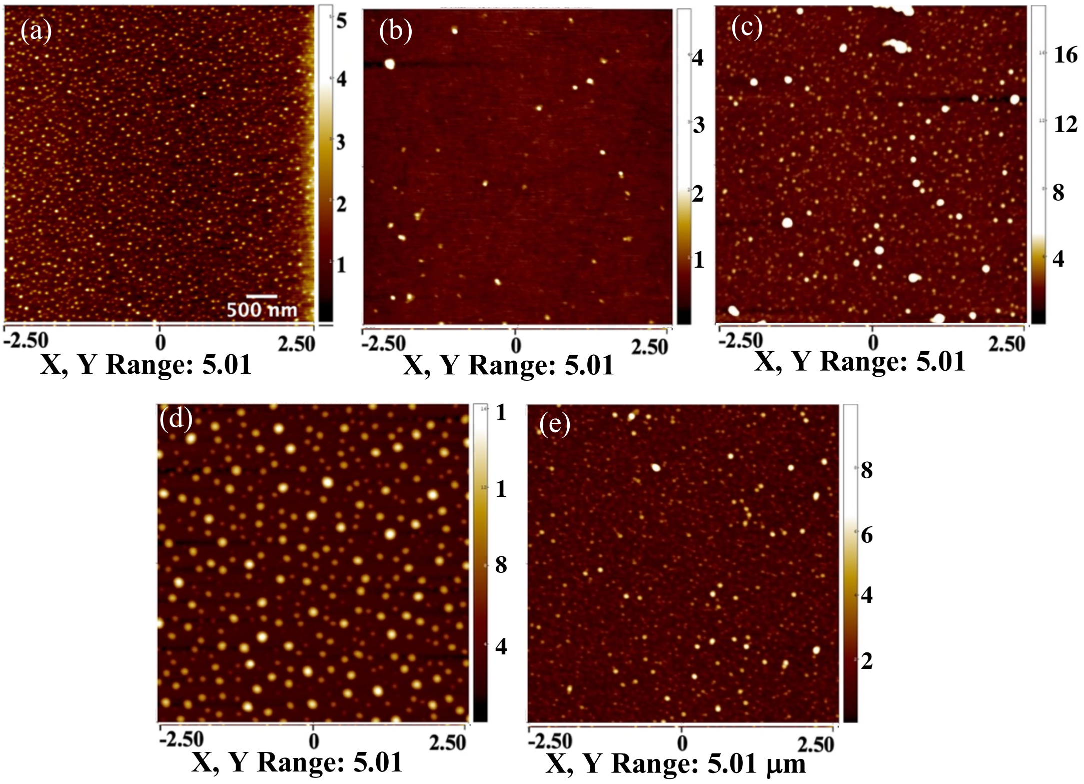

Figure 5.2: The AFM images of a) NCQDs-Urea, (b) NCQDs-Alanine, (c) NCQDs-Arginine, (d) NCQDs-EDTA and (e) NCQDs-Trizma. These AFM images provided insight into the 3D morphology of CQDs

The nanoparticle size analysis obtained from the microscopy imaging techniques (**Table 5.1** and **Figure 5.3**) has shed light on the influence of nitrogen dopants on NCQDs via the CHFS process. **Figure 5.3b** shows the particle size distribution histogram of NCQDs-Alanine, with the smallest mean particle size (2.4 ± 1.3 nm) and a broad distribution (1.0-8.0 nm). NCQDs-Arginine had a slightly larger average particle size (2.9 ± 1.2 nm), with a range of 1.0 - 6.0 nm (**Figure 5.3c**). Both NCQDs-Alanine and NCQDs Arginine exhibited skewed distributions, with modes below 3.0 nm. In contrast, NCQDs-EDTA (**Figure 5.3d**) displayed a multimodal histogram (4.0 ± 1.7 nm, range 1.0-7.0 nm), indicating varied populations affecting optical properties.

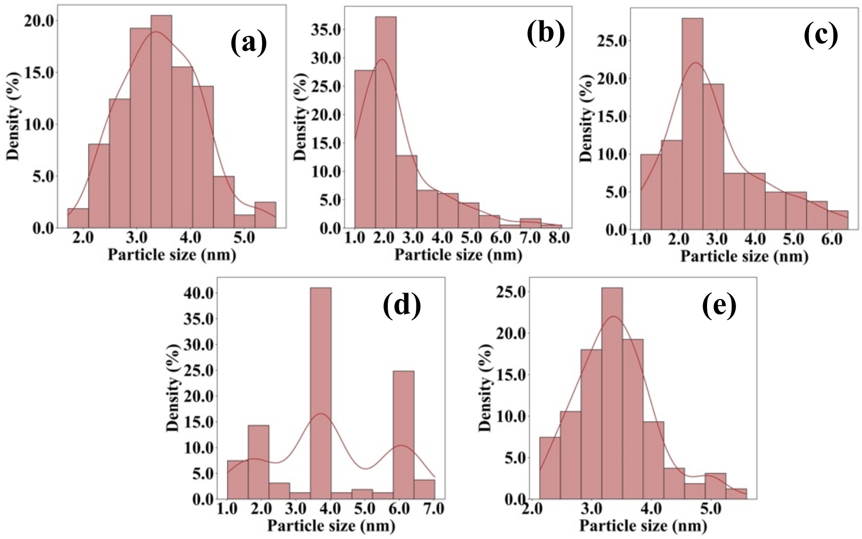

Figure 5.3: The particle size distribution histograms of (a) NCQDs-Urea, (b) NCQDs-Alanine, (c) NCQDs-Arginine, (d) NCQDs-EDTA and (e) NCQDs-Trizma.

Image analysis of NCQDs-Urea and NCQDs-Trizma samples (**Figure 5.2a** and **5.2e)** reveal symmetric histograms and a narrow size distribution, indicating a high degree of uniformity in particle sizes (within the range of 2.5 to 5.5 nm). NCQDs-Urea averaged 3.5 ± 0.8 nm, and NCQDs-Trizma averaged 3.4 ± 0.7 nm. The differences in the size and distribution of nanoparticles among NCQDs-Urea, NCQDs-Trizma, NCQDs-Arginine, and NCQDs-EDTA is expected to lead to distinct optical properties of the NCQDs.

Table 5.1: The mean particle size of the prepared NCQDs.

Sample	Particle size (nm)
NCQDs-Urea	3.5 ± 0.8
NCQDs-Alanine	2.4 ± 1.3
NCQDs-Arginine	2.9 ± 1.2
NCQDs-EDTA	4.0 ± 1.7
NCQDs-Trizma	3.4 ± 0.7

Further investigation and analysis of these materials is crucial for understanding the influence of N-dopants on carbon quantum dots. To investigate the distinctions in chemical functional groups of the as-synthesised NCQDs caused by using different nitrogen dopants during the synthesis process, Fourier Transform Infrared (FTIR) spectroscopy was utilized. The FTIR spectra of NCQDs was displayed in **Figure 5.4a,** providing evidence of characteristic functional groups containing nitrogen and oxygen. This confirms the successful N-doping of carbon quantum dots (CQDs). Across all spectra, a broad band ranging from 2600-3500 cm^{-1} is evident, corresponding to overlapping stretches encompassing various vibrations. These include the O-H bond (-COOH, R-OH) commonly found between 3250 cm^{-1} and 3500 cm^{-1},[17] as well as amine/protonated amine (N-H) vibrations. Additionally, a broad peak is observed below 3000 cm^{-1} attributed to the C-H bond.[18] The presence of C=O bond (~1650 cm^{-1}) was observed only in the NCQDs-Alanine sample, suggesting the absence of the carboxyl group in the other synthesised NCQDs. Instead, these NCQDs exhibited a band at 1575 cm^{-1} corresponding to the stretching vibration of C=N bond.[12] In the fingerprint region, the presence of C-N bond was confirmed by the peak at 1450 cm^{-1}. Moreover, the spectrum of NCQDs-Trizma showed an intense and sharp peak at 1100 cm^{-1}, which is associated with the vibration of C-O bond, while this peak is absent or less pronounced in the other NCQDs, this distinction can be attributed to the higher oxygen content of Trizma.[19,20] Interestingly, the peak at 650 cm^{-1} corresponds to C-H bending and vibrations of nitrogen-substituted aromatic rings, which demonstrates the presence of pyridinic nitrogen integrated structure into the NCQDs structure.[21] Further characterisations were carried out to achieve a deeper understanding about the chemical compound and structure of the as-synthesised NCQDs.

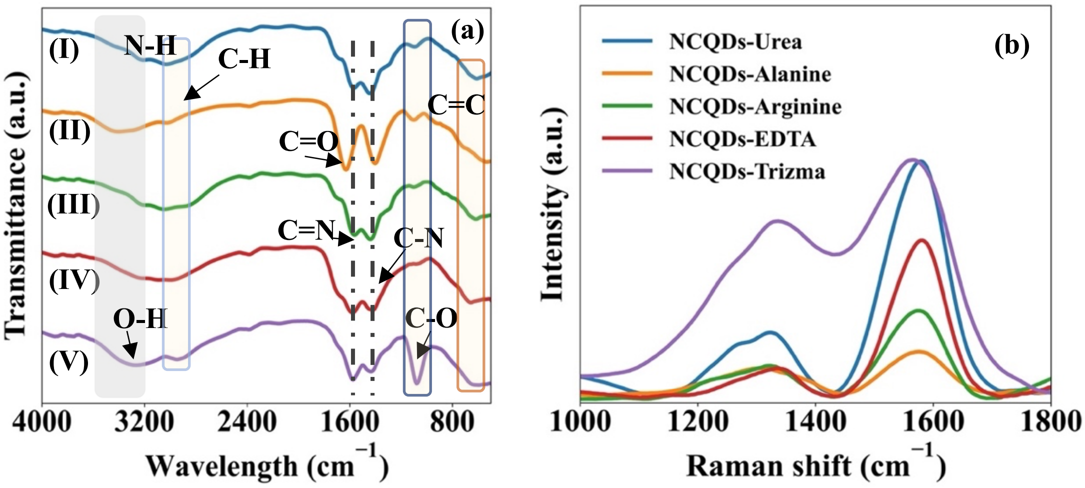

Figure 5.4: (a) Fourier transform infrared spectra of: (I) NCQDs-Urea, (II) NCQDs-Alanine, (III) NCQDs-Arginine, (IV) NCQDs-EDTA and (V) NCQDs-Trizma; (b) Raman spectra of the synthesised NCQDs

The Raman spectroscopy was employed to investigate the level of graphitization revealing the ordered versus disordered structure of the synthesised NCQDs. Raman spectra of NCQDs

(**Figure 5.4b)** shows characteristic D and G bands arising from the carbon core. The G band located around 1580 cm^{-1} corresponds to the E_{2g} vibrational mode of sp^2 graphitic carbon domains, indicating the formation of crystalline graphitic structures within the NCQDs. The D band near 1350 cm^{-1} is associated with structural defects and discontinuities in the carbon framework. Interestingly, the synthesised NCQDs-Urea and NCQDs-Trizma demonstrate relatively lower I_D/I_G ratios (**Figure 5.5**) which implies a higher quality graphitic content in these samples. These findings are consistent with the results obtained from HR-TEM, which also indicate a crystalline nature for NCQDs prepared with urea and trizma base as nitrogen precursors.

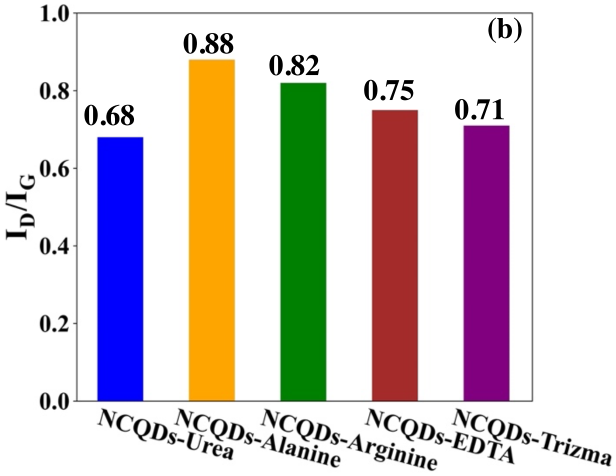

Figure 5.5: The ID/IG ratio of the synthesised NCQDs. The lower I_D/I_G indicated the higher quality graphitic content of NCQDs-Urea and NCQDs-Trizma

Furthermore, XPS investigation was carried out to determine the chemical composition of the samples. The core level spectra were deconvoluted with use of Voigt functions (which incorporate Lorentzian and Gaussian widths along with a distinctive inelastic background for each component). A minimum number of components was selected to achieve an optimal fit for the spectra. The binding energy scale was calibrated based on the C1s standard value of 284.6 eV. The XPS spectra display three typical binding energies ascribed to C1s at 285 eV, O1s at 531 eV and N1s at 399 eV. The high resolution N1s XPS spectrums of the NCQDs (**Figure 6.6)** is fitted with three Gaussian peaks revealed a predominant peak located at the region 398.6 eV – 399.5 eV which is assigned to pyrrolic N, another peak at 396.8 eV – 397 eV attributed to pyridinic N in aromatic, and a third peak at 400.1 eV - 400.4 eV indicated nitrogen exist in hydrogenated pyridinic N.[22] In the NCQDs-Alanine sample the presence of N-graphitic is noted at 401.10 eV. The deconvolution of the high-resolution C 1s spectra

(Figure S4-S9) indicated presence of C=C sp^2 at 284.5 eV, C-O/C-N sp^3 at 286.5 eV, and C=N/C=O at 287.7 eV. This XPS data analysis aligns well with the mentioned FT-IR characterisation.

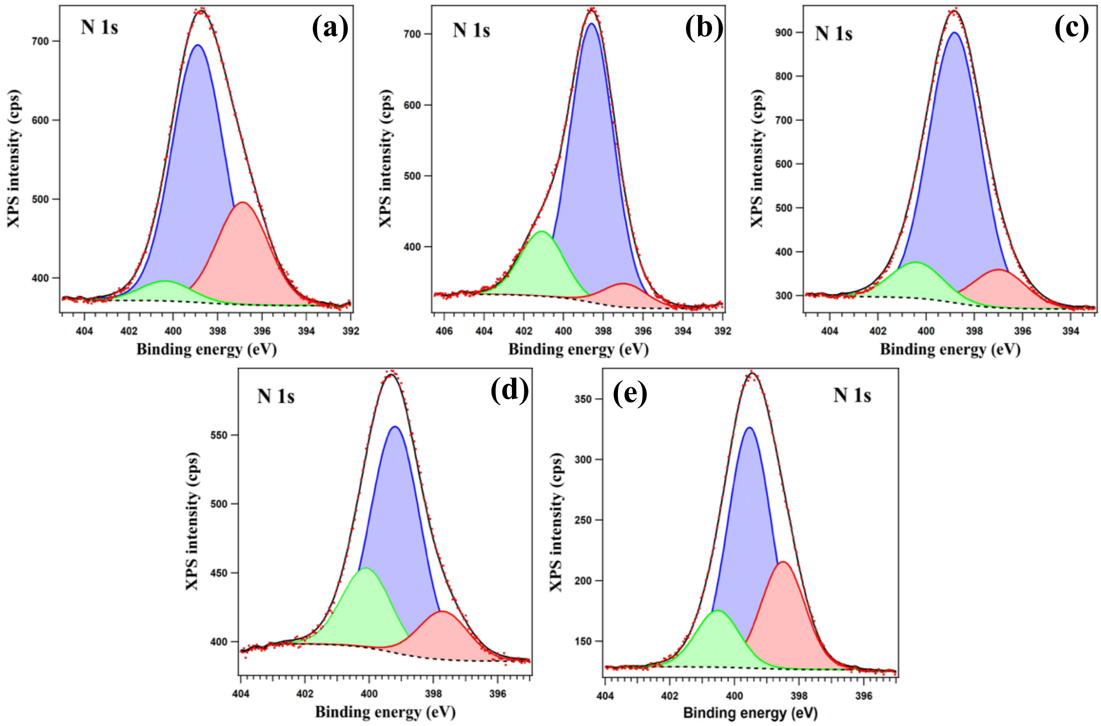

Figure 5.6: The XPS high-resolution of N1s spectrum of NCQDs: (a) NCQDs-Urea, (b) NCQDs-Alanine, (c) NCQDs-Arginine, (d) NCQDs-EDTA, (e) NCQDs-Trizma

While urea and trizma base contain lower carbon content compared to the other nitrogen precursors, XPS data (Figure 5.7a) revealed a high carbon content in the corresponding synthesised nitrogen-doped carbon quantum dots (NCQDs-Urea and NCQDs-Trizma). This confirms that urea and trizma enable efficient carbonisation of the citric acid precursor despite having less intrinsic carbon. Analysis of the relative ratios of carbon, nitrogen, and oxygen (C/N and C/O) shown in **Table 5.2** provides insights into the composition and surface chemistry of the synthesised NCQDs.

Table 5.2: The main elements and the atomic composition for five NCQDs via XPS

Sample	C (%)	O (%)	N (%)	C:N	C:O
NCQDs-Urea	69.0	19.4	11.6	5.9	3.6
NCQDs-Alanine	70.3	14.3	15.4	4.5	4.9
NCQDs-Arginine	73.7	10.2	16.1	4.6	7.3
NCQDs-EDTA	70.0	15.9	6.7	10.5	4.4
NCQDs-Trizma	76.5	15.3	8.2	9.4	5.0

Urea, ß-alanine, and L-arginine, with higher N atom counts, led to NCQDs with lower C/N ratios, indicating greater overall nitrogen incorporation into the carbon core. Meanwhile, the C/O ratio was highest for the NCQDs prepared using arginine, suggesting higher surface oxygen groups. This demonstrates the ability to control doping levels and surface chemistry by tuning the precursor nitrogen source.

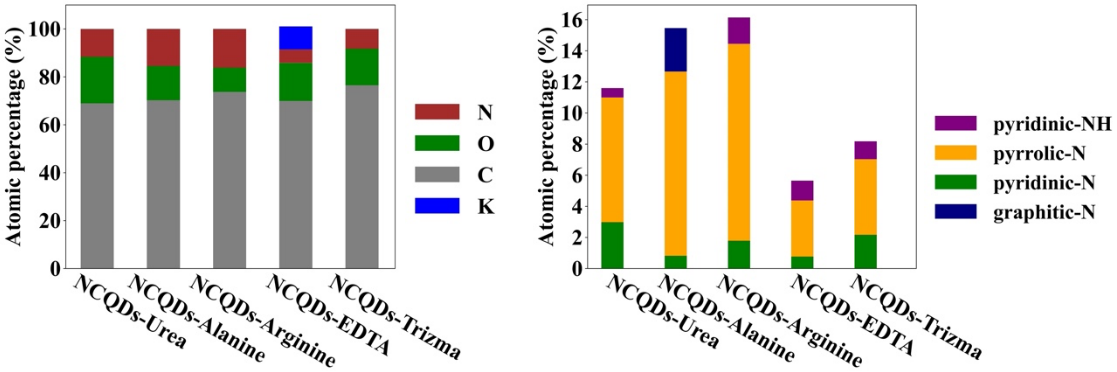

Figure 5.7:The XPS data of the synthesised NCQDs:(a) the atomic composition and (b) atomic percentage of nitrogen component

5.2.2 The optical properties of NCQDs

The effect of the nitrogen dopants on the optical properties of NCQDs was further investigated using UV-Vis absorbance and fluorescence spectrophotometry. The UV-Vis absorbance of the synthesised NCQDs was measured in a 10 mm quartz cuvette using deionised water as reference, and the corresponding spectra for different NCQDs are given in **Figure 5.8**. Notably, that the NCQDs-Alanine, Arginine, EDTA and Trizma samples exhibit similar absorption spectra, featuring a broad absorption band from 275 nm to 375 nm, centred between 300 nm to 350 nm. This absorption band is attributed to the n-π* transitions of C=N bonding, and a shoulder at 290 nm is assigned to the transitions of π-π* of the aromatic carbon atoms in the carbon core. In contrast, the spectrum of NCQDs-Urea displays a sharp peak at the $\lambda_{max} = 330$ nm, which is attributed to n-π transitions of the nitrogen or oxygen containing group, and the shoulder at 270 nm is related to the transition of sp^2 carbon. These absorption spectra offer valuable information about the optical properties and surface functionalization of the NCQDs with different nitrogen dopant precursors. The variations in absorption bands and peak positions are indicative of differences in the electronic structure and chemical environment of the NCQDs.

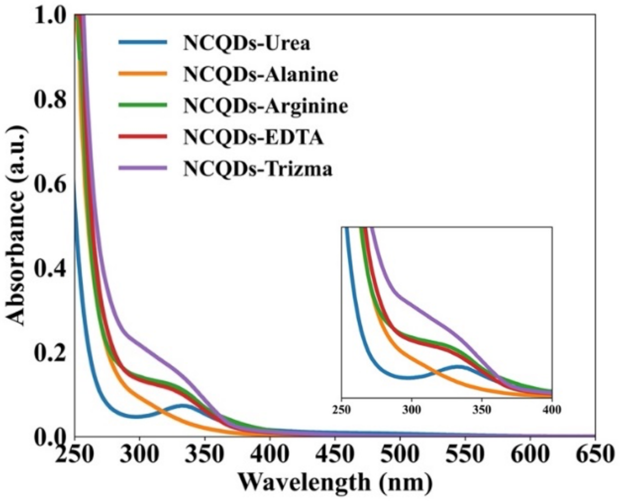

Figure 5.8: The UV-Vis absorbance spectra of the synthesised NCQDs

The fluorescence properties of all NCQDs were also subjected to investigation. Diluted solutions NCQDs were excited at various wavelengths, ranging from 280 to 400 nm with a 20 nm interval as shown in **Figure 5.9.** Interestingly, the synthesised NCQDs exhibit both independent and excitation dependent properties. The spectra of NCQDs-Urea (**Figure 5.9a**) and NCQDs-Trizma (**Figure 5.9e**) exhibit a unique and rarely observed independent excitation property: the emission peak position of these NCQDs remains constant at 440 nm across the entire excitation range. However, the highest photoluminescent (PL) intensity is obtained at an excitation wavelength of 340 nm, it diminishes significantly beyond 360 nm excitation wavelength.

In contrast, the spectra of NCQDs-Alanine (**Figure 5.9b**) and NCQDs-Arginine (**Figure 5.9c**) demonstrate the typical dependent excitation emission property. The PL emission of these NCQDs splits into two distinct regions, each exhibiting different responses to l_{ex}. Excitation in the 280-340 nm range results in a dominant excitation-independent emission peak at 430 nm, corresponding to a single emissive transition. However, when the excitation wavelength is increased beyond 340 nm, the emission undergoes a redshift to longer wavelengths accompanied by significantly lower emission intensities. Similarly, NCQDs-EDTA (**Figure 5.9d**) exhibits the dependent excitation emission with the maximum emission wavelength at 460 nm under excitation at 380 nm. Furthermore, the full width at maximum (FWHM) of the emission spectra provides insights into the homogeneity of the emission source. The computed FWHM (**Table 5.3**) of NCQDs-Trizma and NCQDs-Urea are 67 nm and 70 nm, respectively. Comparing these results to the common reported FWHM value of 100 nm for CQDs indicated that NCQDs-Trizma and NCQDs-Urea exhibit excellent homogenous emission characteristics. It can be seen that NCQDs-Trizma and NCQDs-Urea show an uniform particle size with narrow distribution, as reflected by a narrow FWHM. While, NCQDs-Alanine, NCQDs-Arginine and NCQDs-EDTA exhibit an imbalanced particle size distribution as reflected by a large FWHM, as showed in **Table 5.3**.

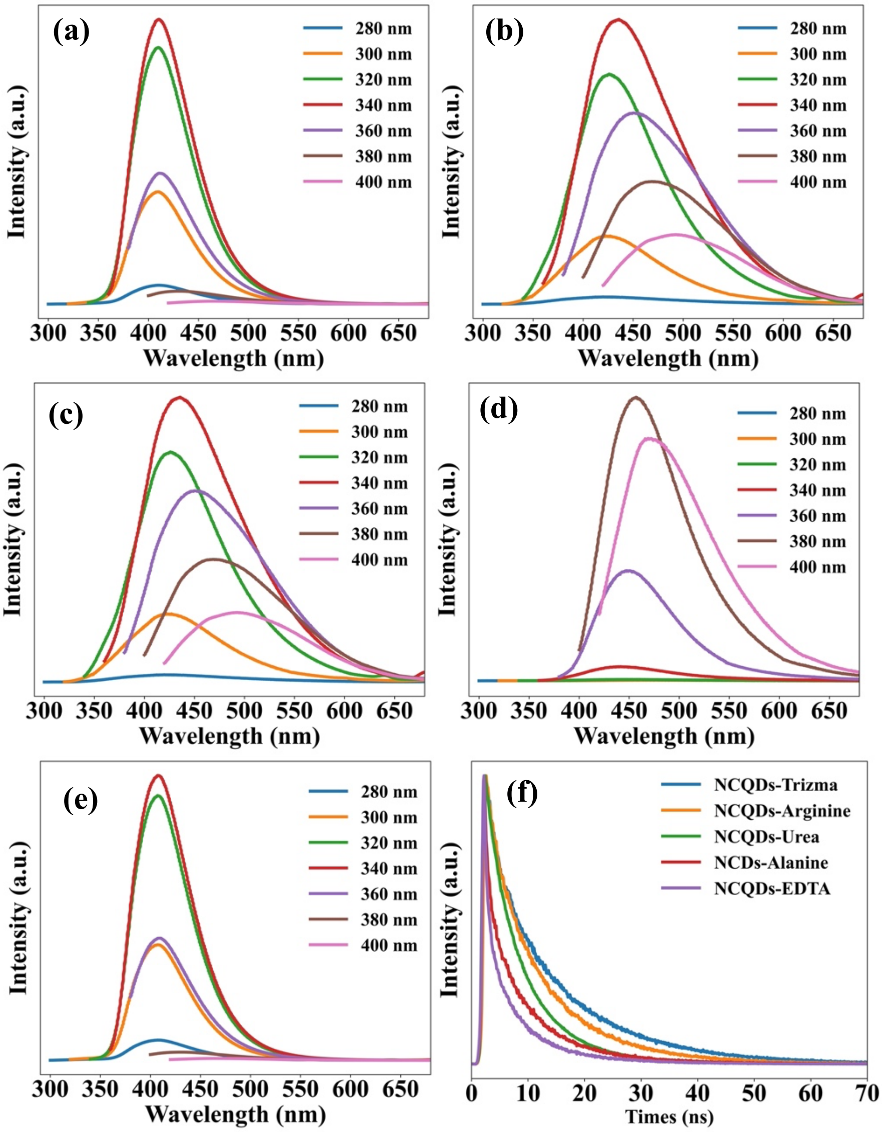

Figure 5.9:Excitation spectrum of: (a)NCQDs-Urea, (b) NCQDs-Alanine, (c) NCQDs-Arginine, (d) NCQDs-EDTA, and (e) NCQDs-Trizma, (f) PL lifetime of the synthesised NCQDs. NCQDs-Urea and Trizma showed rarely observed excitation in-dependent

For further investigation of the effect of different nitrogen dopants on the optical properties of the synthesised NCQDs the photoluminescent quantum yield (PLQY) and PL lifetime of NCQDs were measured. The PL lifetimes data were fitted using mutiexponential decays. The summarised data in Table 3 highlight the significant impact of varying nitrogen precursors on the PLQY results. NCQDs-Trizma demonstrated a high PLQY of 40% representing a significant improvement compared to our previously reported NCQDs.[3,5] On the other hand, NCQDs-Urea showed a PLQY of 14% which is comparable to many other reports of NCQDs.[8] In contrast, NCQDs-Alanine and NCQDs-EDTA exhibited a low PLQY of 1% and 2%, respectively, while the PLQY of NCQD-Arginine showed a PLQY of 5%. These lower PLQY results can be attributed to the large particle size distribution of these materials, causing emitted light from smaller particles to be re-absorbed by the bigger particles.[22]

However, all as-synthesised NCQDs demonstrated comparable PL lifetimes, with NCQDs-Trizma and NCQDs-Arginine displaying PL lifetimes longer than 10 ns, which is rarely observed in carbon quantum dots materials.[23] The computed k_r and k_{nr} rates indicated that NCQDs-Alanine and NCQDs-EDTA possess high non-radiative rates due to the surface defects acting as non-recombination centres, leading to lower PL lifetime and PLQY. These findings reveal the intricate interplay between the nitrogen dopants, particle size distribution, and surface defects in influencing the PLQY and PL lifetime of the NCQDs. By understanding these relationships, we can better tailor the synthesis process and optimize the optical properties of the NCQDs for specific applications.

Table 5.3: The photoluminescence quantum yield (PLQY), PL lifetime of the synthesised NCQDs.

Sample	**PLQY (%)**	**Average lifetime (ns)**	**Radiative k_r (s^{-1})**	**Non-radiative k_{nr} (s^{-1})**	**FWHM (nm)**
NCQDs-Urea	14.0 ± 1.4	7.0 ± 0.7	$1.5x10^7$	$9.1\ x10^7$	70
NCQDs-Alanine	1.0 ± 0.1	8.0 ± 0.8	$1.6\ x10^6$	$1.5\ x10^8$	127
NCQDs-Arginine	5.0 ± 0.5	10.0 ± 1.0	$4.2\ x10^6$	$8.1\ x10^7$	81
NCQDs-EDTA	2.0 ± 0.2	6.5 ± 0.6	$3.0\ x10^6$	$2.0\ x10^8$	97
NCQDs-Trizma	40 ± 4.0	12.6 ± 1.2	$3.5\ x10^7$	$5.2\ x10^7$	67

5.2.3 The effect of nitrogen dopant in the nanoparticle formation of NCQDs

Citric acid (CA) possesses three carboxyl groups and single hydroxyl groups, making it a polyfunctional molecule that can be readily transformed by thermal dehydration, decarboxylation, and cyclization reactions. Under the hydrothermal condition, CA can form five- and six-membered anhydride structures that react readily with alcohols or amines to generate esters, polyesters, amides, and polyamides.[10] Although CA itself is nonfluorescent, it can react with specific amines to produce a diverse range of highly fluorescent compounds.[24]

However, the synthesis of CQDs from CA is highly sensitive to the synthesis conditions, such as decomposition temperature, residence time, and the type of nitrogen source used.[25] The mechanism involved in the nucleation and growth of stable nitrogen-doped carbon quantum dots (NCQD) from citric acid and nitrogen sources is complex and not yet fully understood.[26] The different molecular precursors exhibit varied reactivities, leading to multiple concurrent chemical reactions under supercritical conditions. These complexities in the synthesis process contribute to the diversity in the optical properties and characteristics of NCQDs.

Indeed, the NCQDs synthesised using urea (NCQDs-Urea) and trizma base (NCQDs-Trizma) exhibit uniform particles with a narrow size distribution and excitation-independent fluorescence emission. In contrast, the use of ß-alanine, L-arginine and EDTA resulted in NCQDs with a broader particle size distribution and excitation-dependent fluorescent emission. The particle size distribution plays a critical role in understanding the formation of carbon quantum dots. A narrow size distribution indicates controlled, homogeneous nucleation and growth, while a broader distribution reveals more uneven particle formation kinetics. [27]

During the CHFS process, the use of supercritical water enables the hydrothermal synthesis of carbon quantum dots from citric acid. When an aqueous solution of citric acid is injected into water heated and pressured above 374°C and 22.0 MPa, the tricarboxylic acid rapidly ionizes and hydrolyses into fragments like citraconic and itaconic acids.[28] This generates a multitude of molecular species that recombine into nuclei through esterification and decarboxylation pathways facilitated by the supercritical water. The carbon nanoparticle nuclei derived from citric acid then undergo further growth through polymerisation or carbonization reactions, leading to the formation of π-conjugated carbon core resembling subunits of graphene oxide composed of heterogeneous sp^2 domain.[29] The observed variation in the size of the synthesised nitrogen-doped carbon quantum dots (NCQDs) confirms that the addition of nitrogen-containing precursors modifies the hydrothermal polymerization or carbonization pathway of citric acid. To gain a deeper insight into the effects of the nitrogen precursors, a comparison of the properties of the different nitrogen dopants was conducted listed in **Table 5.4**.

The objective of this comparison is to elucidate the key properties of the nitrogen sources that allow control over nanoparticle sizes and narrow size distribution. The water solubility of precursors significantly impacts nanoparticle formation using supercritical water. Precursors with higher solubility allow more homogeneous dispersal and availability for nanoparticle nucleation.[4,30] This is confirmed in the use of trizma base and urea which have excellent water solubility compared to the other nitrogen dopant precursors. This high solubility allows uniform dispersal and availability of the nitrogen sources during the carbonization process. As a result, the formation of the heterogeneous sp^2 carbon domains occurs more homogeneously and efficiently. Additionally, the alkaline conditions generated by trizma, and urea solutions accelerate the dehydration of citric acid. This faster dehydration kinetics promotes a more rapid carbonization of citric acid.[31] The dependence of nanoparticles size on the water solubility of nitrogen sources is also evident when using ß-alanine, L-arginine and EDTA. The limited water solubility of alanine, arginine and EDTA precursors disrupts the carbonisation process. As a result, the nucleation and growth of the carbon core occur inconsistently, leading to the formation of nanoparticles with a broad size distribution, as illustrated in **Figure 5.3**.

Table 5.4: The chemical and physical properties of different nitrogen sources

Chemical	Molecular weight (g/mol)	Water solubility (g/l)	Decomposition temperature (°C)	pH
Urea	60.06	624.00	160.00	9.5
ß-Alanine	89.09	89.09	202.00	7.5
L-Arginine	174.20	182.00	220.00	8.0
EDTA	412.20	108.00	265.00	7.5
Trizma	121.14	678.00	143.00	10.6

In addition, the differences in the decomposition process of the nitrogen precursors under supercritical water also play a crucial role in causing variations in the structure and properties of the synthesised NCQDs. Citric acid and nitrogen dopants rapidly decompose via decarboxylation, dehydration, polymerisation and carbonization reactions when subjected to continuous hydrothermal flow synthesis.[32] Urea and trizma base decompose at relatively lower temperatures compared to other nitrogen compounds used. Their decomposition temperatures are similar to that of citric acid (at 158 °C).[33] This allows the decomposition processes of citric acid, urea and trizma base to occur concurrently under the same conditions. The well-matched temperatures enable simultaneous carbonization of citric acid and release of nitrogen from urea and trizma for doping during carbon quantum dot formation. Additionally, neither urea nor trizma imparts a strong templating structure directing effect that alters particle formation from the carbonisation of citric acid. The small size of the decomposed units from urea and trizma allows a homogeneous nucleation to produce uniform NCQD particles.[27] In contrast, the smaller mean particles size of the prepared NCQDs-Alanine and NCQDs-Arginine suggest that ß-alanine and L-arginine appear to limit nanoparticle growth. This is due to steric hindrance of bulky groups in alanine and arginine interfere with crystallization and growth of the π-conjugated domains.[34] Additionally, the heterocyclic fragments from L-arginine can distort and limit nanoparticle growth.[35] The freeze-dried NCQD synthesised using ß-alanine and L-arginine displayed a sticky characteristic indicating the presence of polymeric properties. This suggests beta-alanine and L-arginine facilitate formation of short polymer chains that are retained due to incomplete carbonization during NCQD synthesis. The complex polymerization process likely leads to a highly crosslinked polydisperse network structure. This variation in the polymer structure influences the broad nanoparticle size distribution observed for NCQDs prepared with ß-alanine and L-arginine. Recently, other groups also reported about the synthetic polymer-like CQDs using citric acid and amino acids.[36,37] Similarly, EDTA possesses a large molecular weight and high decomposition temperature leading to complex polymerization and incomplete carbonization processes. The intricate molecular structure, coupled with high thermal stability, causes uncontrolled nucleation and growth, yielding non-uniform nanoparticles. As shown in the **Figure 5.3**, the carbon dots synthesised using EDTA display a larger mean particle size and broad size distribution.

In summary, based on characterisation data collected about the morphology and optical properties of the synthesised NCQDs, we propose a mechanism for the conversion of citric acid and nitrogen precursors into fluorescent carbon nanomaterials via CHFS, as illustrated in **Figure 5.10**. The use of urea and trizma promote the crystallization and growth of the carbogenic π-conjugated domains resulting in highly crystallised NCQDs. While the decomposition of nitrogen precursors such as amino acids and EDTA, favours crosslinking and the formation of polymer-based structures indicating that polymerization is the primary reaction pathway. The abundance of functional groups allows for multiple reaction pathways, including esterification, decarboxylation, and condensation reactions, leading to the polymerization and carbonization of the nitrogen precursors. As a result, NCQDs with polymer-like characteristics are synthesised. As shown in **Figure 5.3**, the NCQDs-Urea and NCQDs-Trizma display blue emission under the UV light, and rarely observation of excitation-independent. In contrast, the rest of the prepared NCQDs showed a typical excitation-dependent with the green emission. Additionally, urea and trizma base yielded carbon dots with much higher photoluminescence quantum yields (PLQY) compared to the other nitrogen precursors. In particular, trizma resulted in carbon dots with a PLQY of approximately 40% which is significant improvement compared to our previous reports.[3,4,5]

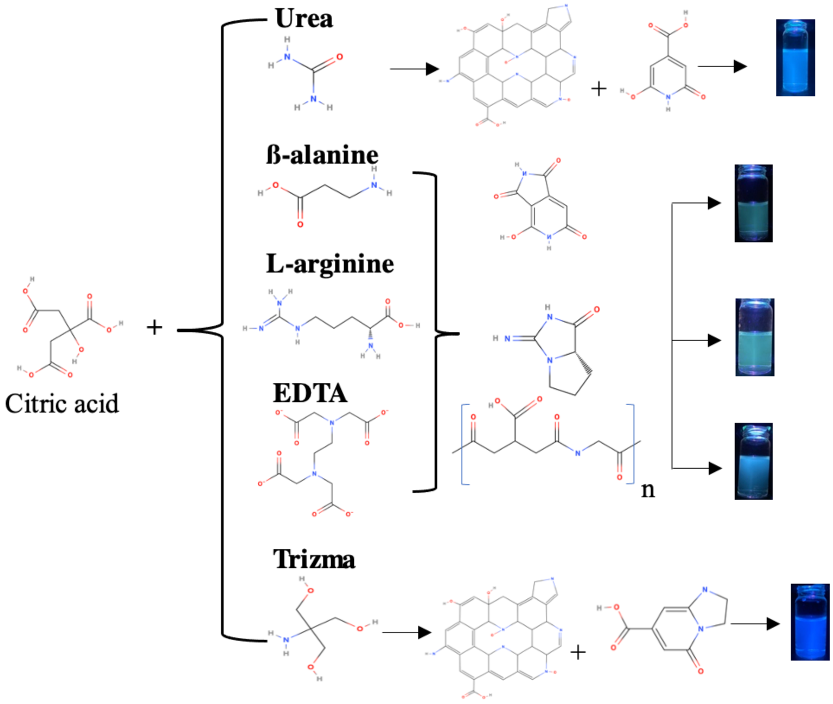

Figure 5.10: The NCQDs formation using different nitrogen precursors via CHFS method. The use of urea and trizma promote the crystallization while the other nitrogen dopants favour the polymerisation

5.2.4 The energy band structure of NCQDs

Ultraviolet photoemission spectroscopy (UPS) is a powerful technique widely employed to investigate the electronic structure and properties of various materials. The work function Φ, a fundamental parameter in materials science, plays a crucial role in determining the energy barrier for electron emission from a material's surface. It can be calculated using the equation 1:

$$\Phi = h\nu - E_k \qquad \text{(Eq.1)}$$

Where: Φ is the work function, h is the Planck constant, ν is the photon energy, and E_k is the kinetic energy of the emitted photoelectrons.[38] By measuring the kinetic energy of emitted electrons, UPS enables the determination of the work function, providing valuable insights into the electron emission properties and surface characteristics of NCQDs. The Fermi level, denoted as E_F, represents the energy level at which electrons have a 50% probability of being occupied at absolute zero temperature. It serves as a reference point for characterizing the energy distribution of electron states within a material. UPS enables the measurement of the

Fermi level by observing the intensity variation of emitted photoelectrons as a function of incident photon energy. The position of the Fermi level provides crucial information about the electronic band structure and charge transport properties.[39] In this study, we utilized UPS to investigate the electronic structure properties of nitrogen-doped carbon quantum dots. By measuring the work function, energy cut-off (E_{cutoff}, and Fermi level), we aim to gain insights into the surface electronic states, charge carrier dynamics, and the influence of nitrogen doping on the electronic properties of NCQDs can be further explored.

The UPS spectra, displayed in **Figure 5.11a** exhibit variations in the measured energy E_{cutoff} of the synthesised nitrogen-doped carbon quantum dots (NCQDs), ranging from 15.37 eV to 15.32 eV. Consequently, the work function (WF) of the NCQDs falls within the range of 5.71 eV to 5.88 eV. Notably, the utilization of different nitrogen dopants results in distinct energy levels within the synthesised NCQDs, indicating varying degrees of surface modification in each sample. The optical bandgap of the synthesised nitrogen-doped carbon quantum dots (NCQDs) was determined using UV-Vis spectroscopy. The absorbance spectra can be seen in Figure 6. The bandgap was calculated using the Tauc plot method,[39] and the results are depicted in Figure 9c, which shows the relationship between $(\alpha h\nu)^2$ and hν (where α is the absorption coefficient and hν is the photon energy). By extrapolating the straight sections of the curves in the short-wavelength region of the spectrum, the bandgap values of the NCQDs were estimated. The Tauc plots revealed that the bandgap of the NCQDs falls within the range of 4.66 eV to 4.94 eV. The energy band structure of the NCQDs is shown in **Figure 5.12**.

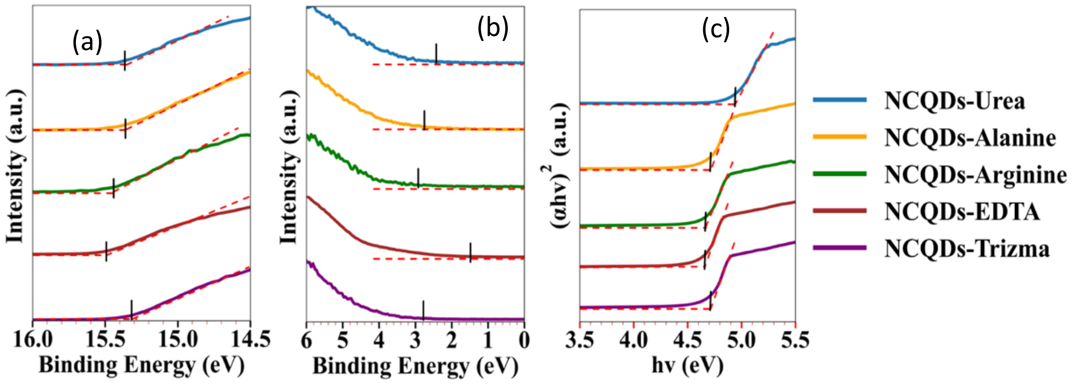

Figure 5.11:The UPS spectra of the NCQDs were used to determine the: (a) work function, (b) valence-band maximum, and (c) Tauc plots of NCQDs providing direct bandgap values.

Hence, the bandgap of the synthesised nitrogen-doped carbon quantum dots (NCQDs) could be tuned by using different nitrogen dopants. The bandgap and energy level structure are influenced by both nanoparticle size and surface functional groups. Notably, NCQDs prepared with urea (NCQDs-Urea) exhibited the largest bandgap at 4.94 eV, which can be attributed to the high content of pyrrolic-N, but a lower amount of protonated pyridinic-N as evidenced by XPS. In contrast, the other synthesised NCQD samples showed similar, smaller bandgap values around 4.70 eV. Additionally, NCQDs-Urea and NCQDs-Trizma displayed higher work functions, which correlates to their higher pyridinic-N content at the NCQD edges. These results obtained from UPS are consistent with the observation in the XPS analysis of the as-synthesised NCQDs.

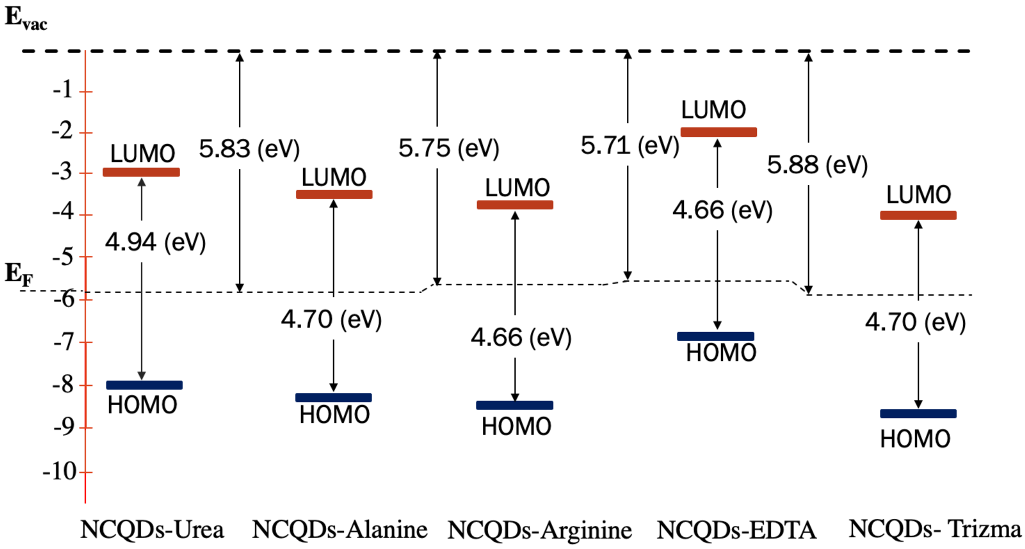

Figure 5.12: The energy band structure of the synthesised NCQDs.

5.3 Conclusion

This study systematically investigated the effects of different nitrogen precursors on optimizing the hydrothermal synthesis process and properties of nitrogen-doped carbon quantum dots (NCQDs). A series of NCQDs was successfully synthesised using citric acid as a carbon source and variations of nitrogen dopants. These NCQDs have proven the capability of the continuous hydrothermal flow synthesis process to simultaneously dope CQDs with nitrogen. A range of characterisations were conducted to investigate the effects of different nitrogen precursors on the nanoparticle formation and properties of the NCQDs, including morphology and chemical functionals. HRTEM analysis revealed that utilizing citric acid as the carbon source, nitrogen dopants like urea and trizma promoted homogeneous formation of NCQDs nanoparticles with higher graphitic crystalline carbon core structures, resulting in narrow particle size distributions. While the use of amino acids or chelating agents yielded heterogeneous nanoparticle sizes of NCQDs, leading to broadened particle size distributions. This finding highlights the importance of precursor reactivity, solubility, and molecular structure on the carbonization process using continuous hydrothermal flow synthesis. Urea and trizma possess high water solubility and similar temperature decomposition profiles to citric acid, which promoted decarboxylation and dehydration of citric acid, enabling good graphitic carbon core formation. In contrast, the amino acids and chelating gent mostly underwent polymerization pathways, yielding polymer-like NCQD structures. These observations from HRTEM analysis are also supported by Raman spectroscopy, with NCQDs-Urea and NCQDs-Trizma having a lower I_D/I_G ratio that confirms a higher quality graphitic carbon core. The FTIR and XPS characterisations revealed the chemical functional groups and composition of the as-synthesised NCQDs. In general, the synthesised NCQDs possess alike functional groups, but NCQDs-Trizma stands out with a distinctly sharp peak related to the vibration of C-O bonding. Also, the XPS analysis indicated the effect of precursors on the configuration of the nitrogen dopant. NCQDs-Alanine uniquely showed a graphitic N doping configuration, while NCQDs-urea and NCQDs-Trizma showed higher contents of pyridinic-N, and these differences resulted in varied optical performance of the synthesised NCQDs. The photoluminescence properties of the synthesised NCQDs are dependent on both particles size and functional groups. The typical excitation-dependent emission was observed in the use of amino acid or chelating agent, while NCQDs-Urea and NCQDs-Trizma showed rarely observed excitation-independent emission with significant quantum yield improvement up to 40%. These outstanding optical properties of NCQDs-Urea and trizma are arise from a uniform particle size with narrow distribution. Furthermore, this study provided the energy band structure of NCQDs which is not often reported, and these values bring benefits for expanding the novel application of NCQDs in electronic applications. Overall, this study provides guidance on selecting suitable nitrogen precursors for optimizing PLQY, controlling particle sizes, and tuning optical properties of NCQDs. It offers mechanistic insights into how precursor chemistry and nitrogen doping influence the carbon core formation, surface states, and photoluminescence. This knowledge will assist in designing appropriate nitrogen precursors for synthesizing tailored NCQDs for diverse applications.

Chapter 5: References

1 S. Yang, Y. Li, L. Chen, H. Wang, L. Shang, P. He, H. Dong, G. Wang and G. Ding, *Small*, 2023, 2205957.

2 K. J. Mintz, Y. Zhou and R. M. Leblanc, *Nanoscale*, 2019, **11**, 4634–4652.

3 I.-A. Baragau, N. P. Power, D. J. Morgan, T. Heil, R. A. Lobo, C. S. Roberts, M.-M. Titirici, S. Dunn and S. Kellici, *J. Mater. Chem. A*, 2020, **8**, 3270–3279.

4 I.-A. Baragau, N. P. Power, D. J. Morgan, R. A. Lobo, M.-M. Titirici, V. Middelkoop, A. Diaz and S. Dunn, *ACS Sustain. Chem. Amp Eng.*, 2021, **9**, 2559–2569.

5 K. G. Nguyen, I.-A. Baragau, R. Gromicova, A. Nicolaev, S. A. J. Thomson, A. Rennie, N. P. Power, M. T. Sajjad and S. Kellici, *Sci. Rep.*, 2022, **12**, 13806.

6 U. Alli, S. J. Hettiarachchi and S. Kellici, *Chem. – Eur. J.*, 2020, **26**, 6447–6460.

7 E. A. Stepanidenko, E. V. Ushakova, A. V. Fedorov and A. L. Rogach, *Nanomaterials*, 2021, **11**, 364.

8 X. Wang, Y. Feng, P. Dong and J. Huang, *Front. Chem.*, 2019, **7**, 671.

9 S. Wu, X. Wang, J. Bai, Y. Zhu, X. Yu, F. Qin, P. He and L. Ren, *Langmuir*, 2022, **38**, 11210–11218.

10 E. O. Miranda, V. H. R. Silva, M. A. Leão, E. C. M. Cabral-Albuquerque, S. Cunha and R. L. Fialho, *IOP Conf. Ser. Mater. Sci. Eng.*, 2020, **958**, 012008.

11 Y. Song, S. Zhu, S. Zhang, Y. Fu, L. Wang, X. Zhao and B. Yang, *J. Mater. Chem. C*, 2015, **3**, 5976–5984.

12 A. Pandey, A. Devkota, Z. Yadegari, K. Dumenyo and A. Taheri, *Nanomaterials*, 2021, **11**, 2012.

13 M. C. Ortega-Liebana, M. M. Encabo-Berzosa, A. Casanova, M. D. Pereboom, J. O. Alda, J. L. Hueso and J. Santamaria, *Chem. – Eur. J.*, 2019, **25**, 5539–5546.

14 D. Qu and Z. Sun, *Mater. Chem. Front.*, 2020, **4**, 400–420.

15 N. Mardirossian and M. Head-Gordon, *J. Chem. Theory Comput.*, 2016, **12**, 4303–4325.

16 S. H. Jin, D. H. Kim, G. H. Jun, S. H. Hong and S. Jeon, *ACS Nano*, 2013, **7**, 1239–1245.

17 S. D. Dsouza, M. Buerkle, P. Brunet, C. Maddi, D. B. Padmanaban, A. Morelli, A. F. Payam, P. Maguire, D. Mariotti and V. Svrcek, *Carbon*, 2021, **183**, 1–11.

18 L. Peplowski, R. Szczesny, L. Skowronski, A. Krupka, V. Smokal and B. Derkowska-Zielinska, *Vib. Spectrosc.*, 2022, **120**, 103377.

19 H. Lin, J. Huang and L. Ding, *J. Nanomater.*, 2019, **2019**, 1–9.

20 N. Papaioannou, A. Marinovic, N. Yoshizawa, A. E. Goode, M. Fay, A. Khlobystov, M.-M. Titirici and A. Sapelkin, *Sci. Rep.*, 2018, **8**, 6559.

21 P. Lazar, R. Mach and M. Otyepka, *J. Phys. Chem. C*, 2019, **123**, 10695–10702.

22 A. Kurzmann, A. Ludwig, A. D. Wieck, A. Lorke and M. Geller, *Nano Lett.*, 2016, **16**, 3367–3372.

23 L. Zhang, X. Yang, Z. Yin and L. Sun, *Luminescence*, 2022, **37**, 1612–1638.

24 J. Schneider, C. J. Reckmeier, Y. Xiong, M. Von Seckendorff, A. S. Susha, P. Kasák and A. L. Rogach, *J. Phys. Chem. C*, 2017, **121**, 2014–2022.

25 R. Ludmerczki, S. Mura, C. M. Carbonaro, I. M. Mandity, M. Carraro, N. Senes, S. Garroni, G. Granozzi, L. Calvillo, S. Marras, L. Malfatti and P. Innocenzi, *Chem. – Eur. J.*, 2019, **25**, 11963–11974.

26 W. Kasprzyk, T. Świergosz, P. P. Romańczyk, J. Feldmann and J. K. Stolarczyk, *Nanoscale*, 2022, **14**, 14368–14384.

27 N. T. K. Thanh, N. Maclean and S. Mahiddine, *Chem. Rev.*, 2014, **114**, 7610–7630.

28 N. Simsek Kus, *Tetrahedron*, 2012, **68**, 949–958.

29 S. Kellici, J. Acord, N. P. Power, D. J. Morgan, T. Heil, P. Coppo, V. Middelkoop, I.-A. Baragau, K. E. Moore and C. L. Raston, *React Chem Eng*, 2018, **3**, 949–958.

30 P. W. Dunne, C. L. Starkey, M. Gimeno-Fabra and E. H. Lester, *Nanoscale*, 2014, **6**, 2406–2418.

31 X. Liu, H.-B. Li, L. Shi, X. Meng, Y. Wang, X. Chen, H. Xu, W. Zhang, X. Fang and T. Ding, *J Mater Chem C*, 2017, **5**, 10302–10312.

32 D. Qu and Z. Sun, *Mater. Chem. Front.*, 2020, **4**, 400–420.

33 P. Wiecinska, *J. Therm. Anal. Calorim.*, 2016, **123**, 1419–1430.

34 T. Morris and T. Zubkov, *Colloids Surf. Physicochem. Eng. Asp.*, 2014, **443**, 439–449.

35 I. M. Weiss, C. Muth, R. Drumm and H. O. K. Kirchner, *BMC Biophys.*, 2018, **11**, 2.

36 A. Kolanowska, G. Dzido, M. Krzywiecki, M. M. Tomczyk, D. Łukowiec, S. Ruczka and S. Boncel, *ACS Omega*, 2022, **7**, 41165–41176.

37 C. Xia, S. Zhu, T. Feng, M. Yang and B. Yang, *Adv. Sci.*, 2019, **6**, 1901316.

38 N. Bhalla, S. Taneja, P. Thakur, P. K. Sharma, D. Mariotti, C. Maddi, O. Ivanova, D. Petrov, A. Sukhachev, I. S. Edelman and A. Thakur, *Nano Lett.*, 2021, **21**, 9780–9788.

39 Y. Yan, J. Chen, N. Li, J. Tian, K. Li, J. Jiang, J. Liu, Q. Tian and P. Chen, *ACS Nano*, 2018, **12**, 3523–3532.

Chapter 6 : Investigating the Effect of N-doping on Carbon Quantum Dots Structure, Optical Properties and Metal Ion Screening

6.1 Motivation

The demand for high-performance CQDs with a wide range of applications, including sensing has been steadily increasing, but the synthesis of CQDs continues to face challenges including high costs, lengthy multistep processes, and the use of hazardous substances.[1,2] Recently, biomass-derived CQDs have attracted considerable attention, and are considered as an optimal and green approach to prepare efficient CQDs. Biomass and biomass waste (agriculture product, agricultural residue, municipal solid waste etc.) are abundant, high in carbon content (45-55%), and are an environmentally friendly renewable resource.[3] Therefore, the utilisation of biomass as carbon resources for nanomaterial synthesis is an eco-friendly process and expected to reduce the total synthetic cost.[4] Although a broad range of biomass materials have been employed in producing CQDs, generally, these synthetic routes faced problems associated with poor control of the CQDs particle size, quality, and homogeneity of the product.[5] In addition, the CQDs synthesised from biomass or biomass waste, commonly possess poor optical properties and a low quantum yield (PLQY). The doping of heteroatom such as (N, P, S) is one of the most common methods to improve the optical properties of biomass-derived CQDs.[6,7] However, the questions related to the origin of the optical improvement with optimised dosing of these heteroatoms still need to be answered. Furthermore, in most conventional methodologies, these doping processes result in a longer synthesis time and higher energy consumption.[8]

In this work, the continuous hydrothermal flow synthesis (CHFS) which is primarily water-based was employed; thus, it is considered the greenest and most promising synthesis method for making CQDs. Notably, the CHFS allows designing or tailoring of the nanoparticles for specific functions based on the nucleation and surface functional processes. The comparison between CHFS and the traditional hydrothermal process revealed that the CHFS consumed less energy and time, while producing a highly homogenous quality product.[9] Moreover, the continuous hydrothermal process can be employed in multi-purposes such as controlling the nucleation to control the particle size and the addition of surfactant coating or dopant without further post-treatments.[10] In this paper, we report the use of CHFS process, to successfully synthesise N-doped carbon quantum dots (NCQDs) from glucose which is an abundant, readily available, cost-efficiently biomass carbon source; and ammonia is used as a nitrogen dopant. Synthesised are a range of NCQDs with different concentrations of ammonia to study the effect of the concentration of nitrogen dopant on the optical properties of CQDs. A range of characterisation techniques was employed to investigate the origin of the optical enhancement. Currently clean water resources are foremost among global challenges facing society today. A significant proportion of the worlds wastewater is disposed untreated in to the environment much of which contain heavy metals as pollutants.[11] Therefore, the application of the prepared NCQDs as chemical sensor to detect chromium (VI) which is carcinogenic, hemotoxic, and genotoxic; the main source being industrial waste water, would be timely. Also, the selectivity and sensitivity of the NCQDs, and the mechanism of quenching behaviour are investigated.

6.2 Results and discussion

The NCQDs samples synthesised from glucose ($C_6H_{12}O_6$) with concentration of 70 mg mL^{-1} and ammonium hydroxide solution (NH_4OH), with varied concentrations (0.25 M, 0.5 M, 0. 75 M, 1.0 M, 2.5 M, 5.0 M, 7.5 M and 10.0 M), were denoted as N-0.25, N-0.5, N-0.75, N-1, N-2.5, N-5, N-7.5, and N-10, respectively; g-CQDs was synthesised from the same source (glucose) but without nitrogen doping.

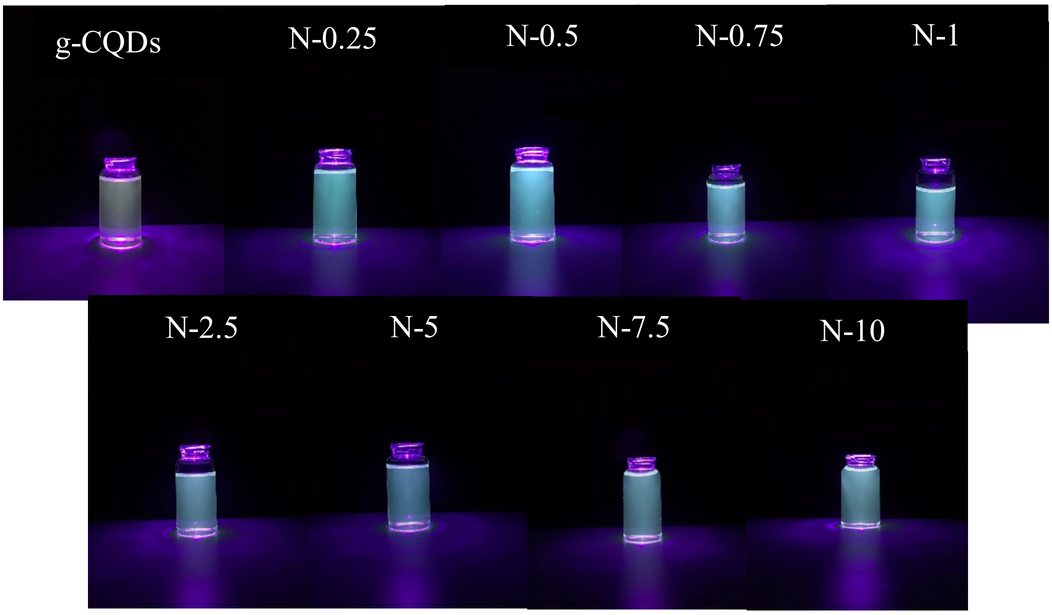

Figure 6.1: Photos of the synthesised g-CQDs and NCQDs in water under UV light. The synthesised NCQDs showed a blue shifter in emission colours compare to the pure CQDs synthesised from glucose

To investigate the morphology of the as-synthesised NCQDs and to identify the effect of dopant concentration on the formation of nanoparticles, high-resolution transmission electron microscopy (HRTEM) was conducted. HRTEM images of NCQDs are provided in Figure 6.2, showing that the as-synthesised NCQDs are round in shape with a crystalline structure, as indicated by the graphite lattice d-spacing of 0.22 nm (**Figure 6.2d**).[12]

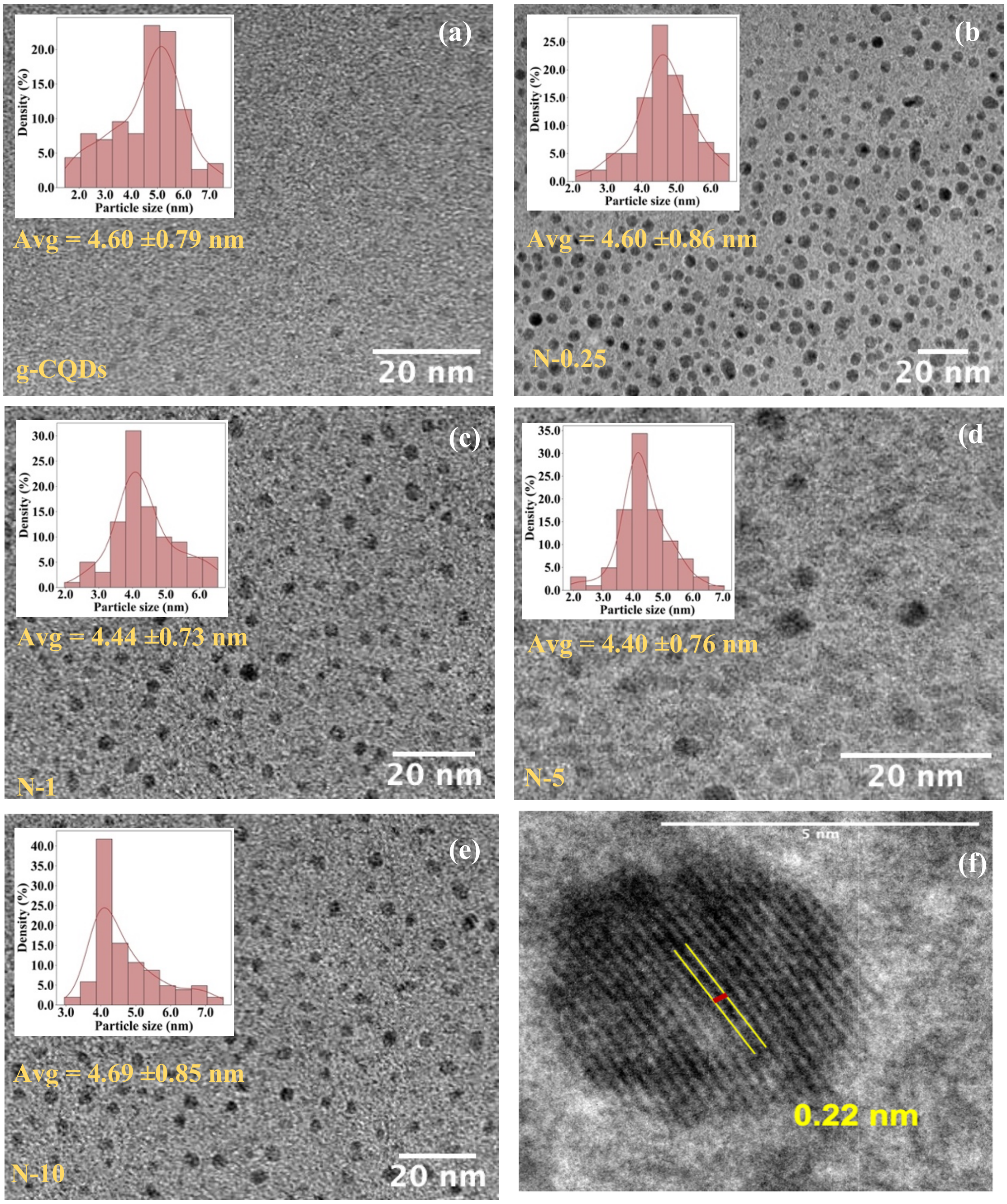

Figure 6.2: HRTEM images of CQD and NCQDs samples: (a) g-CQDs, (b) N-0.25, (b) N-1, (d) N-5, (e) N=10 and (f) graphitic core lattice. The analysis of HRTEM including the mean particles size and distribution histogram is inserted in each image of representative sample

As illustrated in **Figure 6.2**, the HRTEM image analysis of a sample of 150 NCQDs nanoparticles revealed the mean particle size and distribution histogram of the synthesised NCQDs nanoparticles. The use of ammonia solution showed a negligible impact on the average particle size of the as-synthesised NCQDs nanoparticles compared to pure CQDs nanoparticles. For instance, the average particle size of the g-CQDs sample is 4.60 ± 0.79 nm and it changed to 4.69 ± 0.85 nm for the N-10 sample. However, the distribution histogram revealed the mode of the nanoparticle size shifted to smaller sizes with the use of higher concentrations of ammonia solution, and the reason for this could be related to the higher ratio between carbon and nitrogen sources during the synthetic process. The variation in the nanoparticle population affected the emission properties of the synthesised NCQDs which will be discussed further in the following section.

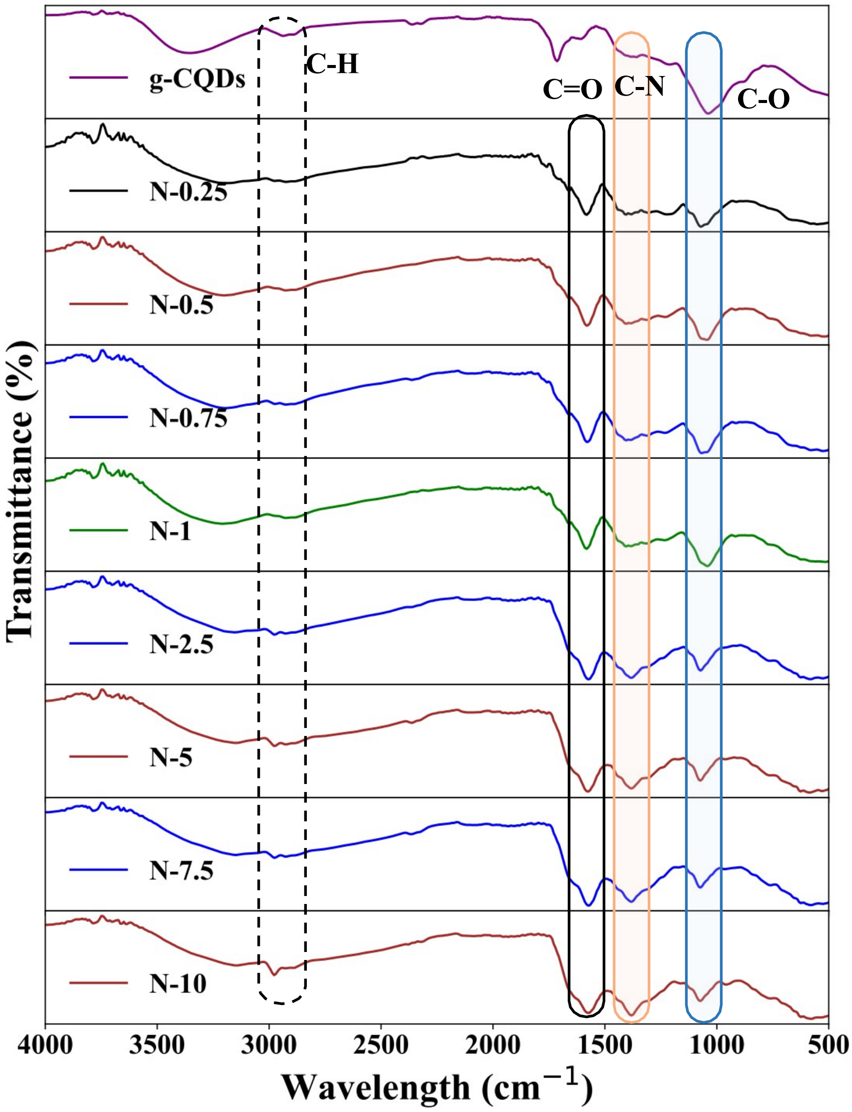

Figure 6.3: FTIR spectra of NCQDs with a lower concentration of ammonia (from N-0.25) and higher concentration of ammonia (N-10)

To determine the nature of the functionalization, the synthesised NCQDs were investigated using the Fourier transform infrared (FTIR) spectroscopy. The FTIR spectra **Figure 6.3** showed that the synthesised NCQDs from different concentration of nitrogen dopant possess common peaks revealing abundant hydrophilic groups on their surface such as O-H (hydroxyl) corresponding to the peak at 3389 cm^{-1} and N-H (3263 cm^{-1}), thus confirming their good solubility in the water. In addition, vibrations of C-H (2950 cm^{-1}), C=O (1581 cm^{-1}), C-N (1435 cm^{-1}) and C-O (1080 cm^{-1}) bonds were also observed in the synthesised sample.[13,14,15] Interestingly, the FTIR spectra of g-CQDs showed a sharp peak at 1720 cm^{-1} corresponding to the vibration of the C=O bond in the carboxylic group, but this peak is absent and shifted to lower energy at 1581 cm^{-1} in the FTIR spectra of the synthesised NCQDs. This peak shift indicates that the C=O bonds present in the synthesised NCQDs are from the carboxylate groups.[16] The comparison of the FTIR spectra of the samples showed that with increasing N-doping (ammonia hydroxide solution concentration, from N-0.25 to N-10) displayed a diminishing stretch in vibration for C-O bond at 1080 cm^{-1}. While the group of samples with a higher concentration of ammonia hydroxide solution (N-2.5 to N-10) showed a sharp vibration of C-N bond at 1435 cm^{-1}. These findings indicate the effect of nitrogen dopant concentration on modifying the functional groups of the synthesised NCQDs.

To achieve a deeper understanding of the surface characterisation of the NCQDs and to investigate the chemical composition of NCQDs, X-ray photoelectron spectroscopy (XPS) was employed. The resultant XPS spectra are shown in **Figure 6.4**. The spectra were fitted with Voigt functions (combination of Lorentzian and Gaussian) with a distinct inelastic background for each component. The XPS spectrum of the NCQDs displays three typical peaks C1s (285.0 eV), N1s (399.0 eV), and O1s (531.0 eV).

Table 6.1:XPS data analyses of the elemental composition of NCQDs

Sample	**Elemental composition (%)**			**N:C ratio**	**C:O ratio**
	Carbon	Oxygen	Nitrogen		
g-CQDs	69.78	30.22	-	-	2.3
N-0.25	71.06	20.11	8.82	0.1	3.5
N-0.5	71.31	20.02	8.66	0.1	3.6
N-0.75	76.11	16.3	7.57	0.1	4.7
N-1	68.66	24.13	7.19	0.1	2.9
N-2.5	61.8	29.6	9.22	0.2	2.0
N-5	67.41	19.89	12.69	0.2	3.4
N-7.5	59.39	28.96	11.74	0.2	2.1
N-10	57.9	31.16	10.94	0.2	1.9

The XPS elemental composition analysis of the synthesised NCQDs is presented in **Table 6.1**, revealing a declining trend in the C content observed in the NCQDs synthesised using higher concentrations of ammonium hydroxide solution. For instance, the C content of sample N-0.25 is 71.06%, while sample N-10 possesses 57.9% of C. This indicates that the carbonization process of the carbon precursor can be tailored by adjusting the concentrations of nitrogen dopants.

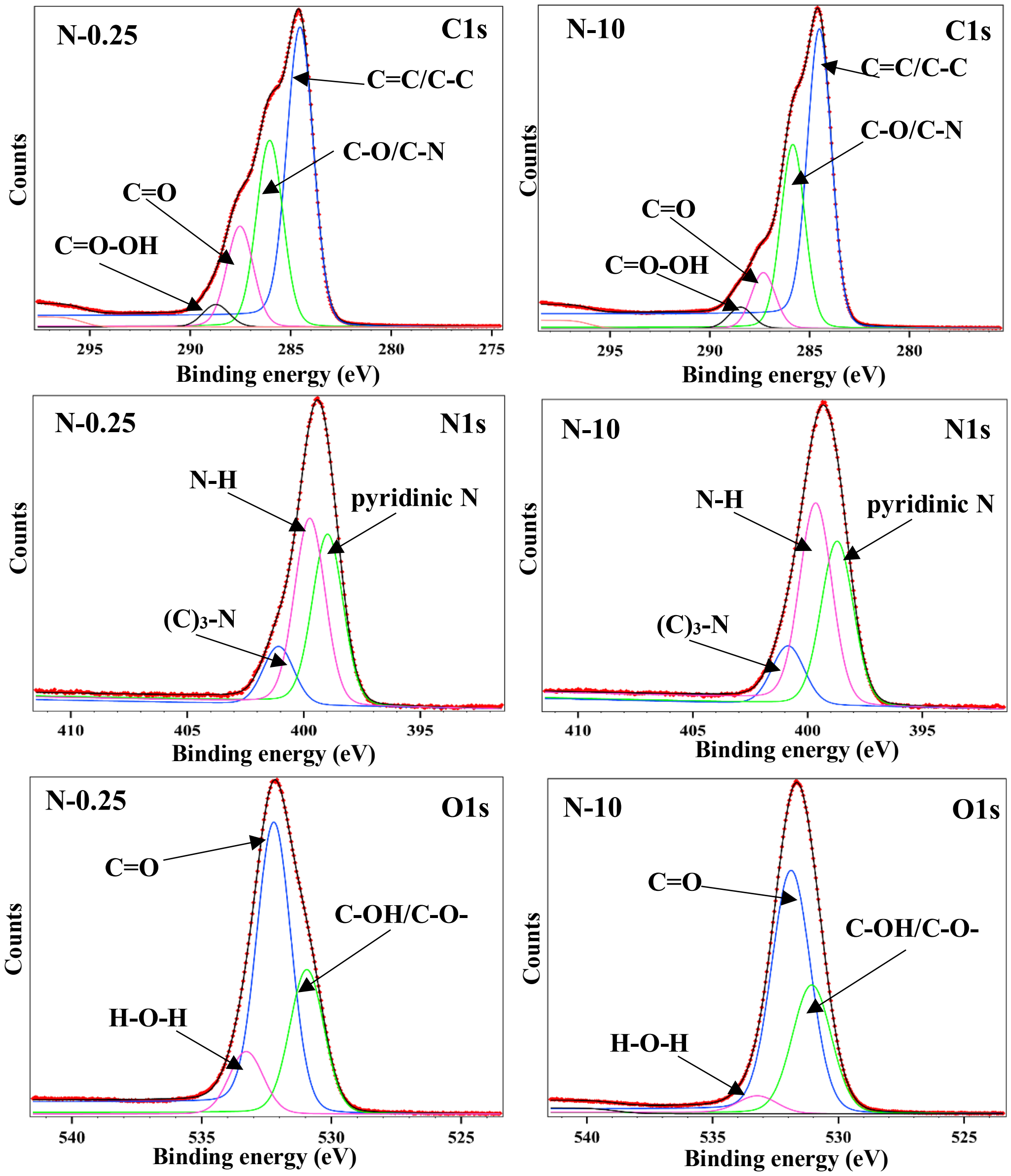

Figure 6.4; Representative XPS spectra of NCQDs showing the lowest (N-0.25) and highest (N-10) nitrogen doped samples. The spectra display three typical peaks C1s (285.0 eV), N1s (399.0 eV), and O1s (531.0 eV). The deconvoluted N1s band showed three peaks representing pyridinic N, N-H and amide C-N

The lower content of C observed in the synthesised NCQDs using higher concentrations of nitrogen dopants is consistent with the results obtained from TEM analysis, which indicated that the use of higher concentration of nitrogen dopant produced smaller particles observed in the sample. Furthermore, this elemental analysis data agrees with the FT-IR results, which revealed a lower intensity of C-O bonds in the synthesised NCQDs using higher concentrations of ammonia solutions. Meanwhile, the content of nitrogen in the as-synthesised NCQDs is not dependent on the concentration of nitrogen dopants used in the synthetic process. The highest N content of 12.69 % is observed in the sample N-5 which is slightly reduced to 10.94% in the case of sample N-10. To elucidate the nitrogen doping mechanism, the XPS spectra are deconvoluted to have a deeper understating of the surface functional groups and nitrogen doping configuration.

The fitted C1s spectrum was deconvoluted into four components, corresponding to carbon in form of C=C/C-C bonds (~ 284.4 eV), C-O/C-N (~285.8 eV), C=O (~287.3) and O=C-OH (~288.4 eV).[17] The O1s region contains three peaks at 530.9 eV, 532.2 eV and 533.3 eV for C-OH/C-O-C, C=O, H-O-H, respectively.[18] These finding chemical bonds from XPS are consistent with the observation mentioned in the FT-IR analysis.

Table 6.2: The XPS N1s elemental composition and N1s species content in each NCQDs sample

Sample	**Nitrogen content (at%)**	**Elemental composition N (1s)**					
		Pyridinic		**Pyrrolic**		**Graphitic**	
		at %	%	at %	%	at %	%
N-0.25	8.82	3.62	41.03	4.00	44.92	1.24	14.05
N-0.5	8.66	3.46	39.92	4.00	45.53	1.26	14.55
N-0.75	7.57	4.66	61.50	2.40	31.7	0.52	6.80
N-1	7.19	3.04	42.25	2.80	39.15	1.34	18.6
N-2.5	9.22	3.26	35.38	4.50	49.00	1.45	15.72
N-5	12.69	4.64	36.53	6.20	48.70	1.87	14.77
N-7.5	11.74	4.14	34.85	6.00	50.25	1.77	14.91
N-10	10.94	1.51	38.90	5.20	47.24	1.51	13.86

Whilst the deconvolution of N1s spectrum showed three peaks after deconvolution which are 398.8 eV, 399.6 eV and 400.8 eV, representing pyridinic-N, pyrrolic-N and graphitic–N, respectively.[19] As commonly reported, the fluorescent property of CQDs can be enhanced by using nitrogen doping yet only the nitrogen bonded to carbon core can improve the emission.[20]

Therefore, the effectiveness of nitrogen doping in improving the photoluminescence properties of nanocrystal quantum dots (NCQDs) depends on the specific nitrogen doping configuration within the synthesised NCQD sample. The detail of nitrogen doping species observed in the synthesised NCQDs are summarised in **Table 6.2**. In addition, the emission property of NCQDs is influenced by the quality of graphitic carbon core. Highly crystalline, sp^2 hybridized carbon networks exhibit enhanced optical emission intensities compared to NCQDs with amorphous or less graphitic carbon cores.[22] Raman spectroscopy was employed to investigate the disorder in the carbon bonding arrangement of NCQDs.

The Raman spectra (**Figure 6.5)** of the NCQDs exhibited typical graphitic features consisting of the D mode (at 1368 cm^{-1}), related to symmetry transformation by the defects, and the G band (at 1586 cm^{-1}), which is assigned to the graphitic core - sp^2 (graphite-like) bonds. This is not surprising as the HRTEM images of NCQDs showed a typical lattice spacing of graphite illustrated in **Figure 6.2 d.** When comparing the Raman spectra between NCQDs, at first glance, those spectra look similar, a common ratio I_D/I_G of 0.95 revealed a balance between the sp^2 and sp^3 bonds in the NCQDs structure. This is different from g-CQDs where an I_D/I_G ratio of 0.83 was observed and assigned the carbon core (sp^2 bonds).[23] This is probably attributed to the changes introduced by the nitrogen doping resulting in the transformation of C-C (sp^2 bonds) into the sp^3 bonding between N, O and C.

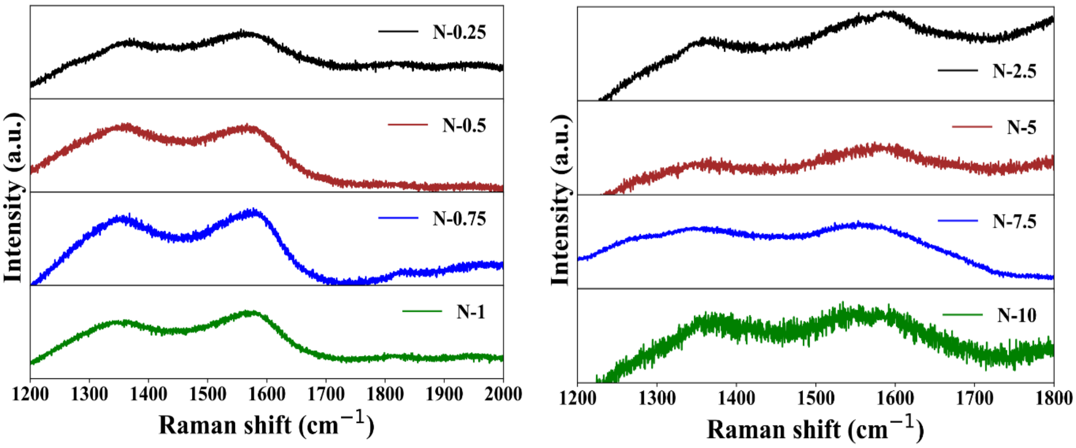

Figure 6.5: Raman spectra of NCQDs with different nitrogen doping showing typical graphitic features consisting of the D mode (at 1368 cm-1), related to symmetry transformation by the defects, and the G band (at 1586 cm-1), which is assigned to the graphitic core-sp2 (graphite-like) bonds

To investigate the optical properties of the synthesised NCQDs, the absorption spectra of the as-prepared NCQDs were first measured using UV-Vis absorption spectroscopy and absorption spectra are shown in **Figure 6.6**.

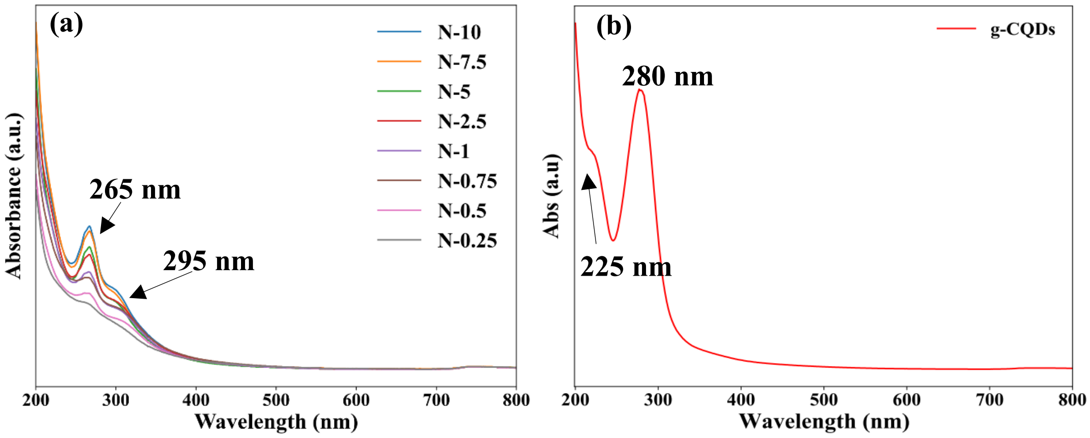

Figure 6.6: UV-Vis absorption spectra of (a) NCQDs and (b) g-CQDs without nitrogen doping. The presence of C-N/C=N bonds is observed at 295 nm.

For comparison, the absorption spectrum of CQDs without nitrogen doping was also measured **(Figure 6.6b)**. The NCQDs samples have a strong peak around 265 nm and a shoulder around 295 nm (**Figure 6.6a**). The 265 nm absorption peak can be assigned to π-π* transitions of the graphitic core (C=C or C-C) of sp^2 domains present in the sp^3 matrix, and the 295 nm can be attributed to both transitions n-π* for C=O and the transitions of the conjugated C-N/C=N bonds.[24, 25]

Table 6.3: The ratio between I_{265} and I_{295}, where I_{265} is the intensity at the peak centred at 265nm and I_{295} is the intensity centred at peak 295nm

Sample	I_{265}/I_{295}
N-0.25	1.2
N-0.5	1.4
N-0.75	1.4
N-1	1.5
N-2.5	1.5
N-5	1.6
N-7.5	1.7
N-10	1.7

However, in the UV-visible absorption spectra of the synthesised NCQDs, the intensity of the peak centred at 265 nm becomes more pronounced and predominant compared to the peak at 295 nm with increasing nitrogen dopant concentration during synthesis (as quantified in **Table**

6.3). This inversion in the relative intensities of the 265 nm and 295 nm absorbance peaks can be attributed to the distinction in the particle size distribution. As mentioned, TEM analysis has shown that using higher concentration of nitrogen dopant resulted in the synthesised NCQDs possessing more smaller nanoparticles. Since greater proportion of smaller NCQDs within the sample leads to the enhancement of the 265 nm peak associated with higher energy absorption by these smaller nanoparticles.[26] The absorption peaks in the case of NCQDs are red-shifted compared to g-CQDs (synthesised from the same source glucose but without nitrogen doping), **Figure 6b** which are observed at 225 nm (π-π^* of the graphitic core), and 280 nm (the n-π^* transitions for C=O).[23] Therefore, the absorption peak observed at 295 nm in the case of the NCQDs is due to the formation of the C-N/C=N bonds and can be related to the electron-doping effect caused by the presence of graphitic nitrogen.[27,28]

The photoluminescence (PL) spectra of as-prepared NCQDs were measured using a range of different excitation wavelengths as shown in **Figure 6.7**. The PL emission of each sample clearly showed the excitation-dependent PL which can be beneficial for a broad range of applications such as biosensors, bio-images, or LED devices.[29,30] The PL emission peaks shifted when different excitation wavelengths were applied, and each sample exhibited an optimal excitation wavelength **(Figure 6.7)**. Overall, the PL study revealed the interesting optical properties of the NCQDs. Firstly, the PL results are consistent with previous reports where the excitation dependent emission phenomenon of CQDs was observed. [31] Secondly, the maximum emission wavelengths shift from 360 nm to 320 nm as the concentration of ammonia solution was increased. This blue-shifted in the maximum emission wavelength of the synthesised NCQDs can be attributed to the greater population of smaller nanoparticle size resulted in a shorter wavelength emission.[31]

However, the mechanisms behind the excitation dependent properties of CQDs is not clear. One of the most comprehensive and broadly accepted mechanism in interpreting the excitation-dependent PL of the CQDs is the quantum confinement effect also known as the size effect.[14,21,32,33] In general, the CQDs possess broad particle size distributions which leads to a range of different energy gaps and is the reason for the variation of emission wavelengths.[34,35] Aside from the quantum confinement effect, surface states theory is rather broadly adopted to interpret the excitation-dependent PL behaviour of CQDs.[36,37,38] UV–Vis absorbance showed that the peak of the NCQDs at 265 nm is related to the π–π^* transition, which suggests the presence of a large number of π-electrons. The surface electronic states can conjugate with these π-electrons due to the surface oxidation, resulting in the modification of the electronic structure of the NCQDs.[37,39]

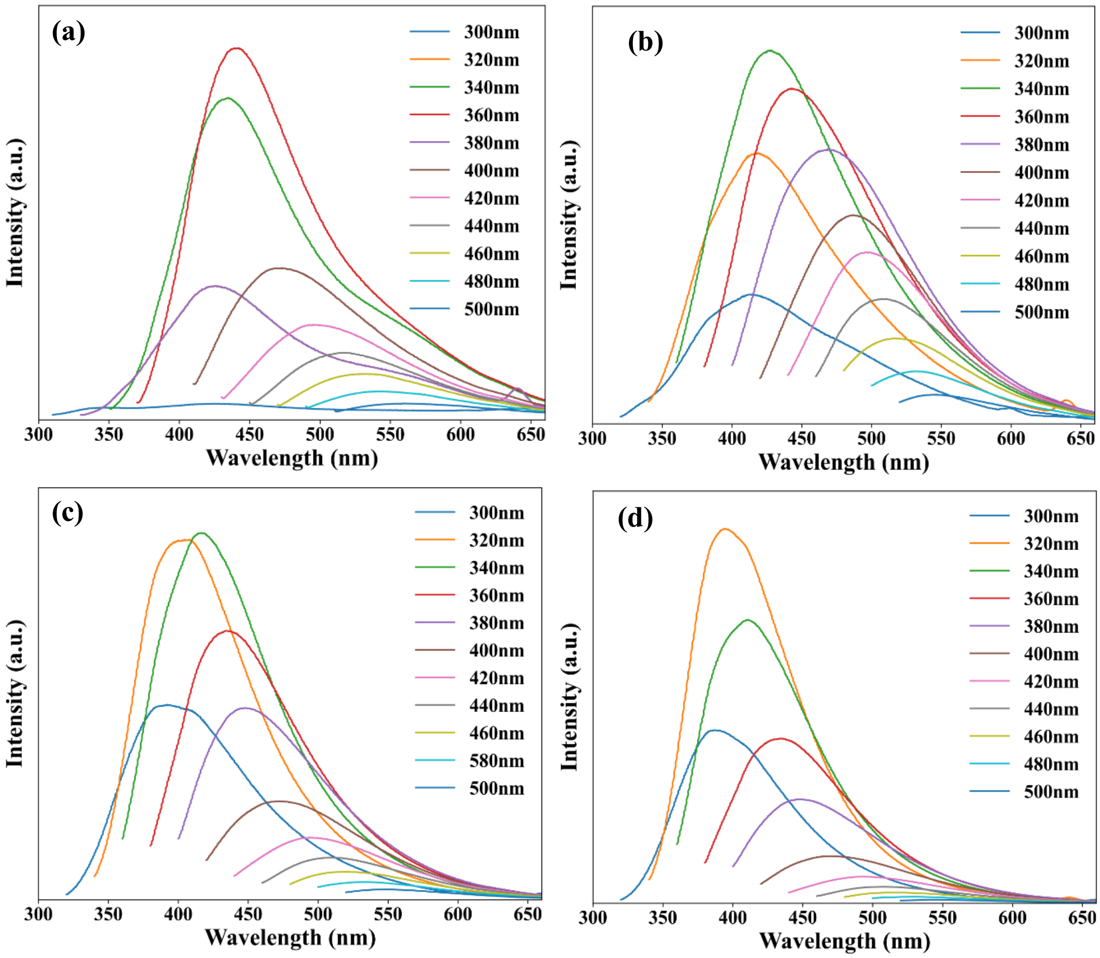

Figure 6.7: Photoluminescence spectra of CQD with and without nitrogen doping measured using excitation wavelengths in the range of 300 to 500 nm, (a) g-CQDs (without nitrogen doping); (b) N-0.25; (c) N-2.5, (d) N-10

To interpret the mechanism of this effect, the PL lifetime and photoluminescence quantum yield (PLQY) of NCQDs were measured. The obtained results (**Table 6.4**) showed an increase in both PL lifetime and PLQY upon nitrogen doping and the highest values of lifetime and PLQY were obtained for $[N] \geq 7.5\ M$. The obtained PLQY value of 9.6 ± 0.9 % for N-10 is significantly higher compared to g-CQDs which showed PLQY of <1%.[23]

The radiative rate (k_r) and non-radiative rate (k_{nr}) were calculated by using the equation (1) and (2) below.[40]

$$k_r = \frac{\Phi}{\tau_{1/e}} \qquad (eq. 1) \qquad\qquad \Phi = \frac{k_r}{k_r + k_{nr}} \qquad (eq. 2)$$

Where Φ is PLQY of NCQDS and $\tau_{1/e}$ corresponds to the lifetime when fluorescence drops 1/e of its initial value.

Table 6.4: The photoluminescence quantum yield (PLQY), average lifetime, radiative (kr) and non-radiative (k_{nr})

Sample	PLQY (%)	Average lifetime (ns)	$\tau_{1/e}$ (ns)	Radiative k_r (s^{-1})	Non-radiative k_{nr} (s^{-1})
g-CQDs	0.7±0.07	4.7±0.5	2.59	$2.7x10^6$	$3.8x10^8$
N-0.25	6.4±0.6	4.8±0.5	2.59	$2.5x10^7$	$3.6x10^8$
N-0.5	6.6±0.7	5.4±0.5	2.98	$2.2x10^7$	$3.1x10^8$
N-0.75	6.6±0.7	5.7±0.6	3.03	$2.2x10^7$	$3.1x10^8$
N-1	6.4±0.6	6.3±0.6	3.27	$2.0x10^7$	$2.9x10^8$
N-2.5	6.7±0.7	6.6±0.7	3.52	$1.9x10^7$	$2.6x10^8$
N-5	7.4±0.7	6.7±0.7	3.81	$1.9x10^7$	$2.4x10^8$
N-7.5	9.3±0.9	6.7±0.7	3.81	$2.4x10^7$	$2.4x10^8$
N-10	9.6±0.9	6.5±0.7	4.69	$2.0x10^7$	$1.9x10^8$

Table 6.4 shows that when a higher concentration of ammonia was used, the non-radiative rates significantly rapidly reduced. This is due to surface coating activities of the nitrogen functional group resulting in enhanced PLQY.[41] In addition, the lower non-radiative constant suggested that NCQDs possess an efficient recombination process which led to an observation of nanosecond scale PL lifetime. These recombination processes suggested strong coupling of excited core states with the surface state. Thus confirming that the π-electron systems affect the surface electronic state leading to the modification of the overall electronic structure of NCQDs. [39,42]

The stability of CQDs for a broad pH range of is essential for sensing applications. Therefore, PL of the NCQDs in pH solution was measured to establish the relationship between the pH level and the emission intensity. NCQDs showed fluorescence stability in a broad pH range from 2 to 11 **(Figure 6.9)**. For example, the fluorescence intensity of sample N-0.25 (**Figure 6.9a**) was dramatically reduced by ~60% at pH = 1, ~35% at pH =12 and ~ 40% at pH = 13; and there were slight decreases at pH = 11 of ~12%. The diminishing fluorescent intensity behaviour of NCQDs in strongly acidic and alkali media can be related to protonation/deprotonation of the surface functional groups causing surface charge disruption.[13]

Whilst H-bonding is eliminated by deprotonation in basic conditions which can cause irregular energy levels resulting in the reduction of the NCQDs fluorescence.[43] In addition, H^+ can introduce surface defects on CQDs by breaking the passivated OH^- shell resulting in PL decreasing and a redshifted spectrum.[44] Indeed, as shown in **Figure 6.9b,** a slight 20 nm red shift was also observed for the NCQDS in the strong acidic condition (pH=1). We have previously assigned this to the prominent emissions deriving from the graphitic core.[10]

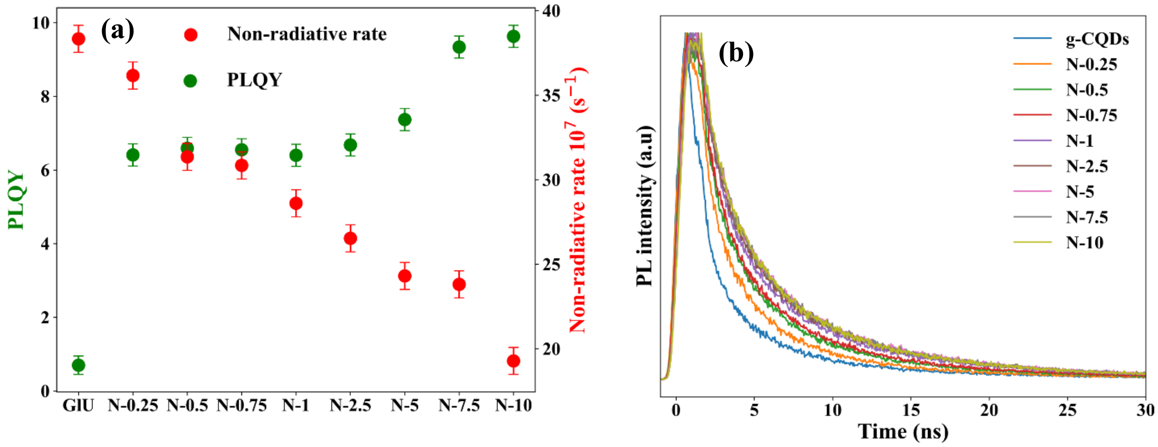

Figure 6.8: (a) PLQY and non-radiative rate (key GIU = g-CQDs), (b) PL lifetime of NCQDs. The analysis revealed an increase in both PL lifetime and PLQY upon nitrogen doping and the highest values of lifetime and PLQY were obtained for [N]≥7.5M

The NCQDs were investigated for ion-sensing applications for a series of cations and anions including chromium (VI) ion ($CrO_4^{2-}/Cr_2O_7^{2-}$) which is a major anthropogenic pollutant in industrial waste water and soils.[45] The obtained results indicated that NCQDs are highly sensitive and showed high selectivity to hexavalent chromium in comparison to a series of other cations and anions as shown in **Figure 6.10**. To identify the sensitivity, limits of detection (LOD) and limits of quantification (LOQ) of NCQDs were determined from measurement of the fluorescent emission quenching as a function of Cr (VI) concentration **(Figure 6.11a and 6.11b).** The reduction of emission intensity indicated a linear dependence for the respective increase in concentrations of Cr (VI) (**Figure 6.11c**) and was fitted with a linear equation $y = mx + c$, where slope m gives the value of quenching constant K_{sv} and c is the intercept. The LOD and LOQ were calculated using equations LOD = $3\sigma/K_{sv}$, LOQ = $10\sigma/K_s$, respectively, where σ is the standard error of the intercept from the Stem-Volmer graph, data for all the samples are shown in **Figure 6.12**. The plotted Stern-Volmer graph for N-10 in **Figure 6.11c** showed a correlation between the concentration of Cr (VI) and the change fluorescent intensity. The data was fitted with y = 0.0238x+0.026 (R^2= 0.9999) which gave a quenching constant value of K$_{sv}$ = 0. 0238. The LOD of 0.955 ppm and LOQ of 3.182 ppm were obtained with a standard error of the intercept of 0.0076 and K$_{sv}$ = 0. 0238. These results showed a significant improvement compared to previously reported result[10] (LOD = 3.62 ppm, LOQ = 11.6 ppm) for CQDs, which was synthesised using the same carbon source, glucose with the same concentration and conditions. This improvement can be related to the enhanced fluorescence intensity of NCQDs as a result of N-doping. To understand the quenching mechanism, the change in PL lifetime of NCQDs in various ion solutions were studied as shown in **Figure 6.11d**.

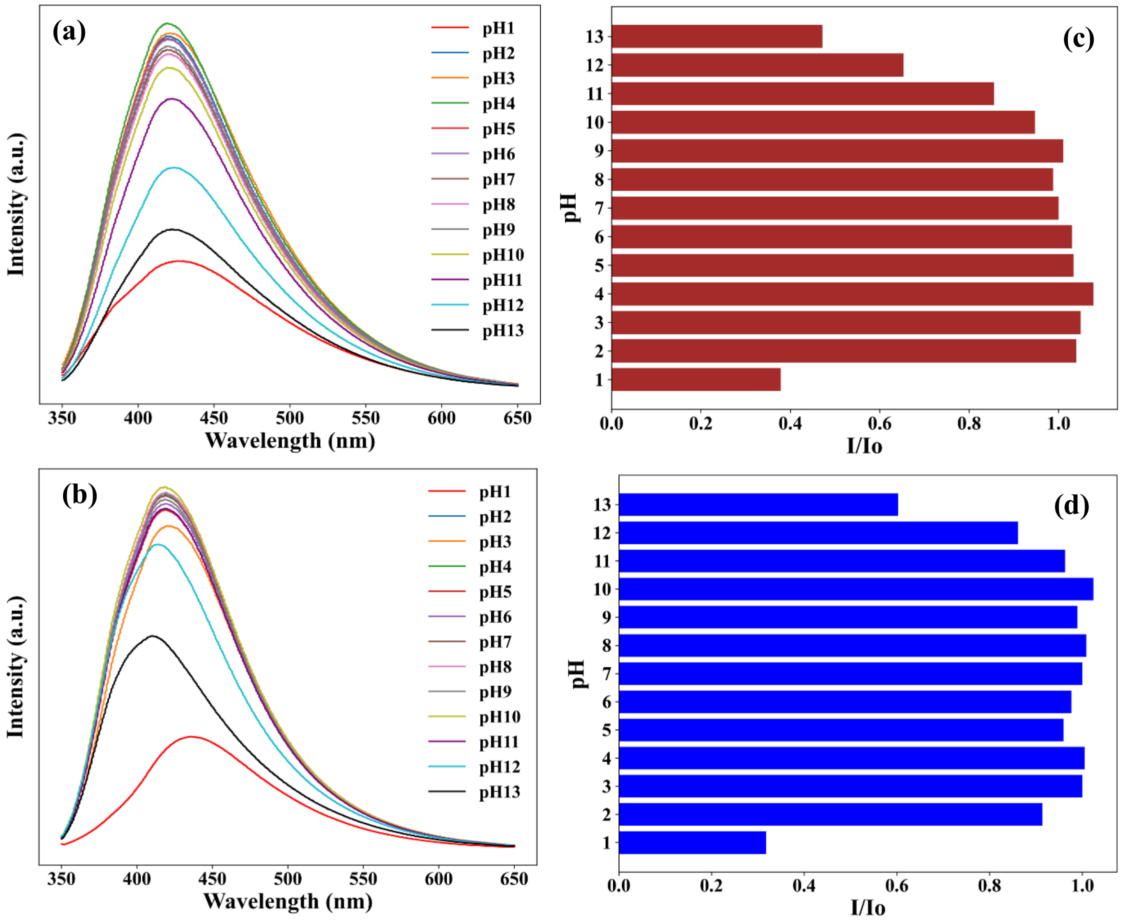

Figure 6.9:pH effect on the emission intensity of NCQDs representative samples selected to show the highest and lowest [N] doping levels: (a) N-0.25, (b) N-10 and data represented in histogram format: (c) N-0.25, (d) N-10

The plotted Stern-Volmer graph for N-10 in **Figure 6.11c** showed a correlation between the concentration of Cr (VI) and the change fluorescent intensity. The data was fitted with $y = 0.0238x+0.026$ (R^2= 0.9999) which gave a quenching constant value of K$_{sv}$ = 0. 0238. The LOD of 0.955 ppm and LOQ of 3.182 ppm were obtained with a standard error of the intercept of 0.0076 and K$_{sv}$ = 0. 0238. These results showed a significant improvement compared to previously reported result[10] (LOD = 3.62 ppm, LOQ = 11.6 ppm) for CQDs, which was synthesised using the same carbon source, glucose with the same concentration and conditions. This improvement can be related to the enhanced fluorescence intensity of NCQDs because of N-doping. To understand the quenching mechanism, the change in PL lifetime of NCQDs in various ion solutions were studied (shown in **Figure 6.12d**).

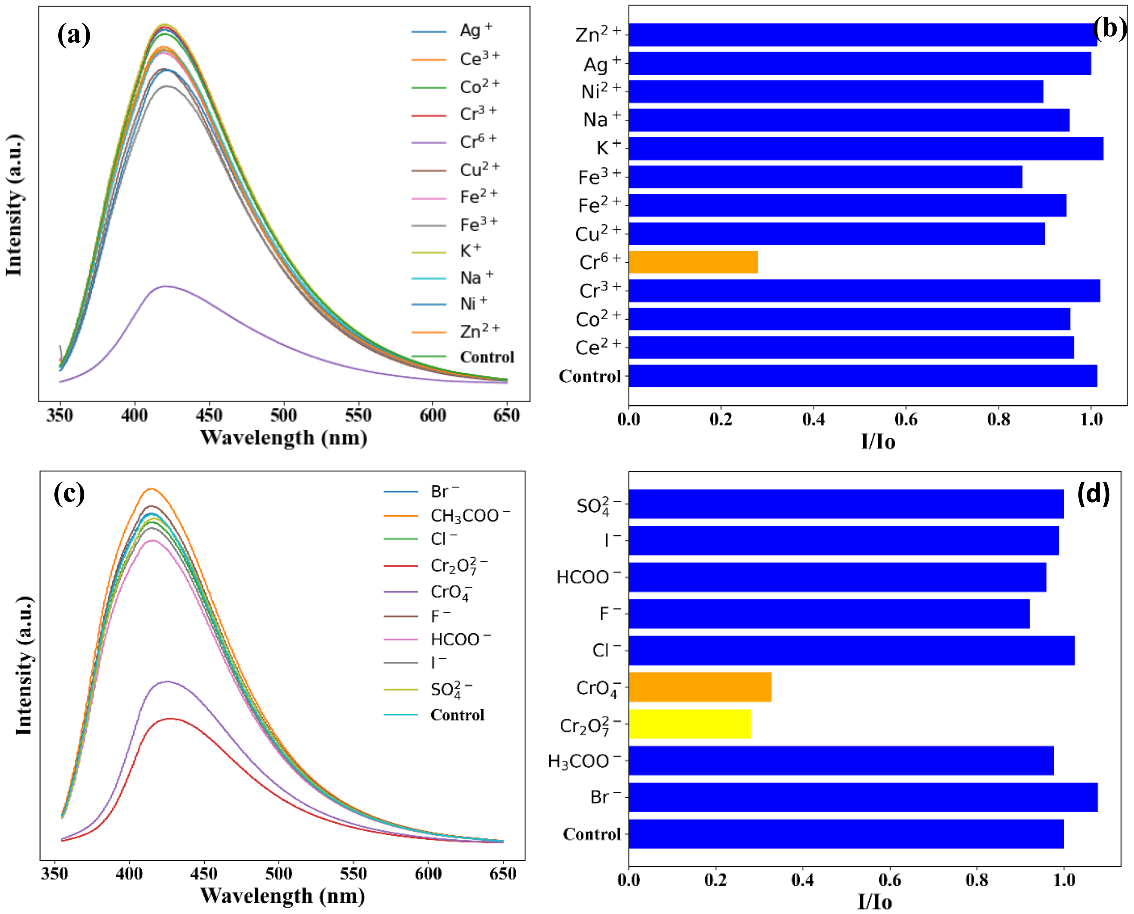

Figure 6.10: (a-b) Selectivity of the NCQDs based chemo-sensor over other ions and (c-d)

The mechanism for this fluorescence quenching behaviour in the presence of Cr (VI) can be assigned to Inner Filter Effect (IFE) which is a physical phenomenon that occurs in a sensing system when the absorption spectrum of the absorber has an overlap with that of excitation and/or emission of the fluorescence leading to the reduced fluorescent emission intensity.[13] The IFE quenching is not related to the radiative and non-radiative transitions in the CQD, thus the intrinsic fluorescence emission is not changed in the presence of the quencher molecule.[46] As illustrated in Figure 6.12a, the NCQDs excitation and emission bands λ_{ex} = 340 nm and λ_{em} = 420 nm) overlapped with the chromate ($CrO4^{2-}$) anions absorption bands at 372 nm.

Moreover, CrO4^{2-} show a second absorption band at 274 nm that also overlaps with the NCQDs most intense absorption band at 265 nm.

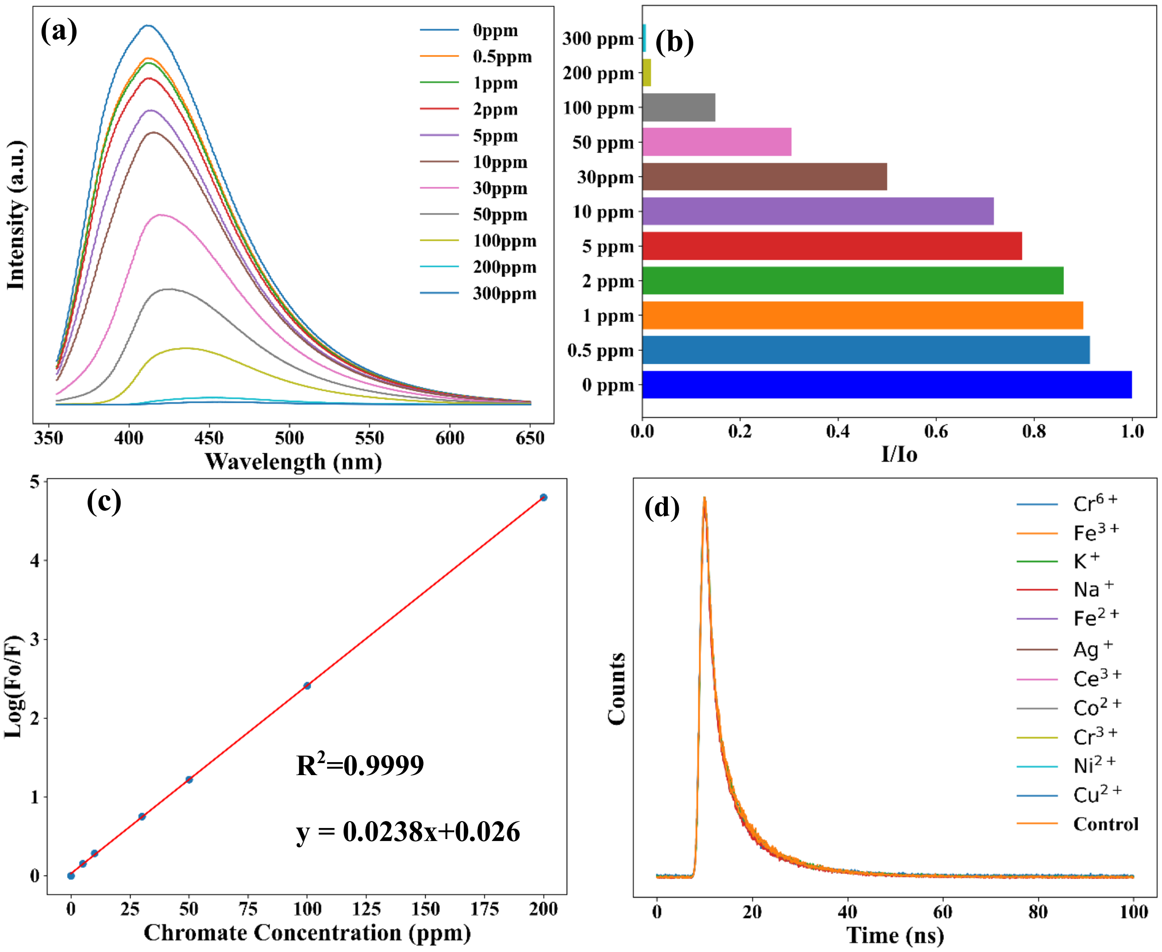

Figure 6.11: The effect of Chromium concentration in the PL intensity of N-10 (a-b), Stem-Volmer graphs as a function of (log(F0/F) versus Cr (VI) concentration (c), and the fluorescent lifetime of NCQDs in various ion solutions (d)

Further, the fluorescence lifetime of NCQDs was not changed with the addition of Cr (VI) (**Figure 6.11d**) which provides evidence that the IFE is the mechanism for the fluorescence quenching phenomenon. In addition, there was a downtrend of NCQDs in the LOD and LOQ results (**Figure 6.12b**). The LOD was decreased from 4.9 ppm for sample N-0.25 to 0.95 ppm for sample N-10, while the LOQ improved from 16.3 ppm to 3.18 ppm. The results revealed that nitrogen doping enhanced the fluorescent properties of CQDs resulting in higher PLQY which then leads to the improvement in LOD and LOQ and consequently the sensing performances.

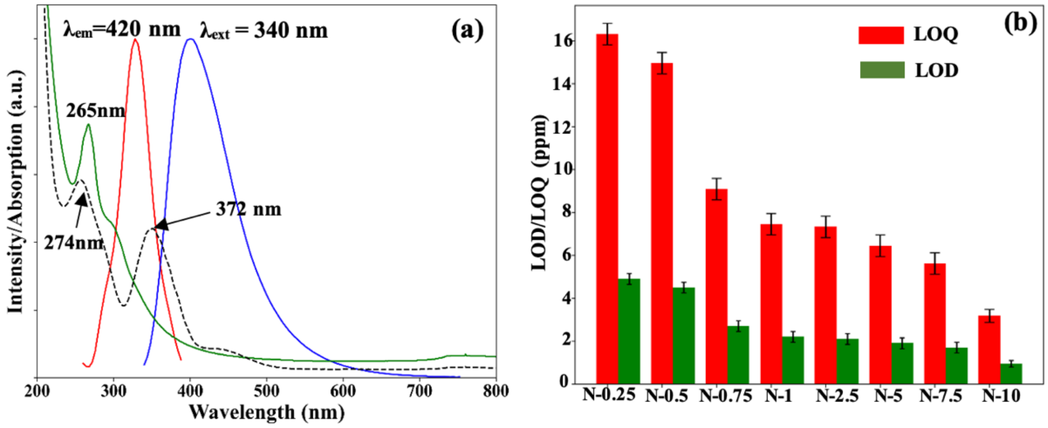

Figure 6.12:spectral overlap of the normalized UV-Vis absorption bands for the Cr (VI) ions (dash black) and the synthesised NCQDs (green line), and the excitation spectrum (λem = 420 nm) (red line) and emission spectrum (λex = 340 nm) (blue line) of the NCQDs. (b) LOD and LOQ of NCQDs

6.3 Conclusions

In conclusion, this work has demonstrated that efficient nitrogen-doped carbon quantum dots (NCDQs) can be successfully synthesised using glucose biomass precursors and ammonia solution via the continuous hydrothermal flow synthesis (CHFS) process. The results confirm that CHFS provides an effective approach for synthesizing high-quality carbon quantum dots. Also, CHFS approach has proved the ability to simultaneously dope heteroatoms like nitrogen while fabricating the carbon nanoparticle structures. This study provided a comprehensive information about the morphology and chemical characterisation of the synthesised NCQDs. By systematically varying the nitrogen dopant concentration, this work revealed the impact of precursor concentration on nanoparticle formation and properties of the synthesised NCQDs. HRTEM image analysis showed rounded NCQDs with a mean particle size range of 4.4 - 4.6 nm. Particle size distribution analysis indicated that higher nitrogen dopant concentrations (>2.5 M) yield a greater population of small NCQDs compared to lower dopant concentrations or no dopant. Chemical characterisation by FT-IR and XPS consistently shows reduced carbon content in the synthesised NCQDs when using higher concentrations of the nitrogen dopant. This finding suggests the particle size can be controlled by selecting the right ratio between the carbon and nitrogen precursors. The synthesised NCQDs possess excellent optical properties with a PLQY of ~10% and also showed excellent pH stability (for pH 2 to 11). The synthesised NCQDs were tested as a chemical sensor for Cr (VI) ion and the LOD value of 0.945 ppm and

LOQ value of 3.182 nm were obtained. In addition, the fluorescence lifetime studies confirmed Inner Filter Effect (IFE) as the mechanism for the quenching behaviour of the nano-sensing. This work provides in-depth guidance for applying carbon quantum dots as nano-sensors, highlighting key factors to consider when conducting sensing applications including pH stability, Stern-Volmer analyses and the mechanism of quenching process.

Chapter 6: References

1 X. Wang, Y. Feng, P. Dong and J. Huang, *Front. Chem.*, 2019, **7**, 671.

2 V. Georgakilas, J. A. Perman, J. Tucek and R. Zboril, *Chem. Rev.*, 2015, **115**, 4744–4822.

3 S. A. Nicolae, H. Au, P. Modugno, H. Luo, A. E. Szego, M. Qiao, L. Li, W. Yin, H. J. Heeres, N. Berge and M.-M. Titirici, *Green Chem.*, 2020, **22**, 4747–4800.

4 S. Zhang, S.-F. Jiang, B.-C. Huang, X.-C. Shen, W.-J. Chen, T.-P. Zhou, H.-Y. Cheng, B.-H. Cheng, C.-Z. Wu, W.-W. Li, H. Jiang and H.-Q. Yu, *Nat Sustain*, 2020, **3**, 753–760.

5 C. Kang, Y. Huang, H. Yang, X. F. Yan and Z. P. Chen, *Nanomaterials*, 2020, **10**, 2316.

6 S. D. Dsouza, M. Buerkle, P. Brunet, C. Maddi, D. B. Padmanaban, A. Morelli, A. F. Payam, P. Maguire, D. Mariotti and V. Svrcek, *Carbon*, 2021, **183**, 1–11.

7 X. Kou, S. Jiang, S.-J. Park and L.-Y. Meng, *Dalton Trans.*, 2020, **49**, 6915–6938.

8 K. J. Mintz, Y. Zhou and R. M. Leblanc, *Nanoscale*, 2019, **11**, 4634–4652.

9 S. Kellici, J. Acord, K. E. Moore, N. P. Power, V. Middelkoop, D. J. Morgan, T. Heil, P. Coppo, I.-A. Baragau and C. L. Raston, *React. Chem. Eng.*, 2018, **3**, 949–958.

10 I.-A. Baragau, N. P. Power, D. J. Morgan, T. Heil, R. A. Lobo, C. S. Roberts, M.-M. Titirici, S. Dunn and S. Kellici, *J. Mater. Chem. A*, 2020, **8**, 3270–3279.

11 A. Azimi, A. Azari, M. Rezakazemi and M. Ansarpour, *ChemBioEng Reviews*, 2017, **4**, 37–59.

12 P. Wu, W. Li, Q. Wu, Y. Liu and S. Liu, *RSC Adv.*, 2017, **7**, 44144–44153.

13 S. D. and S. K. Ioan-Alexandru Baragau, Nicholas P. Power, David J. Morgan, Tobias Heil, Richard Alvarez Lobo, Christopher Simon Roberts, Maria-Madgalena Titirici, *Royal sociiety of chemistry*, , DOI:10.1039/C9TA11781D.

14 H. Ding, S. B. Yu, J. S. Wei and H. M. Xiong, *ACS Nano*, 2016, **10**, 484–491.

15 R. Atchudan, T. N. J. I. Edison, S. Perumal, N. Clament Sagaya Selvam and Y. R. Lee, *Journal of Photochemistry and Photobiology A: Chemistry*, 2019, **372**, 99–107.

16 R. H. Ellerbrock and H. H. Gerke, *J. Plant Nutr. Soil Sci.*, 2021, **184**, 388–397.

17 C. Ji, Y. Zhou, R. M. Leblanc and Z. Peng, *ACS Sensors*, 2020, **5**, 2724–2741.

18 D. Y. Osadchii, A. I. Olivos-Suarez, A. V. Bavykina and J. Gascon, *Langmuir*, 2017, **33**, 14278–14285.

19 B. Lesiak, L. Kövér, J. Tóth, J. Zemek, P. Jiricek, A. Kromka and N. Rangam, *Applied Surface Science*, 2018, **452**, 223–231.

20 S. Bhattacharyya, F. Ehrat, P. Urban, R. Teves, R. Wyrwich, M. Döblinger, J. Feldmann, A. S. Urban and J. K. Stolarczyk, *Nature Communications*, 2017, **8**, 1–9.

21 J. Manioudakis, F. Victoria, C. A. Thompson, L. Brown, M. Movsum, R. Lucifero and R. Naccache, *Journal of Materials Chemistry C*, 2019, **7**, 853–862.

22 M. He, J. Zhang, H. Wang, Y. Kong, Y. Xiao and W. Xu, *Nanoscale Res Lett*, 2018, **13**, 175.

23 I. A. Baragau, N. P. Power, D. J. Morgan, R. A. Lobo, C. S. Roberts, M. M. Titirici, V. Middelkoop, A. Diaz, S. Dunn and S. Kellici, *ACS Sustainable Chemistry and Engineering*, 2021, **9**, 2559–2569.

24 Carbonaro, Corpino, Salis, Mocci, Thakkar, Olla and Ricci, *C — Journal of Carbon Research*, 2019, **5**, 60.

25 S. Kellici, J. Acord, K. E. Moore, N. P. Power, V. Middelkoop, D. J. Morgan, T. Heil, P. Coppo, I. A. Baragau and C. L. Raston, *Reaction Chemistry and Engineering*, 2018, **3**, 949–958.

26 A. Bhattacharya, S. Chatterjee, R. Prajapati and T. K. Mukherjee, *Phys. Chem. Chem. Phys.*, 2015, **17**, 12833–12840.

27 S. Sarkar, M. Sudolská, M. Dubecký, C. J. Reckmeier, A. L. Rogach, R. Zbořil and M. Otyepka, *Journal of Physical Chemistry C*, 2016, **120**, 1303–1308.

28 V. Strauss, J. T. Margraf, C. Dolle, B. Butz, T. J. Nacken, J. Walter, W. Bauer, W. Peukert, E. Spiecker, T. Clark and D. M. Guldi, *Journal of the American Chemical Society*, 2014, **136**, 17308–17316.

29 P. Joshi, R. Mishra and R. J. Narayan, *Current Opinion in Biomedical Engineering*, 2021, **18**, 100274.

30 P. Roy, P. C. Chen, A. P. Periasamy, Y. N. Chen and H. T. Chang, *Materials Today*, 2015, **18**, 447–458.

31 Z. Gan, H. Xu and Y. Hao, *Nanoscale*, 2016, **8**, 7794–7807.

32 W. Liu, M. Li, G. Jiang, G. Li, J. Zhu, M. Xiao, Y. Zhu, R. Gao, A. Yu, M. Feng and Z. Chen, 2020, **2001275**, 1–49.

33 Y. P. Sun, B. Zhou, Y. Lin, W. Wang, K. A. S. Fernando, P. Pathak, M. J. Meziani, B. A. Harruff, X. Wang, H. Wang, P. G. Luo, H. Yang, M. E. Kose, B. Chen, L. M. Veca and S. Y. Xie, *Journal of the American Chemical Society*, 2006, **128**, 7756–7757.

34 W. Wang, B. Wang, H. Embrechts, C. Damm, A. Cadranel, V. Strauss, M. Distaso, V. Hinterberger, D. M. Guldi and W. Peukert, *RSC Advances*, 2017, **7**, 24771–24780.

35 Q. Mei, K. Zhang, G. Guan, B. Liu, S. Wang and Z. Zhang, *Chemical Communications*, 2010, **46**, 7319–7321.

36 Y. Dong, H. Pang, H. Bin Yang, C. Guo, J. Shao, Y. Chi, C. M. Li and T. Yu, *Angewandte Chemie - International Edition*, 2013, **52**, 7800–7804.

37 L. Bao, C. Liu, Z. L. Zhang and D. W. Pang, *Advanced Materials*, 2015, **27**, 1663–1667.

38 L. Bao, Z. L. Zhang, Z. Q. Tian, L. Zhang, C. Liu, Y. Lin, B. Qi and D. W. Pang, *Advanced Materials*, 2011, **23**, 5801–5806.

39 D. S. English, L. E. Pell, Z. Yu, P. F. Barbara and B. A. Korgel, *Nano Letters*, 2002, **2**, 681–685.

40 M. De Laurentis and A. Irace, *Journal of Solid State Physics*, 2014, **2014**, 1–19.

41 S. Ghosh, A. M. Chizhik, N. Karedla, M. O. Dekaliuk, I. Gregor, H. Schuhmann, M. Seibt, K. Bodensiek, I. A. T. Schaap, O. Schulz, A. P. Demchenko, J. Enderlein and A. I. Chizhik, *Nano letters*, 2014, **14**, 5656–5661.

42 M. A. Omary and H. H. Patterson, *Luminescence, theory*, Elsevier Ltd., 3rd edn., 2016.

43 L. Wang, M. Li, W. Li, Y. Han, Y. Liu, Z. Li, B. Zhang and D. Pan, *ACS Sustainable Chemistry and Engineering*, 2018, **6**, 12668–12674.

44 W. Kong, H. Wu, Z. Ye, R. Li, T. Xu and B. Zhang, *Journal of Luminescence*, 2014, **148**, 238–242.

45 A. Azimi, A. Azari, M. Rezakazemi and M. Ansarpour, *ChemBioEng Reviews*, 2017, **4**, 37–59.

46 Y. Song, S. Zhu, S. Xiang, X. Zhao, J. Zhang, H. Zhang, Y. Fu and B. Yang, *Nanoscale*, 2014, **6**, 4676–4682.

Chapter 7 : Synthesis and Characterisation of N-doped Carbon Quantum Dots – TiO_2 Nanocomposites for Photocatalysis

7.1 Motivation

As the global energy crisis and environmental concerns intensify, developing sustainable technologies for solar energy conversion has become imperative. Photocatalysis enables direct harvesting of solar energy to drive chemical reactions, has emerged as a promising solution. In particular, photocatalysts offer an efficient and cost-effective approach for renewable production of fuels and valuable chemicals using only sunlight.[1] Over the past decades, titanium dioxide (TiO_2) has been extensively explored as a photocatalyst owing to its chemical stability, low cost, and photocatalytic activity. However, the large bandgap of TiO_2 allows absorption of only ultraviolet light, which accounts for just 4% of solar spectrum. This greatly limits the solar-to-chemical conversion efficiency and hinders practical applications.[2]

Modifying TiO_2 with nanocarbons such as carbon quantum dots (CQDs) has recently attracted tremendous attention to overcome the limitations of pristine TiO_2 photocatalyst.[3] CQDs are zero-dimensional carbon nanomaterials with sizes below 10 nm and possess unique properties like high chemical stability, tuneable photoluminescence, excellent electron transfer capacity and large specific surface area.[4] Integrating CQDs with TiO_2 into nanocomposite photocatalysts can enable synergistic effects that enhance solar absorption, charge separation and surface reactions. Specifically, CQDs can act as photosensitisers to harvest visible light and inject electrons into the conduction band of TiO_2, thereby reducing its bandgap to extend light absorption from UV to visible region.[5] Furthermore, the excellent electron accepting and transport properties of CQDs facilitate spatial charge separation, suppressing recombination of photogenerated electron-hole pairs. In addition, CQDs also dramatically increase the surface area and introduce new active sites for target reactions on TiO_2 surface. [6]

Herein, nitrogen doped CQDs (NCQDs) were synthesised via CHFS method using citric acid and urea as precursors. Citric acid provides the carbon source while urea acts as the nitrogen source. This single-step green NCQDs synthetic route avoids the use of any toxic chemicals. condition. The successful formation of NCQD-TiO_2 nanocomposite was studied for photocatalytic degradation of organic dye pollutants. Methylene blue (MB) was used as a model organic contaminant to assess the photocatalytic performance of the nanocomposites. MB is a commonly used dye for colouring paper, textiles, and other materials.[7] The aromatic structure of MB makes it resistant to natural biodegradation. Consequently, MB is frequently detected in industrial wastewater from textile, printing, pharmaceutical, and chemical industries. Effective removal of recalcitrant dyes like MB from effluents before discharge is therefore crucial to prevent their accumulation in the environment and protect human health. In a typical photocatalytic reaction involving decomposition of methylene blue, upon illumination, electrons in photocatalyst are excited from the valence band to the conduction band, creating electron-hole (e^-/h^+) pairs. The photogenerated electrons in the conduction band then react with molecular oxygen to form superoxide radicals anions (O^{2-}). Meanwhile, the holes left in the valence band are powerful oxidants that can react with water molecules or hydroxyl ions to produce hydroxyl radicals (OH^-). These reactive oxygen species attack the central aromatic ring of methylene blue via hydroxyl radical addition reactions and oxidation of the central carbon atom. The aromatic ring is rapidly decomposed into several intermediate by-products, which further are oxidised into CO_2, water.[8]

In summary, this study reports an environmentally friendly, rapid approach for synthesising NCQDs-TiO_2 and TiO_2 based nanocomposites as high-performance visible light driven photocatalyst. The synthesised nanocomposites overcome limitations of pristine TiO_2, enabling efficient solar energy conversion. Manufactured using a single step and scalable synthesis combined with exceptional photocatalytic activity, these nanocomposites represent a sustainable platform to harness solar energy for environmental and energy applications.

7.2 Results and Discussions

In this section, TiO_2 based nanocomposite were synthesised from titanium (IV) bis (ammonium lactato) hydroxide - $C_6H_{22}N_2O_8Ti$ as titanium sources and KOH as a reducing agent. The synthesised TiO_2 based nanocomposite is denoted as TiO_2 in the presenting data and graphs. The second nanocomposite was synthesised using the same set up, but the nitrogen doped carbon quantum dots (NCQDs) solution was added as another precursor. This NCQDs was synthesised from citric acid and urea in-situ at LSBU, and the synthesised nanocomposite is denoted as NCQDs-TiO_2 which is used for presenting data and graphs.

More detail about the synthetic process is provided in Chapter 3, (section 3.2.4).

7.2.1 Morphology and composition of TiO_2 and NCQDs nanocomposites.

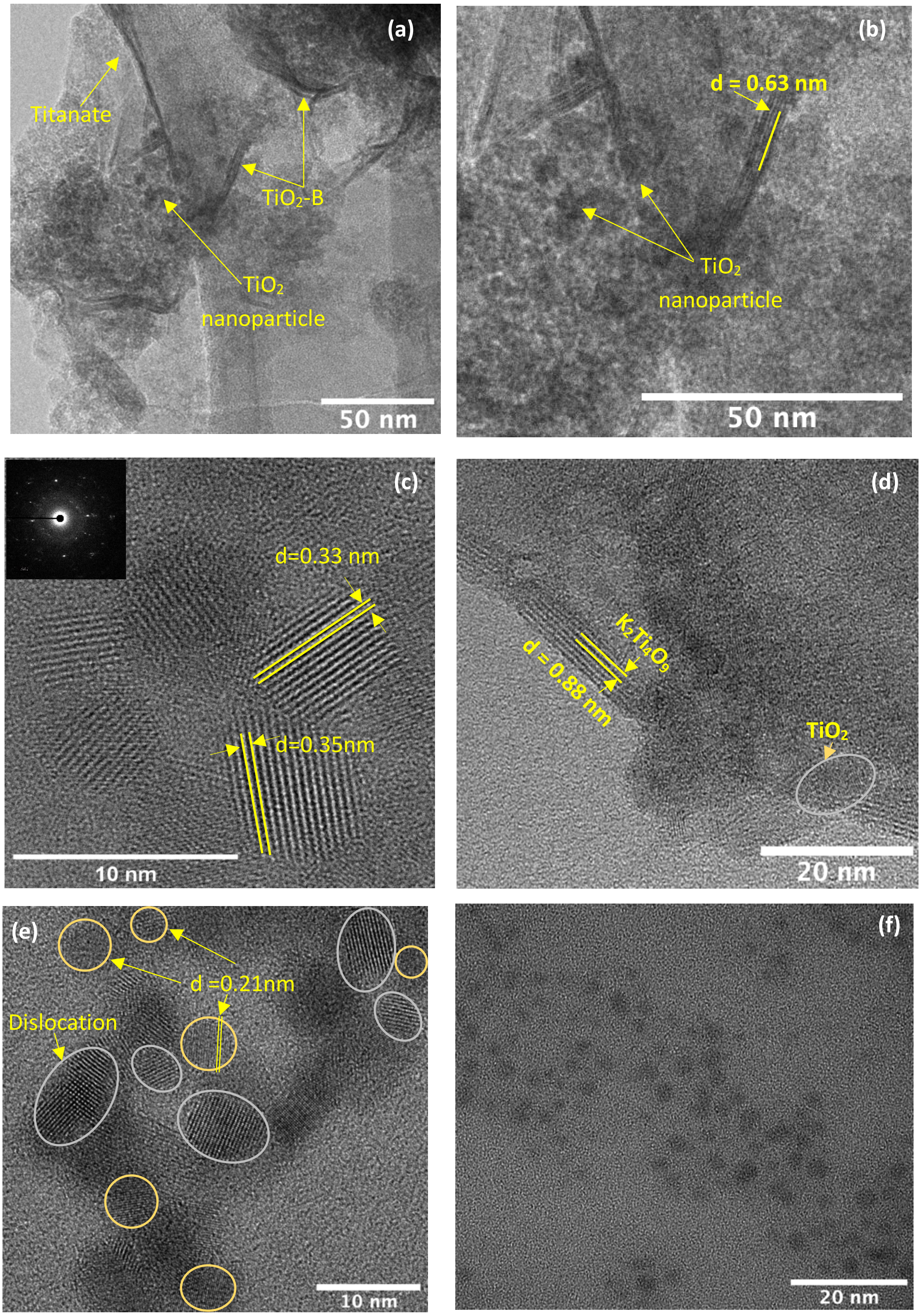

Figure 7.1: The HR-TEM images of (a, b, c and d) TiO_2, (e) NCQDs-TiO_2 and (f)NCQDs. Key: yellow coloured circle represents NCQDs nanoparticles, and white circles represents titania nanoparticles.

High-resolution transmission electron microscopy (HRTEM) reveals critical insights into the morphological architecture and crystallinity of the TiO_2 and NCQDs-TiO_2 nanocomposites. As depicted in **Figure 7.1c**, TiO_2 nanoparticles in the nanocomposite exhibit a mixture of lattice fringes corresponding to the anatase phase. Spacings of 0.35 nm match the (101) lattice plane, while 0.33 nm fringe spacing corresponds to the tetragonal (110) plane.[9] The TiO_2 nanoparticle sizes ranged from 3.0-11.0 nm, with an average diameter of 6.5 ± 0.2 nm computed by measuring 150 particles. The TEM image in **Figure 7.1b** reveals the presence of rod-shaped morphologies in the sample, with a measured d-spacing of 0.88 nm that corresponds to the lattice spacing of potassium titanate composites.[10] Additionally, a closer lattice fringe spacing of 0.63 nm observed in Figure 1b can be indexed to the (001) crystal planes of TiO_2 (B).[11] The overall composite structure containing TiO_2-B nanowire, TiO_2 anatase, and potassium titanate phases is further evidenced in the higher magnification TEM image in **Figure 7.1a**, where the different components can be clearly distinguished. In the NCQD-modified nanocomposite, NCQDs particles were observed, displaying an in-plane lattice spacing of 0.21 nm **(Figure 7.1c).**[4] Upon integration with TiO_2 nanoparticles, dislocations in the lattice fringes were apparent (Figure 1e), confirming the successful embedding of NCQDs into the TiO_2 matrix.

To further investigated in the morphology and crystal phase of the synthesised nanocomposites, X-ray diffraction (XRD) was utilised to examine the structure and composition of TiO_2 and NCQDs-TiO2 nanocomposites; XRD patterns of the two samples were illustrated in **Figure 7.2**. The distinct XRD patterns for the two nanocomposites confirmed that integration of NCQDs induces structural changes in TiO_2 evidencing the role of NCQDs in altering the crystallographic structure of the TiO_2 photocatalyst.

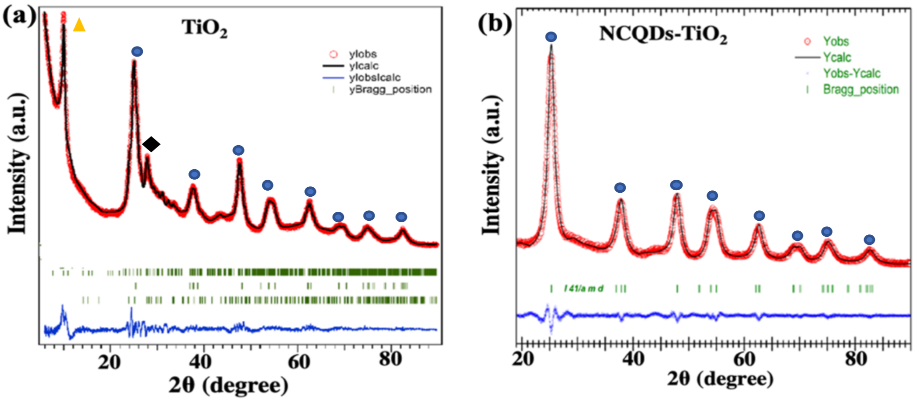

Figure 7.2: The XRD patterns of: (a) TiO_2 and (b) NCQDs-TiO_2, legend: ▲ $K_2Ti_4O_9$, ●anatase, ♦ - TiO_2 (B).

The X-ray diffraction patterns of the NCQDs-TiO_2 nanocomposites revealed characteristic peaks for TiO_2 anatase at 2θ values of 25.6°, 38.3°, 48.0°, 54.8°, and 63.0°, which correspond to reflections from the (101), (110), (200), (211), and (204) crystallographic planes, respectively. In contrast, the diffraction patterns of pure TiO_2 showed additional distinct peaks at 28.6° and 10.2°, which can be indexed to the (002) planes of TiO_2 (B) and the (200) planes of $K_2Ti_4O_9$, consistent with previously reported phase identification.[12,13,14]

The Rietveld refinement technique was utilized to thoroughly analyses the crystal structures present in the as-synthesised samples TiO_2 and NCQDs-TiO_2 by Le Bail Refinement using FullProf software. This refinement method extracts maximal information from XRD data by refining the entire profile rather than just peak positions during pattern fitting. Rietveld analysis revealed phase compositions, lattice parameters, atomic positions, and crystal structural details of TiO_2 and NCQDs-TiO_2. This refinement successfully characterised the presence of distinct crystalline phases which are anatase TiO_2 in the NCQDs-TiO_2, and TiO_2 contains $K_2Ti_4O_9$, anatase TiO_2 and monoclinic TiO_2 (B). In addition, semi-quantitative (S-Q) XRD analysis was performed using the reference intensity ratio (RIR) and spiking methods via Diffract Eva software. This pivotal analytical step elucidates relative proportions of the identified phases within the samples by utilising relative peak heights and I/I_{cor} values from imported PDF patterns. While not providing absolute quantification, S-Q analysis yields valuable insights into approximate phases present in the prepared TiO_2 and NCQDs-TiO_2 samples. The S-Q analysis revealed that NCQDs-TiO_2 consists of 100% of TiO_2- anatase (PDF 00-064-0863), while TiO_2 showed 66.1% of TiO2- anatase (PDF 00-064-0863), 8.9% of TiO_2 (B) (PDF 00-046-1238), and 30% of $K_2Ti_4O_9$ (PDF 01-083-2764). XRD analysis did not detect titanate and TiO_2 (B), possibly due to their low content. However, both XPS and energy dispersive X-ray spectroscopy analysis revealed the presence of potassium (K), which is reduced by 50% when compared to TiO_2 sample. Energy dispersive spectroscopy (EDS) was utilised to analyse the elemental composition of the synthesised nanocomposites. The EDS mapping images presented in **Figure 7.3** demonstrated homogeneous distribution of the potassium element within both synthesised nanocomposites. To gain a more comprehensive understanding of the elements and the chemical structure present on the surface of the nanocomposites, the X-ray photoemission spectroscopy (XPS) was used, the results are discussed as following.

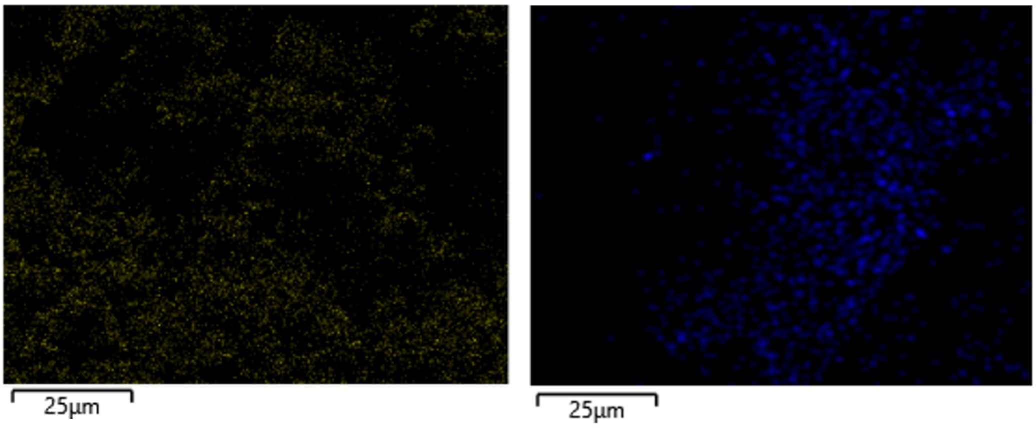

Figure 7.3: The elemental EDS mapping of potassium for: (a) TiO_2, and (b) NCQDs-TiO_2

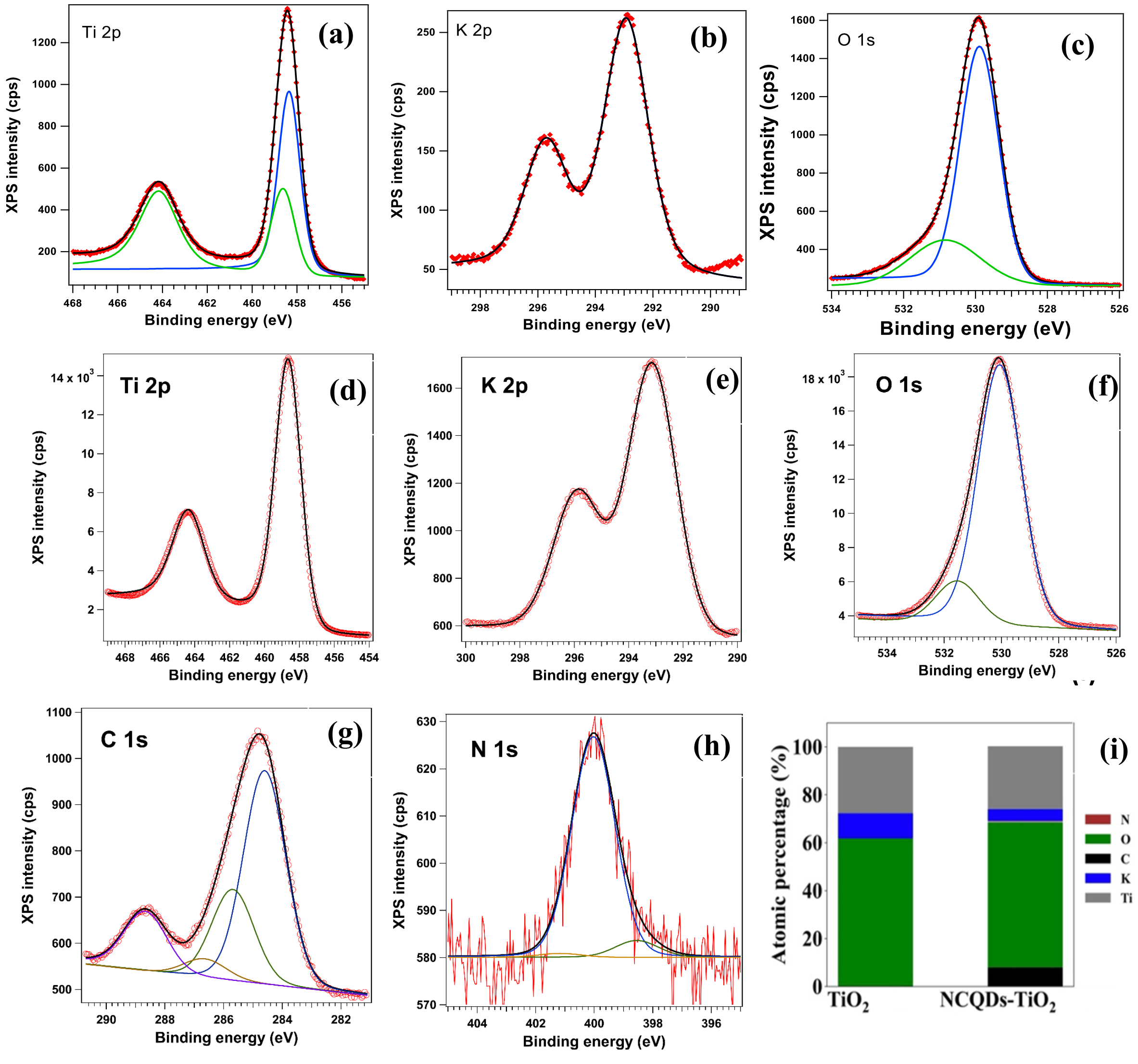

Figure 7.4: The XPS spectra: (a-c) TiO_2, (d-h) NCQDs-TiO_2, and (i) the chemical composition of the synthesised nanocomposites

The XPS survey revealed the presence of Ti_{2p}, K_{2p}, and O_{1s} peaks for the synthesised TiO_2, confirming the presence of potassium in the nanocomposite, aligning with the XRD and EDS data. Meanwhile, NCQD-TiO_2 exhibited additional peaks for C1s and N1s, attributable to the introduction of NCQDs. The element compositions of TiO_2-KOH and NCQDs-TiO_2-KOH are displayed in **Figure 7.4i**. TiO_2 comprises 61.83% O, 10.46% K, and 27.71% Ti, whereas NCQD-TiO_2 exhibits 7.87% C, 60.54% O, 5.06% K, 26.24% Ti, and 0.28% N. Notably, the presence of NCQDs reduced the K content by half, indicating a small amount of potassium titanate in the NCQDs-modified composite, which was not be detected by S-Q XRD analysis. However, the presence of C and N confirms the efficient combination of NCQDs with TiO_2 nanoparticles.

The high-resolution XPS provides insights into the surface functional groups of the nanomaterials. The deconvoluted Ti_{2p} spectra **(Figure 7.4a)** of TiO_2 samples displayed peaks at 458.3 eV and 464.2 eV, which can be assigned to Ti^{4+} $2p_{3/2}$ and Ti^{4+} $2p_{1/2}$ states, respectively. In contrast, the deconvoluted Ti_{2p} signal of NCQDs-TiO2 **(Figure 7.4b)** exhibited a peak at 458.6 eV, corresponding to Ti^{4+} $2p_{3/2}$.[15] The deconvoluted high resolution K 2p signals of both samples showed identical peaks at 293.1 eV, associated with K-O bonds. The O 1s signal of TiO_2 **(Figure 7.4c)** indicated several oxygen species present on the nanocomposite surface. The deconvoluted O 1s XPS spectrum could be fitted with two peaks representing K-O bonds (529.9 eV), Ti-O bonds (530.9 eV).[16] In contrast, the NCQDs-TiO_2 **(Figure 7.4f)** showed (530.06 eV) Ti-O, and (531.54 eV) C-O-C bonds.[17] In addition, deconvoluted C1s of NCQDs-TiO_2 **(Figure 7.4g)** confirmed the presence of sp^2-sp^3 carbon, in which peaks at 284.6 eV (C-C), 285.68 eV (C-O), 286.84 eV (C=O), and 288.65 eV(O-C=).[18] The high resolution N1s **(Figure 7.4h)** showed the present of pyridinic-N (398.54 eV), pyrrolic-N (400.3 eV) and graphitic-N (401.2 eV).[19]

Fourier-transform infrared (FT-IR) spectroscopy was utilised to further investigate the chemical structure of the synthesised nanocomposite. As depicted in **Figure 7.5a**, the FT-IR spectra revealed a broad band between 3000 cm^{-1} and 3500 cm^{-1}, which is attributed to O-H stretching vibrations of surface hydroxyl groups.[20] This broad peak is more pronounced in the spectrum of NCQDs-TiO_2, influenced by hydroxyl groups from the NCQDs surface. The peak around 800 cm^{-1} is observed in the spectrum of TiO_2, indicating the bending vibrations of Ti-O-Ti bonds.

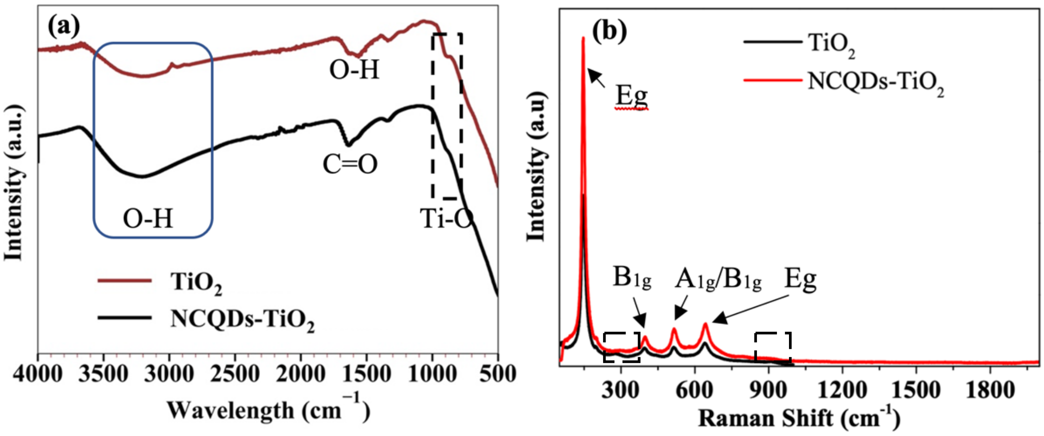

Figure 7.5: FT-IR(a) and Raman (b) spectra of the synthesised nanocomposites

However, this peak is weakened in the spectrum of NCQDs-TiO$_2$, likely due to the presence of Ti-O-C bonds.[21] Additionally, the FT-IR spectrum of TiO$_2$ displayed a peak at 1620 cm^{-1}, which can be assigned to bending and stretching vibrations of O-H groups.[22] The peak located at 1650 cm-1, corresponding to C=O vibration, is present in the spectrum of NCQDs-TiO$_2$-KOH.[4] The synthesised nanocomposites were also characterised using Raman spectroscopy, the spectrum shown in **Figure 7.5b** revealed the , the typical bands located at 146.5 cm^{-1} (E_g), 396.4 cm^{-1} (B_{1g}), 515.5 cm^{-1} (A_{1g}), and 639 cm^{-1} (E_g) corresponding to the TiO$_2$ anatase.[23] The main E_g anatase peak was more intense in NCQDs-TiO$_2$ sample which is expected. Peaks at 280 cm^{-1} and 873 cm^{-1} are associated with the presence of titanate.[24] The most intense Raman peak in TiO$_2$ (B) overlaps with TiO$_2$ anatase ~146.5 eV, and the second most intense peak is usually observed around 640 cm^{-1}.[25,26]

The time resolved photoluminescent (PL) decays were employed to achieve a deeper understanding about the effect of NCQDs in the enhance charge separation process of the synthesised NCQDs. The measurement was conducted by exciting the nanocomposites using a laser at 375 nm, the PL spectra is displayed in **Figure 7.6**. The PL lifetime data was determined by fitting the data with multiple exponentials. The fitting parameters are provided in Table 1. The average lifetime was calculated using the amplitude weighted average of the fitted exponentials according to equation1.[27]

$$\tau_{avg} = \frac{a_1\,\tau_1 + a_2\,\tau_2 + a_3\,\tau_3}{a_1 + a_2 + a_3} \quad \textbf{(eq. 1)}$$

Where a_1, a_2, and a_3 are the amplitudes and τ_1, τ_2, and τ_3 are the lifetimes of the exponential components.

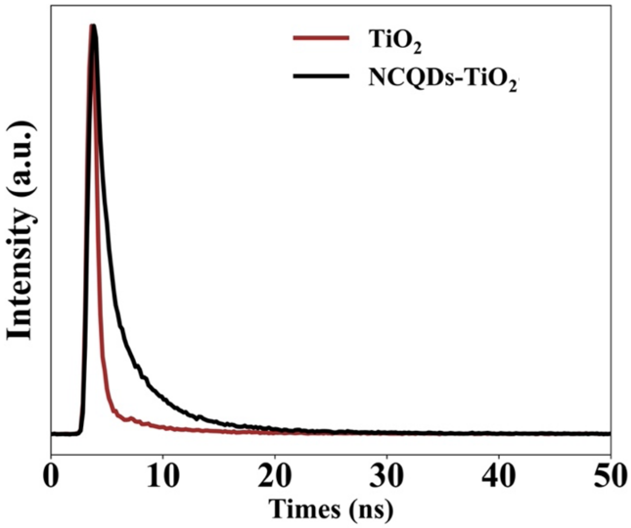

Figure 7.6: Photoluminescence decay of the nanocomposites

The PL lifetime demonstrated that the incorporation of NCQDs into TiO_2 increased the photoluminescence lifetime from 2.88 ns to 3.96 ns. This increase in lifetime implies that the NCQDs facilitated better charge carrier separation in the NCQDs-TiO_2 nanocomposites system.[28]

Table 7.1: Fitting parameter of PL decays of the nanocomposites

Sample	a_1	τ_1 (ns)	a_2	τ_2 (ns)	a_3	τ_3 (ns)	τ_{avg} (ns)
TiO_2	0.64	0.44	0.26	3.91	0.1	7.13	2.88
NCQDs-TiO_2	0.26	0.86	0.59	3.45	0.15	11.28	3.96

7.2.2 Band Gap and Energy structure

The bandgap energy is the most important property that determine the photocatalytic performance of the materials. A suitable bandgap is required to facilitate effective absorption of photons to generate electron-hole pairs.[29] Herein, the bandgap energies of the synthesised TiO_2-based nanocomposite photocatalysts were estimated using the Kubelka-Munk method. This analytical technique allows determination of a semiconductor's optical bandgap by creating a plot of the transformed diffuse reflectance (F(R)) versus photon energy (hv) following the relationship shown in equation 2.[30]

$$F(R) = \frac{K}{S} = \frac{(1-R)^2}{2R} \quad \textbf{(eq. 2)}$$

Where: R is the diffuse reflectance of the nanocomposite measured by using integrating sphere UV-Vis spectroscopy. The plot of $(F(R).hv)^{1/a}$ versus hv was used to estimate the direct and indirect bandgap of the synthesised nanocomposite, where h is the Plank's constant, v is the photon frequency; and a = 1/2 is used for direct bandgap estimation and a = 2 is used to determine the indirect bandgap. The plots are displayed in **Figure 7.7**. The analysis revealed NCQDs integration narrowed the TiO_2 bandgap from 3.3 to 2.8 eV confirming the effect of NCQDs in improving the visible light absorption of TiO_2. The narrowing of the band gap is attributed to the formation of Ti-O-C chemical bonds between the NCQDs and the TiO_2 nanoparticles. These bonds give rise to additional energy states that exist between the bandgap of the CQDs and TiO_2, effectively reducing the overall bandgap of the composite system.[4] In addition, the dopant of nitrogen atom with the amine group on the surface of the synthesised NCQDs also introduce the gap state resulting in narrowing the bandgap.[31]

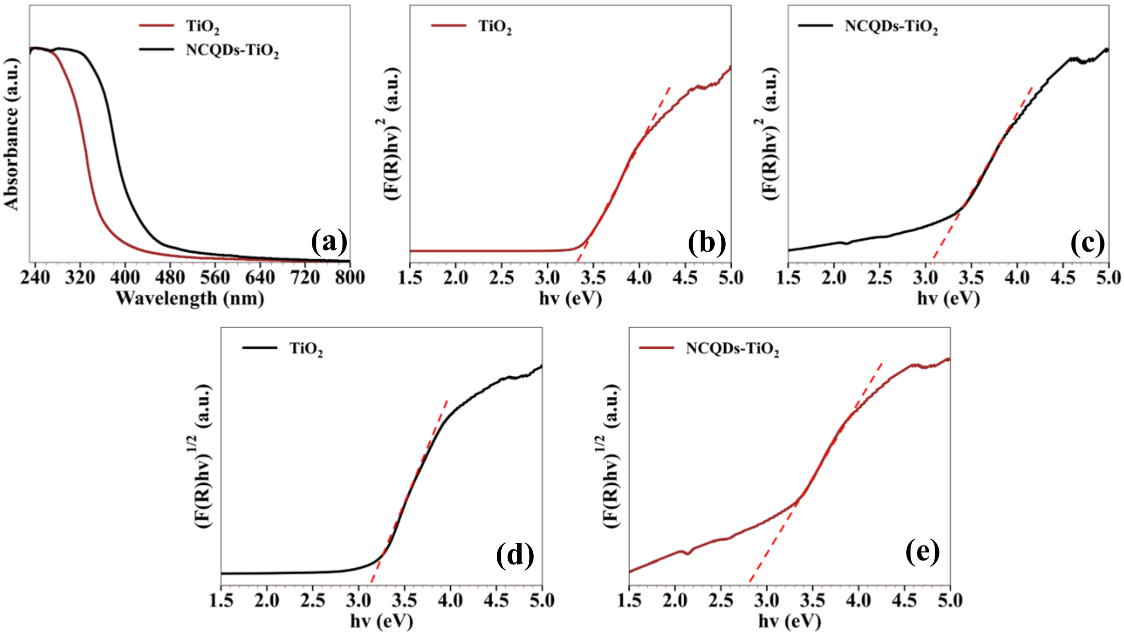

Figure 7.7: The UV-Vis absorbance spectra (a) and the estimated bandgap of the nanocomposite: (b-c) direct bandgap, (c-d) indirect bandgap

In addition, ultra-violet photoemission spectroscopy (UPS) was employed to determine the work function, HOMO and LUMO bands of the prepared nanocomposites. The UPS spectra are displayed in **Figure 7.8**. The work function (Φ) was calculated using the following equation 3.[32] Where: hν is the photon energy of the UV source, E_{cutoff} is the binding energy at the high kinetic energy cut-off of the UPS spectrum. The Fermi level is also determined from the UPS spectrum.

$$\Phi = h\nu - E_{cutoff} \quad \textbf{(eq. 3)}$$

The calculated work function of both sample TiO_2 and NCQDs-TiO_2 is 5.3 eV, and the estimated Fermi energies are -2.5 eV and -1.7 eV, respectively. Thus, the HOMO level of TiO_2 is -8.1 eV, and HOMO level of NCQDs-TiO_2 is -7 eV.

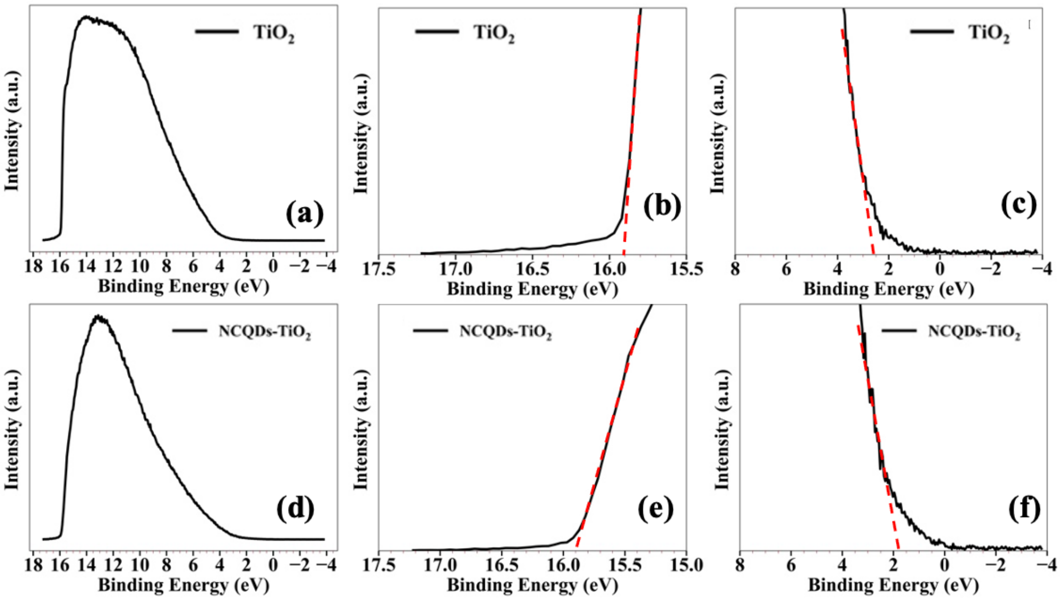

Figure 7.8: The UPS spectra: (a,d), the estimated energy cut-off: (b,e), and the Fermi energy region: (c,f)

The combination of estimated optical bandgap along with HOMO and LUMO levels determined from UPS data provided insights into the detailed band energetics of the synthesised nanocomposites. Previous reports have determined the conduction band minimum (CB) and valence band maximum (VB) potentials of $K_2Ti_4O_9$ and TiO_2 anatase referenced to the normal hydrogen electrode (NHE) at pH 7 to be -0.48 V and 3.06 V for $K_2Ti_4O_9$, and -0.53 V and 2.67 V for TiO_2, respectively.[33] Additionally, the CB and VB positions of monoclinic TiO_2 (B) were reported as -0.56 V and 2.34 V versus NHE at pH 7.[11,34] The combination of experimental data and the literature data revealed the band structure of the synthesised TiO_2 and NCQDs-TiO_2, as depicted in **Figure 7.9**.

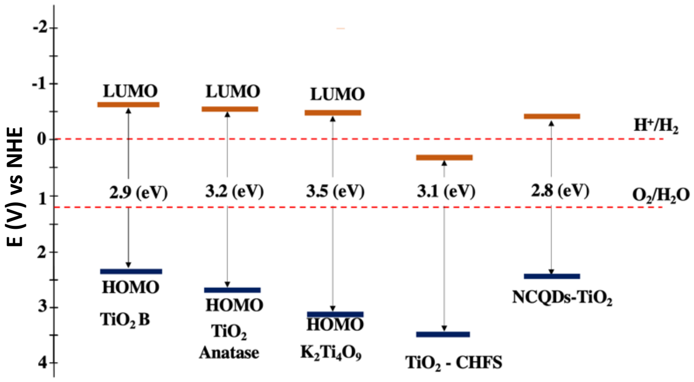

Figure 7.9: The energy band structures of the synthesised nanocomposites TiO_2*-denoted* TiO_2*-CHFS and NCQDs-*TiO_2

7.2.3 Dye degradation

- *Methylene blue photodegradation*

The synthesised nanocomposites TiO_2 and NCQDs-TiO_2 were studied for photodegradation of methylene blue. Firstly, 10 mg of the nanocomposite was dispersed in 50.0 mL of methylene blue solution with concentration C_o = 15 ppm by using a magnetic stirrer. Then, the mixture was constantly stirred (500 rpm) and irradiated using a solar simulator (LSH7320-Newport). The degradation of the dye was evaluated by using a UV-Vis absorbance spectrophotometer, the absorbance at the λ_{max} = 664 nm was recorded after every 15 minute to compute the concentration of the dye remaining in the solution during the photodecomposition using a calibration equation represented the relationship of absorbance intensity and MB concentration. The calibration graph and equation are illustrated in **Figure 7.10**.

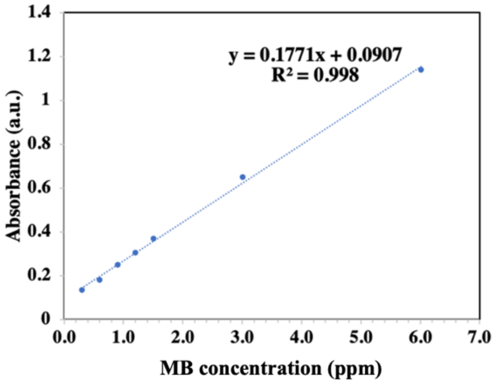

Figure 7.10: The methylene blue concentration against absorbance calibration

The photocatalytic activities of TiO_2 and NCQDs-TiO_2 in photodegradation of MB under different light intensity 1 sun 1 sun (100mW/cm^2) and 0.5 sun (50 mW/cm^2) are displayed in **Figure 7.11**. The MB degradation percentage was calculated using the equation 4.[35]

$$\text{MB Degradation (\%)} = \frac{\text{Co}-\text{Ct}}{\text{Co}} \times 100 \ \textbf{(eq. 4)}$$

Where: C_o is the original concentration of MB solution and Ct is the concentration of MB remained at the time measured.

After the first 15 minutes irradiation under 1 sun intensity, there is more than 50% MB being degraded with the use of NCQDs-TiO_2, while the number for TiO_2 is less than 30%. Interestingly, TiO_2 displayed comparable performance to NCQDs-TiO_2 after another 15 minutes irradiation and was even slightly better in the next 30 minutes. However, after 60 minutes of irradiation, TiO_2 showed only a slight effect on MB degradation, with the percentage slowly increasing from 70% to 77% after 2 hours of irradiation. While in the presence of NCQDs, the MB photodegradation was promptly accelerated after one hour under solar light; this sample degraded about 93% of MB after 2 hours of irradiation. Under lower light intensity conditions, TiO_2 and NCQDs-TiO_2 exhibited slightly reduced photoactivity, resulting in a slower MB degradation process, as shown in **Figure 7.11b**. However, the MB degradation rate of NCQDs-TiO_2 was still higher compared to TiO_2; 85% MB was removed using NCQDs-TiO_2 after 2h under 0.5 sun compared to 76% of TiO_2.

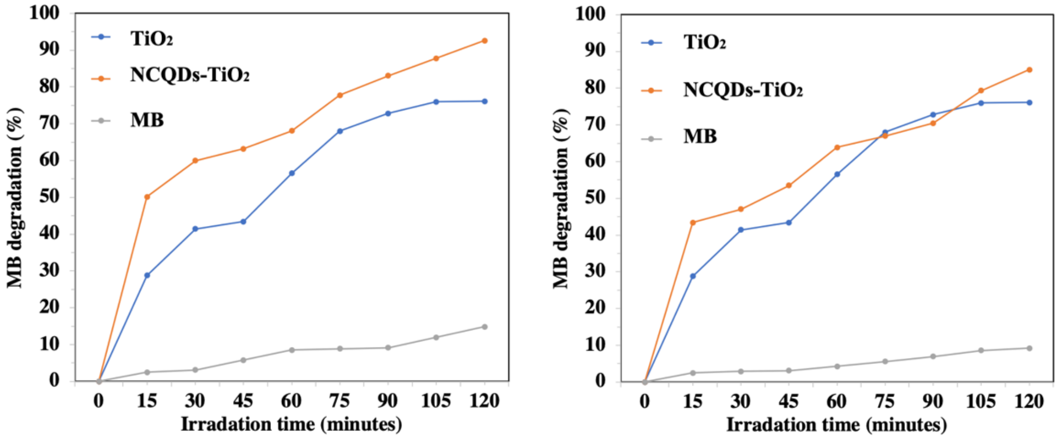

Figure 7.11: The photocatalytic activities of the TiO_2 and NCQDs-TiO_2 nanocomposites in the degradation of MB under different light intensity: (a) 1 sun and (b) 0.5 sun

Furthermore, to investigate the kinetics of the MB degradation process, the Langmuir-Hinshelwood first-order kinetic model was applied to evaluate the degradation rate using equation *5.*[36]

$$Ln\,\frac{Ct}{Co} = k_{app}t \quad (\boldsymbol{eq.5})$$

Where C_0 is the initial concentration of the dye, Ct is the concentration of MB remaining at certain time t, t is the time of solar irradiation, and the k_{app} is the rate constant.

The results in **Table 7.2** revealed that integration of NCQDs improved the degradation rate by approximately 11.1% compared to TiO_2 alone under standard conditions. Furthermore, under lower light intensity, the enhancement in the degradation rate was even greater at 15.4% with the NCQD-modified photocatalyst. This data analysis confirms that incorporation of NCQDs improves the photocatalytic performance of TiO_2 for MB degradation, especially under visible light conditions where the light harvesting is enhanced by NCQDs. The varying photoactivities under lower light intensities demonstrate the distinct roles of the composite components in regulating the photocatalytic mechanisms.

Table 7.2: The summary data of degradation rate constant

Sample	**Rate constant k_{app} (min^{-1})**	
	1 sun	**0.5 sun**
TiO_2	0.017	0.013
NCQDs-TiO_2	0.020	0.015
MB only	$0.005\text{x}10^{-1}$	$0.003\text{x}10^{-1}$

Adsorption provides a crucial bridge between MB molecules in solution and active sites on the photocatalyst surface. To assess the adsorption capability of TiO_2 and NCQDs-TiO_2 nanocomposites, 10.0 mg of the synthesised samples were introduced into 50 mL solutions of 15 ppm MB under dark conditions at room temperature with mild shaking. As shown in **Figure 7.12**, the MB concentration was reduced by 14.7% in the presence of TiO_2 after two hours, while the reduction was 20.5% for NCQDs-TiO_2. This enhancement can be attributed to the increased surface area caused by the introduction of NCQDs into the TiO_2 matrix. Indeed, BET surface area measurements confirmed that the surface area increased from 123.65 m^2/g for TiO_2

to 280.13 m^2/g for NCQDs-TiO_2 nanocomposite. This enhancement in surface area can be attributed to the presence of NCQDs hindering the growth and aggregation of TiO_2 particles during synthesis. The smaller TiO_2 particle size and increased porosity provided more active sites for photocatalysis.

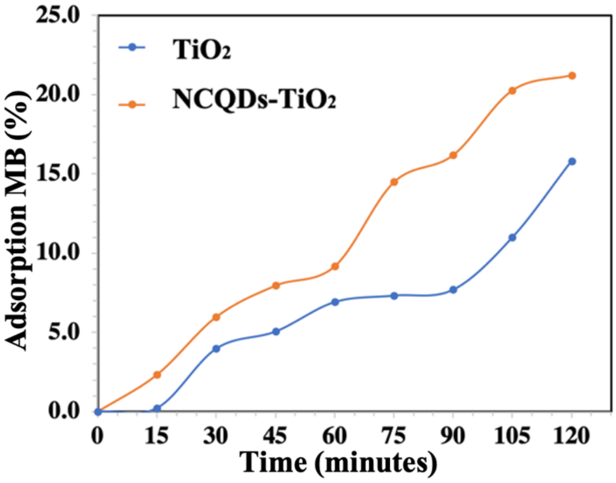

Figure 7.12: The adsorption percentages of MB on the nanocomposites.

The MB adsorption kinetic of TiO_2 and NCQDs-TiO_2 nanocomposites are studied using the pseudo first and second order, which are present by the equation 6 and equation 7, respectively.[37]

$$\mathrm{Log}(qe-qt) = \mathrm{Log}(qe) - \frac{k_1.t}{2.303} \quad \textbf{(eq. 6)}$$

$$\frac{t}{qt} = \frac{1}{k_2 qe^2} + \frac{1}{qe}t \qquad \textbf{(eq. 7)}$$

Where: qe (mg/g) and qt (mg/g) represent the amounts of methylene blue (MB) adsorbed per gram of adsorbent at equilibrium and at time t (minutes), respectively, and k_1 is the pseudo-first-order rate constant (1/min), and k_2 is the pseudo-second-order rate (g/mg.min). A plot of log(qe-qt) versus time (t) was used to determine the k_1, while k_2 was calculated using the slope of the plot of t/qt versus time (t), the plots are displayed in **Figure 7.13**.

The accuracy of the kinetic models was evaluated by comparing correlation coefficients (R^2).[38] The pseudo-second order model showed the best fit ($R^2 = 0.996$) for MB adsorption onto the nanocomposites, indicating chemisorption governed the kinetics. Chemisorption involves the formation of chemical bonds between the adsorbate and surface-active sites, and the rate is controlled by interactions between adsorbate molecules and surface sites of the nanocomposites.[39] In addition, the calculated equilibrium adsorption capacity and rate constant confirmed the improvement of NCQDs-TiO_2 over TiO_2 alone, the equilibrium adsorption capacity was enhanced from 11.6 to 13.1 (mg/g) and the rate constant is also significant improved from 0.01 to 0.03 (g/mg.min).

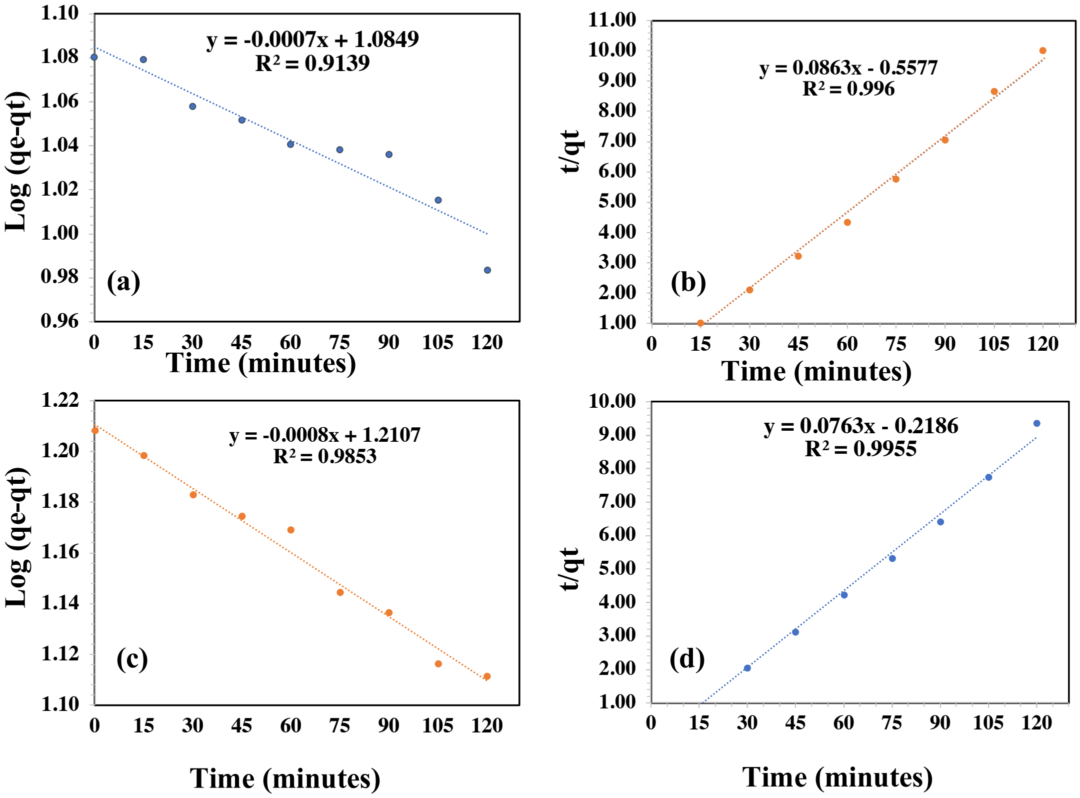

Figure 7.13:The pseudo first and second order kinetic of MB adsorption on the nanocomposites: (a-b) TiO_2, respectively; and (c-d) NCQDs-TiO_2, respectively.

The computed adsorption rate constants, qe and correlation coefficients R^2 of the pseudo first and second order plots are summarised in **Table 7.3**.

Table 7.3: The adsorption rate constant K_1 and K_2, correlation coefficients R^2, and the computed qe of pseudo first and second order kinetic models.

Sample	**Pseudo first order constant**			**Pseudo second order constant**		
	K_1x10^{-3} (min^{-1})	qe (mg/g)	R^2 (%)	K_2 (g/mg.min)	qe (mg/g)	R^2 (%)
TiO_2	1.61	12.03	91.39	0.01	11.6	99.6
NCQDs-TiO_2	1.84	16.15	98.53	0.03	13.1	99.6

7.2.4 Reaction mechanism

During the investigation into the mechanism of dye degradation reactions, we observed an interesting phenomenon with the synthesised nanocomposites. The as-synthesised TiO_2 and NCQDs-TiO_2 degraded MB in complete darkness simply by stirring. This experiment involved introducing 10.0 mg of nanocomposites into 50.0 mL of a 15 ppm MB solution and mixing at 500 rpm. As shown in **Figure 7.14**, under dark conditions and a stirring speed of 500 rpm, TiO_2 reduced the MB concentration by 64.6% compared to 77% under 1 sun irradiation, while the reduction was 52.6% with NCQDs-TiO_2. The rate constants are displayed in **Table 7.4**. Interestingly, under the dark condition, TiO_2 showed better performance compared to NCQDs-TiO_2 with a faster degradation rate, while NCQDs-TiO_2 completely outperformed TiO_2 under solar light. This result suggested different mechanisms between these two samples.

Table 7.4: The dye degradation rate constants under various conditions

Sample	**Rate constant Kapp (min^{-1})**		
	1 sun	**0.5 sun**	**0 sun+stirring**
TiO_2	0.017	0.013	0.0097
NCQDs-TiO_2	0.020	0.0150	0.0063

Based on the morphology obtained from TEM image analysis and the ability to degrade MB in the darkness, we hypothesize that the combination of TiO_2 and titanate performs piezoelectric activities. The piezoelectric effect involves the generation of separated electric charges on opposite faces of certain anisotropic crystals when they are subjected to mechanical deformation or stress applied along asymmetric crystallographic directions. This charge separation occurs due to the strain-induced relative displacement of cations and anions in the crystal lattice, which creates an internal electric dipole and polarization.[40]

Then, piezoresponse force microscopy (PFM) measurement was initially conducted to investigate the piezoelectric activity of the synthesised nanocomposites. Initial data analysis confirmed the piezoelectric activity of the synthesised nanocomposites, as shown in **Figure 7.15**. The initial test led us to the assumption that the synthesised nanocomposites act like a combination of a piezo-catalyst and photocatalyst. The synthesised nanocomposites enable the simultaneous utilisation of both solar energy and mechanical energy during the dye degradation process.[41]

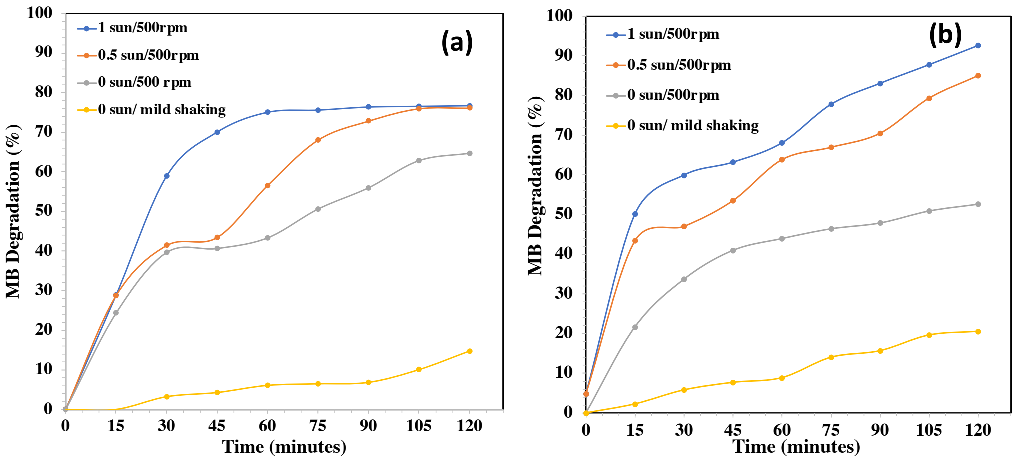

Figure 7.14:MB degradation of the nanocomposites under varied conditions: (a) TiO$_2$-KOH and (b)NCQDs-TiO$_2$-KOH

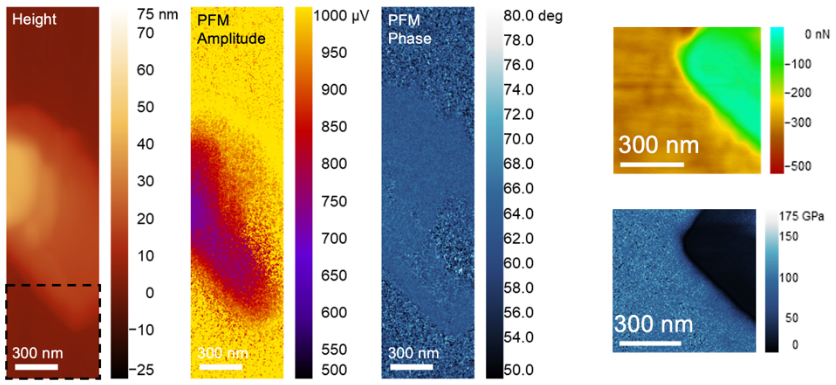

Figure 7.15: The PFM spectra of the synthesised TiO$_2$

It is worth noting that the solar light used in this study possesses a range of 400 nm – 1100 nm. Thus, the reduction of MB concentration by photocatalyst activities when using the synthesised TiO$_2$ is mainly contributed by TiO$_2$ (B) which has a bandgap of 2.9 eV. Herein, under solar light, the electron in the VB of TiO$_2$ (B) is effectively excited to the CB band creating an e-h pair, and this excited electron will migrate to the TiO$_2$ anatase phase at the surface of the nanocomposite where the reduction takes place. The hole left in the VB of the TiO$_2$ migrates to the VB of TiO$_2$ (B) where the oxidation occurs.[42] The proposed process is displayed in **Figure 7.15a**. On the other hand, possessing a narrowed bandgap indicates that NCQDs are inserted into the TiO$_2$ lattice creating new energy band levels.[5] Under solar light, the electron in the VB of NCQDs-TiO$_2$ is excited to the CB creating an e-h pair; this excited electron will migrate to the CB of TiO$_2$, while the hole left in the VB of TiO$_2$ will migrate to the VB band of NCQDs-TiO_2, as showing in **Figure 7.16b**. This typical heterojunction formation is commonly reported to greatly reduce the recombination rate of photogenerated electron-hole pairs.[43] This type II band alignment thus enables longer lifetimes of the charge carriers and enhances photocatalytic efficiency.[4]

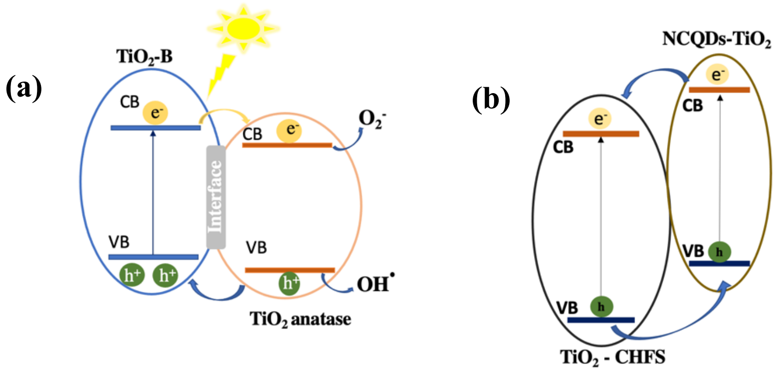

Figure 7.16:The proposed e-h migration in the heterojunction of the synthesised TiO_2 (a) and NCQDs-TiO_2 nanocomposites (b)

We propose that the improved dye degradation performance of the synthesised nanocomposites can also be attributed to the piezoelectricity of the potassium titanate phase.[44,45] When mechanical strain is applied through stirring, the distortion of the crystal lattice displaces cations relative to anions, causing polarization and separation of electric charges. This piezoelectric effect generates an internal electric field across the material, accumulating positive charges on one crystal face and negative charges on the opposite face. This piezo potential acts analogously to an external biasing electric field.[46] Under illumination, the electric field enhances directional migration of photogenerated electrons and holes, funnelling electrons toward the negative side and holes to the positive side.[47] By "steering" the electrons and holes to reactive sites on different crystal facets, this piezoelectric-induced charge separation suppresses recombination.[48] However, the precise mechanistic workings of piezo-catalysts remain incompletely understood, necessitating further research to elucidate the mechanisms underlying piezo-photocatalyst systems.[49] This work constitutes an important initial foundation for utilizing CHFS to synthesize novel categories of materials in this field.

In summary, the proposed mechanism of a hybrid photo-piezocatalytic system in the synthesised nanocomposites is initially supported by the characterisations and experimental data. The synthesised TiO_2 contains more titanate, conferring superior dye degradation in the dark compared to NCQDs-TiO_2. However, under solar irradiation, the synthesised NCQDs exhibit markedly improved dye degradation. Thus, for synthesised TiO_2, the piezoelectric effect appears to be the primary driver of the degradation process. In contrast, photocatalytic activity dominates as the main source of organic dye degradation by NCQDs-TiO_2.

7.3 Conclusion

In conclusion, this study has successfully demonstrated the efficiency of using continuous hydrothermal flow synthesis (CHFS) to rapidly synthesize innovative nanocomposite photocatalysts without the need for further post-treatment. The as-synthesised TiO_2-based nanocomposites exhibited promising results for dye photodegradation applications. Additionally, in-situ synthesised NCQDs were utilised as a secondary precursor to investigate their effect on both the CHFS process for synthesising the TiO_2-based nanocomposites as well as the resulting properties of the nanocomposites. The presence of NCQDs during synthesis induced changes in the structure and chemical composition of the TiO_2 nanocomposites. Specifically, the NCQD-TiO_2 nanocomposite displayed excellent performance in dye photodegradation under various conditions. This work also provided comprehensive details on characteristics of the synthesised TiO_2 nanocomposites, including morphological, chemical, optical and electrical properties. The characterisation results revealed that the synthesised TiO_2 nanocomposite consisted of mixed TiO_2-B, potassium titanate, and TiO_2 anatase phases, while the NCQD-TiO_2 nanocomposite contained primarily TiO_2 anatase with NCQD nanoparticles decorated on the surface. The use of NCQDs resulted in a considerable increased surface area observed in the synthesised NCQD-TiO_2 sample, which is 280.13 m^2/g compared to 123.65 m^2/g of TiO_2 nanocomposite synthesised without NCQDs. This study provided a comprehensive procedure for examining the synthesised samples in photocatalyst applications under different conditions. The methods for analysing the experimental data were also detailed, including rate constant calculations, and applying kinetic models. Both synthesised TiO_2 and NCQD-TiO_2 nanocomposite samples showed comparable, excellent results in dye degradation. Notably, the NCQD-TiO_2 sample removed 93% methylene blue from a 15ppm methylene blue solution under 1 sun intensity after 2 hours, with only a slight reduction to 85% removal under 50% lower light intensity. Interestingly, the nanocomposites exhibited piezo-catalytic activity, enabling dye degradation through vibration alone in the dark. The proposed mechanism for the observed dye degradation is also discussed based on the experimental data and energy band theory. This work demonstrates a novel, rapid approach to synthesising CQDs and conventional semiconductor nanocomposites. The comprehensive details on characterisation and experimental procedures provide a useful foundation and introduction for synthesising and analysing CQDs-based nanocomposites as next-generation photocatalysts. Further studies optimizing operational parameters such as NCQD concentration and semiconductor matrix could help drive these nanocomposites towards practical renewable energy and environmental remediation applications.

While this initial study provides proof of concept for the potential of NCQD-TiO_2 photocatalysts, considerable work remains to optimize these materials and evaluate their performance for specific applications. Key areas for future research should include:

- Exploring different type of NCQDs and optimised the concentration ratios

- Evaluating hydrogen production and test addition of other composites, for example graphene

- Analysing stability and recyclability of the materials over prolonged operation periods.

Chapter 7: References

1 Z. Kuspanov, B. Bakbolat, A. Baimenov, A. Issadykov, M. Yeleuov and C. Daulbayev, *Science of The Total Environment*, 2023, **885**, 163914.

2 J. Schneider, M. Matsuoka, M. Takeuchi, J. Zhang, Y. Horiuchi, M. Anpo and D. W. Bahnemann, *Chem. Rev.*, 2014, **114**, 9919–9986.

3 A. M., B. K. John, A. R. Chacko, C. Mohan and B. Mathew, *ChemPhysChem*, 2022, **23**, e202100873.

4 I.-A. Baragau, J. Buckeridge, K. G. Nguyen, T. Heil, M. T. Sajjad, S. A. J. Thomson, A. Rennie, D. J. Morgan, N. P. Power, S. A. Nicolae, M.-M. Titirici, S. Dunn and S. Kellici, *J. Mater. Chem. A*, 2023, **11**, 9791–9806.

5 Y. Jin, W. Tang, J. Wang, F. Ren, Z. Chen, Z. Sun and P.-G. Ren, *Journal of Alloys and Compounds*, 2023, **932**, 167627.

6 Z. Xu, Z. Chen, T. Ji, D. Jv and P. Guan, *Materials Letters*, 2022, **309**, 131273.

7 I. Khan, K. Saeed, I. Zekker, B. Zhang, A. H. Hendi, A. Ahmad, S. Ahmad, N. Zada, H. Ahmad, L. A. Shah, T. Shah and I. Khan, *Water*, 2022, **14**, 242.

8 A. Houas, *Applied Catalysis B: Environmental*, 2001, **31**, 145–157.

9 S. Bhullar, N. Goyal and S. Gupta, *RSC Adv.*, 2021, **11**, 30343–30352.

10 Y. Ide, W. Shirae, T. Takei, D. Mani and J. Henzie, *Inorg. Chem.*, 2018, **57**, 6045–6050.

11 P. Makal and D. Das, *Applied Surface Science*, 2018, **455**, 1106–1115.

12 Y. Wang and J. Zhang, *Ionics*, 2020, **26**, 1159–1164.

13 S.-O. Kang, J. Choi, I. Hwang, S. Hong, B. H. Park, Y.-I. Kim, S. J. Ahn and K.-S. Yun, *J. Korean Phy. Soc.*, 2008, **52**, 466–470.

14 S. Liu, H. Jia, L. Han, J. Wang, P. Gao, D. Xu, J. Yang and S. Che, *Advanced Materials*, 2012, **24**, 3201–3204.

15 S.-Z. Kure-Chu, H. Sakuyama, E. Suzuki, H. Yashiro, K. Sasaki, H. Segawa and T. Hihara, *J. Electrochem. Soc.*, 2018, **165**, A477–A486.

16 P. Wang, C. Qi, P. Wen, L. Hao, X. Xu and S. Agathopoulos, *Nanomaterials*, 2018, **8**, 294.

17 M. Zhang, Y. Zhou, F. Wang, Z. Chen, X. Zhao, W. Duan, G. Yin, X. Yang, J. Li, Q. Yin and M. Zhao, *Front. Chem.*, 2022, **10**, 1054286.

18 B. Lesiak, L. Kövér, J. Tóth, J. Zemek, P. Jiricek, A. Kromka and N. Rangam, *Applied Surface Science*, 2018, **452**, 223–231.

19 K. Artyushkova, *Journal of Vacuum Science & Technology A: Vacuum, Surfaces, and Films*, 2020, **38**, 031002.

20 K. G. Nguyen, I.-A. Baragau, R. Gromicova, A. Nicolaev, S. A. J. Thomson, A. Rennie, N. P. Power, M. T. Sajjad and S. Kellici, *Sci Rep*, 2022, **12**, 13806.

21 B. Zewde, P. Pitliya and D. Raghavan, *J Mater Sci*, 2016, **51**, 9314–9329.

22 A. Becheri, M. Dürr, P. Lo Nostro and P. Baglioni, *J Nanopart Res*, 2008, **10**, 679–689.

23 N. S. Allen, N. Mahdjoub, V. Vishnyakov, P. J. Kelly and R. J. Kriek, *Polymer Degradation and Stability*, 2018, **150**, 31–36.

24 Q. Wang, Z. Guo and J. S. Chung, *Materials Research Bulletin*, 2009, **44**, 1973–1977.

25 V. Aravindan, N. Shubha, Y. L. Cheah, R. Prasanth, W. Chuiling, R. R. Prabhakar and S. Madhavi, *J. Mater. Chem. A*, 2013, **1**, 308–316.

26 J. R. Jokisaari, D. Bayerl, K. Zhang, L. Xie, Y. Nie, D. G. Schlom, E. Kioupakis, G. W. Graham and X. Pan, *Chem. Mater.*, 2015, **27**, 7896–7902.

27 A. Iborra-Torres, M. Huš, K. Nguyen, A. Vamvakeros, M. T. Sajjad, S. Dunn, M. Mertens, S. Jacques, A. M. Beale, B. Likozar, G. Hyett, S. Kellici and V. Middelkoop, *Mater. Adv.*, 2023, **4**, 3461–3472.

28 M. Akbarimoosavi, E. Rohwer, A. Rondi, J. Hankache, Y. Geng, S. Decurtins, A. Hauser, S.-X. Liu, T. Feurer and A. Cannizzo, *J. Phys. Chem. C*, 2019, **123**, 8500–8511.

29 Y.-J. Yuan, P. Wang, Z. Li, Y. Wu, W. Bai, Y. Su, J. Guan, S. Wu, J. Zhong, Z.-T. Yu and Z. Zou, *Applied Catalysis B: Environmental*, 2019, **242**, 1–8.

30 R. Alcaraz De La Osa, I. Iparragirre, D. Ortiz and J. M. Saiz, *ChemTexts*, 2020, **6**, 2.

31 Z. Xiong, H. Chen, L. Lu, R. Shan, Y. Zhang, H. Yuan and Y. Chen, *ACS Omega*, 2023, **8**, 791–803.

32 J. W. Kim and A. Kim, *Current Applied Physics*, 2021, **31**, 52–59.

33 Z. Xiong and X. S. Zhao, *J. Am. Chem. Soc.*, 2012, **134**, 5754–5757.

34 D. Das and P. Makal, *Applied Surface Science*, 2020, **506**, 144880.

35 A. Jamil, T. H. Bokhari, T. Javed, R. Mustafa, M. Sajid, S. Noreen, M. Zuber, A. Nazir, M. Iqbal and M. I. Jilani, *Journal of Materials Research and Technology*, 2020, **9**, 1119–1128.

36 H. D. Tran, D. Q. Nguyen, P. T. Do and U. N. P. Tran, *RSC Adv.*, 2023, **13**, 16915–16925.

37 W. Rudzinski and W. Plazinski, *Environ. Sci. Technol.*, 2008, **42**, 2470–2475.

38 E. D. Revellame, D. L. Fortela, W. Sharp, R. Hernandez and M. E. Zappi, *Cleaner Engineering and Technology*, 2020, **1**, 100032.

39 D. Robati, *J Nanostruct Chem*, 2013, **3**, 55.

40 Q. Sun, D. Zhang, G. Xue, Q. Liu, X. Zhou, Z. Pei, H. Luo and L. Zhu, *Ceramics International*, 2022, **48**, 23182–23194.

41 S. Deka, M. B. Devi, M. R. Khan, Keerthana, A. Venimadhav and B. Choudhury, *ACS Appl. Nano Mater.*, 2022, **5**, 10724–10734.

42 Q. Li, P. Wu, Y. Huang, P. Chen, K. Wu, J. Wu, Y. Luo, L. Wang, S. Yang, Z. Liu and X. Guo, *International Journal of Hydrogen Energy*, 2022, **47**, 15641–15654.

43 H. Luo, S. Dimitrov, M. Daboczi, J.-S. Kim, Q. Guo, Y. Fang, M.-A. Stoeckel, P. Samorì, O. Fenwick, A. B. Jorge Sobrido, X. Wang and M.-M. Titirici, *ACS Appl. Nano Mater.*, 2020, **3**, 3371–3381.

44 J. Camargo, S. Osinaga, M. Febbo, S. P. Machado, F. Rubio-Marcos, L. Ramajo and M. Castro, *J Mater Sci: Mater Electron*, 2021, **32**, 19117–19125.

45 C. Cui, F. Xue, W.-J. Hu and L.-J. Li, *npj 2D Mater Appl*, 2018, **2**, 18.

46 A. Aabid, M. A. Raheman, Y. E. Ibrahim, A. Anjum, M. Hrairi, B. Parveez, N. Parveen and J. Mohammed Zayan, *Sensors*, 2021, **21**, 4145.

47 N. Sezer and M. Koç, *Nano Energy*, 2021, **80**, 105567.

48 Z. Wei, W. Wang, W. Li, X. Bai, J. Zhao, E. C. M. Tse, D. L. Phillips and Y. Zhu, *Angew Chem Int Ed*, 2021, **60**, 8236–8242.

49 K. Wang, C. Han, J. Li, J. Qiu, J. Sunarso and S. Liu, *Angew Chem Int Ed*, 2022, **61**, e202110429.

Chapter 8 : Conclusions and Future Works

This PhD thesis pioneers the scalable and sustainable production of precision-engineered carbon quantum dots (CQDs) with optimized optical and structural properties using a continuous hydrothermal flow synthesis (CHFS) approach. Leveraging the green, efficient, and tuneable CHFS synthetic process, the overarching goal was to achieve unparalleled control over the deliberate design and synthesis of uniform CQDs with reproducible, application-targeted attributes. Comprehensive studies systematically investigated how key parameters including dopant concentrations, carbon and heteroatom precursor sources, and processing conditions fundamentally impact mechanisms of CQD nucleation, growth, and final particle characteristics. Advanced microscopic and spectroscopic analytical techniques provided unrivalled insights interconnecting the physical, electronic, and chemical essence of CQDs to their underlying synthetic procedures. By elucidating these fundamental structure-property-processing relationships, this work realized the targeted synthesis of finely customizable photoluminescent CQDs through the sustainable CHFS methodology. Specifically, by modulating factors like nitrogen doping levels, this research optimized and customized optical properties of CQDs including emission spectra, quantum yields, and photostability. Additionally, variation of biomass-derived carbon sources revealed connected impacts on particle size distribution, surface chemistry, and defect state photoluminescence. Ultimately, the combination of rationally designed synthetic processes with extensive materials characterisation enabled precision control over CQD properties for matching diverse application requirements. To demonstrate their immense technological potential, the optimized CQDs were implemented as fluorescent nano-sensors for detecting heavy metal ions through fluorescence quenching. Additionally, the utility of CQDs was expanded by synthesising nanocomposite photocatalysts comprising CQDs coupled with conventional semiconductors like TiO_2. This underscores how rationally incorporating CQDs as sensitizers or co-catalysts via scalable methodologies like CHFS can unlock superior performance in catalytic and optoelectronic systems, opening new horizons for hybrid nanomaterials.

This thesis provides an extensive literature review summarizing the current status and ongoing challenges in the rapidly developing field of carbon quantum dots (CQDs) research. It establishes broad foundational knowledge covering the classification systems, versatile properties, diverse applications, and the wide range of synthetic strategies established for CQDs. Numerous methodologies including top-down approaches as well as bottom-up techniques for CQDs production are critically analysed and contrasted. However, the highlight of this thesis lies in the detailed introduction and examination of the continuous hydrothermal flow synthesis methodology for scalable CQD production. The fundamental principles underlying this process, from supercritical fluid properties to nanoparticle nucleation and growth mechanisms in the unique reaction environment are elaborated. Additionally, the specific reactor designs and engineering considerations to enable steady, optimized synthesis of CQDs using this technique are underscored. Altogether, while addressing the current advances and limitations in CQD-related research domains, this thesis places particular weightage on providing an in-depth understanding of the unique continuous hydrothermal production systems for enabling sustainable and scalable CQD manufacturing. In addition, the thesis provided a detailed explanation of the synthetic process for a series of CQDs, NCQDs and nanocomposites using CHFS method. The details of a range of characterisations techniques were described to assess the synthesised nanomaterials' morphology, chemical composition, and optical properties, including TEM, XRD, FTIR, XPS, Raman spectroscopy, fluorescence spectroscopy, and photoluminescence lifetime and quantum yield measurements. Furthermore, the thesis elaborated procedures and assessment methods for the synthesised carbon-based nanomaterials, as nano sensors and photocatalysts.

The study about the effect of various carbon precursors on nitrogen carbon quantum dots structure and optical properties, demonstrates a CHFS method to produce nitrogen-doped carbon quantum dots (NCQDs) rapidly and sustainably from biomass precursors including chitosan, lignin, humic acid, and citric acid. The morphology analysis reveals precursor structure impacts NCQD size, with more complex precursors yielding larger NCQDs. Comparing NCQDs from different precursors provides insights into photoluminescence mechanisms, citric acid yields NCQDs with excitation independent, higher efficiency emission. In contrast, high molecular weight precursors give excitation-dependent, red-shifted, lower quantum yield emission. This highlights the role of precursor chemistry in dictating optical properties of NCQDs, as well as nanoparticle size and nitrogen doping configurations. This study provides understanding of the relationships between carbon source, synthesis method, and unique NCQD emission properties.

The investigation of the crucial role of nitrogen precursors in tailoring enhanced optical and chemical properties of NCQDs, reveals the effects of different nitrogen precursors on optimizing the properties of NCQDs synthesised via CHFS. Various NCQDs were successfully synthesised using citric acid and nitrogen dopants consisting of urea, trizma-base, amino acids and chelating agents. HRTEM analysis revealed nitrogen precursors impact NCQD formation and morphology, urea and trizma promote homogeneous nanoparticles with higher graphitic carbon cores, while amino acids and chelating agents yield heterogeneous sizes and polymer-like structures. This highlights the importance of precursor solubility and reactivity on carbonization pathways. Raman and XPS characterisation also support urea and trizma producing higher quality graphitic NCQDs. The nitrogen precursors influence chemical functional groups and nitrogen configurations, subsequently affecting optical properties. The excitation dependent emission NCQDs were observed in the use of amino acids/chelating agents, whereas urea and trizma yielded rare excitation-independent emission with 40% quantum yield. Furthermore, this study provided insights into NCQDs energy band structures and guidance for selecting nitrogen precursors to optimize PLQY, controlled nanoparticle size.

The research in the effect of nitrogen dopant concentration on carbon quantum dot's structure and optical properties, indicated efficient synthesis of NCQDs from glucose and ammonia solution using CHFS. By systematically varying nitrogen dopant concentration, the impact on NCQD nanoparticle formation, morphology and properties was revealed. Higher dopant concentrations yield a greater of percentage of smaller nanoparticles, with reduced carbon content, suggesting precursor ratios control particle size. The synthesised NCQDs possess excellent pH stability with the PL intensity remains in a wide range of pH from 2-11. The NCQDs were applied as a chemical sensor for Cr(VI) ions, exhibiting a 0.945 ppm limit of detection. Fluorescence lifetime studies confirmed Inner Filter Effect as the NCQD sensor quenching mechanism. Also, this study provided guidance for applying NCQDs in nano sensors, highlighting factors like pH stability, Stern-Volmer analysis and quenching mechanisms.

The last study presented in this PhD thesis revealed efficient synthesis of TiO_2-based nanocomposite photocatalysts with NCQDs using continuous hydrothermal flow synthesis without need for post-treatment processes. The NCQD-TiO_2 nanocomposites displayed excellent dye degradation performance under various conditions. Characterisation revealed CHFS synthesis induces structural and chemical changes, NCQD-TiO_2 contains primarily TiO_2 anatase phase. While without the use of NCQD, the synthesised TiO_2 nanocomposite consist of TiO_2 anatase, TiO_2-B and $K_2Ti_4O_9$ phases. Both TiO_2 and NCQD-TiO_2 nanocomposites showed comparable, outstanding dye degradation capabilities. Notably, NCQD - TiO_2 removed

93% methylene blue (15.0 ppm) in 2 hours under 1 sun, only slightly dropping to 85% removal under 0.5 sun intensity of light. This work introduces a rapid CHFS synthesis method for NCQD-semiconductor nanocomposites as next-generation photocatalysts.

In conclusion, the studies presented in this thesis have demonstrated the potential of carbon quantum dots and the capability of the continuous hydrothermal flow synthesis method. However, there remain opportunities for further research to further optimise the CQD synthetic process, with the aims of enabling productive scaling up from lab to industrial production volumes and facilitating translation from the research lab setting to real-world applications.

Suggestion for future works:

- Further optimise NCQD properties by testing additional nitrogen dopant precursors and sustainable carbon sources based on the obtained data. Systematically investigate how different functional groups and precursor structures influence NCQD photoluminescence, charge transfer capabilities, and the formation of fluorophore.

- Evaluate the synthesised NCQDs as co-catalysts for other key processes like hydrogen production. Optimise NCQD loading and test catalytic performance to expand their demonstrated photocatalytic enhancement effects.

- Optimize continuous flow synthesis parameters including temperature, pressure, and residence time to allow gram-scale production of NCQDs for testing in practical systems. Also, optimise the filtering process.

- Establish collaborations to translate lab-based NCQD synthesis into scalable manufacturing processes. Explore the application of NCQDs in electronic devices.